UNIVERSIDAD COMPLUTENSE DE MADRID

FACULTAD DE CIENCIAS FÍSICAS
Departamento de Física de Materiales

INTERACTIONS IN NOVEL LOW-DIMENSIONAL QUANTUM SYSTEMS: ARRAYS OF COLD ATOMS AND GRAPHENE MONOLAYERS.

MEMORIA PARA OPTAR AL GRADO DE DOCTOR

PRESENTADA POR

Javier Sabio González

Bajo la dirección de los doctores

Francisco Guinea López
Fernando Sols Lucía

Madrid, 2010

ISBN: 978-84-693-8781-8

Universidad Complutense de Madrid

Departamento de Física de Materiales

INTERACTIONS IN NOVEL LOW-DIMENSIONAL QUANTUM SYSTEMS: ARRAYS OF COLD ATOMS AND GRAPHENE MONOLAYERS

Memoria de la tesis presentada por

Javier Sabio González

para optar al grado de Doctor en Ciencias Físicas

Directores:

Francisco Guinea López y Fernando Sols Lucia

Madrid, Marzo de 2010

Agradecimientos

Los físicos son las únicas personas que conozco que con treinta años todavía creen que pueden hacer carrera de bailarina profesional.

A.I. Fernández-Domínguez

Durante esta tesis he tenido la oportunidad de conocer a muchos físicos. El físico es una especie particular (y por físico me refiero al colectivo de los físicos y de las físicas). Es inquieto por naturaleza, y suele tener muchas aficiones. Gusta de las generalizaciones, pero se deleita por las cosas pequeñas, casi ínfimas. Las montañas suelen ser su refugio, a las que acude con toda la asiduidad que una vida por lo general desorganizada puede permitirle. Entre mis mejores amigos se cuentan físicos, y no creo que sea únicamente porque me pase el tiempo rodeado de ellos. El físico es solitario, independiente, pero disfruta de una buena conversación. Puede ser una buen compañía en los viajes, de esos en los que se disfrutan las pausas y se saborean los silencios, sobre todo cuando preceden al rumor de las risas aderezadas por una buena cerveza. Porque es, sin duda el físico, un buen bebedor. Ha probado todas las cervezas del mundo, y de seguro tiene más de una teoría sobre ellas. No le hace ascos tampoco al vino. Cualquier rumor etílico estimulará su fantasía, que dicha en palabras recuerda a ecuaciones que no siempre resultan ser tan buenas metáforas de esa realidad que pretenden homenajear. Y es que para el físico, qué duda cabe, todo es entendible en el lenguaje de la Física. Es después de todo el regalo merecido tras muchos años de dedicación al estudio, pero también la cárcel que lo retiene en un mundo de abstracciones para pocos comprensibles. Con el discurrir del tiempo, les he visto componer modelos cuánticos sobre el comportamiento emocional, describir el convulso mundo de la política con la misma lógica que guía a un fluído. Pero las personas están lejos de la belleza intangible de su realidad subyacente, y eso lo entiende cada físico en su fuero interno. Quizás por eso son todos ellos tan buenos músicos. Tal vez porque buscan un poco de evasión en las fugaces notas, aquella que ni siquiera encuentran en el eco de las simas montañosas. Es el físico, no obstante, también arrogante. Se sabe buen entendedor de casi todo, y exporta su manera de hacer las cosas a cada faceta de la realidad que le rodea. En un mundo de físicos, cada detalle se coordinaría para dar lugar a un grán mecanismo por el cual todo giraría armoniosamente, al compás quizás de una sonada sinfonía. En la realidad, ni la pequeña parcela del mundo dejada a su gestión termina por encajar del todo. Es quizás que los asuntos humanos son demasiado tediosos, o tal vez que una vez discernida la solución al problema, implementarla sería tan obvio que ni merece intentarlo. En cualquier caso, si de algo estoy seguro, es que ningún esquema concreto podría encasillar bien al

físico. A este lo podrás encontrar dirigiendo la más venturosa empresa, escudriñando los límites del universo, explorando los confines del mundo, o dirimiendo asuntos de relevancia internacional. Ya lo he dicho, puede que sea por ese regalo, el que nos da la seguridad de que lo podemos entender todo, aunque no lo hagamos en realidad. Porque no tiene edad, no, el físico, para dejar de descubrir y de explorar. Por eso, creo yo, no se le puede cerrar las puertas a emprender, incluso con treinta años, la carrera de bailarina profesional.

Esta tesis es de alguna manera producto del esfuerzo coordinado de todos esos físicos que me honra haber conocido durante los más de cuatro años que tardé en componerla. Algunos, porque me ayudaron a rellenar huecos entre compás y compás. Otros, los que más, haciendo de mi lugar de trabajo, ya fuese en España o el extranjero, un sitio agradable en el que querer pasar las horas. Es por ello el momento y el lugar –privilegios de un mundo clásico– para agradecérselo explicitamente.

Como no, lo primero es agradecer a esos dos excelentes físicos que son mis directores de tesis, Fernando Sols y Francisco Guinea. A Fernando lo conocí cuando estaba en tercero de carrera, y desde entonces me hizo ver el atractivo de este mundo donde lo mucho se dice ser diferente. Por él conocí también a Paco, en uno de esos veranos tórridos que nos toca pasar a los madrileños que no emigramos. Fue en cuarto de carrera. Ambos se han tomado la molestia de enseñarme el arte de la composición en Física, y de compartir conmigo sus ideas. Y sin ningún problema, me han dejado tomar la batuta allá donde lo deseaba, lo cual me ha ayudado a mí, creo yo, a medrar como científico. No puedo resumir mejor mi gratitud a ellos dos sino diciendo que, sin duda, y con esa panorámica que sólo te ofrece el ver las cosas desde el final, esta es la tesis que quería escribir cuando empecé hace más de cuatro años. Y cuan Pierre Menard de la Física, creo que de intentar escribir otra me saldría la misma.

Pero no son los únicos que generosamente me dieron sus ideas para definir los temas principales de este trabajo. A Antonio H. Castro Neto, he de agradecerle además que me diese los mejores meses de esta tesis en cuanto a ambiente de investigación se refiere. El entusiasmo con el que se discutía Física en su grupo de Boston University sentó un referente para mí, y qué duda cabe de que él era el principal responsable del mismo. Stefan Kehrein amablemente me acogió en su grupo de la Ludwig-Maximiliam Universität, en Munich, y gracias a él no sólo me introduje en un campo de investigación fascinante, sino que también me ayudó a entender muchos conceptos que había dejado aparcados en los años anteriores de la tesis e incluso la carrera.

He de mencionar también a mis varios colaboradores. Todos juntos, codo con codo, nos esforzamos en hacer que la obra sonase medianamente afinada. Quiero destacar a Laszlo Borda, que me recibió hospitalariamente en Budapest en mi primera estancia en el extranjero, y con suma paciencia me enseñó los fundamentos de una enrevesada técnica numérica. En Johan Nilsson tuve el placer de encontrar a una persona con la que discutir los problemas a los que nos enfrentábamos de forma sumamente divertida y siempre inteligente, gracias a su profundo entendimiento de la Física. Y cómo no, dar las gracias a César, mi *hermano mayor* de tesis, que en mis primeros anõs de tesis siempre estuvo ahí para responder a cualquiera de las muchas preguntas que me surgían. Finalmente, agradecer a Simone Fratini las discusiones que surgieron durante su estancia aquí un par de años, que supimos canalizar eficazmente en un artículo.

Hasta aquí he mencionado a todos aquellos que directamente han impreso su huella de forma explícita en este trabajo. Pero hay muchas otras personas que también han influido en el producto final de variopintas maneras, y que por eso merecen un lugar en estos agradecimientos. Como no quiero entrar demasiado en lo que esas personas han significado para mí en el plano personal, trataré de limitarme, en lo posible, a aquellas cosas que creo que están más relacionadas con el contexto de esta tesis.

A Carlos me gustaría darle las gracias por todas esas conversaciones sobre metafísica doctorantil que si bien no están directamente incluídas en la tesis, de seguro que pueden leerse entre líneas. La oportunidad de haber compartido con él la aventura de elaborar una tesis, así como el haber podido forjar una amistad en este periodo de cuatro años, es una de esas escasas experiencias en la vida que, cuando acaban, se es consciente de que ya no se espera encontrar algo mejor mirando hacia el futuro.

De Antonio quiero elogiar su infatigable creencia en mi capacidad para hacer Física. Creo que podría decir sin duda que eso me motivó, día a día tras desayunar con él, a superarme a mí mismo no sea que le decepcionase. En realidad era al revés, Antonio, y siempre fuiste tú del que los demás teníamos mucho que aprender.

A Jose me gustaría gradecerle esa otra tesis no escrita sobre dinámica de atascos y transiciones de fase en los bares de tapas. Quede ahí, si acaso, perdida junto al murmullo de las hojas que pueblan la sierra madrileña.

A David le agradezco que después de tantos años de inagotable amistad todavía lo tuviese a mi lado cuatro anõs más para mantener el despacho silencioso, lo que seguro aceleró la gestación de la tesis. No cabe sino preguntarme si es aquí donde el destino tiene decidido que nuestros caminos se separen, o todavía habremos de compartir alguna otra aventura juntos.

Especial mención me gustaría hacerle a Fernando (de Juan). De mis amigos, es posiblemente quien más ha contribuído al contenido de estas páginas. De él aprendí lo importante que es tratar de entender de verdad las cosas, y he tenido la suerte de tenerlo siempre cerca (ya sea espalda con espalda en el despacho, en el remoto valle de la muerte o escalando el Aneto entre charla y charla) para discutir cada minucia que se nos iba ocurriendo. Indudablemente, de todas esas conversaciones saqué algo inteligente que a mí no se me había ocurrido.

Pero todavía hay más gente a la que agradecer. A Alberto, maestro del frikismo en todas sus facetas, de cuya desbordante capacidad creativa en la Física hay tanto que aprender. A Elena, por haber contribuido de forma inspiradora al arte de escribir una tesis. A Fiona le agradezco haberme enseñado las sutilezas de la investigación con mayúsculas, la que se juega en las grandes ligas. A Silvia el haberme procurado entretenimiento durante mi estancia en Boston, base de la estabilidad intelectual de la que al fin y al cabo salieron dos papers... Y por supuesto, no olvido a Gladys y Laura, inapreciables compañeras de merienda. A Fito darle las gracias por dejarme el buen sabor de boca de que el entusiasmo del relevo generacional no parece que vaya a decaer. A Bea y Josemi por aguantarme dos años de convivencia durante la tesis, con todos los vaivenes motivacionales que eso conlleva. A Belen su incapacidad de perder la fe en la investigación, que es como la luz de un faro en una tormenta. Y a Geli que siempre haya tratado con tanto tesón de mejorar el ambiente de investigación allá donde esté.

El ritmo se acelera, el final ya se intuye cerca. Quiero dar las gracias a todos los que participaron

en los Seminarios de Formación: Rafa Roldán, Juan Salafranca, Rafa Sánchez, Samuel, César, Carlos, David, Juan Luis, Alberto, Fernando, Elena, Antonio, Dani Figueroa, Fernando Domínguez, Virginia, etc. Y cómo no, a tantos colegas del departamento de los que muchas cosas he podido aprender: Ramón Aguado, Gloria Platero, Luis Brey, Leni Bascones, Sigmund Kohler, y Pilar López Sancho. Y a mis antiguos compañeros de carrera, que siempre me han animado a explicarles lo que hago de manera comprensible para un físico de otro campo: Ana, Paula, Emilio, Javier Abajo, Antonio Benayas, Eva Gallardo, y en especial a Dani G. Figueroa, con el que queda pendiente un paper que mezcle cosmología y materia condensada, y Juanjo López, lo mismo pero de fundamentos de Mecánica Cuántica y, quien sabe, tal vez uno de política cuantitativa. En otro tercio distinto, le agradezco a Guillermo López Santos que me tutelase la investigación para obtener el Diploma de Estudios Avanzados.

Finalmente, pero ni mucho menos última en importancia, a Maria le agradezco que me haya acompañado durante los últimos compases de esta pieza. No satisfecha con haberle dado un sentido al final del camino, me ha ayudado a revisar la obra entera, sin que eso sirva para evadir mi responsabilidad de cualquier error que permanezca.

No es tan importante que la audiencia se estremezca. El que aplaude aquí soy yo. Gracias a todos.

Contents

List of Figures

Abstract

Graphene made us all learn how to draw hexagons.
A. H. Castro Neto

This thesis is devoted to the study of interactions in novel low-dimensional quantum systems from a theoretical point of view. Quantum Physics in the verge of dimensionality is not a recent subject. One might say that it already started when the Hydrogen atom was studied from a quantum mechanical point of view, though its golden age belongs to the seventies and the eighties, when a great improvement of experimental techniques for the synthesis and characterization of artificial nanostructures was achieved. However, in the recent years we have witnessed a real revolution in the field due to the experimental realization of genuinely low-dimensional systems like graphene, a carbon based two-dimensional crystal, or the possibility of engineering highly isolated and tunable lattices where cold atoms become trapped. The particles that propagate along these systems are not independent, but they interact with each other, something that might lead to collective phenomena never observed before in nature.

The unraveling of some of the effects that interactions could have in these systems is the *leitmotiv* of this thesis. Interactions can be present within the system, but also the existence of an environment may produce important perturbations that drive it far from its isolated expected behavior. Therefore, both kinds of interactions will be studied here.

The first part of the thesis concerns interactions in arrays of ultracold atoms. This field has allowed us to realize in the laboratory models of interacting particles that were before considered of purely academical interest. This has stimulated a lot of new theoretical studies with the hope that the improvement of the experiments, still in their early phases despite the marvelous phenomena already reported, will permit to find the physics predicted in the equations and numerical simulations. Hence, this part of the thesis is more speculative than the next one, where experiments will play a pivotal role. It has two chapters. In the first one, the influence of environments on a quantum particle living in a one-dimensional finite lattice is studied, finding that due to this coupling the particle might become localized in one of the lattice sites. The research described in the second chapter is motivated by the controversial issue of thermalization in quantum isolated systems. Experiments are already providing partial answers, but a consistent theoretical framework is still required *in extremis*. In order to shed some light on this elusive question, the dynamics of the well-known sine-Gordon model after a sudden quench of interactions will be studied, in its weak coupling regime. The long-time

regime of this one-dimensional model should provide us with a new piece to complete the puzzle, at the same time that it gives orientations to future experiments of one-dimensional fermions with backward interactions.

The second part of the thesis concerns electron interactions in graphene monolayers, with an important emphasis on experimental results. The low-energy behavior of electrons in graphene turns out to be described by a massless Dirac equation, something that –added to the exotic structural properties that this novel material already presents, has given physicists the opportunity to explore a variety of new unknown phenomena. Three contributions are included in this part. The first one is about interactions between graphene monolayers and the experimental environment where current experiments are performed. These interactions have their origin in the electrostatic coupling between graphene and the different elements required to study its amazing properties. The second chapter is mostly of theoretical interest, since it derives an exact identity that theories of interacting electrons in graphene must fulfill, the f-sum rule. Such an identity also allows for the study of the relative importance of many-body excitations, of relevance when experimental outputs are investigated. Finally, the third chapter addresses the question of strong coupling phases in graphene from the point of view of two-body instabilities. The problem of two interacting Dirac particles in a graphene sheet is addressed, finding that it shows many interesting novel features never reported so far. From this one, the many-body problem is confronted, first by studying the problem of a single exciton in graphene, and then by proposing a variational ansatz to describe the ground state of a possible excitonic phase that might change the metallic properties of graphene samples.

In order to give a self-contained presentation, three introductory chapters are included. A general one, where the field of low-dimensional quantum systems is reviewed, including the novel realizations that will constitute the subject of this thesis. And another two, one at the beginning of each part of the thesis, with a summary of results and techniques concerning interactions that will set the basis of the research described afterwards.

List of acronyms

This is a list of the acronyms used in the text:

- **2DEG** Two-dimensional Electron Gas
- **AF** Antiferromagnetic
- **AFM** Atomic Force Microscopy
- **ARPES** Angle Resolved Photoemission Spectroscopy
- **BCS** Bardeen-Cooper-Schriefer
- **BEC** Bose-Einstein Condensate
- **CDW** Charge Density Wave
- **CL** Caldeira-Leggett
- **DFT** Density Functional Theory
- **DOS** Density of States
- **ETH** Eigenstate Thermalization Hypothesis
- **FE** Flow Equation
- **FQHE** Fractional Quantum Hall Effect
- **HOP** Highly Oriented Pyrolytic
- **IS** Infrared Spectroscopy
- **KT** Kosterlitz-Thouless
- **LL** Luttinger Liquid
- **MC** Monte Carlo
- **MOSFET** Metal-Oxide-Semiconductor Field Effect Transistor
- **NRG** Numerical Renormalization Group
- **QHE** Quantum Hall Effect
- **RPA** Random Phase Approximation

- **RG** Renormalization Group
- **SB** Spin-Boson
- **SC** Superconductor
- **SDW** Spin Density Wave
- **SEM** Scanning Electron Microscope
- **STM** Scanning Tunnelling Microscopy
- **TF** Thomas-Fermi
- **VdW** Van der Waals

Throughout this thesis, natural units such that $\hbar = 1$ and $k_B = 1$ are employed, unless otherwise indicated.

1 Low-dimensional quantum systems

Imagine a vast sheet of paper on which straight lines, triangles, squares, pentagons, hexagons, and other figures, instead of remaining fixed in their places, move freely about, on or in the surface, but without the power of rising above or sinking below it, very much like shadows - only hard and with luminous edges - and you will then have a pretty correct notion of my country and countrymen.

E. A. Abbott (Flatland)

1.1 Introduction

In an introductory chapter one usually seeks a compromise between giving a broad overview of the field and introducing the relevant aspects required to understand the detailed chapters that come afterwards. Low-dimensional quantum systems is already a well-established field, and therefore it would deserve a complete text-book to account for the variety of systems, models and techniques that have been developed in the last years for their synthesis, characterization and analysis. In this thesis I have investigated new realizations of low-dimensional quantum systems that have been created in the laboratory during the last decade. These systems share some properties with the previous realizations, but also include new features that make them somehow unique. In order to keep a good balance between old and new, I will try to find the desired optimum by splitting the chapter into two parts: in the first one, I will give an overview of the already well understood features of the field by pointing out some general facts that should contribute to set the landscape where we will move around later. Then, in the second part I will describe in more detail the new realizations that will be studied in the thesis, setting the subsequent language and the basic formalism.

1.2 General facts on low-dimensional quantum systems

Pushing dimensionality to the quantum limit

The first thing that must be kept in mind is the meaning of a reduced dimensionality. Lower dimensions have drawn the interest of philosophers since the advent of culture. After all, it can be said that roughly a low-dimensional system is present wherever a boundary of a higher dimensional body is found. This way, for every three-dimensional object we can define a two-dimensional surface at the boundaries. It does not require a big imagination to realize that already these lands on which we wander all along our lives, or the very sea surface that so many poets has inspired, are good examples of these kind of boundaries. But then, surfaces can be shaped forming edges, where the one-dimension

naturally arises, as it does at the cutting edge of a sword. And finally, the zero-dimension awaits us in these points where sometimes edges abruptly converge, raising corners. Therefore, being surfaces, edges and corners part of our everyday experience, it makes sense that a lot of thought has traditionally been devoted to these systems. Then, what about low-dimensional quantum systems?

As usual, the quantum world introduces nuances and subtleties that leave obsolete our classical intuitions. When Quantum Mechanics is regarded, the meaning of low-dimensionality gets a more precise –but also demanding– definition. As happens with its classical counterpart, it has something to do with the finiteness of systems. But yet another ingredient is required, since the question of size only makes sense when there is something to compare with. Let me address this issue by invoking an example. In order to see the emergence of systems of lower dimensionality in the quantum world, it proves useful to study the problem of a single quantum particle, described by the Schrödinger equation. If we introduce hard walls in the three dimensions, it will get confined to a finite box of sizes L_x, L_y and L_z, respectively. The energy spectrum becomes quantized by virtue of these boundary conditions [1]:

$$E_{n_x,n_y,n_z} = \frac{\hbar^2\pi^2}{2m}\left(\frac{n_x^2}{L_x^2} + \frac{n_y^2}{L_y^2} + \frac{n_z^2}{L_z^2}\right) \tag{1.1}$$

where $n_{i=x,y,z} = 0, 1, ..., \infty$ and m is the mass of the particle. For the purposes of our discussion, it suffices to consider the energy separation between the ground state and the first excited level:

$$\Delta E_i^{(0)} = \frac{\hbar^2\pi^2}{2mL_i^2} \tag{1.2}$$

that only depends on the mass of the particle and the size of the $i-$dimension of the box. Now we are ready to introduce a first definition of low dimensionality from a quantum mechanical point of view: *a system lowers one dimension when the ground state occupation dominates over the rest of the levels*. On the contrary, the effects of this dimension become notable when the energy levels are densely populated. The crossover between both regimes is nobody's land, where neither the system has lowered its dimensionality, nor it is completely higher dimensional in a classical sense, since the effects of level discretization are still notable. In order to access this lower dimensionality in real systems, typical energy scales, like for instance the temperature T of the environment that embeds it, must be smaller than the first excited state energy, $k_BT \ll \Delta E_i^{(0)}$. Something that can immediately be translated into a condition over the size of the system with respect to the temperature or any other typical energy scale of relevance.

From this definition it is easy to achieve different dimensionalities if the sizes of the system differ substantially –recovering, somehow, the intuitive picture of low dimensionality. We just need to study the system at the appropriate energy scale:

- two-dimensional systems (2D): $\Delta E_i^{(0)}, \Delta E_j^{(0)} \ll k_BT \ll \Delta E_k^{(0)}$
- one-dimensional systems (1D): $\Delta E_i^{(0)} \ll k_BT \ll \Delta E_j^{(0)}, \Delta E_k^{(0)}$
- zero-dimensional systems (0D): $k_BT \ll \Delta E_x^{(0)}, \Delta E_y^{(0)}, \Delta E_z^{(0)}$

Confinement

This is of course just a simple picture, in which actual size is what makes energy levels discrete. In reality, boundaries that give rise to quantization of energy levels may certainly be of a different nature, not necessarily being related to the actual spatial limits of the system. As we will have the opportunity to see, many systems owe their lower dimensionality to the confinement that may arise, for instance, due to the existence of external electric or magnetic fields that constrain the motion of particles, lowering effectively the dimensionality. Actually, we might claim that this is the common general situation, leaving system-size just as a particular case of confinement. To sketch the connection, let me write the following one-dimensional Schrödinger equation:

$$\left(-\frac{\hbar^2}{2m}\frac{d^2}{dx^2}+V(x)\right)\psi(x)=E\psi(x) \tag{1.3}$$

The following two formulations of the problem are physically equivalent:

$$\begin{array}{lll} i) & V(x)=0 & \psi(0)=\psi(L)=0 \\ ii) & V(x)=0, 0<x<L & V(x)=\infty, elsewhere \end{array}$$

Moreover, in real systems there never is a perfect boundary, and $V(x) < \infty$ in the external region, giving a vanishing but non-zero wave-function that yields experimentally measurable consequences. But again, by working in the proper energy range, these effects are expected to be negligible and the previous concept of low dimensionality will be recovered.

Genuinely low-dimensional

There is an obvious exception to this rule of thumb for low-dimensionality, reading: what if the system is low-dimensional because its typical size is already at the atomic scale?. For zero-dimension, a single atom already fits this definition. One-dimensional atom chains can be synthesized in the laboratory, as exemplified by the striking experiments with gold atoms reported in [2]. As for two-dimensional systems, graphene is the one to be mentioned, since it is the first genuinely two-dimensional crystal ever observed in nature. In all these examples, dimensionality is not reduced due to energy scales, but because of the actual composition of the system.

A call for awareness should be made at this point. Neither these systems nor the ones introduced before will ever be truly low-dimensional, at least in a purely mathematical sense. Even on the ground state of the quantized energy level structure, the wave-functions have some spreading on the restricted dimension, due, for instance, to the delocalized electronic orbitals of the atoms that compose the system. Moreover, electromagnetic fields always propagate in three dimensions, since they do not tend to be confined by the same mechanisms that apply for real particles. This is, however, the best implementation of a real low-dimensional system in this, our world, of three spatial dimensions. Mathematically, real low-dimensional systems can be envisaged, where even interactions are restricted to the lower dimensions. So far, however, these belong to the realm of pure theoretical abstractions, and realistic calculations must account for the existence of extra dimensions embedding the system under study.

More about size

The field of low-dimensional quantum systems is quite interconnected with Mesoscopic Physics, whose object of study are systems with sizes ranging between the macroscopic and the microscopic –henceforth the name. Mesoscopic systems, put in the verge of lower dimensionality, can give rise to a plethora of amazing phenomena that have been explored for the last thirty years. Remarkably, it happens that realizations of low-dimensional quantum systems tend to fall into the realm of Mesoscopic Physics, due to their actual sizes.

In order to give a more rigorous demarcation of this field of mesoscopic systems, we need to resort to Quantum Mechanics. Once again, it is just a matter of scales, and a full delimitation of this field requires the introduction of a new length scale. If the system has a typical size L, and the particles are in interaction, we can define the so-called phase-coherence length, L_ϕ, as the scale beyond which the particle loses the coherence of its wave-function due to the influence of interactions [3]. A mesoscopic system is one that is larger than a cluster of a few particles but whose size is still of the order of its typical phase-coherence length. Therefore, its properties are ruled by quantum mechanical laws, that may lead, for instance, to the existence of experimentally measurable interference phenomena. It turns out that this phase-coherence length usually has a strong dependence on temperature, so in order to fall into the mesoscopic category it is crucial to achieve low enough temperatures.

Realizations of mesoscopic systems can be found along different fields, from Nuclear Physics to Condensed Matter Physics. However, the pursuit of low dimensionalities has been a quest typically characteristic of the latter. Particularly in nanostructures, which are solid-state systems with typical sizes ranging between 1-100 nm. Most of their amazing properties arise from the behavior of the valence electrons of the atoms that conform them, which turn out to be easily manipulated at the laboratory, entailing a high-degree of tunability that makes them ideal for applications. Recently, however, the rising field of cold atoms trapped in optical lattices is setting a new paradigm in all what concerns this intersection between the small and the highly confined. One of the things that really makes these novel realizations so remarkable is their extremely high isolation from the experimental environment, something that for nanostructures represents a real limitation difficult to beat, since it tends to spoil the necessary quantum properties to exploit their full potential. I will discuss this issue in more detail later.

Engineering low-dimensional quantum system

For every dimension one could recount a brief history of the challenges and breakthroughs that experimentalists had to face in order to envisage low-dimensional quantum systems. In this quest, a large variety of candidates has been explored, ranging from the early studies using polymers to the infamous two-dimensional electron gas (2DEG) in $GaAs/AlGaAs$ heterostructures. This is, actually, an ongoing field of research, where new realizations are continuously proposed and tested in order to find new exotic phenomena.

Experimentally, lower dimensionality is somehow connected with Surface Science, since many of these systems are synthesized, manipulated and/or analyzed on surfaces. The design of low-dimensional systems shares a lot of common features with that of devices, and actually most of

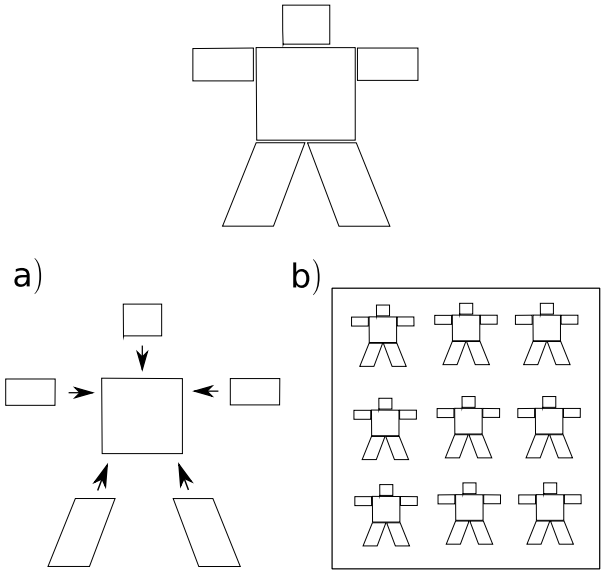

Figure 1.1: How to build a two-dimensional box-man. a) Bottom-up approach: we assemble the different parts that compose the box-man. b) Top-down: we manipulate a macroscopic sample in order to make it self-assemble an army of 2D box-men. Then either we concentrate on a single one or make use of the whole sample.

these systems are proposed, in the end, with the idea of developing technological applications. It should not be surprising, hence, that this field is twinned to Nanotechnology. In the design process, there are essentially two usual approaches. The first one is termed the *bottom-up* approach, and the idea is to build a low-dimensional system or device by assembling its components in a controlled manner. For instance, atom by atom on a surface, or *drawing* a pattern nanolithographically (see below). Within this approach, the system can be engineered in a really detailed way, making it the obvious procedure when the emphasis is put on fundamental aspects of the problem, that typically require extremely high tuning. However, when large-scale applications are regarded, this approach turns out to be quite difficult to scale up, and it must be resorted to alternative proposals in which devices are made by implementing a *top-down* hierarchy. In this case, the strategy relies on envisaging a technique whose output is a macroscopic sample that is composed of smaller subsystems of reduced dimensionality. This approach has connections with the fascinating field of self-assembled structures, and already may count among its achievements the synthesis of both arrays of zero-dimensional dots and one-dimensional chains over surfaces.

In the next subsections, I will try to summarize shortly the most relevant experimental setups traditionally employed to study low-dimensional systems. I will not refer to the newest realizations, for which special sections will be devoted.

Two-dimensional systems

Two-dimensional electron systems are mainly realized with electrons in heterostructures [4], by trapping them at the interface between two different media. Not being my purpose to give a historical

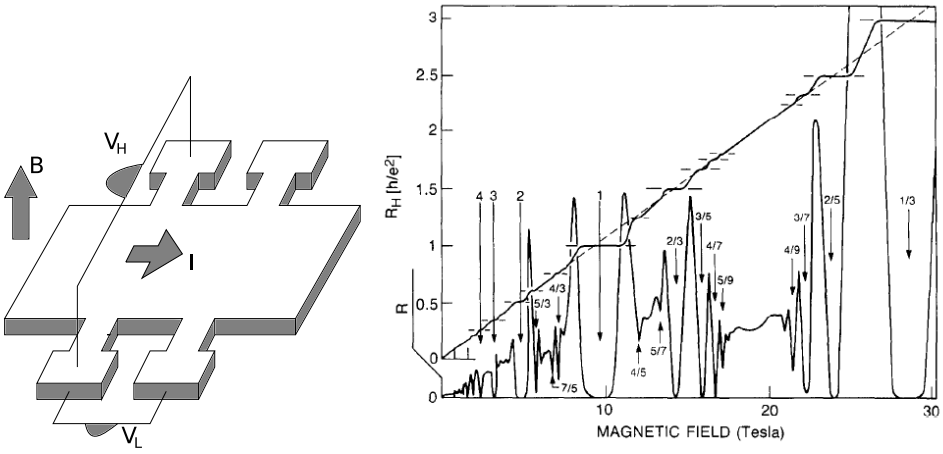

Figure 1.2: Left: Sketch of a Hall bar geometry, with four terminals. The Hall resistance, the inverse of the Hall conductance, is equal to $R_H = V_H/I$, while the longitudinal resistance is $R = V_L/I$. Right: Hall and longitudinal resistance measured in a FQHE experiment, where integer and fractional quantization is shown (figure taken from [9])

review of the field, it is yet interesting to mention one of the first experimental realizations of two-dimensional electron systems: the surface of liquid helium [5], whose first studies date from the sixties. In the latter, electrons deposited from an external source become confined at the interface between Helium and vacuum, i.e, the helium surface. The confinement arises from the fact that helium cannot absorb these electrons due to its negative electronic affinity, repelling them, but at the same time they get attracted by their image potential. Overall, the resulting potential has a minimum close to the helium surface, where they become trapped. By driving the system to the low temperature regime, very small densities can be achieved, and signatures of electron crystallization have been reported experimentally [6].

However, there is no doubt that the most interesting devices for what concerns us in this thesis are the $GaAs/AlGaAs$ heterostructure and the MOSFET (Metal-Oxide-Semiconductor Field Effect Transistor). In both systems it has been possible to engineer a 2DEG by confining electrons at the interface between two different materials when applying external electric fields. Probably the most striking phenomenon observed so far is the Quantum Hall Effect, first reported in a MOSFET by the group of Klaus von Klitzing in 1980 [7]. Two years later, in 1982, experimentalists from Stony Brook University in New York would report the observation of Fractional Quantum Hall Effect in extremely pure $AsGa$ samples[8]. The $GaAs/AlGaAs$ heterostructure also shows a remarkable high mobility of electrons at low temperatures, making it specially suitable for fundamental studies.

The Quantum Hall Effect is expected on general grounds when quantum particles are subjected to an external magnetic field, since the latter gives rise to energy quantization and a discrete spectrum of so-called Landau Levels [1]. At the laboratory, the main signature of the QHE is the quantization of the Hall conductance in units of the universal quantum of conductance e^2/h. The term Hall conductance stands for the transverse conductance that is measured when the 2DEG is arranged in a Hall-bar

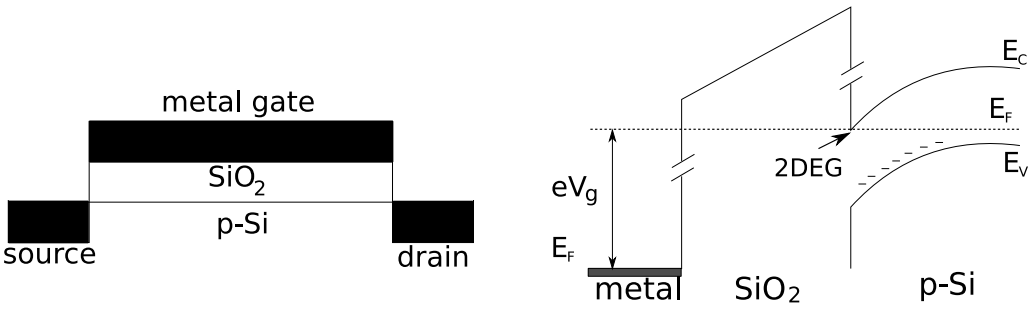

Figure 1.3: Left: Sketch of a MOSFET. Right: Scheme of the electronic bands in a MOSFET device.

geometry, as shown in Fig. 1.2. Remarkably, this behavior was not theoretically expected at the time of its discovery, and a rigorous explanation of this phenomena turns out to be quite more subtle than the simple Landau-levels picture sketched so far. In order to satisfactory explain it, propagating modes along the edges of the sample, that cannot backscatter, must be regarded. These so-called edge states of the QHE, due to their quantum nature, only exist in a discrete set of propagating channels, that in turn explains the observed quantization of conductance. Both explanations are, of course, related, since edge states are nothing but the realization of Landau levels at the boundaries of the sample, while genuine Landau levels remain at the bulk of the 2DEG. They do not conduct charge, preventing the scattering of edge states to the other side.

The Fractional Quantum Hall Effect (FQHE) occurs when, at very low temperatures and by using extremely pure samples, quantization of the universal conductance also manifests itself at fractions of the latter, $n = 1/2, 1/3, ...$ While the *integer* QHE is essentially a single-particle effect, the FQHE is currently understood as a consequence of electron-electron interactions, that would give rise to a complicated quantum many-body state that still today fascinates scientists with its intriguing properties [10].

MOSFET's: The MOSFET system is composed of a SiO_2 (insulating) layer deposited on a p-doped Si substrate (semiconductor) [4]. On the top of the SiO_2 layer, a conducting metallic layer is placed, typically Al. The latter is usually referred to as the gate, while the semiconducting p-doped Si layer is called the inversion layer. Being the latter doped by holes, the application of a positive bias on the gate expels them from the interface, producing an accumulation of negative charge that bends down the bands, as shown in Fig. 1.3. By using strong enough potentials, the bending of the bands can be tuned to make the conduction band (E_C) intersect with the Fermi level (E_F), therefore populating with electrons the first energy level of the effective well that arises in the direction perpendicular to the interface. The electrons, however, remain free to move at the interface. In the general lines described above, one dimension of the system has been effectively ruled out. In the case of electrons in the MOSFET, their motion in the two-dimensional plane is well described by a Schrödinger equation with an effective mass.

GaAs/AlGaAs heterostructures: This heterostructure is composed of a $GaAs$ layer (semiconductor), on top of which a layer of $Al_xGa_{1-x}As$ is grown (n-doped semiconductor, typically by using Si impurities) [3]. Being both semiconductors, the effect of adding Al to the $GaAs$ is to open up a wider

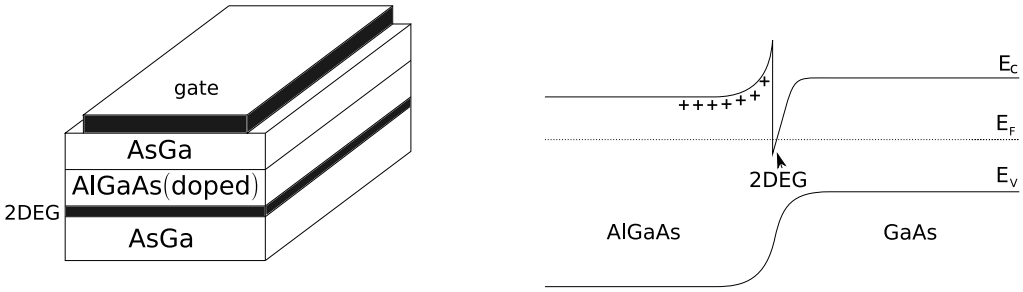

Figure 1.4: Left: Sketch of a $GaAs/AlGaAs$ heterostructure. Right: Scheme of the electronic bands in a $GaAs/AlGaAs$ heterostructure.

gap, as shown in Fig. 1.4. Therefore if the latter is doped, conduction electrons will be introduced to the system, and they will gain energy by migrating to the $GaAs$ conduction band. This translates into an excess of positive charge in the $AlGaAs$ coming from the Si ions, producing an electrostatic potential that, once equilibrium is reached, bends down the $GaAs$ bands. The net effect is similar to the one described in MOSFETs: electrons become confined at the interface, where a quantized level structure results from the resulting triangular quantum well that arises. Now, by placing a metallic gate on top of the heterostructure, the electronic density at the interface can be varied by applying a (as opposite to the MOSFET) negative bias potential, which expels electrons away from the interface. This way, the Fermi level E_F can be moved to populate only the lowest energy level of the quantum well, reducing the dimensionality of the electrons at the interface, that behave like a 2DEG. Again, this system of electrons is well described by a Schrödinger equation with an effective mass. Typical densities achieved in these systems range around $n \sim 10^{11} - 10^{12} cm^{-2}$ [3]. As mentioned before, one of the most remarkable features of this 2DEGs are the high mobilities that can be achieved for their electron carriers: at low temperatures and by using clean samples, mobilities of the order of $30 \times 10^6 cm^2 V^{-1} s^{-1}$ have been reported .

In order to investigate the fundamental properties of 2DEGs in both MOSFETs and $GaAs/AlGaAs$ heterostructures, it is convenient to deplete the electron gas from some regions to produce special geometrical configurations. This can be achieved with techniques of electron beam nanolithography [11], that can be used to mould the gate on top of the heterostructure with the shape of interest. When now the bias gate voltage is applied, the density of electrons will be lowered in those regions where the gate is present, shaping the geometry of the 2DEG according to the pattern initially casted to the gate, as shown in Fig. 1.5. This is the usual approach to create two-dimensional nanostructures and, as we will see later, can be used to further explore lower dimensionalities.

As mentioned, one of the most remarkable manifestations of electrons confined in two dimensional systems is the Quantum Hall Effect. But there are others also worth to be mentioned. For instance, Shubnikov-De Haas oscillations, weak localization (see [12] and references therein), as well as electron crystallization [13]. Moreover, by using particular geometries of the 2DEG, new amazing phenomena can be accessed: when narrow channels are patterned, quantization of the conductance [14]; or with ring-shaped geometries, the Aharonov-Bohm effect [15].

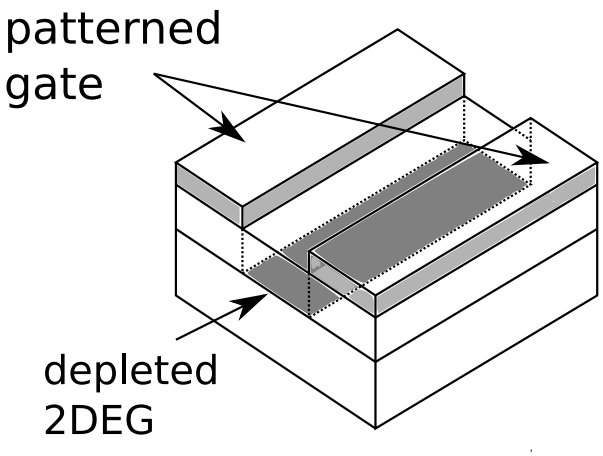

Figure 1.5: Sketch of a patterned gate on top of a 2DEG. Due to the bias voltage applied to the gate, the electron gas is depleted to the region where the gate was subtracted by electron beam nanolithography.

One-dimensional systems

There is a large variety of systems where the one-dimensional world can be studied. Again, most of the research is carried out on the properties of valence electrons of atoms forming molecular and solid-state systems. Theoretically, the field of one-dimensional systems has recurrently drawn the attention of physicists and even mathematicians, due to the variety of exotic phenomena that they are expected to manifest, mostly when electrons (or, in general, fermions) are regarded. Not to mention the large amount of techniques that have become increasingly available to address its study, and the possibility of finding exact solutions of many one-dimensional models [16]. However, from an experimental point of view, the isolation of real one-dimensional systems comes along with various difficulties [10]: sometimes it is due to their complicated chemical structure, which is detrimental when band effects and electron interactions want to be disentangled; it might also be due to the always disruptive influence of the environment, whose effect on nanostructures becomes more dominant as the dimensionality is reduced, since the system gets more exposed; or it can happen that the reduced dimensionality is not completely achieved, in the sense that even though the effects of energy level quantization are pivotal, there are still several energy levels populated. In this case, we would talk about quasi one-dimensional systems.

The necessity of overtaking such a broad range of issues in order to observe truly one-dimensional physics might explain why for years so many candidates have been proposed in the literature. And every new proposal would produce a lot of excitement in the community, carrying as it did the hope of helping to give one step further into this elusive world.

Among the exotic effects that are expected to occur in one-dimensional systems of electrons, probably the most pursued one has been the observation of the so-called Luttinger liquid [16]. This novel state of matter is predicted to arise in a one-dimensional system of electrons in interaction, whose elementary excitations would follow Bose-Einstein statistics, and spin and charge degrees of freedom would be decoupled into two kinds of bosonic excitations: holons and spinons. The expected signa-

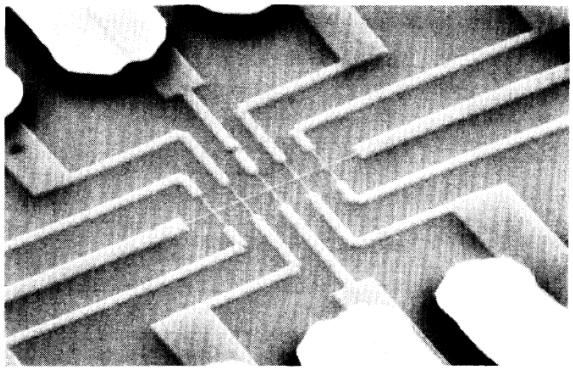

Figure 1.6: A quantum wire produced in a $GaAs/AlGaAs$ heterestructure (taken from [20])

tures of this peculiar electron liquid when experiments are regarded include, for instance, a strong suppression of the electronic density of states at the Fermi level. However, the Luttinger liquid is not the only possible state of one-dimensional matter, since other remarkable effects may arise from the interactions between electrons when other regimes are studied, like the metal-to-insulator transition (or Mott transition) [17].

In the way to fulfill this goal, quasi one-dimensional systems (where, as mentioned, the single occupation of the ground state is not achieved) also offer interesting features that already reflect the emergence of the one-dimensional world. This is the case of the Peierls transition, where at low temperatures a gap in the electronic spectrum opens up due to a dimerization of the atoms that compose a one-dimensional crystal [18]. Or, of course, the onset of superconducting states [16].

Quasi one-dimensional organic conductors: They were the first systems where the one-dimensional world was studied, in the seventies. Essentially, they are one-dimensional chains of molecules, with a complicated band structure that, as mentioned, can make difficult the observation of fundamental effects [10]. A metal-to-insulating transition occurs in the charge-transfer salt $TTF-TCNQ$, below a certain critical temperature. Bechgaard salts, the family of compounds $(TMTSF)_2X$ and $(TMTTF)_2X$ (with X standing for different ions), have a very rich electronic phase diagram with a superconducting (SC) phase, antiferromagnetic (AF) spin-density waves, and signatures of Luttinger Liquid behavior (particularly, charge-spin separation [19]). Again, however, their complicated band structure prevents a truly satisfactory isolation of Luttinger liquid physics.

Quantum wires: As the name suggests, these systems are very narrow wires where the effects of the quantized energy levels are dominant in two spatial directions, restraining the motion of electrons along the wire. They are produced from 2DEGs by using techniques of nanolithography, as explained above. A picture of a typical experimental setup, taken with electronic microscopy, is shown in Fig. 1.6. Since the energy levels are quantized in the perpendicular direction, transport measurements in these systems show quantization of conductance in units of the universal quantum of conductance, $2e^2/h$ [14]. Moreover, in very pure samples, it is possible to track features of purely one-dimensional systems, like Luttinger liquid physics [21]. Another still-to-understand phenomenon found in late experiments with quantum wires is the 0.7-anomaly, where an anomalous plateau at a non-integer

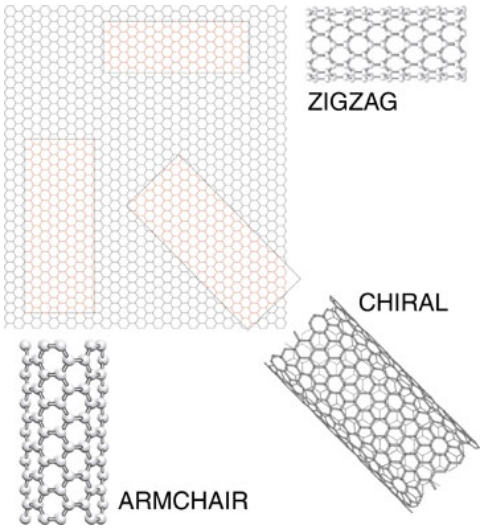

Figure 1.7: Wrapping up a nanotube from a graphene layer. Picture taken from http://www.seas.upenn.edu/mse/research/nanotubes.html

value of the universal quantum is found in conductance measurements [22].

Carbon nanotubes: Carbon, one of the most versatile elements in nature, is known to form one-dimensional wires when carbon sheets, single layers of graphite named graphenes, are rolled up into a cylinder. As shown in Fig. 1.7, depending on the wrapping vector chosen, different kinds of nanotubes are produced, whose properties may differ substantially, ranging from metallic behavior to semimetallic (zero gap semiconductor) and insulating. Carbon nanotubes can be produced in the form of single-walled nanotubes or multi-walled nanotubes, the latter consisting on a hierarchy of nanotubes wrapped up one around the other. Single-walled nanotubes are the most interesting samples for fundamental purposes. They can be found in various diameters, as little as nanometers. The latter, at room temperatures and lower, show strong effects of energy quantization in the radial direction, being only the lowest energy level effectively occupied. Hence, they are natural candidates for the study of one-dimensional systems, mostly when their relatively simple structure, as compared to organic salts, is regarded.

Single-walled nanotubes are isolated in the laboratory, where transport measurements can be conducted in order to study their electronic properties. Luttinger liquid behavior has been invoked to explain the power-law dependence found in several experimental magnitudes [23, 24]. However, even though Luttinger liquids have been theoretically predicted to occur in carbon nanotubes [25], it is still controversial if experimental results are really showing traces of this exotic state [16]. Finally, let me point out that in carbon nanotubes, the coupling of electrons to phonons is very strong, and could give rise to a superconducting phase [26].

Edge states of the quantum Hall effect: As it has been already pointed out, a detailed explanation of the Quantum Hall Effect makes use of propagating electronic states at the edges of the 2DEG [3]. In fact, they can only move in one direction of the edge, since backscattering is strongly suppressed. A classical picture in terms of cyclotron orbits of electrons under a magnetic field is useful to understand

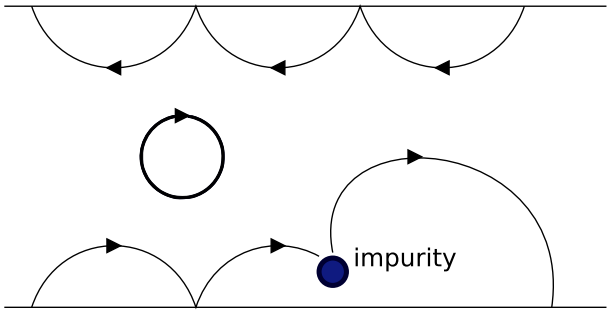

Figure 1.8: Edge states of the Quantum Hall Effect, as depicted in a classical picture. A magnetic field perpendicular to the sample gives rise to closed cyclotron trajectories, that do not conduct charge. This is in contrast to the edges, where electrons can propagate, but only in one direction. The presence of disorder (impurities) does not change the direction of the motion, preventing the existence of backscattering.

edge states, like the one shown in Fig.1.8. As electrons only propagate along the edges, they actually can be seen as a particular case of one-dimensional system. A chiral one, since their movement is limited to only one direction. This connects the observed quantization of conductance in the QHE and the same phenomenon found in narrow electron wires: after all, both can be rooted to the existence of a discrete set of conducting channels due to the lateral confinement [1]. Edge states of the QHE are a powerful tool to study a variety of electronic properties, thanks to the possibility of using nanolithographic techniques to make circuits with edge states. Remember that the system is no more than a $GaAs/AlGaAs$ 2DEG with a perpendicular magnetic field, where the gate can be shaped in order to mold the geometry of the electron gas. Backscattering can be introduced in a controlled way by producing narrow point contacts, where the wave-functions of the edge states overlap, and electrons can hop from one edge to the other. From this, a prolific experimental field has rapidly grown, in which analogous experiments to those performed with photons in Quantum Optics are carried out with fermions, measuring correlations between electrons or making them interfere in Mach-Zender and Hanbury-Brown-Twiss geometries [27, 28].

Even more exciting is the possibility of using edge states of the Fractional Quantum Hall Effect in this kind of experiments. The FQHE is explained as a complicated correlated many-body effect, and theoretical studies suggest that edge states of the FQHE behave as a special kind-of Luttinger Liquid, a chiral one [29]

Other realizations: the fauna of candidates to study one-dimensional systems is really large, and unfortunately I have no space here to describe all of them. For completeness, let me name some of the missing ones, like spin chains [16] or one-dimensional gold atom chains deposited on a substrate.

[1] The main difference being the degeneracy of the channels, that is reduced in the case of edge states, where the electronic spin is fully polarized

In the latter, features of Luttinger-Liquid behavior have been reported [30].

Zero-dimensional systems

In zero-dimensional systems, confinement effects are present in the three dimensions. Electrons trapped in atoms are likely the best example, being ubiquitous in nature. However, those are difficult to isolate and manipulate in the laboratory, so research in zero-dimensional systems has been mostly concentrated on creating their artificial counterparts, named quantum dots. As we discussed above, there are two approaches to synthesize them, the *bottom-up* approach and the *top-down* one. The first one is, with difference, the most successful in order to perform fundamental studies, since the degree of control of the system is extremely high. The most successful realization, in this regard, is the nanolithographically patterned $GaAs/AlGaAs$ quantum dot, though there are other remarkable studies involving systems like quantum dots in carbon nanotubes [31] or metallic nanoparticles [32]. The second approach essentially consists of making self-assembled quantum dots, which are more promising for applications, where large scale production schemes are essential.

$GaAs/AlGaAs$ **quantum dots:** As it has already been explained, they are produced by nanolithographically sculpting the gate on top of the $GaAs/AlGaAs$ heterostructure, in order to confine the 2DEG to a small region of space (an alternative procedure is that of using etching techniques). By means of an external bias potential, the density inside this region can be tuned, and hence the number of electrons populating the energy levels [33]. Due to Pauli's exclusion principle, in order to restrict the occupations strictly to the ground state, the number of electrons inside the nanostructure must be controlled with high accuracy, since only two of them can occupy the lowest level. Such a endeavor has been achieved experimentally, and effects of charge quantization are nowadays a current subject of research (for instance, see [34]). As shown in Fig. 1.9, in order to test the properties of these systems, the dot is not completely isolated from the 2DEG, since a couple of point contacts are added in order to make current flow through the dot and measure the conductance. The geometry shown in this figure corresponds to a horizontal quantum dot, where current flows within the plane. There exist also vertical quantum dots, in which current flows perpendicular to the plane.

Quantum dots have been used to carry out a large number of experiments, in which it was possible to observe a number of fundamental phenomena. Coulomb repulsion between electrons makes electrostatically unfavorable the addition of new electrons to the dot, requiring an extra *charging* energy. The quantum dot is then said to be in the Coulomb blockade regime [36]. Another striking effect that has been possible to observe in quantum dots is the infamous Kondo effect [37]. First studied in the context of quantum impurities in solids, it has attracted the attention of many researchers since the sixties, mostly due to the many theoretical issues that brought into the field of Condensed Matter Physics. The Kondo effect happens for impurities having an electron with spin degeneracy in interaction with an electron gas. The latter strongly screens the impurity spin below a certain crossover temperature, by the formation of a singlet state between the spin of one of the electrons of the gas and that of the impurity. The rest of the electron gas then decouples from the strongly correlated system. This effect fails to be described by conventional perturbation theory, and in order to address it, new sophisticated tools like the Renormalization Group were in turn necessary. Regarding quantum dots,

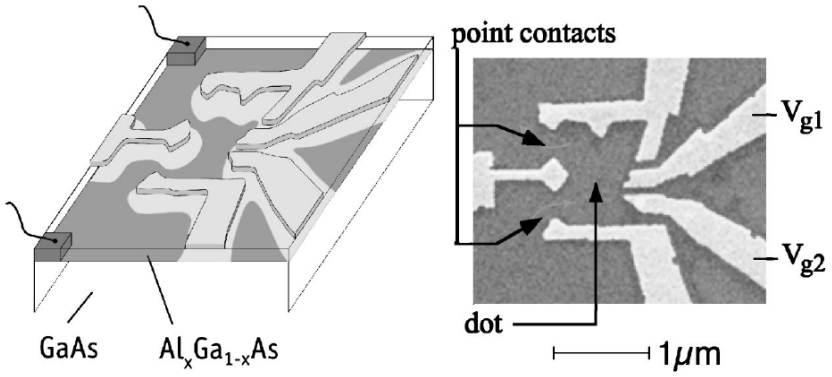

Figure 1.9: Left: Sketch of a nanolithographically patterned quantum dot, created from a $GaAs/AlGaAs$ nanostructure by Folk *et al* [35]. Right: small point contacts are added to allow for some current to pass through the dot. Pictures taken from [33].

a single electron in the valence energy level of a quantum dot can also give rise to this Kondo singlet when coupled to the 2DEG from the leads. The signature of the Kondo effect is the appearance of a resonance at the Fermi level, as it was shown in a remarkable experiment [38].

The variety of phenomena that quantum dots have opened up the possibility to explore is quite more extensive, though. Up to today, waiting for the improvement of experiments regarding ultra cold atoms, quantum dots represent the simplest and best tunable realization of a quantum system coupled to an environment. Therefore, they have drawn the interest of researchers working in fundamental fields as Decoherence and the Quantum-to-Classical Transition [39], Quantum Dissipation [40] and, in general, Open Quantum Systems [41]. All these fields are interrelated, since they share the common interest for understanding how the presence of environments affects the properties of quantum systems: energy transfer (relaxation and dissipation), lost of coherence of wave functions (decoherence and dephasing), and emergence of classical behavior.

From the point of view of applications, quantum dots are also highly promising devices. On the one hand, they can be used as single-electron transistors, a key-piece in the quest to miniaturize electronic devices down to the nanoscale, the main subject of study of the novel field of Nanoelectronics [42]. On the other hand, quantum dots have been for years one of the most solid candidates to produce quantum bits (qubits), the basic component of a quantum computer [43]. However, while $GaAs/AlGaAs$ quantum dots have undoubtedly supposed a cornerstone in the development and understanding of qubits, they are no longer considered for many people as viable candidates to do large scale quantum computation. First, due to the strong coupling of the electron spin to the environment in these systems, that fastly spoils the required quantum properties. And second, due to the difficulties to scale them up to produce devices with a macroscopic number of coupled qubits.

Self-assembled quantum dots: Nowadays, there is a bunch of techniques developed to produce quantum dots in a self-assembled manner. Probably the most popular one is that based on epitaxial growth by using Molecular Beam Epitaxy (MBE). The idea is to grow a layer of a certain material on a different substrate with mismatched lattice structure, like for instance $InAs$ over $GaAs$. Such a type

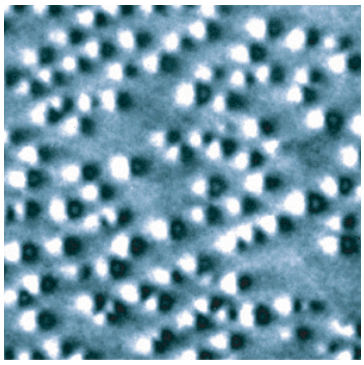

Figure 1.10: Array of $InAs$ self-assembled quantum dots growth by MBE techniques over a $GaAs$ substrate. Picture taken from http://www.nist.gov/public_affairs/update/quantumdots.htm.

of growth is known as Stranski-Krastanov [44], and the net effect is the appearance of a strain on the deposited material, responsible for the formation of a periodic array of islands with typical sizes ranging between $5 - 20nm$. Electrons inside these island are confined in the three dimensions, giving rise to energy level quantization. After burning the possible remains of the $InAs$ layer (the so-called *wetting layer*, necessary for the island formation), an array of quantum dots over $GaAs$ is attained (Fig. 1.10)

As mentioned, there are hopes that this sort of quantum dots may have applications in Quantum Computation. In the meanwhile, however, they are being used extensively in experiments of quantum optics: being somehow artificial atoms, they can be tuned to contain electron transitions not present in real atoms, what allows for new kinds of lasers to be produced [45].

Lower dimensionality means a rising weirdness

After this overview of the *traditional* realizations of low-dimensional systems, there should be no question about the variety and complexity of phenomena that is present in these systems. Apparently, when dimensions are lowered, even the simplest system, like an electron gas, shows amazing features not expected in its higher dimensional counterpart. But somehow, our intuition dictates that it should be the other way round, with systems behaving in a more simplistic way as dimensions are lowered.

A good understanding of this issue is still an ongoing problem. However, some pivotal aspects of it have been already dilucidated. The central idea would be that lower dimensionalities translate into higher constraints of the particles that compose the system (fermions, bosons,..). Interesting physics might be said to be a tale of competing effects, and the introduction of new constraints reduces the playground where these effects are confronted. For instance, the paradigm in the physics of the interacting electron gas, the Fermi Liquid Theory, breaks down in one-dimension because the system is so constrained that particles lose effectiveness for the screening of the interactions between them. Moreover, the Fractional Quantum Hall Effect is only possible when electrons are restricted to a plane, something that can be rooted to the different properties that symmetry groups have in different dimensions. This happens to be true even for non-interacting systems, since already at the level of

the symmetrization principle, dimensionality plays an important part determining the correlations between particles.

Here I will finish this general introduction to the nowadays well-established realizations of low-dimensional quantum systems. But do not mistake me. There is yet a large number of people working in these systems, and they cannot be considered fully understood, not to mention that most of their applications are still to be engineered. However, in the last years two new exciting fields have attracted the attention of a considerable part of the community. These systems, arrays of cold atoms and graphene layers, are the central topics of this thesis, and I will devote the rest of the chapter to introduce them.

1.3 Arrays of cold atoms, engineering the quantum world

During the decade of the nineties the advances in cooling and confinement of weakly interacting atom gases led to the experimental observation of new phases of quantum matter: the Bose-Einstein condensate [46, 47] and the degenerate Fermi gas [48]. These discoveries were somehow the culmination of a challenging quest to improve the cooling techniques necessary to access temperatures below μK or even nK. New sophisticated methods, like laser trapping, evaporative cooling and Sisyphus cooling were combined to reach, in several stages, the low temperatures required to produce the phase transition to the Bose-Einstein Condensate (BEC) in alkaline atoms like ^{87}Rb or Na. These particular atomic species were pivotal to bypass the condensation to a liquid phase that happens to almost every gas in nature, since they are weakly interacting (neutral) atoms. But even so, highly diluted concentrations were required to preserve the gaseous phase down to the BEC critical temperature. A few years later, these techniques would be successfully applied to cool down fermionic gases, like ^{40}K, paving the way for the observation of a truly degenerate Fermi gas.

The field, however, did not stay there, and the last years have witnessed new exciting developments that have quite enlarged its potential to explore new physical phenomena (for an extensive review, see [49]). First, the Feshbach resonance, that allows for the tuning of the interaction strength between particles in a cold gas, conferring on experimentalists even a control of its sign. Interactions, hence, can be changed from attractive to repulsive, and from weak to strong coupling. Second, optical potentials, with which cold gases can be confined into optical lattices, whose dimensionality can be manipulated at will by conveniently adjusting the different lattice spacings. The experimental possibilities that these developments are bringing to the field are yet far from being dilucidated. One of the most exciting applications so far has been the study of the BCS-BEC crossover, in which by tuning the interactions with Feshbach resonances, a molecular gas in the BEC regime can be transformed into a condensate of weakly bounded Cooper pairs [50, 51]. Another striking example of the sort of things that can be achieved with these systems is the observation of a quantum phase transition from a superfluid phase to a Mott-insulator [52]. This transition is very well described within the relatively simple Bose-Hubbard model, whose fermionic counterpart had been already widely studied by the condensed matter community. Therefore, this achievement did not leave that community indifferent, who had spent a lot of time studying these interacting models. They found the rising field of cold

gases in optical lattices a promising way to experimentally simulate many of those models that originally were envisaged as simplifications of more complex systems like solids. After all, most of their exciting theoretical predictions turned out to be quite elusive in the world they were trying to depict. A world where most of the parameters of the model were typically fixed, when the experimental output was not blurred by the presence of disorder or other external agents. Cold atoms may thus provide those athirst beauty seekers with the evasive substance their dreams are made of [2].

The field of low-dimensional quantum systems, the one we are mostly interested in here, has also benefited from ultracold atoms experiments. As mentioned, optical lattices can be used to effectively reduce the dimensionality, since the lattice spacing can be controlled individually for every direction of space. Far from being a proposal, it has already been performed experimentally with the study of the hard-core Bose gas in one dimension [53, 54], or the Kosterlitz-Thouless crossover in a two-dimensional gas [55].

The possibility of engineering quantum systems with optical lattices has revived the interest in topics that were traditionally considered of pure academical interest. This is the case, for instance, for the field of out-of-equilibrium dynamics of isolated many-body quantum systems. Real quantum systems are strongly influenced by the experimental environment where they live, and decoherence and dissipation fastly muddle their intrinsic evolution. Therefore, long-time properties of isolated quantum systems in interaction remained out of the experimental realm for many years. This situation is changing thanks to the high degree of isolation that can be achieved in experiments with ultra cold gases, as already shown in a remarkable study of the out-of-equilibrium dynamics of a one-dimensional Tonks-Girardeau gas [56]. Theoretically, the way a quantum system reaches equilibrium in the long run is still an open and not fully clarified issue. We will have the opportunity to discuss this fascinating problem more extensively in another chapter, being one of the topics selected for this thesis.

My aim in this section is to give a basic introduction to those aspects of the field necessary to understand how a highly tunable interacting low-dimensional quantum system can be produced in the laboratory. I will start describing the generation of optical lattices, to continue then with the Feshbach resonance.

1.3.1 Optical lattices

In order to explain how to generate an optical lattice I will resort to a simple model of optical trapping [57]. Let us consider a neutral atom with a valence electron that can hop between two available levels, the ground state, $|g\rangle$, and the first excited state, $|e\rangle$. An external electric field $\mathbf{E}(\mathbf{r}, t)$ is applied in order to trap the atom. The interaction is of dipolar-kind, with the following Hamiltonian:

$$\mathcal{H}_d = -\mathbf{d}(\mathbf{r}, t) \cdot \mathbf{E}(\mathbf{r}, t) \tag{1.4}$$

[2] I really recommend the introduction to the book of S. Weinberg on Quantum Field Theory, where I was first introduced to the idea of beauty seekers and truth seekers populating the world of Physics.

where $\mathbf{d}$ is the electric dipole moment operator of the electron. If the polarization is induced by the field, the *interaction potential* that the atoms feels is given by [58]:

$$U_{dip} = -\frac{1}{2}\langle \mathbf{d}(\mathbf{r},t)\cdot\mathbf{E}(\mathbf{r},t)\rangle_t \tag{1.5}$$

where $\langle ...\rangle_t$ denotes averaging over time. The force exerted on the atom is then:

$$\mathbf{F}_{dip}(\mathbf{r}) = -\nabla U_{dip}(\mathbf{r}) \tag{1.6}$$

Let us define $d_E = \frac{\mathbf{d}\cdot\mathbf{E}}{E}$, which is the projection of the dipole moment along the electric field direction. By Fourier transforming the equation for the potential we get:

$$U_{dip} = -\frac{1}{2}\sum_{\omega} d_E(\mathbf{r},\omega)E(\mathbf{r},-\omega) \tag{1.7}$$

Now, in linear response, the dipole moment operator can be related to the electric field by introducing the polarizability $\alpha(\mathbf{r},\omega)$ in the way $d_E(\mathbf{r},\omega) = \alpha(\mathbf{r},\omega)E(\mathbf{r},\omega)$. If, for simplicity, we assume the form $E(\mathbf{r},t) = E_0(\mathbf{r})\cos(\omega_0 t)$, the final expression reads:

$$U_{dip} = -\frac{1}{2}\Re\alpha(\omega_0)E_0^2(\mathbf{r}) \tag{1.8}$$

The polarizability $\alpha(\omega)$ can be calculated by using linear response theory:

$$\alpha(t-t') = i\theta(t-t')\langle[d_E(\mathbf{r},t), d_E(\mathbf{r},t')]\rangle_0 \tag{1.9}$$

If the spatial dependence of the electric field changes slowly, the atom will follow it adiabatically, implying that spatial vector $\mathbf{r}$ becomes an external parameter of the equations of motion. In the frequency domain, this translates into:

$$\alpha(\omega) = -\frac{1}{\hbar}|\langle g|d_E(\mathbf{r})|e\rangle|^2\left(\frac{1}{\omega-\omega_{eg}+i\eta} - \frac{1}{\omega+\omega_{eg}-i\eta}\right) \tag{1.10}$$

where $\omega_{eg} \equiv \frac{1}{\hbar}(E_e - E_g)$, i.e., the frequency associated to the excitation energy. Notice that the real part is related to the optical potential, but there is also an imaginary part to account for the broadening of energy levels (i.e., the life-time of the states). Near the resonance, $\omega \sim \omega_{eg}$, and by introducing the Rabi frequency $\Omega_R = \frac{1}{\hbar}|\langle g|d_E E_0|e\rangle|^2$ and the detuning parameter $\delta = \omega_0 - \omega_{eg}$, the expression for the interaction potential becomes:

$$U_{dip} = \frac{\hbar\Omega_R^2\delta}{\delta^2+\eta^2} \tag{1.11}$$

The interaction of the electric field with the neutral atom translates into a trapping potential whose sign depends on the frequency of the field. For $\delta < 0$ it is repulsive, while for $\delta > 0$ it is attractive. In terms of the field intensity $I \equiv 2\epsilon_0 c E_0^2(\mathbf{r})$, this means that for attractive potentials the atoms tend to localize at the minima of the intensity (i.e., those points of space where $E_0^2(\mathbf{r})$ is minimum). In the case of repulsive potentials the behavior is reversed.

The effect described so far is the basic ingredient required to set up an optical lattice. By using laser beams, the standard sources of monochromatic light in experiments, the frequency of the electric

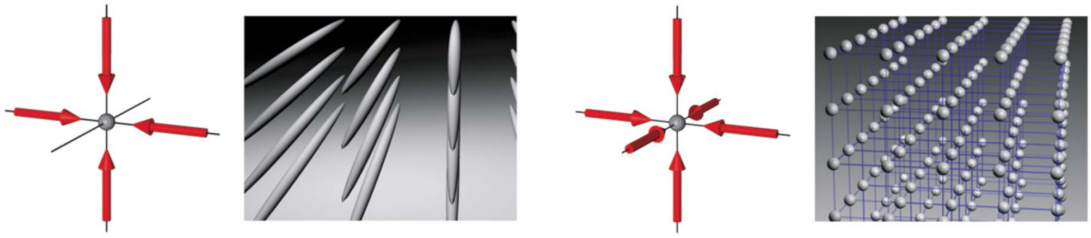

Figure 1.11: Left: Two-dimensional optical lattice made by imposing counter-propagating laser beams in two spatial directions. Notice that for enough large potential depths, the system behaves like a collection of one-dimensional quantum wires. Right: Three-dimensional optical lattice. Pictures taken from [49].

field is well-defined, with a value that can be conveniently selected to induce attractive or repulsive potentials. Now, since neutral atoms tend to locate at the minima or maxima of the intensity profile, by superimposing laser beams from different directions, spatial lattices are generated where the atoms become trapped. In figure 1.11 two and three-dimensional optical lattices are shown. Notice that dimensionality can be lowered by conveniently selecting the lattice depth. For instance, let us suppose we have implemented the following optical potential for a two-dimensional optical lattice:

$$V(x,y,z) = \frac{V_0}{2}\left(\cos(\frac{2\pi x}{d_x}) + \cos(\frac{2\pi y}{d_y})\right) \tag{1.12}$$

where d_x and d_y are the spatial periods. By using large enough values of V_0, the atoms will be constrained to move along the z-axis, giving rise to a collection of nearly independent one-dimensional quantum wires [53, 54].

Ultra-cold atoms trapped in optical lattices behave somehow like electrons in crystals, with the advantage that the lattice spacing and the depth of the periodic potential can be tuned in the laboratory. Therefore due to the periodicity of the system, and in absence of interactions, the atoms will tend to delocalize forming energy bands. However, so far I have not discussed the role of interactions, which actually turns out to be, under certain conditions, another tunable parameter. This will be discussed in the next section.

1.3.2 Interactions between neutral atoms and the Feshbach resonance

Neutral atoms interact due to thermal or quantum fluctuations of charge around the neutrality point, which yields an effective coupling, the van der Waals force. A simple model of van der Waals interactions between neutral atoms is the following:

$$V(r) = \begin{cases} -C_6/r^6 & if \quad r > r_c \\ \infty & if \quad r \leq r_c \end{cases} \tag{1.13}$$

where C_6 depends on the polarizability of the atoms, and r_c is of the order of the atomic dimension. Being attractive, and with a large value of C_6 for alkali metals, which are highly polarizable, it can support many bound states. However, we will be interested here in the collision regime of a dilute

gas at low energies, where the scattering states are the ones relevant for the discussion. From scattering theory, it is well known that the scattering between two particles interacting through a central potential can be described by the accumulation of phase shifts in the different angular-momentum channels, which are good quantum numbers of the two-body problem. For every channel, the wavefunction of the relative problem (once the center-of-mass coordinate gets uncoupled) will have the asymptotic form [1]:

$$R_l(k,r) \to \frac{1}{kr}\sin(kr - l\frac{\pi}{2} + \delta_l(k)) \tag{1.14}$$

where k is the radial momentum, and $\delta_l(k)$ the phase shift. Now, at low energies the scattering is known to be dominated by the lowest channel available. This is, in general, $l = 0$ (s-wave). However, in the presence of an external strong magnetic field, something typical in many experiments, the situation can differ due to the symmetrization principle: it would be $l = 0$ for bosons (s-wave) but $l = 1$ for fermions (p-wave). Quantitatively, this regime is accessed when the condition $ka_c \ll 1$ holds, being $a_c = (2M_rC_6/\hbar^2)^{1/4}$ a characteristic length of the van der Waals potential, defined as the distance at which the kinetic energy equals the potential energy (notice that M_r is the reduced mass for the relative problem).

For the s-wave channel and small momenta, the phase shift goes like $\delta_0(k) \to -ka$, where a is the *scattering-length*, related in turn to the characteristic length of the van der Waals potential [49]. It is important to notice here that, in the low-energy limit, the scattering between two particles (bosons in this case) is specified only by the scattering-length, which somehow means that the problem can be mapped to that of a contact pseudo-potential:

$$V(\mathbf{r}) = g\delta(\mathbf{r}) \tag{1.15}$$

where $g = 4\pi\hbar^2 a/2M_r$ in order to make the equivalence. In the case of polarized fermions, as mentioned, when $ka_c \ll 1$ the scattering is dominated by the p-wave channel, whose cross-section vanishes at low-energies. This means that in the low-energy regime the system behaves essentially like a non-interacting Fermi gas.

But this is not the end of the story. The scattering-length turns out to be sensitive to the presence of an external magnetic field, thus providing experimentalists with a way of tuning externally its value, increasing it or even changing its sign. This phenomenon opens up the possibility of controlling the interactions between neutral atoms in experiments with ultra cold gases. Its origin is basically explained in terms of the so-called Feshbach resonance, a complicated effect whose detailed description unfortunately exceeds the scope of this introductory chapter. The reader interested in more information should check the specialized reviews that are already available in the literature, for instance see [59, 60]. Here I will limit the discussion to a sketch of the underlying physics.

The Feshbach resonance arises due to the scattering of atoms with various internal states, like the spin degree of freedom. For reasons that I will not discuss here, this mechanism works better for fermionic atoms than for bosonic ones. Let me consider the simple case of two atoms with a single valence electron of spin $1/2$, which determines the spin of the atom as a whole. The two-particle system, by virtue of the symmetrization principle, will have two channels of scattering: the singlet channel, $|S\rangle$, and the triplet channel, $|T\rangle$. Being fermions, the scattering will be pervaded by the singlet

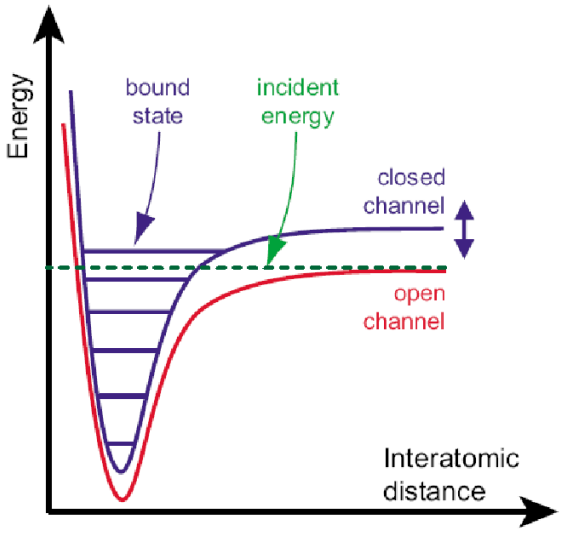

Figure 1.12: Van der Waals central potentials for the scattering of two neutral atoms. The presence of an external magnetic field gives rise to an open and a closed channel. The hyperfine interaction couples both channels. The Feshbach resonance occurs due to coupling between a state prepared in the open channel with a bound state of the closed channel close in energy. Picture taken from [49].

channel, since the triplet one gets less energetically favorable as the two particles approach each other. So far, however, spin interactions have been kept aside from the discussion, but they actually may change this simple picture. They are present as: 1) hyperfine interactions between the electron spin $\mathbf{S}$ and the nuclear one $\mathbf{I}$, in the usual form $V_h = \frac{a_h}{\hbar^2}\mathbf{I}\cdot\mathbf{S}$, and 2) Zeeman splittings $\mathcal{H}_Z = -\mu_z B$ due to the coupling of the magnetic dipole ¯ with an external magnetic field (placed conveniently in the z-direction). The complete Hamiltonian, when written in the singlet and triplet basis, reads:

$$\mathcal{H} = \begin{pmatrix} -\frac{\hbar^2}{2M_r}\nabla^2 + V_{op}(r) & V_h \\ V_h & -\frac{\hbar^2}{2M_r}\nabla^2 + V_{cl}(r) \end{pmatrix} \tag{1.16}$$

where $V_{op}(r) = V_T(r)$ is called the *open channel* potential and $V_{cl}(r) = \Delta\mu B + V_S(r)$ the *closed channel* potential. Notice that the latter includes the Zeeman energy splitting relative to the triplet channel, by introducing $\Delta\mu$, the relative magnetic dipole. $V_T(r)$ and $V_S(r)$ are the effective van der Waals potentials for the triplet and singlet channels, respectively. A plot of both open and closed channel potentials is shown in Fig. 1.12. The closed channel is said to be *closed* because, for energies much smaller than the Zeeman splitting, it is forbidden as an asymptotic scattering channel. This is opposed to what happens for the other one, hence the denomination *open*. By definition, the closed channel does not contain scattering states, but it does have bound states, as is depicted in the figure. Moreover, due to the hyperfine interaction present in the non-diagonal matrix elements of the Hamiltonian, both channels become coupled.

A Feshbach resonance occurs when a couple of particles initially prepared in the open channel, couple to a bound state of the closed channel whose energy is close to that of the incoming state, $E(k) = \hbar^2 k^2/2M_r$. By virtue of the Zeeman splitting, the magnetic field B can be used to modify the

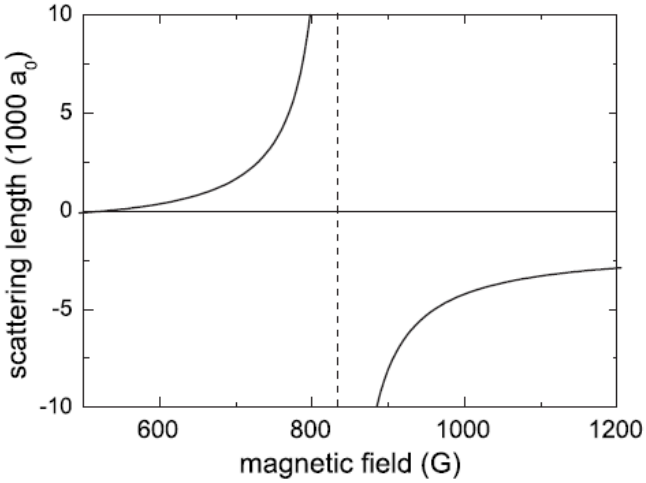

Figure 1.13: Dependence of the scattering-length on the external magnetic field in the Feshbach resonance scenario. Representative parameters for the scattering-length dependences have been chosen for convenience. Picture taken from [49].

position of the bound state. Scattering theory can now be applied to this resonant problem, providing us with the analytical expressions for the phase shifts and the effective scattering-length, which has the following form:

$$a(B) \propto [1 - \Delta B/(B - B_0)] \tag{1.17}$$

where B_0 and ΔB are parameters that denote the width and the position of the resonance. A plot of this function is shown in Fig. 1.13. By inserting this expression into the coupling constant of the contact potential discussed above, Eq. (1.15), we immediately understand the mechanism by which the Feshbach resonance leads to an externally tunable interaction between particles.

In the introduction to this section we learnt that the use of Feshbach resonances to manipulate the scattering-length of ultra cold gases, in combination with the generation of optical lattices, has opened up the possibility of engineering many-body systems in the laboratory. Several examples of this exciting new physics have already been implemented, leading to the observation of a superfluid-Mott transition [**?**] or the realization of a one-dimensional Tonk-Girardeau gas [53], among other exotic phenomena.

1.3.3 Atom chips

To conclude this introduction to the experimental possibilities of ultra cold gases, I will briefly discuss another setup where promising experiments are currently being performed. They are called atom chips, since the idea is to confine neutral atoms close to a insulating substrate where a metallic pattern has been drawn by means of nanolithographic techniques [61, 62]. The atoms become trapped in this case by means of the magnetic fields produced by currents flowing through the metallic

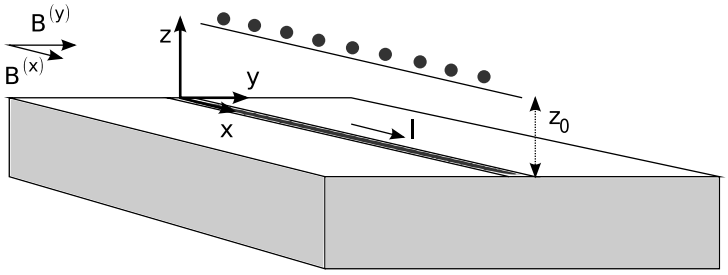

Figure 1.14: Sketch of the geometry of an atom chip designed to produce a one-dimensional wire of cold atoms.

nanostructures. Thus the geometry of the chip will in turn be reflected in that of the trap, allowing for the design of atom wires or even atom circuits where interferometry experiments may be conducted [63]. Moreover, these devices have been proposed as strong candidates for the implementation of quantum bits.

Their main disadvantage, however, comes precisely from the proximity of the atoms to the surface, since they become exposed to a variety of interactions with the active elements present in the substrate, producing decoherence and dissipation phenomena that can ruin the properties of the isolated quantum system [64].

As mentioned, the confinement induced by atom chips is of magnetic nature, as opposed to the electric confinement employed in optical lattices. The magnetic field couples to the magnetic moment of the atom, giving rise to a Zeeman splitting. The Hamiltonian reads:

$$\mathcal{H}_Z = -\bar{} \cdot \mathbf{B} = -\mu|\mathbf{B}| \tag{1.18}$$

where $\mu = \bar{} \cdot \mathbf{B}/|\mathbf{B}|$ is the projection of the magnetic moment along the direction of the magnetic field vector. If the magnetic field varies slowly in space, the adiabatic approximation holds. For positive μ, the atom tends to move towards maxima of $|B(\mathbf{r})|$, hence being referred as *high field seeker*, while for negative μ it moves towards minima, and is denoted as *low field seeker*. In these so-called magnetic microtraps, in order to confine cold atoms, magnetic field configurations with a minimum in its modulus are generated. Therefore neutral atoms must be prepared in a low field seeker state. For instance, a one-dimensional trap can be made by superimposing the magnetic field created by a metallic wire in the chip and a static magnetic field parallel to the surface (see Fig. 1.14). If the chip is located at the plane $z = 0$, the analytic expression of the magnetic field necessary to realize this trap reads:

$$\mathbf{B}(z) = \frac{\mu_0 I}{2\pi} \frac{1}{y^2 + z^2} \begin{pmatrix} 0 \\ -z \\ y \end{pmatrix} + \begin{pmatrix} B^{(x)} \\ B^{(y)} \\ 0 \end{pmatrix} \tag{1.19}$$

where I is the current flowing through the wire, and $B^{(i)}$ are the static magnetic fields applied in order to produce a line of minima at $z_0 = \mu_0 I/(2\pi B^{(y)})$.

However, it is important to remark that the presence of the surface is prone to induce decoherence in the system. Understanding the origin and magnitude of the couplings to the elements of the substrate

is thus of major relevance, in order to improve or at least demarcate the range of operation of the magnetic trap. Essentially, there are two sources of decoherence. The first is related to the electric polarizability of the neutral atoms. As happens with the interactions between neutral atoms, their dipolar fluctuations may also couple to polarizable agents in the atom chip, giving rise to van der Waals forces. Or, for large enough separations to the substrate, retarded Casimir-Polder forces [65]. The second source of decoherence is due to the magnetic noise, which a detailed analysis reveals to be the most relevant. Magnetic noise fluctuations arise from those of the current flowing through the wire, that translate in turn into fluctuations of the confining magnetic field. But there is also another source of magnetic noise: spontaneous currents in the substrate induced by thermal fluctuations, usually termed in the literature *near field noise*. The effectiveness of atom chips devices relies strongly on the ability to bypass these sources of decoherence.

1.4 Graphene, the new king of the two-dimensional world

In 2004 the community of people working on low-dimensional quantum systems got perplexed by the news about the isolation and characterization of a genuinely two-dimensional material: graphene [66]. Graphene is the name for a single-layer of graphite, uncoupled from the bulk. Therefore it is a carbon-based compound, and belongs to the family of the carbon allotropes, like diamond, graphite, carbon nanotubes and fullerenes. Chemically, it is a two-dimensional crystal where carbon atoms are arranged in a honey-comb lattice, as shown in Fig. 1.15. The bonding between carbon atoms occurs by virtue of three sp^2 orbitals, leaving one electron of the four in the valence layer free of bondings, located in p orbitals that spread along the direction perpendicular to the plane of graphene. Due to the overlapping of these orbitals, the electrons tend to delocalize forming bands (so-called π bands), as happens in metals, that are in turn responsible for some of the exotic electronic properties of this material. From the point of view of lattice structure, graphene can be described, as shown in Fig. 1.15, as a two-dimensional Bravais lattice with two atoms per unit cell, that henceforth will be called A and B. Actually, the honey-comb lattice is a superposition of two triangular lattices, one for the A and other for the B atoms.

Since the advent of real graphene samples, the field has become a true scientific phenomenon, reflected on the large number of scientists, contributions and conferences that can be found on the topic [67]. It would be difficult to elucidate the one reason that explains why attracted so much attention. For some people, it is the realization of something apparently impossible [68]: a two-dimensional crystal. How its structure is stable is still a subject of debate, though much has been clarified thanks to the already well-established field of thin membranes [69]. Graphene, after all, is a one-atom thick membrane, with quite interesting elastic properties [70]. But probably the most remarkable features of this material come from its electronic properties, that at low-energies are described by an effective massless Dirac equation [71]. Suddenly, all the lore that was known for electrons ruled by the Schrödinger equation had to be translated into the language of the Dirac equation. And most of the theoretical tools were already implemented. For theorists it was simply a good deal: new exciting phenomena to explore, accessible in the laboratory, that in most cases only required to work out a

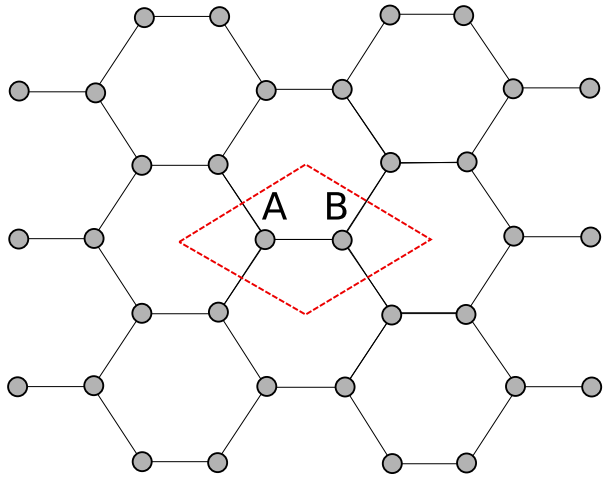

Figure 1.15: Atomic structure of a single layer of graphene: the carbon atoms are arranged in a honey-comb lattice. In terms of lattice structure, it is a Bravais lattice with two atoms per unit cell, which is depicted at the center of the figure. The bond length is approximately $0.14nm$.

single-particle problem. In finance, this is called a good investment, that surely, as always seems to happen with human nature, gave rise to a speculative bubble easy to track in terms of publications[3]. From the experimental point of view, things were not so easy, which explains why the evolution of the field in this direction was more moderate in the first years, with theorists avid of new experimental results.

But there are even more reasons to explain the popularity of graphene. Experiments in graphene early showed that some of the theoretical predictions were not reproduced out of the box [72], and a lot of attention was paid to the actual environment that surrounds graphene [73]. Then, new ways to produce cleaner and more isolated samples were envisaged [74, 75]. Of course, another major source of interest on this novel material is the promise of applications in Nanoelectronics, encouraged by the high electronic mobilities observed, and the possibility of producing mesoscopic samples like graphene nanoribbons [76]. Theoretically, as the field quickly grew up, new aspects of the problem started to attract attention. For instance, the way electronic properties get influenced by structural properties [77, 78], a debate that became hot when experimental results suggested that real graphene samples are not flat but rippled [70]. And last but not least, one may not forget that for some researchers graphene represents an experimental laboratory for exotic phenomena that traditionally belonged to the realm of high energy physics and cosmology [79, 80][4].

In this section I will try to summarize some of the relevant aspects of the field, trying to reflect the excitement that, for five years now, has impregnated the graphene community. However, for a more

[3] The difference being, of course, that returns in science, this is, citations, involve longer time-scales than those of the financial market, making almost impossible a bubble burst.

[4] A call for prudence must be done here: in practice, though there are effects that have reminiscences or are inspired from High Energy Physics, the peculiarities of graphene are too strong to consider that the electrons of this system mimic their counterparts in Particle Physics. This fact enriches graphene physics, but spoils its use to test some of the subtle predictions expected to occur in the high energy regime of nature.

detailed and extensive review, I will refer the reader to [81]. For a more non-technical introduction, I suggest [82, 83].

1.4.1 Experimental fabrication and characterization of graphene layers

Graphene is a single layer of graphite. Since graphite is composed of a stack of graphene layers electrostatically coupled through van der Waals interactions, but not chemically bounded, statistically it is not unlikely to produce graphene from graphite. However, it seems to be more complicated that simply drawing with a pencil, as sometimes is colloquially suggested. In the first report about graphene, by the Manchester group [66], highly oriented pyrolytic graphite (HOP graphite) had to be used in order to find monolayers of graphene. HOPG is a high quality sample of graphite, in which the different graphene layers have an angular spread of 1, not the one found at the tip of your pencil.

Let me clarify this issue in a few lines. Although not being trivial, it is true that a very sophisticated experimental procedure is not required in order to produce graphene samples. Difficulties come rather from the side of their isolation. Graphene is easy to produce, but no too easy to find and isolate. This can be considered the big achievement of the 2004 experiment. Moreover, in order to claim that graphene has been isolated, the samples must show intrinsic properties expected from a two-dimensional carbon crystal. For instance, the presence of massless Dirac fermions as electronic carriers. This entails that the graphene sheet is enough isolated from its environment: single layers of carbon were known to be produced by epitaxial growth many years before 2004, but they were strongly coupled to the substrate, not showing the expected properties. Therefore, in any sensible experiment, graphene not only must be synthesized, but found, isolated and characterized. In the following I will discuss the most typical experimental procedures.

Mechanically exfoliated graphene on top of SiO_2

The discovery of single-layers of graphene in 2004 can be considered, somehow, accidental. After all, the purpose of the research was to study thin graphite films. The method to produce them is called mechanical exfoliation, that popularly is referred to as the *Scotch tape* method, since essentially consists on peeling 3D HOP graphite crystals. The thin graphite films created by exfoliation are then transferred to a substrate made of a $300nm$ thick SiO_2 layer on top of a heavily doped Si metallic gate. The actual width of the insulating layer of SiO_2 turns out to play a major role in the search of single-layers [83]: by virtue of interference effects, they are visible in an optical microscope when placed on top of this particular substrate. Small deviations from the $300nm$ width lead to a blurring of the effect. The graphene crystals found by this technique have sizes up to $100\mu m$. Once graphene is found, AFM experiments can be carried out to confirm the one-atom thickness of the samples. Later, it has been found that single layers of graphene can also be characterized by their Raman signal, though some help from optical methods is still required [84].

However, having produced graphene layers does not imply that they are isolated from the environment. In order to prove that they are pure enough, the samples must be processed into multi-terminal Hall bar devices, where conductivity measurements can be done. An important role in graphene experiments is played by the Si gate below the SiO_2, that allows for the generation of an homogeneous

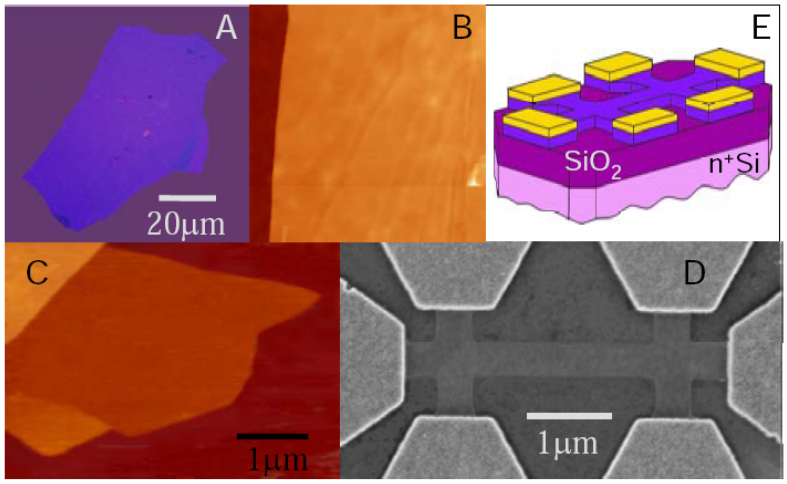

Figure 1.16: Details of the original experiment where graphene was found by mechanical exfoliation. a) Photograph of a few-layer graphene sample. b) AFM characterization of the same sample. c) AFM image of a single-layer graphene sheet. d) SEM Micrograph of a multi-terminal Hall bar built to study the conductivity of graphene samples. e) Scheme of the device shown in d). Pictures taken from [66]

electric field on the sample by applying a gate potential V_g. I will explain shortly why this is important. In Fig. 1.16 details of the experiment are shown. The original characterization of graphene samples was the subject of a couple of articles [66, 72]. In the first one, it was shown that graphene layers have a high Field Effect, meaning that the density of electrons on the sample can be experimentally adjusted by the gate voltage V_g. By using this effect, in later experiments it has been possible to measure resistivity as a function of the density, showing that the electronic carriers have a linear energy spectrum, and that there are two bands that touch at a single point, where conductivity has a controversial minimum (first thought to be universal, now apparently dependent on the presence of disorder in the environment). Fig. 1.17 shows the actual curves from the 2005 experiment. As we will see in the next section, the results correspond well to those theoretically expected from the band structure of the honey-comb lattice, where an effective Dirac equation rules the motion of the electron at low-energies. The second plot in Fig. 1.17 belongs to the 2005 paper as well, and it shows that graphene samples show an anomalous Quantum Hall Effect, with plateaus at half-integers of $4e^2/h$, instead of integers, and a prominent plateau at zero magnetic field. This effect was shown later to persist at room temperatures [85]. Together with the so-called Manchester group, whose results have been discussed so far, people from Columbia university also reported the QHE in graphene samples in 2005 [86], in a work in which high mobilities of the carriers were found, around $\mu \sim 10^4 cm^2/Vs$. This result for the QHE is of major importance, since it serves to definitely state that electronic carriers in graphene are massless Dirac fermions: after all, such an anomalous QHE is one of the more prominent theoretical predictions of a Dirac equation for massless carriers.

Experiments using mechanically exfoliated graphene on top of SiO_2 are, by far, the leading ones in fundamental research on graphene. They have been notoriously improved in the years following

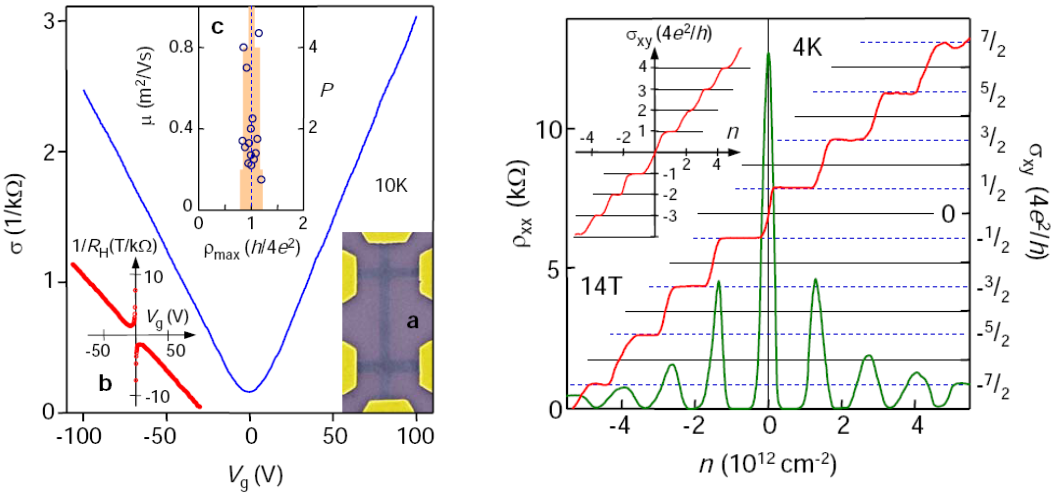

Figure 1.17: Characterization of a graphene sheet by measuring the conductivity in a Hall-bar geometry. a) Conductivity at zero-magnetic field, as a function of density induced by the Field Effect, with a gate voltage V_g. b) Quantum Hall Effect in graphene, with plateaux at half-integers of $4e^2/h$ and a zero-magnetic field plateau. Pictures taken from [72]

the discovery, achieving cleaner samples where the nature of electronic carriers is easier to delucidate. In this regard, notice that when graphene is deposited on surfaces, the contamination from the environment, including the effect of the SiO_2, charge impurities and water, typically produces a lot of distortions in the experimental data. A considerable improvement has been made possible by thermally annealing the samples [83], removing part of the charge scatterers in the environment, and contributing to clarify the controversy about the minimum of conductivity. Another substantial advance has been achieved by removing part of the SiO_2 substrate, thereby producing suspended graphene samples, with a much higher degree of isolation from the environment [74, 75]. Ultra-high mobilities of around $\mu = 200.000 cm^2/Vs$ have been reported in these samples [87]. Most strikingly, recent experiments seem to suggest the existence of the Fractional Quantum Hall Effect in these suspended samples [5]. As I will discuss in chapter 5, effects coming from electron-electron interactions are rare in graphene, whose many features are usually explained in terms of a single-electron picture. This is not necessarily expected from the theoretical side, as already pointed out by Linus Pauling, who early suggested that graphene samples might be a Mott insulator [88].

Epitaxially grown graphene on silicon carbide

There are several ways to epitaxially grow graphene monolayers on different substrates, as for instance metals like ruthenium [89]. Among them, the most successful approach so far is graphene growth on SiC, that is produced by heating the SiC to high temperatures in order to desorb the Si from the top layers, leaving a few layers of graphene on the surface [90]. By controlling the temperature, the typical times involved in the process and the quality of the samples, the number of graphene

[5] Both from the groups of E.Y. Andrei and P. Kim, still to be published

layers produced can be adjusted [91].

Epitaxial graphene samples are different from its mechanically exfoliated counterparts in many ways. First, several layers of graphene are always required in *SiC* setups, since the first layer is strongly bounded to the substrate. The second one, however, is more decoupled, and properties of isolated graphene have been detected, like the linear spectrum expected for massless Dirac carriers [92]. The second difference comes from the possibility of controlling the density of charge carriers: due to the coupling to the substrate, epitaxial graphene samples are heavily doped, making substantially more difficult to access the interesting (at least for fundamental purposes) Dirac point, where the valence and the conduction band touch to each other. The coupling to the substrate is also responsible for some other peculiarities of epitaxial graphene, like the appearance of gaps in the spectrum [93]. The existence of gaps is of major importance regarding the applications of graphene in Nanoelectronics. Actually, epitaxial graphene is considered nowadays the most suitable candidate for a large scale fabrication that, eventually, could be required in real applications. So far, mechanically exfoliated graphene is simply too expensive to produce.

1.4.2 Electronic properties of graphene

I have mentioned a few times that one of the most remarkable properties of graphene is the fact that its charge carriers are massless Dirac fermions. This result was early obtained by P.R. Wallace [71], whose purpose was to derive the band-structure of graphite from a bottom-up perspective. The calculation essentially considers graphene as a system of non-interacting electrons coming from the p orbital perpendicular to the plane. Since the orbitals overlap, the electrons seek to minimize their kinetic energy by becoming spatially delocalized, forming the π band. Electron-electron interactions are not considered in this description, something *a priori* not realistic, but that suffices to explain most of the experimental results.

Let us go back to Fig. 1.15, where the two-dimensional honey-comb lattice is represented. As I already mentioned, the lattice can be described in terms of a Bravais lattice with two inequivalent atoms per unit cell, A and B. This is shown in Fig. 1.18. Every atom A has three nearest neighbors B, and six next nearest neighbors B. The same holds for B atoms, but the other way round. The hopping energy for nearest neighbors is $t = 2.7eV$, while for next nearest neighbors $t' = 0.1eV$. Hence, it is reasonable to restrict ourselves to the nearest neighbors, neglecting the contributions of next nearest neighbors in a first approximation to the electronic structure of graphene. The Hamiltonian reads now:

$$\mathcal{H} = -\frac{t}{2}\sum_{\mathbf{n}} a^{\dagger}_{\mathbf{n}}(b_{\mathbf{n}-\mathbf{a}_1} + b_{\mathbf{n}-\mathbf{a}_2} + b_{\mathbf{n}}) - \frac{t}{2}\sum_{\mathbf{n}} b^{\dagger}_{\mathbf{n}}(a_{\mathbf{n}+\mathbf{a}_1} + a_{\mathbf{n}+\mathbf{a}_2} + a_{\mathbf{n}}) + \text{H.c.} \tag{1.20}$$

where $a^{\dagger}_{\mathbf{n}}$ and $b^{\dagger}_{\mathbf{n}}$ creates an electron at the sites A and B, respectively, of the unit cell $\mathbf{n} = n_1\mathbf{a}_1 + n_2\mathbf{a}_2$. The latter is defined by the vectors $\mathbf{a}_1$ and $\mathbf{a}_2$, as can be seen in Fig. 1.18. As usual, we can take advantage of the periodicity of the structure to apply Bloch's theorem:

$$a_{\mathbf{n}} = \sum_{\mathbf{k}} e^{i\mathbf{k}\cdot\mathbf{n}} a_{\mathbf{k}} \tag{1.21}$$

$$b_{\mathbf{n}} = \sum_{\mathbf{k}} e^{i\mathbf{k}\cdot\mathbf{n}} b_{\mathbf{k}} \tag{1.22}$$

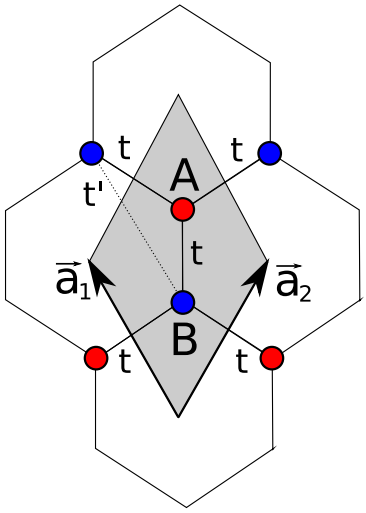

Figure 1.18: Detailed sketch of the unit cell of the honey-comb lattice. There are two atoms per unit cell, A and B. For every atom, its nearest neighbors belong to the other sublattice. The hopping between nearest neighbors is t. The Bravais lattice is defined by translations of the unit cell vectors $\mathbf{a}_1$ and $\mathbf{a}_2$, i.e., $\mathbf{n} = n_1\mathbf{a}_1 + n_2\mathbf{a}_2$.

Introducing this into the Hamiltonian, we can readily show that it has the following form:

$$\mathcal{H} = -t\sum_{\mathbf{k}} \begin{pmatrix} a^\dagger_{\mathbf{k}} & b^\dagger_{\mathbf{k}} \end{pmatrix} \begin{pmatrix} 0 & \alpha^*(\mathbf{k}) \\ \alpha(\mathbf{k}) & 0 \end{pmatrix} \begin{pmatrix} a^\dagger_{\mathbf{k}} \\ b^\dagger_{\mathbf{k}} \end{pmatrix} \tag{1.23}$$

where $\alpha(\mathbf{k}) \equiv 1 + e^{-i\mathbf{k}\cdot\mathbf{a}_1} + e^{i\mathbf{k}\cdot\mathbf{a}_2}$. Being a 2×2 matrix for every $\mathbf{k}$, it can easily be diagonalized. The eigenenergies are $E_\pm(\mathbf{k}) = \pm t|\alpha(\mathbf{k})|$, where:

$$|\alpha(\mathbf{k})| = \sqrt{3 + 2\cos(\mathbf{k}\cdot\mathbf{a}_1) + 2\cos(\mathbf{k}\cdot\mathbf{a}_2) + 2\cos(\mathbf{k}\cdot(\mathbf{a}_2 - \mathbf{a}_2))} \tag{1.24}$$

The eigenvectors read:

$$\begin{aligned} E_+(\mathbf{k}) = t|\alpha(\mathbf{k})|, \quad & \tfrac{1}{\sqrt{2}} \begin{pmatrix} e^{-i\theta_{\mathbf{k}}/2} \\ e^{i\theta_{\mathbf{k}}/2} \end{pmatrix} \\ E_-(\mathbf{k}) = -t|\alpha(\mathbf{k})|, \quad & \tfrac{1}{\sqrt{2}} \begin{pmatrix} e^{-i\theta_{\mathbf{k}}/2} \\ -e^{i\theta_{\mathbf{k}}/2} \end{pmatrix} \end{aligned} \tag{1.25}$$

where I have introduced $\theta_{\mathbf{k}} = \arctan(\frac{Im\{\alpha(\mathbf{k})\}}{Re\{\alpha(\mathbf{k})\}})$. The dispersion $E(\mathbf{k})$ is depicted in Fig. 1.19. There are two symmetric bands, coming from the eigenvalues $\pm t|\alpha(\mathbf{k})|$. They touch at six points, where $E(\mathbf{k}) = 0$, but only two of them are inequivalent. Henceforth they will be call Dirac points, with momenta $\mathbf{K}$ and $\mathbf{K}'$, respectively. This band structure is symmetrical with respect to the Dirac points, and since there is one electron per atom, a neutral graphene sample will be at half-filling. However, corrections coming from considering next nearest neighbors and orbital overlappings can break this electron-hole symmetry.

As shown in Fig. 1.19, the dispersion relation close to the Dirac points can be linearized. Let us take one of the Dirac points, say $\mathbf{K}$, and make an expansion around it, $\mathbf{k} = \mathbf{K} + \mathbf{q}$, for small $\mathbf{q}$ compared

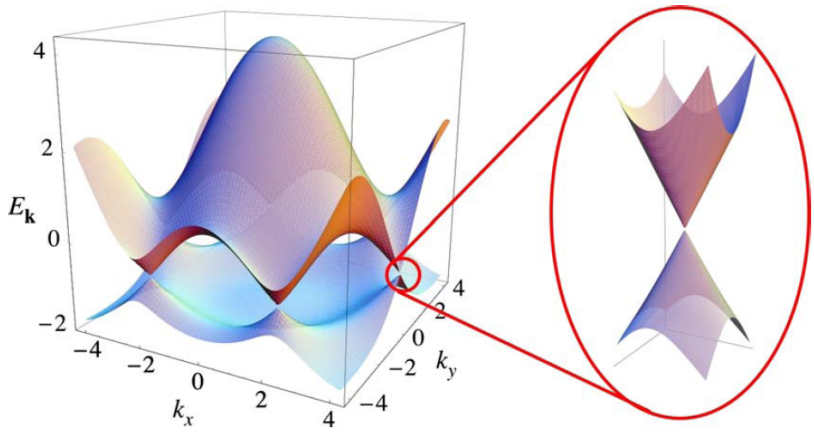

Figure 1.19: Electronic dispersion relation in the honey-comb lattice, as calculated from the tight-binding model with first nearest neighbors. Inset: detail of the dispersion close to the Dirac points, where it becomes linear. Taken from [81]

to **K**. As expected, we find:

$$E_{\pm}(\mathbf{q}) \simeq \pm v_F |\mathbf{q}| \tag{1.26}$$

where $v_F \equiv 3ta/2$ is called the Fermi velocity, being a the lattice spacing in graphene. By inserting the numbers, we find $v_F \sim 10^6 m/s$. A similar result can be obtained for $\mathbf{K}'$, where another *valley* exists. Notice that a plot of this dispersion relation, like the one shown in Fig. 1.19, has a peculiar shape of two opposed cones whose tips touch at the Dirac point. This is the reason why the upper band and the lower band are commonly called Dirac cones.

Therefore, for graphene samples whose chemical potential is placed near the *neutrality point*, that corresponds to the upper cone empty and the lower cone full, then its low-energy excitations have a linear dispersion relation. Moreover, there are four equivalent fermion species with a degenerate energy spectrum, corresponding to the two spin degrees-of-freedom and the two valleys, the latter being a consequence of the existence of two inequivalent Dirac points. The low-energy eigenstates preserve the mathematical structure given in Eq. 1.25, with a simpler expression for the angle, $\theta_{\mathbf{q}} = \arctan(q_x/q_y)$.

In the low-energy regime excitations have long wave-lengths, since $q \to 0$. This means that there is a lost of information about the detailed structure of the honey-comb lattice. In most solid state systems, typically the low-energy electronic spectrum has a quadratic dispersion relation, which implies that the elementary excitations are ruled, back to real space, by an effective Schrödinger equation with a renormalized mass, that depends on the curvature of the band. It is important to notice that this is somehow a coincidence. The fact that the equation describing the motion of real electrons in vacuum is Schrödinger-like does not necessarily imply that the same equation holds for the low-energy excitations of a metal. But it turns out, as it was early realized by particle physicists, that the number of equations that can be proposed to rule the motion of electrons at low energies is not so large on

general grounds. The Schrödinger equation is actually the low-energy limit of the Dirac equation for massive particles. The reason for this can be rooted to deep symmetry considerations.

In graphene, low energy excitations have a linear dispersion relation, which is different from conventional solids, and has consequences for the equation of motion in real space. Mathematically, neglecting the spin, which is decoupled from the motion of the particle, the wave-function is described in terms of a four-spinor, whose motion in real space is ruled by the following Hamiltonian:

$$\mathcal{H} = -iv_F \left(\mathcal{I} \otimes \sigma_x \partial_x + \tau_z \otimes \sigma_y \partial_y \right) = -iv_F \begin{pmatrix} \sigma_x \partial_x + \sigma_y \partial_y & 0 \\ 0 & \sigma_x \partial_x - \sigma_y \partial_y \end{pmatrix} \tag{1.27}$$

This is the infamous Dirac Hamiltonian. It has a Hilbert space of dimension 4, that can be decomposed in two Hilbert subspaces of dimension 2, corresponding to the valley and the sublattice (A or B) degrees-of-freedom. The valley sector of the Hamiltonian is described in terms of τ Pauli matrices of dimension 2×2. The same applies for the sublattice sector, where now σ stands for the corresponding Pauli matrices that act on this subspace. In the second equality of the Hamiltonian, the valley subspace of the Hamiltonian is written explicitly in a matrix notation, every component representing a different valley. It can readily be seen that the equations of motion for the two valleys are related by time-reversal symmetry.

In the physical situations considered along this thesis, both valleys will turn out to be decoupled at low energies, sufficing to consider this Hilbert subspace as an extra degeneration, as happens with the spin when there is no external magnetic field or spin-orbit coupling. Therefore, in the following I will use a two-component Dirac equation, corresponding to one of the valleys.

Most of the electronic properties of graphene at the neutrality point (undoped) or close enough to it (doped), can be explained by using this equation. The local density of states is given by [81]:

$$\rho(E) = \frac{N_s N_v}{2\pi} \frac{|E|}{v_F^2} \tag{1.28}$$

where $N_s N_v$ is the spin and valley degeneracy [6]. It has the very important property that it vanishes at the Dirac point, $E = 0$. Many of the exotic properties of undoped and slightly doped graphene can be related to this vanishing density of states. For instance, as we will have the opportunity to see in Chapter 5, this implies that electron-electron interactions are poorly screened, since there are not enough excitations at low-energy to account for an effective response. Therefore one expects that close to the Dirac point, the usual picture of a Fermi liquid breaks down, and interactions may play an important role. However, as I have already mentioned a few times, it happens that in reality most of the experiments are well fitted by the single-particle model, where interactions are neglected. It could simply happen that real experiments never reach the Dirac point, that for various reasons turns out to be quite elusive. Or it might be that the role of interactions must yet be clarified. I will discuss these issues in the aforementioned chapter.

Another striking property of the low-energy electronic excitations of graphene comes from their *helicity*, sometimes referred to as *chirality*, in analogy to the three-dimensional case. The Hamiltonian for a single valley introduces a coupling between the *pseudospin* σ (i.e., the sublattice in which the

[6] The global density of states is obtained by multiplying this expression by the volume element, $n(E) = L^2 \rho(E)$

electron lives) and the motion of the particle. The eigenstates of this Hamiltonian are also eigenstates of the *helicity* operator:

$$h = \frac{1}{2}\sigma \cdot \frac{\mathbf{q}}{|q|} \tag{1.29}$$

with eigenvalues $\pm 1/2$. This means that σ and $\mathbf{q}$ are aligned in the same direction, but depending on the eigenstate they are parallel or opposite. The main consequence of this extra quantum number is the fact that it must be conserved in many processes. For instance, in the presence of a potential barrier, it can be shown that electrons are completely transmitted when they approach perpendicularly to the barrier, as opposed to the case of Schrödinger electrons. This effect, that was already studied in the context of relativistic particles, is named Klein tunneling [94].

Another interesting phenomenon that was also known in relativistic theory is the so-called *Zitterbewegung* [79]. It essentially states that, due to Heisenberg's principle, an electron in the upper cone in graphene, when spatially confined, has a non-zero projection in the lower cone: i.e., the wavefunctions of electrons and *holes* in graphene overlap during its time-evolution, producing a *jittery motion* that is somehow equivalent to an intrinsic scattering. One of the most striking consequences of this fact is the existence of a finite conductivity at the Dirac point (undoped graphene). By using particular geometries, it can be seen to rise from pseudo-diffusive states (zero energy states of the Dirac equation), and to have a universal value of $4e^2/(\pi h)$[7] [96].

Finally, a general discussion on the electronic properties of graphene would not be complete without mentioning that by solving the Dirac equation in the presence of an external magnetic field, the observed half-integer Quantum Hall Effect is recovered, with the Landau levels given by [97]:

$$E_{\nu\sigma} = \sqrt{2|e|Bv_F^2(\nu + 1/2 \pm 1/2)} \tag{1.30}$$

where $\nu = 0, 1, 2, ...$ and $\pm 1/2$ is connected with the helicity σ. The physics of graphene in the presence of an external magnetic field is a rich topic which, however, I will not emphasize more, since it is out of the scope of the present thesis. For more information, I refer the reader to the references given throughout this section.

1.4.3 Structural properties

So far, I have concentrated the discussion on the electronic properties of graphene. However, as it was already mentioned, one of the most amazing properties of this novel material is the fact that it is a two-dimensional crystal, a one-atom thick membrane. Purely two-dimensional systems with long-range order, like a two-dimensional crystal, were supposed not to exist both because they had never been found in nature, and because there were reasonable theoretical arguments supporting this absence. Mainly, the explanation was given by Landau and Peierls (see references in [83]) and later Mermin [68]. It is essentially based on the Mermin-Wagner-Hohenberg theorem [98, 99], that states

[7] Other calculations yielded $\pi e^2/(2h)$ [95], starting an issue that drew the attention of many theorists for a while, *the missing π problem*. Today, it is understood that is just a matter of how different limits are taken in the course of the calculation, which reflects the fact that the thermodynamic limit is not defined with precision in graphene, and hence quantities like conductivity are sometimes ill-defined.

that continuous symmetries cannot be spontaneously broken at finite temperature in systems with short-range interactions in dimensions $d \leq 2$.

Lattice formation implies precisely the breaking of the continuous translational symmetry, due to the interactions between atoms. The mathematical proof of the absence of crystalline order makes use of the Goldstone modes that arise from the spontaneous breaking of the translation symmetry, which are the phonons in a lattice: low-energy excitations that *tend to reinstate* the broken symmetry. Let us suppose that these phonons are described by a massless scalar field $\phi_i(\mathbf{r})$, where $i = x, y$ is the spatial coordinate. Then, the spatial correlation function reads:

$$\langle \phi_i(\mathbf{r})\phi_j(0)\rangle \propto \int \frac{d^d k}{(2\pi)^d} \frac{e^{i\mathbf{k}\cdot\mathbf{r}}}{k^2} \tag{1.31}$$

For $d \leq 2$, this integral diverges, meaning that thermal fluctuations of phonon modes are not bounded, leading to the destruction of the long-range order.

How is it then that graphene does exist? There are different (but not necessarily incompatible) explanations. On the one hand, graphene samples are not of infinite size and σ bonds between carbon atoms are very strong, preventing that thermal fluctuations destroy them even at high temperatures [83]. Graphene, then, would be a metastable state extracted from the truly stable three-dimensional graphite, but with typical life-times much beyond the observational ones [8]. The second explanation comes from the classical theory of flexible membranes [69]. Graphene is a two-dimensional crystal living in a three-dimensional world, and the latter can provide a mechanism to stabilize the in-plane stretching fluctuations by coupling them to out-of-plane bending modes. Hence, real samples would be crumpled, something that seems to be experimentally confirmed [70], and numerically supported [100]. After all, there is a wide agreement in that graphene is not a perfectly flat crystal, but has *ripples*, static undulations of typical sizes around $5 - 10nm$ and height variation of about $0.5nm$.

The origin of these ripples is still controversial, since it is not clear if they were either formed spontaneously or induced by corrugations from the substrate, or by some chemical agent present in the environment. In the case of graphene on top of SiO_2, there are experimental evidences indicating that the corrugations come from the substrate, because a clear correlation between both of them was observed [101]. However, in the case of suspended graphene is not that clear, and spontaneous formation of ripples after heating and cooling the samples has recently been reported [102].

A different issue is that of the consequences that the existence of ripples may have on the electronic properties of graphene. It is tempting to think of graphene as a realization of the Dirac equation in curved space [103]. However, such a connection has not been rigorously derived so far[9]. From microscopic considerations regarding the atomic structure and the bondings between carbon atoms, it seems that the curvature has two effects on electrons [77]: a) on the one hand, it changes the overlap between p orbitals, translating into a modification of the nearest neighbor hoppings. This effect can be modelized, for small curvatures, by introducing a gauge field $\mathbf{A}(\mathbf{r})$. b) On the other hand, it produces an hybridization between π and σ orbitals, that can be recounted by means of a spatially variating

[8] It is funny to mention that actually, diamond seems to be a metastable state of graphite under the normal conditions on the surface of Earth. However, time-scales involved in the transformation are enormously large to observe such a transition.

[9] F. de Juan, private communication

chemical potential $\Phi(\mathbf{r})$. The Dirac Hamiltonian, for a single valley, will read then:

$$\mathcal{H} = -iv_F \boldsymbol{\text{œ}} \cdot (\nabla + \mathbf{A}(\mathbf{r})) + \Phi(\mathbf{r}) \tag{1.32}$$

The pervading effect is supposed to be the one associated to curvature-induced gauge fields. An analysis of gauge fields produced by ripples whose features were taken from the experimental data was done in [78], where they were shown to produce midgap states and lead to an instability towards charge separation. Such a formation of charge puddles has been observed experimentally [104]. However, its origin is still a controversial issue, since different mechanisms have been proposed in the theoretical literature that apparently explain the experimental results. Among them, probably the strongest candidate would be that puddles are induced by charge impurities present in the environment [105].

The effect of gauge fields induced by curvature may have more striking consequences. If graphene strain is conveniently engineered, effective magnetic fields larger than $10T$ have been predicted, something that could lead to the observation of Quantum Hall Effect without the presence of external magnetic fields [106].

Part I

Interactions in arrays of ultracold atoms

2 Introduction: Scaling approaches to interacting problems

Nothing is particularly hard if you divide it into small jobs.
Henry Ford

2.1 Introduction

If queried about it, many physicists would not hesitate in stating scaling and renormalization ideas as the most important intellectual achievement in Physics during the second part of the twentieth century. These ideas provided a connection between many different and apparently unrelated problems, like the ill-behavior of quantum field theories and the critical phenomena in Statistical Physics. The Renormalization Group (RG), developed during the sixties and the seventies, played the role of the unifying concept, specially since the ideas of Kenneth Wilson broke into the field [107]. He was awarded the Nobel prize for such a real *tour de force*.

A satisfactory explanation of this topic would require a complete textbook, and there are already many of them that address some of its different aspects [108, 109]. Having shed light on such a variety of areas in Physics, it results quite challenging to give a comprehensive but at the same time understandable overview. Here, I will emphasize how scaling ideas have provided us with powerful tools to study interacting systems in Condensed Matter Physics. This has translated into a variety of techniques that, by using the deep ideas behind scaling and renormalization, rely on a wise selection of the relevant degrees of freedom of a complicated Hamiltonian. Along the chapter, central concepts in the development of the field, like criticality, scale invariance and renormalization, will come along in a natural way, so they will be introduced in due time.

2.2 Scaling, effective low energy theories and the renormalization group

Condensed matter systems usually involve different energy scales. Let us consider a three-dimensional metal, where the electrons live in energy bands with a certain band-width D. There is also the temperature, T, which by setting the Boltzmann constant to $k_B = 1$ (privileges of theorists), yields a second energy scale to consider. However, so far this is a non-interacting problem whose only peculiarities could arise, at most, from a complicated band structure. In order to grasp the importance of energy scales in a problem, we need to include interactions. Let me follow the pedagogical approach given

by Kehrein in his excellent book [110] and introduce a short-range potential $V(\mathbf{r}) = g\delta(\mathbf{r})$, of strength g, that perturbs the electron gas. This translates into the following Hamiltonian:

$$\mathcal{H} = \sum_k \epsilon_k c_k^\dagger c_k + \frac{g}{N} \sum_{k,k'} c_{k'}^\dagger c_k \tag{2.1}$$

where we made use of second quantization to describe the electron system, with creation and destruction of electron operators $c_k^\dagger$ and c_k that fulfill anticommutation relations $\{c_k, c_{k'}^\dagger\} = \delta_{k,k'}$. The number of states available is a discrete set of N energy levels that compose the band. Notice that the Hamiltonian is effectively one-dimensional, since it has been bypassed the intermediate step in which only the lowest-angular momentum scattering channel, the s-wave, is considered. Since by definition, this channel is spherically symmetrical with respect to the impurity, the problem loses its angular dependence, leaving the radial coordinate as the only relevant. Moreover, we will be interested in the continuous limit, where $N \to \infty$ and the density of states, $\rho(\epsilon) = \sum_k \delta(\epsilon - \epsilon_k)$, acquires the simple form:

$$\rho(\epsilon) = \begin{cases} 1/D & 0 < \epsilon < D \\ 0 & \text{otherwise} \end{cases} \tag{2.2}$$

The widely known issue regarding this apparently simple Hamiltonian already arises when one considers its weak-coupling regime, $\rho g \ll 1$. Here, it is expected on general grounds that a perturbative approach does apply. After all, if the impurity is weakly coupled to the electron gas, it would be unreasonable to presume a drastic change of its properties. However, things are more subtle, as shows a calculation of the (small) corrections to the energy levels of the electron gas, due to the presence of the impurity, in second order perturbation theory:

$$\epsilon_k^{(2)} = \epsilon_k + \frac{g}{N} - \frac{\rho g^2}{N^2} \log\left(\frac{D - \epsilon_k}{\epsilon_k}\right) \tag{2.3}$$

The result diverges when $\epsilon_k \ll D$, i.e., in the low-energy sector of the theory. On general grounds, from the lore accumulated on the theory of many-body systems, logarithmic divergences and the breaking of perturbation theory are considered signatures of a problem that lacks of characteristic scales. Let me address this issue with an example. If we are interested in the low-temperature physics of a metallic system, our intuition would reckon that only energy scales of the order of this small temperature will play a leading role. This means that we do not expect the band-width to be plaguing our results, since we are considering $T \ll D$. However, it happens that in many situations such a *rule of thumb* simply does not work, and a logarithmic divergence is usually the herald of these news. Its presence signals that corrections to the energy level $\epsilon_k \ll D$, in perturbation theory, are receiving contributions from energy scales between 0 and D on an equal foot. To better understand this point, let us consider the following integral:

$$\int_{E_0}^{nE_0} \frac{dE}{E} = \log n \tag{2.4}$$

This is the very integral that arises in perturbation theory for the impurity problem, and it has the peculiarity that the result does not depend on the absolute energy scale E_0, only on the range of integration. Therefore this kind of integrals are said to be scale-invariant, because they lack of a characteristic scale. This is something typical in *critical systems*, or systems near criticality, a term that

was coined in Thermodynamics when it was realized that systems approaching a critical point (like the vapor-liquid one, in water) show fluctuations of any scale. In other words, in a critical system a particle is correlated with any other, no matter the distance that mediates between them, giving rise to coherent phenomena at every length scale. In systems far from criticality this is no longer the case, and particles are correlated usually only below a typical characteristic length, termed the *correlation length*. This is the usual situation in most of the systems, where criticality is only present at a particular point of their phase diagram, demanding an extremely high tuning of parameters to reach it. Say, for instance, pressure and temperature for the critical point in water. In other systems, however, criticality emerges in the low-energy regime, something that happens with many condensed matter models and some quantum field theories proposed to describe interactions at the fundamental level. This is a consequence, as we will see, that arises naturally from the Renormalization Group.

Criticality is probably the most astonishing consequence that arises from systems in interaction. It produces clear signatures in the behavior of the system, so characteristic that they can be tracked back and reverse the argumentation followed so far: if a system behaves as expected near criticality, then we can conclude that interactions must be playing an important part. Though this affirmation seems almost vacuous in some cases, it can be useful for systems in which the underlying behavior is completely obscure due to its complexity, but a simple picture seems to arise from the experimental or observational data. This could be the case, actually, in financial markets [111].

In short, the combined effect of every energy scale of our simple impurity model, when evaluating observables on the low-energy sector, manifests itself through divergences in perturbation theory, even though the short-ranged potential was a weak-perturbation of the electron gas. Notice that the situation is not that tantalizing when corrections to energy levels in the high-energy sector are addressed. There, the logarithmic correction is small, and perturbation theory yields small corrections to the energy levels, as expected. A couple of remarkable things can be learnt from this discussion:

- The low-energy sector of the theory seems to be qualitatively different from the high-energy one.
- It seems to be an *emerging* energy scale below which perturbation theory breaks down and the system no longer has a characteristic scale that moderates the effects coming from the high energy sector.

2.2.1 Low-energy effective theories and scaling perturbation theory

In order to see the effect that high-energy scales are playing in the physics at low-energies, the *standard* procedure nowadays is to *integrate out* the high-energy degrees-of-freedom, and see how the low-energy theory looks then. If both sectors of the theory are not really coupled, we expect the latter to remain unaltered after this operation. There are many procedures to complete this task. For instance, the theory can be expressed in terms of path integrals (by means of its partition function), where the integration of high-energy degrees-of-freedom literally is a matter of carrying out integrals. Other techniques, such as *poor man's scaling*, deal directly with the Hamiltonian, where the idea is to reduce the Hilbert space by using projections on the low-energy states of the theory. Whatever

way you accomplish the integration out, the idea is that finally it will lead you to a sequence of Hamiltonians that differ from each other on the highest energy scale accessible. For instance, back to the simple impurity model, this would be the effective band-width, generating a sequence of Hamiltonians parametrized as $\mathcal{H}(D_0) \to \mathcal{H}(D_1) \to ... \to \mathcal{H}(D_{eff})$. Every step must be infinitesimally related to the one before: $\delta D = D_n - D_{n+1} \to 0$. Why is that? Is mostly a technical issue, since the integration of high-energy degrees-of-freedom relies in a majority of cases on perturbation theory, that will take advantage of this small scale to give a finite correction to the effective Hamiltonians where there was a divergence before. It results somehow suggestive to think that by following this scheme, it is possible to tame perturbation theory in a way that finally will yield sensible results.

On general grounds, such a procedure will produce, during this *flow*, corrections to the terms of the Hamiltonian that were already present, but also may yield new terms as far as they are compatible with the symmetries and degrees-of-freedom of the system. Every new Hamiltonian generated can be considered as an effective description of the original one, only valid up to the energy scale D_{eff}. They are called low-energy effective theories. If the new terms generated during the flow become important, then we are certainly in troubles, as those terms will in principle generate other ones, and so on, making the low-energy theory intractable (actually, nowadays this point-of-view has changed, as I will discuss later). However there is a particular class of theories whose new terms produced remain small during the integration of high-energy degrees-of-freedom, and hence can be discarded. Every effective Hamiltonian then maps into the previous one, and the effect of the high-energy sector is encoded in corrections to the coupling constants. As usual, this is better understood by resorting to our simple example, where the effective Hamiltonians can be generated in the *poor man's scaling* fashion [110]:

$$\mathcal{H}(D_{eff}, g_{eff}) = \sum_{k:\epsilon_k < D_{eff}} \epsilon_k c_k^\dagger c_k + \frac{g_{eff}}{N} \sum_{k,k':\epsilon_k,\epsilon_{k'} < D_{eff}} c_k^\dagger c_{k'} \tag{2.5}$$

Here, g_{eff} is defined iteratively with respect to the previous infinitesimal energy scale, $D_{eff} + \delta D$:

$$g_{eff}(D_{eff}) = g - \rho g^2 \frac{\delta D}{D_{eff}} + \mathcal{O}(g^3) \tag{2.6}$$

Notice that, as mentioned, the calculations are perturbative in g. However, perturbation theory in g is employed in this case to generate the sequence of effective low-energy Hamiltonians, whose couplings are no longer g but g_{eff}. Keep this in mind for later. Now, we saw that logarithmic divergences can be tracked to the equal contribution of all the energy scales of the problem. When integrating out the high-energy degrees-of-freedom, we actually encode the effect of these energy scales in the new effective coupling constant. The combined effect of *all* these energy scales above D_{eff} can be obtained by working out the solution to the differential equation that arises from (6.2), when $\delta D \to 0$:

$$\frac{dg_{eff}(D_{eff})}{d\log D_{eff}} = \rho g_{eff}^2 \tag{2.7}$$

This is called a *flow-equation*. It dictates the way the couplings of our theory change with the energy scale D_{eff}. Setting as the initial condition the original bandwidth D, we get:

$$g_{eff}(D_{eff}) = \frac{g}{1 + \rho g \log(D/D_{eff})} \tag{2.8}$$

This result already contains a resummation of the perturbative (and therefore small) effects of every iteration. It provides us with a useful tool to analyze the combined effect that the high-energy sector has on the low-energy theory as the energy scale is lowered. For repulsive potentials, $g > 0$, when $D_{eff} \ll D$ we get $g_{eff} \to 0$, meaning that the potential does not have any effect on the low-energy properties. This does not imply that both sectors of the theory are decoupled. On the contrary, the high-energy degrees of freedom have *renormalized* the potential strength to zero, which means that the low-energy electrons behave effectively like free electrons. They no longer feel the interaction with the impurity, because it has been collectively screened. In a different language, which we owe to Landau, we may say that the low-energy excitations of the electron gas in the presence of an impurity are non-interacting (quasi)electrons. This is not, however, the case for attractive potentials, $g < 0$. Here, we see that there is a scale at which the denominator vanishes:

$$D_C \equiv De^{-\frac{1}{\rho|g|}} \tag{2.9}$$

This emerging scale separates naturally the low-energy and the high-energy sectors of the theory, signaling the breaking of perturbation theory. The effective coupling constant becomes large, and the effective low-energy theory no longer belongs to the perturbative realm. Notice that the new energy scale cannot be expanded in powers of the coupling constant even for small couplings, $|g| \to 0$, meaning that this effect cannot be accessible by using conventional perturbation theory. How can it be that we gain access to non-perturbative physics by using perturbation theory? Well, somehow, by integrating out high-energy degrees-of-freedom iteratively, we are making a resummation of small perturbative effects that finally leads to non-perturbative results. Apparently, it might be true that *nothing is particularly hard if you divide it into small jobs*.

An important consequence of the analysis performed so far is that, by using this *scaling* perturbation theory for the *repulsive* potential, in principle intractable due to the divergences, we can obtain well-behaved results for the corrections to the low-energy levels. The key point relies in the use of g_{eff} and not g as the perturbative parameter. The effective coupling constant already contains the non-trivial effect of the high-energy sector, treated in a way that no longer produces ill-results. Therefore, we can employ the Hamiltonian $\mathcal{H}(D_{eff})$ to carry out the calculations. Some nuances must be clarified at this point. After all, which D_{eff} is the one to be used? Or said in other words, where should we stop the flow of the effective Hamiltonians? Well, once again, this is just a matter of typical scales. D_{eff} should be the largest scale that plays a role in the energy regime we are studying. If the temperature is zero, and we want to study corrections to the energy level ϵ_k, we will stop the flow at $D_{eff} = \epsilon_k$[1]. The result will read then:

$$\epsilon_k^{(2)} = \epsilon_k + \frac{1}{N}\frac{g}{1+\rho|g|\log(D/\epsilon_k)} + \mathcal{O}(g_{eff}^2) \tag{2.10}$$

[1]This issue about where to stop the running of the coupling constants is, in my opinion, poorly explained in the literature. As mentioned, you are allowed to carry out the flow down to the largest energy scale that is important in your low-energy calculation. This can be an energy level, as it happens here. But it can be the temperature as well, since an external bath at a certain temperature typically will produce excitations up to the energy scale defined by it. It can also be the frequency at which an observable is measured, because this frequency is related to the energy of the proves used to explore the system, energy that can be used to generate excitations. Or finally, of course, it can be the renormalized full dimensional coupling itself if it turns out to grow during the flow.

The lesson to learn here is that scaling approaches can provide us with powerful tools to deal with the subtleties of interacting models. This is the idea behind the two techniques that I will explain below. However, before that, let me move on from the particular example studied so far to give some general statements.

2.2.2 Scaling and the Renormalization Group

The term *scaling* in our approach inherits its name from the sequence of transformations that is done on the Hamiltonian when we integrate out high-energy degrees-of-freedom. This is because every Hamiltonian is related to any other one by a scaling transformation of the band-width, that henceforth will be generically referred to as the ultraviolet cutoff Λ. We have seen that it is expected on general grounds that by integrating out high-energy degrees of freedom, new terms compatible with the constraints of the Hamiltonian come along into the low-energy theory. However, for a particular class of *well-behaved* Hamiltonians, like the one studied in the last section, the new terms can be discarded, and the Hamiltonian preserves its structure during the flow, with all the effects of the high-energy sector encoded within the effective couplings. In order to formalize the way a Hamiltonian evolves while the integration of high-energy degrees-of-freedom is carried out, we need to be able to compare the different Hamiltonians. This requires an extra step not accounted for so far, that is, rescale variables and operators in the Hamiltonian in order to set again the original cutoff Λ [2]. The complete transformation, including integration of degrees-of-freedom and rescaling of variables and operators, can be generically written as follows:

$$R_\lambda \left[\mathcal{H}(\Lambda, g_2, g_2, ...)\right] = \mathcal{H}(\Lambda, g_1', g_2', ...) \tag{2.11}$$

where $\lambda = \Lambda'/\Lambda$ is the scaling parameter, and $\{g_1, g_2, ...\}$ represents a complete set of all the possible terms of the Hamiltonian that can be generated during the flow. This transformation is called a *Renormalization Group* (RG) transformation [112].

Despite its name, the Renormalization Group transformation does not have the structure of a real group, but a semi-group, since in general lacks an inverse. Nevertheless, it does have an identity element, read R_1, defined by:

$$R_1 \left[\mathcal{H}(\Lambda, g_1, g_2, ...)\right] = \mathcal{H}(\Lambda, g_1, g_2, ...) \tag{2.12}$$

and fulfills the addition property, since:

$$R_{\lambda_1\lambda_2} \left[\mathcal{H}(\Lambda, g_1, g_2, ...)\right] = R_{\lambda_2}\left[R_{\lambda_1}\left[\mathcal{H}(\Lambda, g_1, g_2, ...)\right]\right] \tag{2.13}$$

With the RG transformation we are in position of understanding better the properties of the effective low-energy theories that are generated by integrating out high-energy degrees-of-freedom. Before,

[2] For instance, by defining the scaled momentum $k' = k\Lambda/\Lambda'$; rescaling operators is more subtle, and usually is conveniently selected to keep invariant a certain part of the Hamiltonian. This requires some wisdom about the Hamiltonian where the flow is leading, since the idea is to keep *this* one invariant. In theories whose low-energy sector has weak interactions, this is the free part of the Hamiltonian.

however, it is convenient to introduce a pivotal concept in the RG lore. Given an RG transformation, it could happen that there are certain Hamiltonians $\mathcal{H}^*$ that are invariant under the transformation:

$$R_\lambda \left[\mathcal{H}^*(\Lambda, g_1^*, g_2^*, ...)\right] = \mathcal{H}^*(D, g_1^*, g_2^*, ...) \tag{2.14}$$

These Hamiltonians are called *fixed points* of the RG transformation. During the RG flow, a complicated Hamiltonian can converge to a fixed point. Then, any further iteration will not produce additional changes, by definition of fixed point. Interestingly, it somehow implies that the effect of integrating out high-energy degrees-of-freedom does not translate anymore in a different low-energy behavior. From this point forth, the physical behavior of the system will not depend on the energy scale, becoming *scale invariant*. Fixed points of the RG transformation are important to understand the concept of *universality*: apparently unrelated systems have a similar low-energy behavior, irrespectively of their microscopic (*high-energy*) details. If they flow to the same fixed point of the RG, they belong to the same class of universality.

However, this is not yet the whole story, since most of the properties of a system come from its response to external probes, that produce excitations from the ground state, meaning that the correct theory describing such a response is defined up to a finite energy scale. This immediately implies that the response of a system might not be fully characterized by the fixed point, having to account also for the small corrections around it. In order to understand this point, it is convenient to linearize the transformation close to a fixed point:

$$\mathcal{H}(\Lambda, g_1', g_2', ...) = \mathcal{H}^* + T_\lambda \mathcal{H}(\Lambda, g_1, g_2, ...) \tag{2.15}$$

where T_λ is the linearization of the RG transformation. This transformation, actually, has eigenvectors and eigenvalues: those operators that scale purely with the RG transformation:

$$T_\lambda \mathcal{O}_i = \mu_i O_i \tag{2.16}$$

Let us suppose, for simplicity, that the original set of operators corresponds to some eigenvectors of the RG close to the fixed point. Then the n-iteration of the RG transformation yields:

$$\mathcal{H}_n(\Lambda, g_1', g_2', ...) = \mathcal{H}^* + \sum_i \mu_i^n g_i \mathcal{O}_i \tag{2.17}$$

Now it is easy to see that, if $\mu > 1$, then the effective coupling increases and draws the Hamiltonian far from the fixed point. These operators are said to be *relevant*, and their presence is an indication that the fixed point is unstable towards perturbations that entail them. If $\mu < 1$, then the effective coupling decreases and the operators become less important as the cutoff is reduced, drawing the Hamiltonian to the fixed point. They are called *irrelevant terms*. Finally, if $\mu = 1$, then the transformation leaves invariant the operator, and in order to know the direction of the flow, non-linear corrections to the transformation must be analyzed. Such a family of operators are coined *marginal*. In Fig. 2.1, a schematic depiction of this situation is given, showing a *saddle-point* sort of unstable fixed point, which corresponds to a Hamiltonian with both an irrelevant and a relevant operator. The latter draws the flow far from the fixed point, so it requires an extremely high tuning of the initial conditions of the flow to reach the fixed point. In contrast to that, a stable fixed point is one whose nearby region

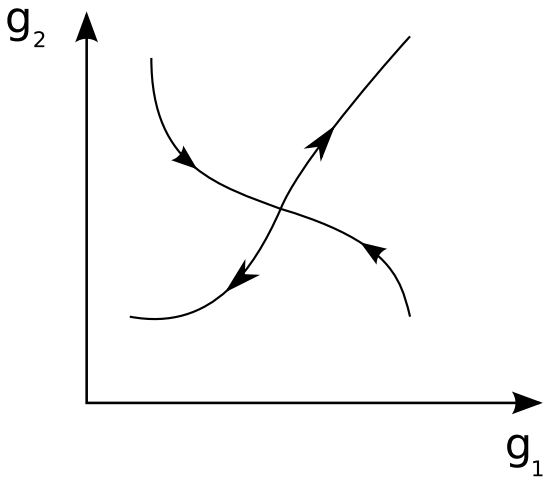

Figure 2.1: Flow of the RG transformation for a simple Hamiltonian with two couplings. The figure shows a fixed point with a *saddle-point* structure.

is ruled by irrelevant or marginally irrelevant operators (the latter being marginal operators whose higher order corrections make them irrelevant).

Let us suppose, then, that our Hamiltonian flows towards a stable fixed point. Despite the fact that irrelevant terms tend to be less important as the flow is carried out, they are actually the ones that mainly determine the response of the system, as I have already mentioned. These operators are not scale-invariant, but they have well-defined scaling properties under the RG transformation, being eigenvectors of the linear transformation. In terms of criticality, we say that the fixed point characterizes the class of universality of the critical point, but the critical properties of the different observables follow from the irrelevant terms. They are crucial, for instance, to work out analytical expressions of the critical exponents that characterize observables close to a critical point. In condensed matter systems the situation is analogous: a low-energy theory will be defined by the fixed point plus the irrelevant terms close to it. The main example being that of Landau's theory of Fermi liquids [113].

A somewhat more involved scenario entails a space of couplings with different fixed points, some of them stable and others unstable. Once the initial conditions of the flow are chosen (which usually means to set as the starting Hamiltonian the original microscopic theory defined up to a certain cutoff), then the flow will draw the Hamiltonian to one of those fixed points. Let us suppose that the initial conditions place the Hamiltonian close to an unstable fixed point. This one might be ruling the high-energy behavior of the theory. The RG flow, then, will produce a *crossover* from the high-energy regime to the low-energy one. This is the case of our simple Hamiltonian studied in the previous section: one of the fixed points is the non-interacting one, with $g = 0$. By introducing a small perturbation in the form of an attractive potential, the effective Hamiltonian moves to a different fixed point in the low-energy regime, where $g = \infty$. Hence, the RG flow produces a crossover from weak-coupling to strong-coupling, with the crossover energy scale given by Eq. (2.9).

2.3 Numerical Renormalization Group

Now we are in position to understand the fundamentals of the Numerical Renormalization Group (NRG), a successful tool that relies on all the scaling and RG ideas discussed so far. It was developed by K. Wilson himself to address the solution of the Kondo problem [114], in which the presence of a spin impurity embedded in an electron gas, even for weak couplings, renders divergences in perturbation theory and a highly non-trivial low-energy behavior [112, 115, 116]. By the time Wilson proposed the NRG, most of the peculiarities of this problem had already been understood, something that required the introduction of scaling techniques like the ones described in the last section. As we saw that happens with the impurity problem, perturbation theory must be reorganized in a way that divergences are parametrized in the effective coupling constant, that flows towards a strong-coupling regime for antiferromagnetic couplings. This analysis provides us with a crossover scale, the Kondo temperature, that marks the onset of non-perturbative behavior in the low-energy regime, where a different approach must be employed to shed light on the nature of the ground state. In that direction, variational ansätze were proposed, suggesting the formation of a singlet between the spin of one electron of the electron gas and that of the impurity. The rest of the gas, apparently, would decouple, behaving essentially like a normal system of electrons. Wilson's NRG served not only to support this picture, but also to describe the complete crossover from weak to strong coupling regime, at the price of resigning to obtain analytical results.

The NRG has been successfully applied to multiple quantum impurity problems where there exists a non-trivial strong-coupling regime at low energies. In origin, its spectrum of applications was reduced to address the study of quantum systems with a few degrees-of-freedom coupled to a continuous band of fermions, like electrons in metals. However, its scope has been enlarged during the last thirty years, becoming a field of research itself, and demanding an increasing degree of specialization to catch up with the constant evolution of the codes. A couple of relevant extensions worth to mention are Dynamical Mean Field theory, and the study of non-equilibrium dynamics of open quantum systems [117]. Here, I will only describe its extension to quantum systems coupled to bosonic baths [118], which is relevant for the fields of Quantum Decoherence and Quantum Dissipation, and the one I will use throughout this thesis.

2.3.1 An introduction to the NRG through the Spin-Boson model

Instead of giving a general and abstract introduction to the NRG, let me just sketch the basis of this technique by describing its celebrated application to bosonic baths, particularly to the Spin-Boson model. For technical details, I refer the reader to the original article by R. Bulla et al [118].

The Spin-Boson (SB) model addresses the problem of a quantum particle in a two-level system coupled to an external bath whose low-energy excitations are gapless bosons [119]. The structure of a two-level quantum system is defined in terms of operators that follow the $SU(2)$ algebra, analogous to the spin, hence the name. As I will explain in more detail in the next chapter, bosonic baths provide us with a simple description of a large class of dissipative models that belong to the same universality class. This means that, despite of their apparent simplicity, they already contain the

basic ingredients relevant in the more complicated systems addressed in the fields of Open Quantum Systems, Quantum Dissipation, and related ones.

The Hamiltonian of the Spin-Boson model reads:

$$\mathcal{H}_{SB} = -\frac{\Delta}{2}\sigma_x + \sum_n \omega_n a_n^\dagger a_n + \frac{\sigma_z}{2}\sum_n \lambda_n (a_n + a_n^\dagger) \tag{2.18}$$

The first term correspond to a degenerated two-level quantum system. Here, σ_x and σ_z are the corresponding Pauli matrices and Δ is the tunnelling parameter, that is related to the probability of a particle to hop between states. The second term describes the bosonic bath: $a_n^\dagger$, a_n operators create and destroy, respectively, a boson of energy ω_n. The excitations are gapless, meaning that there are excitations for arbitrary low energies. Finally, the last term describes the coupling between bath and system, realized through σ_z, with strength couplings λ_n. This coupling is completely characterized by the so-called *bath spectral function*:

$$J(\omega) = \pi \sum_n \lambda_n^2 \delta(\omega - \omega_n) \tag{2.19}$$

Unfortunately, I do not have enough space here to explain the rigorous origin of this function, that should be found in the originally work by Caldeira and Leggett [120]. Let me just point out that it is the only quantity that must be constrained in order to recover the classical limit of the model, i.e., when we aim to derive the classical equations of motion of dissipative dynamics from a quantum point of view. In the low energy limit, $\omega \to 0$, a power-law is sufficient to describe the main regimes of classical dissipation:

$$J(\omega) = 2\pi\alpha\omega_c^{1-s}\omega^s, 0 < \omega < \omega_c \tag{2.20}$$

where ω_c is an ultraviolet cutoff, that will be taken equal to one henceforth. The case $s = 1$, the one we are interested in, is commonly named in the literature ohmic dissipation. Why? Because in this limit, the corresponding classical friction is that given by the Ohm's law.

A few words about this model: it has been widely studied since the eighties with a variety of techniques, since it can be shown to be a good low-energy description of a quantum particle tunnelling between two minima of a potential, in the presence of a dissipative environment. Variational techniques, Renormalization Group, and other powerful tools have proved useful to explore its equilibrium and non-equilibrium properties, the latter being revived since the advent of the field of Quantum Computation, whose main building block, the *qubit*, is essentially a two-level quantum system. Here I will concentrate on the phase diagram of the model. It shows a continuous quantum phase transition (i.e., at zero temperature) for $\alpha_c = 1 + \mathcal{O}(\Delta)$ [119]. In the RG language, the phase $\alpha < \alpha_c$ is described by the fixed point $\tilde{\alpha} = 0$, $\tilde{\Delta} = \Delta_r$. It is called the delocalized phase, since the effect of the bath is essentially to renormalize the tunnelling probability to Δ_r. Therefore the particle still tends to become delocalized in the two minima in order to minimize its kinetic energy. $\alpha > \alpha_c$ corresponds to the localized phase, ruled by a different fixed point, $\tilde{\alpha} = \alpha$, $\tilde{\Delta} = 0$. The bath renormalizes to zero the hopping probability, and the particle must become localized in one of the two minima.

In this section, I will pursue to show how the NRG reproduces correctly this phase transition, yielding a different low-energy behavior below and above a certain critical coupling α_c, that can be

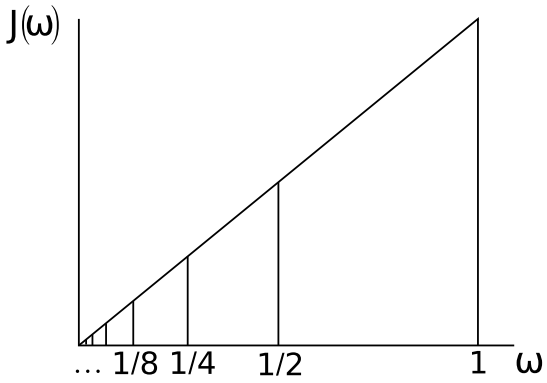

Figure 2.2: Logarithmic discretization of the bath spectral function, for the ohmic case, and $\lambda = 2$. The ultraviolet cutoff ω_c has been taken equal to one, for simplicity.

elucidated within this scheme as well. Moreover, for every phase it succeeds to describe the crossover between high-energy and low-energy physics. The first step in order to implement the NRG is to rewrite the Hamiltonian in a continuous fashion:

$$H = -\frac{\Delta}{2}\sigma_x + \int_0^1 d\epsilon g(\epsilon) a_\epsilon^\dagger a_\epsilon + \frac{\sigma_z}{2}\int_0^1 d\epsilon h(\epsilon)(a_\epsilon + a_\epsilon^\dagger) \tag{2.21}$$

The spectral function for this version of the model is given now by:

$$\frac{1}{\pi}J(\omega) = \frac{d\epsilon(\omega)}{d\omega}h^2[\epsilon(\omega)] \tag{2.22}$$

where $\epsilon(\omega)$ is the inverse function of $g(\omega)$ and $h(\epsilon)$ is the new (continuous) coupling function. Both parameters can be calculated easily from the bath spectral function [118].

The NRG method can somehow be seen as an almost exact numerical diagonalization of the Hamiltonian. The crucial observation is how it carries out this diagonalization, and why it results more convenient than a *brute force* approach. The latter, when applied to the class of models that fall into the NRG range of interest, turns out to present several issues: (i) mostly at the time it was developed, the number of degrees-of-freedom required to get a good description of a macroscopic bath was too large for ordinary computers, and any approximation that could reduce the size of matrices was welcome, (ii) even at the time such a computer power was available, still quantum impurity problems are subtle, since their low-energy regime emerges below a certain crossover scale that is in most of the cases exponentially small as compared to the initial cutoff. Remember the case of the short-range potential and the Kondo problem as well. Hence, an ordinary linear discretization of the band would underestimate the exponentially small region of energies relevant for the low-energy behavior, as compared to the number of states taken above. The NRG overtakes both problems by using scaling ideas, which serve to wisely select the relevant degrees of freedom for any energy scale, specially the low-energy regime.

The issue raised in (ii) is addressed by using a logarithmic discretization of the spectral function, as shown in Fig. 2.2, that resolves accurately the exponentially small energy scales involved in the usual crossover to the low-energy regime. The discretization parameter is λ, being $d_n = \lambda^{-n}(1-\lambda^{-1})$ the

width of the n-interval. In every interval, we can define a complete set of orthonormal functions:

$$\psi_{np}(\epsilon) = \begin{cases} \frac{1}{\sqrt{d_n}} e^{i\omega_{np}\epsilon}, & \lambda^{-(n+1)} < \epsilon < \lambda^{-n} \\ 0, & outside \end{cases} \tag{2.23}$$

where $p = 0, \pm 1, \pm 2, ..., \omega_n = 2\pi/d_n$. The original operators can then be expressed as a linear combination of the new ones as follows:

$$a_\epsilon = \sum_{np} a_{np}\psi_{np}(\epsilon) \tag{2.24}$$

$$a_\epsilon^\dagger = \sum_{np} a_{np}^\dagger \psi_{np}^*(\epsilon) \tag{2.25}$$

We can now choose the function $h(\epsilon)$ to be constant in every n-interval, an approximation that gets improved as the continuous limit is recovered. Then, it is not difficult to see that all the components $p \neq 0$ contributing to the coupling term can be neglected. Notice that these components will still be coupled to the impurity via the free bosonic term in the Hamiltonian. One of the main approximations in the NRG method is actually not taking into account these components, which turns out to be exact also in the continuous limit $\lambda \to 1$. In order to carry out the numerical calculations, however, a finite discretization must be used, and therefore the accuracy of the results will be improved as λ approaches the unity. Of course, the price to pay is a larger amount of states to account for in the in numerical calculations.

With the approximations made so far we are ready to write a somewhat simplified Hamiltonian. By redefining the operators $a_{np=0} \equiv a_n$, this new Hamiltonian reads:

$$\mathcal{H} = -\frac{\Delta}{2}\sigma_x + \sum_{n=0}^{\infty} \xi_n a_n^\dagger a_n + \frac{\sigma_z}{2\sqrt{\pi}} \sum_{n=0}^{\infty} \gamma_n (a_n + a_n^\dagger) \tag{2.26}$$

It has a similar form as the one we started from. However, the new parameters have the peculiarity of decaying logarithmically with n, as a power law in λ:

$$\xi_n = \gamma_n^{-2} \int_{\lambda^{-(n+1)}}^{\lambda^{-n}} dx J(x) x = \frac{2}{3}\left(\frac{1-\lambda^{-3}}{1-\lambda^{-2}}\right)\lambda^{-n} \tag{2.27}$$

$$\gamma_n^2 = \int_{\lambda^{-(n+1)}}^{\lambda^{-n}} dx J(x) = \pi\alpha(1-\lambda^{-2})\lambda^{-2n} \tag{2.28}$$

i.e., $\gamma_n \propto \Lambda^{-n}$. In figure 2.3, a schematic picture of the coupling structure of Hamiltonian Eq. (2.26) is shown. The impurity is coupled directly to every bosonic site, resembling the shape of a star. This particular version of the NRG is named precisely after this star, it is the *Star-NRG*, as opposed to the *chain-NRG* used typically in calculations with fermionic baths, that requires an extra transformation of the Hamiltonian that maps it to a chain structure. However, I will not describe it here. Those two in principle equivalent versions, when applied to bosonic baths, have virtues and defects, but the common lore advises us to use the star-NRG in equilibrium calculations, mostly when the approach is generalized to more complicated impurity Hamiltonians. This will be one of the issues risen in the next chapter.

The NRG makes use of the logarithmically decaying energy structure that couplings and energies have in the new Hamiltonian. It is an iterative diagonalization of this Hamiltonian, that allows for a

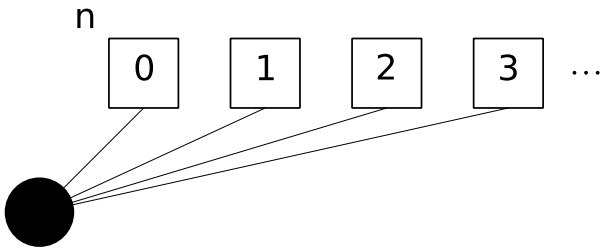

Figure 2.3: Structure of the Hamiltonian used in the *Star-NRG* approach. The black circle stands for the impurity, and the boxes for the bosonic sites.

truncation scheme based on RG and scaling ideas that can be used to account for a solution of the issue raised in (i). The first thing to notice is that a Hamiltonian including N sites should be enough to describe physics down to energy scales of the order of λ^{-N}. The complete star-NRG Hamiltonian can then be conveniently written as a series of rescaled Hamiltonians $\mathcal{H}_N$ with N sites:

$$\mathcal{H}_N = \lambda^N[-\frac{\Delta}{2}\sigma_x + \sum_{n=0}^{N} \xi_n a_n^\dagger a_n + \frac{\sigma_z}{2\sqrt{\pi}} \sum_{n=0}^{N} \gamma_n (a_n + a_n^\dagger)] \tag{2.29}$$

$$\mathcal{H} = \lim_{N\to\infty} \lambda^{-N} \mathcal{H}_N \tag{2.30}$$

The factor λ^N is included in order to keep the energy scale of every N-Hamiltonian of the same order, for comparison purposes. This probably will remind us of the rescaling operation of fields and vectors introduced in the last section to complete the RG transformation. It is essentially the same thing. Actually, the whole NRG can be mapped into the RG transformations described in the last section. The analogue of the integration of high-energy degrees-of-freedom is the combination of diagonalizing a certain Hamiltonian $\mathcal{H}_N$, and then only retaining low-energy states in order to diagonalize the next Hamiltonian $\mathcal{H}_{N+1}$. Both Hamiltonians are related by:

$$\mathcal{H}_{N+1} = \lambda H_N + \lambda^{N+1}[\xi_{N+1} a_{N+1}^\dagger a_{N+1} + \frac{\sigma_z}{2\sqrt{\pi}} \gamma_{N+1}(a_{N+1} + a_{N+1}^\dagger)] \tag{2.31}$$

This truncation scheme is expected to work precisely by virtue of the RG ideas discussed before. Of course, the number of states that are kept in every step is not arbitrary. There is a threshold above the procedure that gives meaningful results, and a careful check of convergence is mandatory in every calculation.

By using the NRG, we can gain access to the physics at a certain energy scale $T_N \propto \lambda^{-N}$ by carrying out the iterative diagonalization of the chain of Hamiltonians $\mathcal{H}_0$, $\mathcal{H}_1$, ..., $\mathcal{H}_N$. If the physics below this scale is not of interest, it can be stopped here. Every Hamiltonian contains the same number of degrees-of-freedom thanks to the truncation scheme, but those are wisely selected to account for the relevant phenomena present at T_N. The effects of the high-energy sector are already included in the effective Hamiltonian $\mathcal{H}_N$, since it inherits its level and coupling structure from the previous iterations. Comparison between different Hamiltonians is provided by the aforementioned global rescaling.

In short, we have a Renormalization Group transformation implemented numerically. The output are eigenenergies $E_N(r)$ of the different r states obtained in the diagonalization of the N-Hamiltonian.

As a function of N, it can be seen as a flow of the lowest eigenenergies in a RG transformation. Notice that due to its numerical nature, it does not provide us with the actual form of the effective Hamiltonians. After all, we are dealing with numerical matrices, and reconstructing the corresponding Hamiltonian can be a prodigious task, unless we study perturbations close to the fixed point, where general analytic considerations can serve as a guide. Still, the information contained in the eigenenergies flow is enough to characterize the crossovers and phases.

Certain issues, however, related to the iterative diagonalization procedure, must be pointed out. As mentioned, the numerical diagonalization of Hamiltonian $\mathcal{H}_N$ gives its, say, N_s states $|r\rangle_N$, with $r = 1, ..., N_s$. The corresponding eigenergies were defined as $E_N(r)$. In order to diagonalize now $\mathcal{H}_{N+1}$, we need a suitable basis that contains the new bosonic degrees-of-freedom added by the new $N+1$ site. And any bosonic mode contains in principle an infinite number of states. In principle, if we were able to project the Hamiltonian on the complete set of site bosonic states, the choice of a particular basis would make no difference. However, due to computational limits, whatever they are, the number of bosons per site must be truncated, say, to N_b of them, this number selected in order to achieve convergent results. This fact promotes the choice of basis to a non-trivial issue. In the original approach by Bulla et al. it was shown that the basis of eigenvectors of the number operator $a^\dagger_{N+1}a_{N+1}$, $|s\rangle_{N+1}$, renders convergent results for ohmic baths and small enough coupling to the bath (but still, above the critical coupling). With this choice, the basis to diagonalize $\mathcal{H}_{N+1}$ would read:

$$|r;s\rangle_{N+1} = |r\rangle_N \otimes |s\rangle_{N+1} \tag{2.32}$$

which has $N_s N_b$ elements. Once it is diagonalized, only the lowest N_s energy states are kept. Other choices of basis can also be tried, in case convergence with this basis starts to be extremely demanding. For instance, one with conveniently displaced oscillators [117].

Another issue arises from the actual projection of $\mathcal{H}_{N+1}$, that must be worked out. The matrix elements read:

$$_{N+1}\langle r;s|\mathcal{H}^{(1)}_{N+1}|r';s'\rangle_{N+1} = \lambda E_N(r)\delta_{r,r'}\delta_{s,s'} \tag{2.33}$$

$$_{N+1}\langle r;s|\mathcal{H}^{(2)}_{N+1}|r';s'\rangle_{N+1} = \lambda^{N+1}\xi_{N+1}s\delta_{r,r'}\delta_{s,s'} \tag{2.34}$$

$$_{N+1}\langle r;s|\mathcal{H}^{(3)}_{N+1}|r';s'\rangle_{N+1} = \lambda^{N+1}\gamma_{N+1}\,{}_N\langle r|\frac{\sigma_z}{2\sqrt{\pi}}|r'\rangle_N\left(\delta_{s,s'-1}\sqrt{s+1}+\delta_{s,s'+1}\sqrt{s}\right) \tag{2.35}$$

Notice that the matrix elements of the impurity operator, $_N\langle r|\sigma_z|r'\rangle_N$, must be calculated iteratively from the previous ones, by using the unitary transformation that diagonalizes $\mathcal{H}_N$.

2.3.2 NRG description of the SB phase transition

Let me now outline the results of the NRG approach to the Spin-Boson model, that will give us orientations to understand the contents of the next chapter. As mentioned, the NRG technique yields as an output the lowest energy levels for every iteration of the numerical algorithm, conveniently rescaled in order to allow for a comparison of the level structure during the *flow* of the transformation. In addition, it is possible to compute expectation values of observables evaluated in the N-site basis. For instance, the already mentioned $_N\langle r|\sigma_z|r'\rangle_N$ matrix elements. This is the main source of information in order to get quantitative and qualitative results from the NRG.

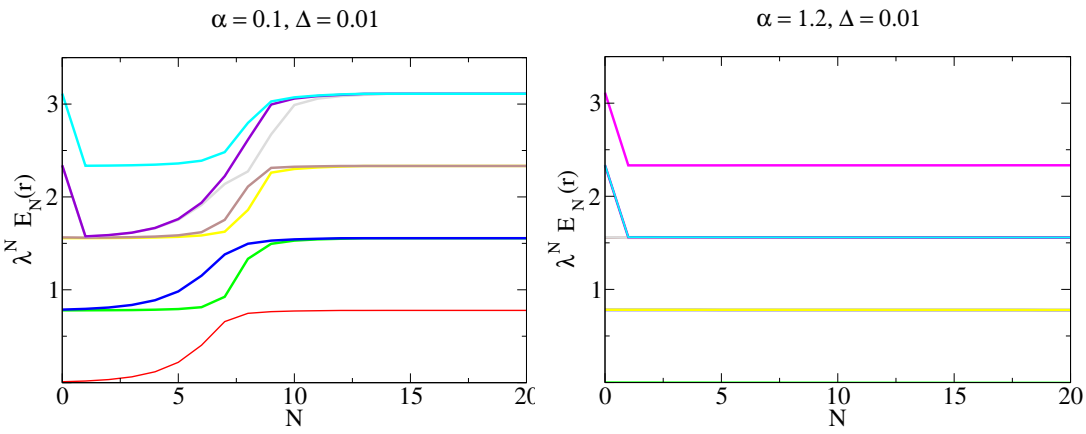

Figure 2.4: Flow energy diagrams of the NRG applied to the Spin-Boson model. The lowest energy levels are shown, conveniently rescaled for comparison issues, with the ground state energy subtracted. Every iteration is representative of an energy scale $T_N \propto \lambda^{-N}$. Left: results for $\Delta = 0.01$ and $\alpha = 0.1$. Right: results for $\Delta = 0.01$ and $\alpha = 1.2$. The NRG parameters are $Ns = 80$, $N_b = 8$ and $\lambda = 2$.

In Fig. 2.4 the NRG output is plotted for two different sets of parameters of the model. They are a good example of those typically found in a NRG calculation. The results show qualitatively different behaviors for couplings α larger or smaller than $\alpha_c \simeq 1$. In order to characterize the different regimes, it is convenient to study some of the limits of the SB Hamiltonian. The case $\alpha = 0$ is the simplest one, corresponding to the impurity uncoupled from the environment. The solution to this Hamiltonian can be exactly worked out in the basis $|\sigma\rangle \otimes |n_1, n_2, ...\rangle$, where $|\sigma\rangle$ are the eigenvalues of σ_x and $|n_1, n_2, ...\rangle$ the number states of the bosonic operators. The eigenenergies are:

$$E(\sigma, n_1, n_2, ...) = -\frac{\Delta}{2}\sigma + \sum_i \xi_i n_i \tag{2.36}$$

In the NRG language, this is a fixed point, the delocalized one, whose lowest eigenenergies are expected to be, at iteration N:

$$\lambda^N (E_N(r) - E_N(0)) = \lambda^N \xi_r n(r) \tag{2.37}$$

There is yet another simple limit, that also corresponds to a fixed point, the localized one. It is defined by setting $\Delta = 0$ and arbitrary α, which actually means that it is a line of fixed points. This Hamiltonian also has an exact solution, when projected to the basis $|\sigma_z\rangle \otimes |\bar{n}_1, \bar{n}_2, ...\rangle$, where now new number states have been introduced from a set of displaced operators characterized by the projection σ_z as well:

$$\bar{a}_{n,\sigma_z} = a_n + \frac{\sigma_z \gamma_n}{2\sqrt{\pi}\xi_n} \tag{2.38}$$

Interestingly, the projected Hamiltonian:

$$\langle \sigma_z | \mathcal{H} | \sigma_z \rangle = \sum_n \xi_n \bar{a}^\dagger_{n,\sigma_z} \bar{a}_{n,\sigma_z} \tag{2.39}$$

does have the same energy spectrum as the other fixed point, with the only difference that the degeneracy is now double, since displaced oscillators with both $\sigma_z = 1$ and $\sigma_z = -1$ can be defined, not having influence on the energies.

These simple limits give us a lot of insights on the NRG data. This is also a typical situation with the NRG. It usually requires the assistance of analytical guesses of the low-energy Hamiltonians in order to understand the flows. Let us therefore analyze the given eigenenergies. Remember that, for every iteration, it gives the lowest energy levels conveniently rescaled for comparison issues, and that this iteration N is related to an increasingly lower energy scale. This means that the NRG resolves (logarithmically) smaller scales as N becomes larger. For $\alpha < \alpha_c$, the flow shows a crossover from a region in which the lowest excitations correspond to the impurity internal states, since yet the bosonic excitations have energies larger than the renormalized Δ_r, and a region in which the lowest excitations are purely of bosonic nature and non-degenerated. This corresponds to the fixed point $\alpha = 0$, as mentioned, something that the actual values of the energy levels account for. There are two things worth to be noticed. The first is that there is an abrupt change in the first iterations of the NRG, indicating a rapid renormalization of Δ due to the effect of high-energy bosons. After these iterations, however, its value is essentially preserved all along the flow. This is indicated by the energy levels splitting, that goes like $\lambda^N \Delta_r$, as shown in the figure. The second thing to notice is that once the energy levels associated with the internal structure of the impurity cross the first excited bosonic state, the crossover between high-energy and low-energy behavior is essentially completed, reaching the fixed point (this happens around $N \sim 8$ for $\alpha = 0.1$). This very point defines a crossover *temperature* T_N, whose detailed study can shed light on the nature of the phase transition, which turn out to be of Kosterlitz-Thouless kind [118].

For $\alpha > \alpha_c$ the situation is different. Again, the plot shows a rapid renormalization of Δ, but in this case leading to $\Delta_r = 0$. Then the flow converges to a regime where again the lowest energy levels correspond to the bath bosonic excitations, with the difference being that they are now doubly degenerated. This is, as mentioned, the signature of the localized fixed point, the one that rules the low-energy regime above the critical coupling.

To finish this introduction to the NRG, let me mention that once the code is set up, it can be used to study a larger variety of properties of the SB model, something that applies for extension to other impurity models. For instance, the quantum phase transition can be studied in more detail, and information about the numerical value of α_c and its dependence on the initial tunnelling parameter Δ can be extracted from the data. In this task, it is convenient to approach the continuous regime $\lambda \to 1$ as close as possible, something that can be done by interpolating results from different values of λ. Moreover, thermodynamic quantities can also be studied by analyzing the evolution during the flow of certain observables. Last, but no least, the NRG is not restricted to ohmic models, but can be extended to other couplings to the bath, like the more subtle sub-ohmic case [118].

2.4 Flow Equations

The Flow Equations method also inherits the scaling and Renormalization Group ideas discussed throughout this chapter. It was proposed independently by Glazek and Wilson [121, 122] and by Wegner [123]. The former, in the context of high-energy Particle Physics, while the latter in Condensed Matter Physics.

We have seen that both RG and NRG rely on scaling transformations of the Hamiltonian by integrating out high-energy degrees-of-freedom. The disadvantage of these approaches lies precisely in the loss of those high-energy degrees-of-freedom as the flow is carried out. This is all right as far as we are only interested in the low-energy regime. However, in some situations keeping the whole Hilbert space could be of interest. This has actually been the last course of development of the NRG, where high-energy states would be saved despite being somehow integrated out, in order to use them later [124, 125]. The Flow Equation approach pursues the same aim, but the way to implement it differs considerably.

I will introduce here the Flow Equation method as it was proposed by Wegner, being this the version I have used throughout this thesis. An extensive reference on this approach can be found in the book by S. Kehrein [110].

2.4.1 The general idea of the Flow Equation approach

Most of the general ideas underlying the Renormalization Group also apply for this method. The Flow Equation (FE) approach consists as well in infinitesimal transformations of the Hamiltonian, in which new effective Hamiltonians are generated during the flow. The main difference is that, in this method, the transformations carried out do not integrate out high-energy degrees-of-freedom, but matrix-elements that involve very different energy scales. Let us suppose we have a Hamiltonian in the form $\mathcal{H} = \mathcal{H}_0 + \mathcal{H}_I$. In the basis given by the *free* Hamiltonian $\mathcal{H}_0$, say $|n\rangle_0$, the matrix-elements of the *interacting* part are in general off-diagonal, reading ${}_0\langle n|\mathcal{H}_I|n'\rangle_0$. These matrix-elements involve free states with energy differences $E_n - E_{n'}$. In this matrix-representation, the more off-diagonal the elements are, the larger the energy differences that involve. The Flow Equation approach pursues then to construct a transformation that increasingly removes those matrix-elements with the highest energy differences, but preserving the size of the Hilbert space. A schematic picture of this, and its comparison to the ordinary RG method, is shown in Fig. 2.5.

How can such a transformation be implemented? Let us suppose that, since the transformation preserves the Hilbert space, a Hamiltonian generated this way is unitarily equivalent to any other one. Then, if we introduce a parameter B, that controls the flow of the transformation, an infinitesimal transformation of the Hamiltonian can generically be expressed by:

$$\frac{d\mathcal{H}(B)}{dB} = [\eta(B), \mathcal{H}(B)] \tag{2.40}$$

where $\eta(B)$ is the antihermitian generator of the transformation, and the initial condition is set as $\mathcal{H}(B = 0) = \mathcal{H}$. The choice of the generator is the most tricky point of the procedure, and there is no unique choice that works for every case. The main requisite is to achieve the goal of making the

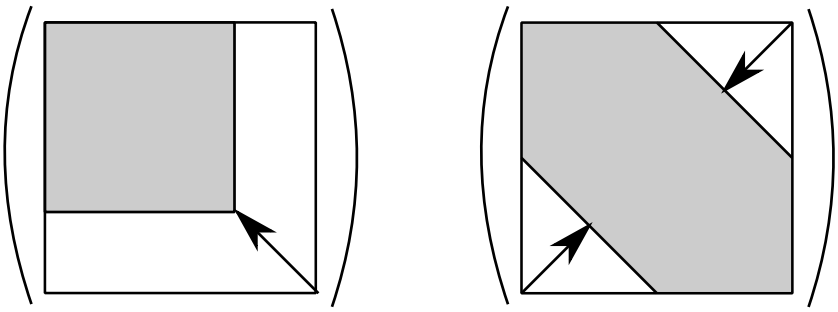

Figure 2.5: Comparison of the RG philosophy and the FE one. Left: RG integration of high-energy degrees-of-freedom. Right: FE elimination of matrix-elements bearing large energy differences. Notice that the second one preserves the size of the Hilbert space, as opposed to the first one.

Hamiltonian increasingly diagonal as the transformation is carried out. In his seminal paper, Wegner proposed a particular generator that has proven to be suitable in many situations:

$$\eta(B) = [\mathcal{H}_0(B), \mathcal{H}_I(B)] \tag{2.41}$$

This *canonical generator* is indeed antihermitian, $\eta(B) = -\eta^\dagger(B)$, and makes the Hamiltonian progressively more diagonal since it fulfills[3]:

$$\frac{d}{dB} Tr(\mathcal{H}_I^2(B)) \leq 0 \tag{2.43}$$

By examining the units of $\eta(B)$, we see that the flow parameter B has units of (Energy)$^{-2}$, so it might be tempting to make a correspondence $\Lambda_{FE} = B^{-1/2}$ to reconnect with the RG results. Of course, it is mandatory to keep in mind that the cutoff in the FE approach remains always the same, and the flow is related to the elimination of matrix-elements bearing large energy differences. The connection, however, still holds, and it can be generally stated that the FE one contains RG as a limiting case. How can this be? Well, the Flow Equation method is, after all, based on energy scale separation, like the RG, so it can be expected that, as the flow is carried out, the low-energy sector of the increasingly diagonalized Hamiltonian becomes decoupled from the high-energy sector. The latter will be reflected on the former by means of renormalization of couplings and generation of new Hamiltonian terms. In essence, the same thing that we found when integrating out high-energy degrees-of-freedom. This justifies the correspondence $\Lambda_{RG} = \Lambda_{FE}$ in the low-energy sector of the FE generated Hamiltonians, and the same flow equations for the coupling constants should be recovered within this new approach.

The FE method can be seen as a diagonalization of a Hamiltonian by carrying out a continuous sequence of unitary transformations. This is so because in the limit $B \to \infty$ the Hamiltonian becomes

[3]To get an intuition of how this property implies that the Hamiltonian gets increasingly more diagonal, it is useful to take simple cases, like the simple two-level system considered in the last section, whose interacting term reads:

$$\mathcal{H}_I(B) = \begin{pmatrix} 0 & t(B) \\ t(B) & 0 \end{pmatrix} \tag{2.42}$$

Notice that $Tr(\mathcal{H}_I^2) = 2t(B)^2$, and therefore it becomes more diagonal if $dt(B)^2/dB < 0$

completely diagonal. Of course, the advantage of this novel method does not lie on the possibility of exactly diagonalizing the Hamiltonian, but in the versatility it turns out to have to introduce controlled approximations to the flow that considerably simplify the study of the model in certain limits. As happened with scaling perturbation theory, by using infinitesimal transformations we gain access to non-perturbative regimes of some Hamiltonians, mostly when it happens that the parameters used to make approximations of the flow do not coincide with the coupling constants. Of course, quoting R.A. Hanlein, *there is no such thing as a free lunch*, and the pay-back comes from the fact that the infinitesimal transformation tends to produce an uncontrollable sequence of new terms in the effective Hamiltonian. Those must be truncated in order to get closed flow equations that can be worked out. Hence, a truncation scheme must be found. In the quest of finding one, it may happen that we find that the canonical generator is no longer a good choice, and less standard generators must be envisaged.

Remarkably, the same approach described so far can be used to study the evolution of observables. For a certain observable $O(B)$, we use the chosen generator to produce an infinitesimal sequence of unitary transformations:

$$\frac{dO(B)}{dB} = [\eta(B), O(B)] \tag{2.44}$$

Notice, however, that in contrast to the Hamiltonian, $O(\infty)$ does not necessarily have to be diagonal. Indeed, in general it will be non-diagonal, and therefore difficult to handle in the new basis, for instance when computing correlation functions or other observables of interest. This is the same issue that usually happens with exact solutions, where knowledge of the latter does not imply that calculations of actual observables are accessible.

2.4.2 An application to the Spin-Boson model

In order to get familiar with the method, let me now sketch its application to the Spin-Boson model [126, 127], whose Hamiltonian we already studied in the NRG section. Here, I will follow the lines given in the book by Kehrein [110].

As we have seen, the first task to accomplish in order to implement the FE program is to find a suitable generator for the transformation. The canonical generator reads, in this case:

$$\eta(B) = i\sigma_y \sum_n \frac{\lambda_n(B)}{2} \Delta(B)(a_n + a_n^\dagger) - \sigma_z \sum_n \frac{\lambda_n(B)}{2} \omega_n (a_n - a_n^\dagger) \tag{2.45}$$

With this generator, the commutators $[\eta, \mathcal{H}]$ must be worked out. It can be seen that this entails the generation of new terms not contained in the original Hamiltonian. On general grounds, we should proceed by introducing these new terms into the flowing Hamiltonian $\mathcal{H}(B)$, and then working out again the commutator $[\eta(B), \mathcal{H}(B)]$. Of course, they might yield other terms not regarded before that must be included in the Hamiltonian, and so on, until closed equations are found. In practice, however, it can easily happen that new terms are always generated and no convergence is found. A truncation scheme is required, based on a particular approximation to the model, as for example restrictig us to the weak-coupling regime. For the SB model, it happens that by using a simple generalization of the

canonical generator:

$$\eta(B) = i\sigma_y \sum_n \frac{\lambda_n(B)}{2} \Delta(B) f_n^{(y)}(B)(a_n + a_n^\dagger) - \sigma_z \sum_n \frac{\lambda_n(B)}{2} \omega_n f_n^{(z)}(B)(a_n - a_n^\dagger) \tag{2.46}$$

where we have introduced the dimensionless coefficients $f_n^{(y)}$ and $f_n^{(z)}$, we can already simplify the structure of the flow equations. With this choice, the commutator $[\eta(B), \mathcal{H}_0(B)]$ reduces simply to:

$$[\eta(B), \mathcal{H}_0(B)] = -\sigma_z \sum_n \frac{\lambda_n}{2} (\omega_n - \Delta(B))^2 (a_n + a_n^\dagger) \tag{2.47}$$

as far as the new coefficients are imposed to take the form $f_n^{(y)} = -f_n^{(z)}$ and $f_n^{(z)} = \frac{\omega_n - \Delta}{\omega_n + \Delta}$. On the other hand, the commutator with the interacting term reads:

$$\begin{aligned} [\eta, \mathcal{H}_I] &= \frac{\sigma_x}{2} \sum_n \lambda_n^2 \Delta \frac{\omega_n - \Delta}{\omega_n + \Delta} (2n_n + 1) \\ + \frac{\sigma_z}{2} \sum_{n,m} \frac{\Delta}{2} \lambda_n \lambda_m \left(\frac{\omega_n - \Delta}{\omega_n + \Delta} + \frac{\omega_m - \Delta}{\omega_m + \Delta} \right) &: (a_n + a_n^\dagger)(a_m + a_m^\dagger) : - \frac{1}{2} \sum_n \lambda_n^2 \omega_n \frac{\omega_n - \Delta}{\omega_n + \Delta} \end{aligned} \tag{2.48}$$

where $: O :$ stands for normal-ordering of the operator O. The second term of the commutator introduces a new interaction. At leading order in the flow equations expansion, however, it can be neglected, since the feedback it would produce in the flow equations in case of introducing it in the flowing Hamiltonian $\mathcal{H}(B)$ is negligible. The consistence of this approximation must be checked *a posteriori* [127].

The flowing Hamiltonian that contains all the terms generated during the expansion can be written now:

$$\begin{aligned} \mathcal{H}(B) = -\frac{\Delta(B)}{2} \sigma_x + \sum_n \omega_n a_n^\dagger a_n + \frac{\sigma_z}{2} \sum_n \lambda_n(B)(a_n + a_n^\dagger) \\ - \frac{1}{2} \sigma_x \sum_{n,m} \omega_{n,m}(B) : (a_n + a_n^\dagger)(a_m + a_m^\dagger) : + E(B) \end{aligned} \tag{2.49}$$

where the flow equations for the different coefficients that arise are set from equation (2.40), reading:

$$\frac{d\Delta(B)}{dB} = -\Delta(B) \int \frac{d\omega}{\pi} J(\omega, B) \frac{\omega - \Delta(B)}{\omega + \Delta(B)} \coth(\beta\omega/2) \tag{2.50}$$

$$\frac{d\lambda_n(B)}{dB} = -(\omega_n - \Delta(B))^2 \lambda_n(B) \tag{2.51}$$

$$\frac{d\omega_{n,m}(B)}{dB} = -\frac{\lambda_n(B)\lambda_m(B)}{2} \Delta(B) \left(\frac{\omega_n - \Delta(B)}{\omega_n + \Delta(B)} + \frac{\omega_m - \Delta(B)}{\omega_m + \Delta(B)} \right) \tag{2.52}$$

$$\frac{dE(B)}{dB} = -\frac{1}{2} \int \frac{d\omega}{\pi} J(\omega, B) \omega \frac{\omega - \Delta(B)}{\omega + \Delta(B)} \tag{2.53}$$

here, $\beta = 1/T$ is the inverse of the temperature, and we have introduced a flowing bath spectral function:

$$J(\omega, B) = \pi \sum_n \lambda^2(B) \delta(\omega - \omega_n) \tag{2.54}$$

which can be seen to satisfy a differential flow equation too:

$$\frac{dJ(\omega, B)}{dB} = -2(\omega - \Delta(B))^2 J(\omega, B) \tag{2.55}$$

These equations can be worked out in order to carry out the flow to infinity. In the final Hamiltonian, the interacting term will be, as expected, removed:

$$\mathcal{H}(\infty) = -\frac{\Delta(\infty)}{2}\sigma_x + \sum_n \omega_n a_n^\dagger a_n - \frac{1}{2}\sigma_x \sum_{n,m} \omega_{n,m}(\infty) : (a_n + a_n^\dagger)(a_m + a_m^\dagger) : + E(\infty) \tag{2.56}$$

Once again, the renormalized tunnelling parameter is the one that characterizes the quantum phase transition found in the ohmic case at zero temperature, where $J(\omega, 0) = 2\pi\alpha\omega$. For $T = 0$, the equation for the tunnelling parameter can be solved analytically:

$$\log\left(\frac{\Delta(\infty)}{\Delta(0)}\right) = -\frac{1}{2}\int d\omega \frac{J(\omega, 0)}{\omega^2 - \Delta^2(\infty)} \tag{2.57}$$

It gives a self-consistency equation for $\Delta(\infty) \equiv \Delta_r$. If $\alpha > 1$, then the solution reads $\Delta_r = 0$, and the particle becomes localized. For $\alpha < 1$, it yields a finite renormalized tunnelling parameter:

$$\Delta_r = \Delta\left(\frac{\Delta}{\omega_c}\right)^{\frac{\alpha}{1-\alpha}} \tag{2.58}$$

where ω_c is the ultraviolet cutoff up to which the theory is valid, and we have set the initial condition $\Delta(0) = \Delta$. We readily see how the Flow Equation method can be useful to describe non-perturbative effects like the localized-to-delocalized quantum phase transition that happens at $\alpha = 1$. Of course, once the Flow Equations have been worked out, many other observables and properties of the system can be analyzed, something that I will not discuss at this introductory level.

As a final remark, I reckon that the main message of this chapter should be that scaling and renormalization ideas can be quite useful in order to implement very powerful techniques to study interacting problems even in the non-perturbative regime. Effective low-energy theories, flow of coupling constants and energy scale separation are central concepts I will recurrently use throughout this thesis, where these notions will be applied to study exotic phenomena due to interactions in low-dimensional quantum systems.

3 Phase diagram of a quantum particle in a finite chain, in the presence of an environment

There is nothing like looking, if you want to find something. You certainly usually find something, if you look, but it is not always quite the something you were after.

J. R. R. Tolkien

Summary

In this chapter I explain in detail my research on the phase diagram of a dissipative confined particle, in a quantum context. Environments can dramatically alter the properties of an isolated quantum system, by inducing decoherence and dissipation, but also by perturbing its ground state. The latter is the subject of study of this chapter. I will address how an environment coupled to a particle living in a finite one-dimensional chain, induces a rich phase diagram, with a quantum phase transition in the strong coupling regime. I will start introducing the field of Open Quantum Systems, as well as the general features of the model I will use throughout, the Caldeira-Leggett model. This section is completed with the next one, where the Caldeira-Leggett model for a confined particle is described, as well as its possible experimental relevance. Next two sections include the actual calculations. In the first one, a simple variational ansatz is proposed, that nevertheless is able to account for some relevant aspects of the problem. Then I will switch to a generalization of the NRG for Caldeira-Leggett-like Hamiltonians, which require to take into account some particular issues of the model. Results are obtained and compared with the variational ansatz. A last section will be then devoted to the conclusions. The work described in this chapter is published in Ref. [128–130], and was done in collaboration with L. Borda.

3.1 Introduction: Open Quantum Systems and the Caldeira-Leggett model

Purely isolated quantum systems studied in textbooks rarely exist in nature, and even less in real experiments. Environments are ubiquitous when addressing most of the experiments. After all, it might be said, quoting Albert Einstein, that *the environment is everything that isn't me*. Somehow, this is meaning that when we talk about environments we are covering a variety of things, from the

substrate where the sample lies on to the actual measurement apparatus employed to study it. Not to say that sometimes, theorists entertain themselves thinking of a large system as a small piece of it surrounded by the rest, where this rest will be playing the part of an environment. Therefore it seems reasonable that a considerable effort has been devoted to study the effects of these environments on the properties of quantum systems. This is the central aim of research in the field of Quantum Mechanics of Open Systems.

When a quantum system stops to be isolated, it means that there exist open channels that communicate it with the environment. Through them it might flow energy, leading to the quantum analogous of dissipative phenomena. The way this can be theoretically addressed, and how classical dissipation emerges from the quantum world, is the subject of the subfield of Quantum Dissipation [40]. Nowadays we understand that information can also flow from the system to the environment. And in the process, some of this information is lost, an observation that is at the heart of Quantum Measurement Theory [39]. Information is somehow related to coherence and entanglement, both properties genuinely quantum that are known to flow when quantum systems are coupled to environments. Its flow, however, turns out to be more elusive to quantify, since coherence and entanglements are themselves quantities whose precise definition in terms of observables is still under debate. But there is a general consensus on the fact that coherence is lost in the presence of environments, an effect that is known as *decoherence* [131] or *dephasing* [1]. Written in an appropriated basis, usually the one that diagonalizes some observable through which the environment is coupled to the system, this means that the reduced density matrix of the quantum system, ρ_{red}, becomes increasingly diagonal as a dynamical consequence of the external coupling:

$$\frac{d\mathrm{Tr}(\rho_{red}^2)}{dt} < 0 \tag{3.1}$$

This quantity is called *purity*, and is one of the observables proposed to quantify the entanglement of a certain quantum system. A diagonal reduced density matrix is our best description of a quantum system that has become classical: there are no longer subtle effects due to interference between quantum states, at least in the basis in which the density matrix is defined. The latter, as mentioned, is not arbitrary, being the one in which the effect of the environment translates into destruction of non-diagonal matrix elements. Notice, however, that this does not imply a knowledge of the output of a measurement, whose determination is beyond the standard quantum theory, that only yields, after decoherence, classical probabilities [132]. The question is, was coherence really destroyed in the course of coupling to the environment? Not really. The reduced density matrix is defined as a trace over the environment degrees-of-freedom performed on the system plus environment density matrix: $\rho_{red} = \mathrm{Tr}_E \rho$, where Tr_E stands for such a trace. If we consider the whole system as isolated, then the following property follows:

$$\frac{d\mathrm{Tr}(\rho^2)}{dt} = 0 \tag{3.2}$$

i.e., the total purity is conserved. From this equation, an intuition about this aforementioned flow of coherence can be grasped. When the environment couples to the quantum system, both of them

[1] The latter, rigorously, being related to loss of coherence without dissipation

become entangled. The quantum system, considered like an independent theory through the eyes of the reduced density matrix, tends to increasingly behave as expected from a classical system. However, when system and environment are studied as a whole, the overall quantum properties of the system remain alive. This is probably one of the most striking consequences of Open Quantum Systems theory: there is no real *quantum-to-classical transition* that emerges from the quantum formalism [133]. The observer, considered as an environment, sees a system becoming classical in the process of both of them getting entangled, and global coherence is not lost.

How is an open quantum system modelized? This is yet a controversial academical issue, though in practice researchers reached a consensus about it some time ago. Early claims pointed to the fact that the Hamiltonian formalism, the one underlying Quantum Mechanics, stops to be applicable when energy is not overall conserved. The answer, as was already mentioned, requires to consider the Hamiltonian of the quantum system plus environment as a whole, which is by definition an isolated system. Therefore, in order to follow this approach, a Hamiltonian for the environment is needed, not to mention that the coupling between system and environment must also be envisaged. On general grounds, certainly, this should depend on the real system that is considered. The same physics is not expected to occur when the electron in a quantum dot is coupled through the spin to the spins of the atoms in the surrounding $GaAs/AlGaAs$ environment, and when the same electron is coupled to the phonons of this environment via its charge. Or the case of this very electron coupled to charge fluctuations of a nearby electron reservoir. However, as sketched above, it happens that in the end it is only the reduced system, where the environment is integrated out, the one we are concerned about. And, moreover, since temperature usually tends to spoil quantum properties, the low-energy (temperature) regime is the one usually considered. In this regard, scaling ideas can provide us with assistance again. For a rough description of the effective perturbation produced by the environment at low energies, it usually suffices to consider a simple model that leads to the same universality class, in a Renormalization Group sense, than the more complicated real microscopic Hamiltonian. In the last chapter, we had the opportunity to see that, in the course of the RG flow to lower energies, very different starting Hamiltonians might end up converging to the same fixed point. Were this the situation, would be not enough to consider the simplest case within the whole family of Hamiltonians that falls into the same universality class?

This is in fact the case of the so-called Caldeira-Leggett model. It describes the environment as a simple collection of independent harmonic oscillators, i.e., in the language of second quantization, as a bosonic bath. This sort of description was earlier employed to study open quantum systems, pioneered by R. Feynman [134]. However, it is named after A. O. Caldeira and A. J .Leggett because of the extensive analysis that these researchers performed on this model, as well as because of the simple coupling they selected for the study, and the way they improved the model in order to deal with some subtle issues that can be seen to arise in many situations [135, 120]. Their motivation was to study the way classical equations of motion of a dissipative particle emerge from a purely quantum mechanical framework.

The simplest realization of the Caldeira-Leggett model is probably the one that couples the environment to a two-level quantum system, the already widely studied Spin-Boson model. However, the general Hamiltonian turns out to be more complicated. Let us restrain ourselves to one-dimensional

systems. The Hamiltonian of the CL model reads:

$$\mathcal{H}_{CL} = \mathcal{H}_0 + \sum_n \omega_n a_n^\dagger a_n + q\sum_n \lambda_n (a_n + a_n^\dagger) + q^2 \sum_n \frac{\lambda_n^2}{\omega_n} \tag{3.3}$$

The first term, $\mathcal{H}_0$, corresponds to the isolated quantum system. For instance, in case of having a one-dimensional particle moving in an external potential:

$$\mathcal{H}_0 = \frac{p^2}{2m} + V(q) \tag{3.4}$$

where the following canonical commutation relation holds, $[q, p] = i$, that binds together the position q and the momentum p.

The second term of the Caldeira-Leggett model describes a gapless bath of oscillators in second quantization, being a_n and $a_n^\dagger$ destruction and creation operators, respectively, of a bosonic excitation of energy ω_n. In principle, in order to avoid that energy eventually flows back to the system, an infinite number of oscillators is required. These will be compacted within a finite energy interval up to a certain cutoff ω_c. The third term describes the coupling between system and environment. This coupling is realized through the position operator, q. However, identical results could be obtained by coupling it to its canonical conjugate, the momentum p. λ_n give the coupling strengths to every mode. By selecting this particularly simple coupling, the model can be seen to reproduce Newton's equations of motion for a dissipative particle in an external potential. It happens, however, that the specific equations of motion depend on the mechanism of dissipation, which is fully described by the following function:

$$J(\omega) = \pi \sum \lambda_n^2 \delta(\omega - \omega_n) \tag{3.5}$$

This was already introduced when we addressed the study of the Spin-Boson model, and is named the *bath spectral function*. As I mentioned, the simplest type of dissipation, the Ohmic one, is realized by taking $J(\omega) = 2\pi\alpha\omega$ up to the ultraviolet cutoff ω_c.

Finally, the last term of the Caldeira-Leggett Hamiltonian is a counter-term introduced to ensure that dissipation is homogeneous. Were this term non-existing, the strength of couple would depend on the location of the particle, when the aim of the model is precisely to describe a translationally invariant dissipation mechanism. Even with the addition of this term, that the whole model preserves this symmetry can be obscure, and in order to understand this point is better to resort to an unitary equivalent Hamiltonian. This is obtained after applying the transformation $U = e^{q\sum_n \frac{\lambda_n}{\omega_n}(a_n^\dagger - a_n)}$ to the CL model with $V(q) = 0$, yielding:

$$\tilde{\mathcal{H}}_{CL} = \frac{1}{2m}\left(p - i\sum_n \frac{\lambda_n}{\omega_n}(a_n^\dagger - a_n)\right)^2 + \sum_n \omega_n a_n^\dagger a_n \tag{3.6}$$

This Hamiltonian, explicitly translationally invariant, indicates that the coupling between bath and system is a realization of a minimal coupling to the quantum particle [2].

The Caldeira-Leggett model has been mostly studied in the field of Quantum Dissipation, while its minimal realization, the Spin-Boson model, is the one that has featured most of the research

[2] It has been pointed out later, however, that the counter-term might not cure inhomogeneities in a dynamical context [136]. However, this is not the case we will address here.

concerning decoherence. As it has been mentioned already a few times, in the context of Quantum Dissipation, the most outstanding result that follows from this model is likely the one already found by Caldeira and Leggett in their seminal work: in the classical limit, i.e., when $\hbar \to 0$, the model is able to reproduce the classical equations of motion of a particle with friction [120]:

$$m\frac{d^2}{dt^2}q(t) = -\frac{\partial V(q)}{\partial q} - \int_0^T dt'\alpha(t-t')(q(t)-q(t')) \tag{3.7}$$

where we have introduced the kernel:

$$\alpha(t-t') = \frac{1}{2\pi}\int_0^\infty J(\omega)e^{-\omega|t-t'|}d\omega \tag{3.8}$$

When Ohmic dissipation is regarded, as well as Markovian baths (the latter meaning that the bath does not keep memory of feedback effects coming from the particle), then these equations reduce to the simple description of friction used in Classical Mechanics:

$$m\frac{d^2}{dt^2}q(t) = -\frac{\partial V(q)}{\partial q} - \eta\frac{d}{dt}q(t) \tag{3.9}$$

where η is the friction coefficient. A related problem, also extensively addressed with the CL model, is that of Quantum Brownian Motion [137].

Other fruitful applications of the CL model concern the study of the phase diagram of quantum particles in the presence of an environment, the latter being strongly dependent on the Hamiltonian for the quantum particle. For instance, the case of a free particle was addressed in [138], and that of a particle in a periodic potential in [139, 140]. In general, the properties of the quantum particle are influenced by the environment, whose first consequence is to instantaneously follow the motion of the particle. An external observer would interpret this situation in terms of a renormalized or dressed particle. However, the effect that finally has the environment on the particle depends on the particular Hamiltonian for the particle, as mentioned. It can lead, for example, to a phase transition in which the particle becomes completely localized at a certain position. This sort of studies are the ones I am interested to perform in this chapter. Here, I will address the phase diagram of the Caldeira-Leggett model for a particle living in a one-dimensional finite chain, which is a discrete realization of the dissipative quantum particle in a box.

However, before introducing these novel result, let me address briefly the connection of the CL model with real experiments. As mentioned, the Caldeira-Leggett model must be considered as a minimal description of the environment and its coupling to the system. On general grounds, we expect it to give a somewhat rough but essentially good picture of the physics behind more complicated environments, as far as they all belong to the same low-energy universality class described by the CL model, which of course might not be true for every environment considered. The CL model usually works fine for environments whose low-energy excitations are of bosonic nature, as it happens with phonons in a solid or magnons in a spin system. Particle-hole excitations, not purely of bosonic nature, can also be seen equivalent to CL dissipation [141]. In this regard, it is known that CL dissipation can arise from charge fluctuations coming from nearby gates in experiments in $GaAs/AlGaAs$ nanostructures [142], and any other quantum system close to a metallic structure. For what concerns us in this thesis, this may apply both for graphene layers on top of SiO_2 and for cold gases in atoms chips.

Last, but not least, CL dissipation was in fact first applied to the description of friction in Josephson Junctions [135].

3.2 The model: motivation and description

In this chapter I will address the study of the equilibrium properties of a one-dimensional quantum particle living in a finite chain and coupled to an environment in the way Caldeira and Leggett envisaged. As we already know from the first chapter of this thesis, the low-energy limit of a confined particle in one dimension is a zero-dimensional system. This is due to the discrete level structure, that for energies (temperatures) lower than the typical energy separation, only the ground state is essentially occupied, and the effects of lateral confinement leave a clear imprint on the behavior of the system.

The motivation to address this problem is multiple. First of all, it aims at continuing previous works from the eighties, already cited in the last section, where the equilibrium properties of quantum particles perturbed by Caldeira-Leggett baths were investigated. And probably the first task to accomplish in this direction is the understanding of the phase diagram, both at zero and finite temperatures. The quantum particle in a finite chain can be seen as a discretization of the continuous model of a quantum particle in a box. If this problem was never addressed before is not due to a lack of interest, but certainly because the typical analytical strategies first employed fail when applied to this model. The source of this issue can be rooted to the few symmetries that can be exploited in the problem. Most of previous works cited rely on the translation symmetry, no matter if this is a continuous one, as it is the case of the free particle [138], or discrete, as happens with the particle in a periodic potential [139, 140]. In the case of the confined particle, only parity symmetry is preserved, and this turns out not to be sufficient to simplify its study.

If the confined particle Hamiltonian is discretized, which is the case I will address here, the situation changes, since we can take advantage of working with a small number of sites in the chain. The new Hamiltonian has the general form of a tight-binding one with M sites. In second quantization, this reads:

$$\mathcal{H}_0 = -t \sum_{m=1}^{M} c_m^\dagger c_{m+1} + h.c. \tag{3.10}$$

where t is a hopping parameter related to the probability of jumping from one site to its nearest neighbor. When this model is a lattice discretization of the continuum, the parameter t is related to the continuous ones by $t = \hbar/2ma^2$, being a the lattice spacing. In the limit $a \to 0$, $M \to \infty$ and $L \equiv Ma$ constant, we recover the continuous model. c_m and $c_m^\dagger$ are destruction and creation operators of one electron at the site m. They already incorporate the boundary conditions of a box, as $c_0 = c_{M+1} = 0$. The use of second quantization language is convenient if we aim to generalize the results of this chapter to a many-body context. However, notice that henceforth only one-particle situations will be addressed. Moreover, in what follows I will set $a = 1$.

A note on this line of motivation of the problem. As mentioned, if the interest in the problem relies on overtaking the difficulties that its continuous counterpart has when trying an analytical approach, it happens that the limit of only a few sites is typically accessible. This is specially true when

numerical techniques like the NRG are employed, due to computational limitations. The continuous limit, however, requires $M \to \infty$. Therefore, although some insights can be obtained within this approach, a completely satisfactory solution remains yet elusive.

However, the study itself of a chain of finite length results of interest, since it happens that many low-dimensional systems can be realized with this chain configuration. For instance, arrays of quantum dots, relevant for Quantum Computation and Nanoelectronics, or ultracold gases trapped in optical lattices and atom chips. In the case of optical lattices, as we saw in Ch. 1, problems related with noise and environments are minor, though in certain situations an effective environment could arise from the combined influence of multiple one-dimensional arrays. A more accurate description of the physics in terms of Caldeira-Leggett dissipation should occur in an atom chip, where multiple sources of noise come from the nearby substrate, some of them falling into the category described by the CL class of universality. Therefore, the general consequences derived throughout this chapter should apply for arrays of quantum dots in atom chips, where the discrete model becomes specially applicable.

In this chapter I will concentrate on the case of Ohmic dissipation, one of the most interesting and common ones. This allows us to introduce a particular choice of parameters for the bath energies and couplings that automatically accounts for the right spectral bath function. Those are $\omega_n \to \omega_k = k$ and $\lambda_n \to \lambda_k = \lambda\sqrt{k}$. The complete model reads then:

$$\mathcal{H} = -t\sum_{m=1}^{M}\left(c_m^\dagger c_{m+1} + c_{m+1}^\dagger c_m\right) + \sum_{k<\omega_c} k a_k^\dagger a_k + \lambda q \sum_{k<\omega_c}\sqrt{k}(a_k + a_k^\dagger) + \lambda^2 q^2 \sum_{k<\omega_c} 1 \tag{3.11}$$

where, as usual, $J(\omega) = 2\pi\alpha|\omega|\theta(\omega_c - \omega)$, being now $\alpha = \lambda^2/4\pi$. The position operator for the tight-binding chain has the form, in terms of creation/destruction operators: $q = \sum_{m=1}^{M}(m - m_0)c_m^\dagger c_m$, where m_0 denotes the center of the chain (notice that the center is a site only for odd chains). In general, we will be interested in the case $t \ll \omega_c$, which is sometimes called the *universal* limit, where we expect that the low-energy properties of the model depend only on the dimensionless quantities M, t/ω_c and α.

Symmetries

As I have already mentioned, one of the drawbacks of this model is precisely the lack of symmetries, that are reduced to parity. Let Π be the parity operator, under which the operators of the Hamiltonian transform like:

$$\begin{aligned} \Pi c_m^\dagger \Pi^\dagger &= c_{-m} \\ \Pi a_k^\dagger \Pi^\dagger &= -a_k^\dagger \\ \Pi q \Pi^\dagger &= -q \end{aligned} \tag{3.12}$$

Bosonic number states have a well defined parity, $\Pi(b_k^\dagger)^{n_b}|0\rangle = (-1)^{n_b}(b_k^\dagger)^{n_b}|0\rangle$. This is not true for the particle operators, an issue easily workable by introducing new operators with parity as a good quantum number. For even M, we have

$$c_{m,p} = \frac{1}{\sqrt{2}}(c_m + p c_{-m}) \tag{3.13}$$

being p the parity quantum number, with values $p = \pm 1$. For odd M, the main difference is that we must treat separately the zero site:

$$c_{m,p} = \tfrac{1}{\sqrt{2}}(c_m + pc_{-m}), \quad m \neq 0 \tag{3.14}$$

$$c_{0,+} = c_0 \tag{3.15}$$

where $+$ is standing for $p = +1$.

Let us now write the tight-binding Hamiltonian in terms of these operators with well defined parity number. Interestingly, the Hamiltonian splits up into two parts, $\mathcal{H}_0 = \mathcal{H}_+ + \mathcal{H}_-$. Again, there are differences depending on the number of sites considered. When M is odd, we have:

$$\mathcal{H}_+ = t \sum_{m=1}^{(M-1)/2} \left(c^\dagger_{m,+} c_{m+1,+} + H.c \right) + \sqrt{2} t c^\dagger_{0,+} c_{1,+} + h.c \tag{3.16}$$

$$\mathcal{H}_- = t \sum_{m=1}^{(M-1)/2} \left(c^\dagger_{m,-} c_{m+1,-} + H.c \right) \tag{3.17}$$

For even M:

$$\mathcal{H}_+ = t \sum_{m=1}^{M/2} \left(c^\dagger_{m,+} c_{m+1,+} + H.c \right) + t c^\dagger_{1/2,+} c_{1/2,+} \tag{3.18}$$

$$\mathcal{H}_- = t \sum_{m=1}^{M/2} \left(c^\dagger_{m,-} c_{m+1,-} + H.c \right) + t c^\dagger_{1/2,-} c_{1/2,-} \tag{3.19}$$

The two sectors are coupled by the position operator q, since the latter reads:

$$q = \sum_m (m - m_0) c^\dagger_m c_m = \sum_{m=1}^{M_{max}} (m - m_0) c^\dagger_{m,+} c_{m,-} \tag{3.20}$$

where $M_{max} = M/2$ for even M, and $M_{max} = (M-1)/2$ for odd M.

Limiting cases

It turns out to be important to study the different limits of this Hamiltonian, as we already did with the Spin-Boson model. The limit $\alpha = 0$ corresponds to the confined particle decoupled from the bath. The single-particle Hamiltonian is then easily diagonalized in the basis:

$$|p\rangle = \sqrt{\frac{2}{M+1}} \sum_{m=1}^{M} \sin(pm) |m\rangle \tag{3.21}$$

with energies $\epsilon_p = -2t \cos p$, being $p = \pi q/(M+1)$, $q = 1, ..., M$.

The limit $t = 0$ is the second one of interest. In this case, the Hamiltonian is diagonal in the site basis, $|m\rangle$. Therefore, it is possible to obtain a reduced Hamiltonian for the bosonic degrees-of-freedom by projecting it into the single-particle sites states. This reduced Hamiltonian is readily diagonalized by shifting the bath operators:

$$\langle m | \mathcal{H}_{CL} | m \rangle = \sum_{k < \omega_c} k \left(a^\dagger_k + \lambda \frac{\tilde{m}}{\sqrt{k}} \right) \left(a_k + \lambda \frac{\tilde{m}}{\sqrt{k}} \right) \tag{3.22}$$

where $\tilde{m} \equiv m - m_0$. A compact expression is obtained by defining displaced oscillator operators as $\tilde{a}_k \equiv a_k + \lambda \tilde{m}/\sqrt{k}$. Such a displacement is in fact generated by the unitary operator $U = e^{q \sum_k \frac{1}{\sqrt{k}}(a_k - a_k^\dagger)}$, well-known in the context of the polaron problem [143], that shares many features with the CL physics. The usual interpretation of this limit is that of quasiparticles composed of a particle plus a cloud of harmonic oscillators.

Localization transition from RG arguments

It is useful in many situations to apply the aforementioned transformation, read $U = e^{q \sum_k \frac{1}{\sqrt{k}}(a_k - a_k^\dagger)}$, on the full Hamiltonian. It yields the following unitarily equivalent Hamiltonian:

$$\tilde{\mathcal{H}}_{CL} = \sum_{k<\omega_c} k a_k^\dagger a_k - t \sum_{m=1}^{M} (c_m^\dagger c_{m+1} e^{-\lambda \sum_k \frac{1}{\sqrt{k}}(a_k^\dagger - a_k)} + h.c.) \tag{3.23}$$

If this Hamiltonian is now projected to the ground state of the bath, $a_k|0\rangle = 0$, which is no longer a good eigenstate of the Hamiltonian when $t \neq 0$, we obtain an effective (low-energy) Hamiltonian for the quantum particle:

$$\langle 0|\tilde{\mathcal{H}}_{CL}|0\rangle = -t_{\text{ren}} \sum_{m=1}^{M} \left(c_m^\dagger c_{m+1} + h.c. \right) \tag{3.24}$$

where $t_{\text{ren}} \equiv t\langle 0|e^{\sum_k 1/\sqrt{k}(a_k - a_k^\dagger)}|0\rangle$ is a renormalized hopping due to the fact that oscillators follow in their motion to the particle, dressing it. This is equivalent to normal order the Hamiltonian, $:\mathcal{H}:$ with respect to the oscillators.

From the renormalized hopping, a differential flow equation in the RG sense can be obtained, by including only a differential fraction of high-energy oscillators, and studying its effect on the renormalized hopping. This allows us to recover the celebrated result [144]:

$$\frac{d}{d \log \omega_c} \left(\frac{t(\omega_c)}{\omega_c} \right) = (\alpha - 1) \frac{t(\omega_c)}{\omega_c} \tag{3.25}$$

This flow equation for the effective hopping proves to be sufficient to predict a localization phase transition at $\alpha = 1$, which is a fixed point of the Renormalization Group. We expect, then, that $\alpha = 1$ delimitates a regime in which t_{ren} is finite from one in which is effectively renormalized to zero, thus suppressing quantum fluctuations. In general, however, in order to obtain a better picture, more sophisticated calculations are required. These corrections are in turn necessary to determine if the critical line has also a dependence on the finite hopping parameter. This is the case, as it is well known, for the dissipative two level system, where the transition can be shown to be Kosterlitz - Thouless (KT) like [145] when higher corrections to the flow equations are computed [146, 147]. On the contrary, for the dissipative particle in a periodic potential there are no higher order corrections to the flow equations and the transition line in the $\alpha - t$ phase diagram is vertical [140].

A similar analysis can be attempted for the dissipative confined particle, but the computation of higher order corrections to the transition is considerably tedious, because of the large number of coupled flow equations that must be analyzed. This is again due to the lack of symmetries of the model, failing to restrain the number of counter-terms that must be taken into account in the

critical region close to $\alpha = 1$. This has prevented so far to perform a more detailed analysis of the localization transition for the model studied here, hence obliging us to resort to other techniques, like the Numerical Renormalization Group.

3.3 Variational approach

Yet, a variational calculation can give us more information than the RG one. Regarding the quantum phase transition, it does not give a more detailed picture, but it serves to characterize the different phases, and has the advantage of easily allowing for a generalization of the results to finite temperatures. I will use the approach proposed by Silbey and Harris [148] to study the Spin-Boson model. The method relies on the unitary transformation that we used in the previous section to get the Hamiltonian (3.23). As I mentioned, its effect is to displace the oscillators in order to accommodate them to the position of the particle, translating into an effective dressing of the bare properties of the particle. What Silbey and Harris proposed was to leave the among of this displacement as a free variational parameter f_k:

$$U = e^{-q\sum_k (f_k/k)(b_k - b_k^\dagger)} \tag{3.26}$$

Such a variational approach is conventionally referred to as the *displaced-oscillator ansatz*. The transformed Hamiltonian reads:

$$\hat{\mathcal{H}}_{CL} = \sum_{k<\omega_c} k a_k^\dagger a_k + gq^2 + q\sum_{k<\omega_c}(\lambda\sqrt{k} + f_k)(a_k + a_k^\dagger) + te^{\sum_k \frac{f_k}{k}(a_k - a_k^\dagger)} \sum_m^M \left(c_{m+1}^\dagger c_m + H.c\right) \tag{3.27}$$

$$\tag{3.28}$$

where we have defined the potential strength $g \equiv \sum_k (\lambda + \frac{f_k}{\sqrt{k}})^2$. Notice that this Hamiltonian reduces to (3.23) by setting $f_k = \lambda\sqrt{k}$. It is convenient to rewrite it in a more convenient way, that will provide us with a natural expansion to do the variational calculation. This is based on adding and subtracting its thermal average with respect to the free bosonic Hamiltonian, getting:

$$\hat{\mathcal{H}}_{CL} = -t_{\text{ren}} \sum_m^M (c_m^\dagger c_{m+1} + H.c) + \sum_{k<\omega_c} k a_k^\dagger a_k + gq^2 + V_+ \sum_m^M c_{m+1}^\dagger c_m + V_- \sum_m^M c_m^\dagger c_{m+1} + V_0 q \tag{3.29}$$

Here, we have introduce a renormalized hopping with a similar form that the one studied in the previous section, $t_{\text{ren}} \equiv \langle te^{\sum_k (f_k/k)(a_k - a_k^\dagger)}\rangle_T$. Furthermore, this expression is generalized to finite temperature and includes the variational parameter. Its analytical expression can be carried out, yielding:

$$t_{\text{ren}} = t\exp[-\frac{1}{2}\sum_k \frac{f_k^2}{k^2}\coth(\frac{\beta k}{2})] \tag{3.30}$$

In addition, in Hamiltonian (3.29) new operators have been conveniently introduced:

$$V_+ = V_-^\dagger \equiv te^{\sum_k \frac{f_k}{k}(a_k - a_k^\dagger)} - t_{\text{ren}} \tag{3.31}$$

$$V_0 \equiv \sum_{k<\omega_c} (\lambda\sqrt{k} + f_k)(a_k + a_k^\dagger)\,, \tag{3.32}$$

in a way they have zero thermal expectation values, $\langle V_i \rangle_T = 0$ ($i = \pm, 0$). This allows for a decomposition of the new Hamiltonian in $\hat{\mathcal{H}}_{CL} = \hat{\mathcal{H}}_0 + \hat{\mathcal{H}}_{res}$, where the first term corresponds to a confined particle with renormalized parameters and decoupled from the bath:

$$\hat{\mathcal{H}}_0 = -t_{\text{ren}} \sum_m^M (|m\rangle\langle m+1| + H.c) + gq^2 + \sum_{k<\omega_c} k a_k^\dagger a_k \tag{3.33}$$

and the second one, called *residual term*, reads:

$$\tilde{\mathcal{H}}_{\text{res}} = V_+ \sum_m^M |m+1\rangle\langle m| + V_- \sum_m^M |m\rangle\langle m+1| + V_0 q$$

This term inherits its zero thermal expectation value from the operators in terms of which is written. It provides us with a parameter to perform an expansion of the Bogoliubov-Feynman upper bound of the free energy [149]:

$$A_B = -\beta^{-1} \log \text{Tr}(\text{e}^{-\text{fi}\tilde{\mathcal{H}}_0}) + \langle \tilde{\mathcal{H}}_{\text{res}} \rangle_{\text{T}} + \mathcal{O}(\langle \tilde{\mathcal{H}}_{\text{res}}^2 \rangle_{\text{T}}) \tag{3.34}$$

where it should be noticed that now thermal averages are taken with respect to $\hat{\mathcal{H}}_0$. Therefore, the variational parameter f_k is included in the calculation in a self-consistent manner.

Let me now summarize the differences between this approach as applied to the SB model and the CL one. The first remarkable novelty that the Caldeira-Leggett includes is that now the Hamiltonian $\tilde{\mathcal{H}}_0$, with respect to which the thermal averages are taken, contains a potential term quadratic in the position of the particle, with potential strength $g > 0$. The effect of such a term is a certain localization of the particle at the center of the chain, making the diagonalization of the Hamiltonian more difficult, since the actual eigenenergies and eigenstates depend on t_{ren} and g. Although a closed expression for A_B cannot be worked out, if now we impose the condition for a minimum in order to determine the optimum f_k in the ansatz, a self-consistent equation for this parameter can be derived:

$$f_k = \frac{-\lambda k^{3/2}}{k - \frac{1}{2}\frac{\langle \tilde{\mathcal{H}}_{0,\text{kin}} \rangle_T}{\langle q^2 \rangle_T} \coth(\frac{\beta k}{2})} \tag{3.35}$$

where $\tilde{\mathcal{H}}_{0,\text{kin}} \equiv -t_{\text{ren}} \sum_m (|m\rangle\langle m+1| + \text{H.c.})$. Plugging this expression into the definitions of the renormalized hopping and the potential strength, it can be seen that the actual number of self-consistent equations can be reduced to the set of parameters that define the effective Hamiltonian, instead of the collection of f_k. In order to do this, we define $s_T(t_{\text{ren}}, g) \equiv \left| \frac{1}{2} \frac{\langle \tilde{\mathcal{H}}_{0,kin} \rangle_T}{\langle q^2 \rangle_T} \right|$, hence rendering:

$$t_{\text{ren}} \equiv t e^{-B(t_{\text{ren}})}$$

$$B(t_{\text{ren}}) = \alpha \int_0^{\omega_c} d\omega \frac{\omega \coth(\frac{\beta\omega}{2})}{[\omega - s_T \coth(\frac{\beta\omega}{2})]^2} \tag{3.36}$$

$$g(t_{\text{ren}}) = \frac{\alpha}{2} \int_0^{\omega_c} d\omega \left[\frac{s_T \coth(\frac{\beta\omega}{2})}{\omega - s_T \coth(\frac{\beta\omega}{2})} \right]^2 \tag{3.37}$$

In order to obtain the solution for these equations, we must resort to numerical calculations, since an analytical solution is not possible. The idea is simple. Starting from a seed, Hamiltonian $\tilde{\mathcal{H}}_0$ is diagonalized to calculate the thermal expectation values and the corresponding renormalized hopping

and potential strength. These values are used as the new seed until convergence is reached. The bare values of t and λ, together with the number M of sites in the chain and the temperature T, constitute the parameters to study the phase-diagram of the model.

A note on this approach. As pointed out in previous works that made use of this approach, the variational solution regulates the strength of the coupling between bath modes and the particle in a way that preserves the spirit of the adiabatic approach [119], but at the same time it takes control of the infrared divergences introduced by the slow modes of the bath. This sort of separation between fast and slow modes in a controlled manner is undoubtedly one of the main virtues of the variational approach.

Zero temperature

Let me start by studying the case of zero temperature, i.e., when $\beta \to \infty$. The equations for the Hamiltonian can be integrated analytically, yielding:

$$t_{\text{ren}} = t\left(1+\frac{1}{s_0}\right)^{-\alpha} e^{\frac{\alpha}{s_0+1}} \tag{3.38}$$

$$g = \frac{2\alpha s_0}{s_0+1} \tag{3.39}$$

where we have taken $\omega_c = 1$ for simplicity. The free energy bound reduces to an actual energy bound, which can also be worked out analytically:

$$A_B(T=0) = E_B = \langle \tilde{\mathcal{H}}_{0,\text{kin}} \rangle_0 + g\langle q^2 \rangle_0 \tag{3.40}$$

For every α and t we have a trivial solution of the equations, corresponding to $t_{\text{ren}} = 0$ and, by virtue of their relation, $g = 0$. This would correspond to a particle localized at any site of the chain with a cloud of oscillators dressing it. An interesting implication arises from the relation between g and t_{ren}. As g controls the non-homogeneous effects induced by the environment on the density profile, in the localized solution the particle will not show any preference for a particular site.

Notice that the energy associated to the trivial solution is zero. Hence, the existence of non-trivial solutions of the equations with lower energy will determine the phase diagram at $T = 0$, in terms of the number of sites M and the parameters t and α. As shown in Fig. 4.2, the region where there are non-trivial solutions with lower energy depends on the number of sites being even or odd. For odd chains there is a non-trivial solution with finite t_{ren} and g for every value of α. In this solution, the potential induced by the environment confines increasingly the particle at the center, having in fact a crossover to a sector in which the particle at all instances becomes localized there (Fig. 4.3). Such a crossover is also reflected in the renormalized hopping (inset of Fig. 4.3), because in this region the hopping gets less renormalized for increasingly large couplings to the bath. For chains with an even number of sites there is no longer a non-trivial solution for $\alpha > 1$, and a phase transition occurs to a localized phase in which the parity is broken. In the delocalized phase ($\alpha < 1$), the presence of the environment results also in a certain confinement of the particle, to the two central sites in this case. The hopping is further renormalized as the coupling increases, an no crossover is observed. I will discuss this effect later.

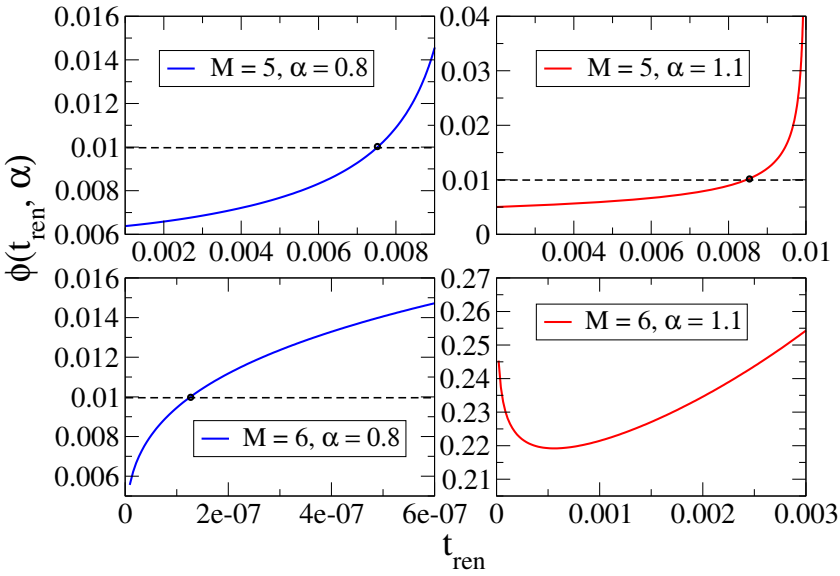

Figure 3.1: Graphical solution of the self-consistent equation (3.38). The function plotted is defined as $\phi(t_{\rm ren},\alpha) \equiv t_{\rm ren}(1+1/s_0)^{\alpha}e^{-\alpha/(s_0+1)}$, where $s_0 = s_0(t_{\rm ren})$. The condition for non-trivial solutions is therefore $\phi(t_{\rm ren},\alpha) = t$. In the figures, two representative cases of odd and even chains, $M = 5, 6$, have been plotted. The value of the hopping is $t = 0.01$.

Finite temperature

For finite temperatures, in general, the self-consistent equations have to be integrated and solved numerically. Again, the results depend on the number of sites of the chain being even or odd. In both cases, for couplings $\alpha < 1$, there is a phase transition at some critical temperature T^* from a so-called *coherent regime*, where $t_{\rm ren}$ and g are finite, to an *incoherent* high-temperature region where $t_{\rm ren} = g = 0$. In the latter, the Hamiltonian has degenerate energy levels, that are equally occupied in a statistical thermal mixture. In Fig. 4.6 we see a typical plot of the behavior of $t_{\rm ren}(T)$ as a function of the temperature. Notice that for small coupling to the bath, $\alpha \ll 1$, and high temperatures, $T \gg t_{\rm ren}$, we find:

$$s_0 = \left| \frac{1}{2} \frac{\langle \tilde{\mathcal{H}}_{0,kin} \rangle_0}{\langle q^2 \rangle_0} \right| = \frac{M\beta t_{\rm ren}^2}{\sum_m^M (m-m_0)^2} \tag{3.41}$$

This dependence is similar to the one found in [150] for the Spin-Boson model in the same regime. Here, it is trivially generalized to the case of M sites by adding the factor $M/\sum_m (m-m_0)^2$. As stated already in the aforementioned reference, the critical temperature can be worked out analytically and has the form:

$$T^* \sim \frac{t_{\rm ren}}{\alpha} \left[\frac{M}{\sum_m^M (m-m_0)^2} \right]^{1/2} \tag{3.42}$$

Another interesting issue is that, at low temperatures, the renormalized hopping $t_{\rm ren}$ gets larger, instead of smaller (see Fig. 4.6). This result was also observed in the Ohmic and sub-Ohmic Spin-boson model [40, 151, 150], and it is associated to the fact that, at low temperatures, only slow bosonic

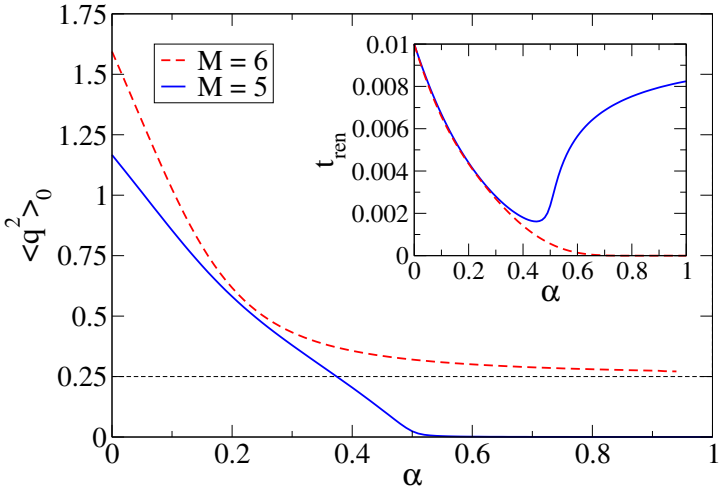

Figure 3.2: Mean squared position deviation for the dissipative confined particle in chains of $M = 5$ and 6 sites. In both cases the coupling to the environment leads to a narrowing of the density distribution of the particle towards the center. Here, $\langle q^2 \rangle_0 = 0.25$ is the mean squared position corresponding to a two-site system. Notice that, for odd chains, there is a crossover to a region in which the particle is effectively localized at the central site. Inset: renormalization of the hopping, $t_{\rm ren}$, as a function of the coupling to the environment, also for $M = 5$ and $M = 6$. The crossover for odd chains is reflected in the behavior of the renormalized hopping.

modes are excited, whose net effect is an increasing of the hopping (as opposed to the effect of fast modes).

In the case of even chains, for $\alpha > 1$ there is not such a phase transition, and only the incoherent phase prevails. For an odd number of sites, the phase transition still occurs for arbitrary α, a reminiscence of the lack of phase transition at $T = 0$, that we discussed in the previous section. A phase diagram with these features has been included in Fig. 4.7, where the two representative cases of $M = 5, 6$ have been addressed.

Discussion of the variational results

The variational calculation predicts a non-trivial phase diagram both at zero and finite temperatures. Being a sort of sophisticated mean-field calculation, it gives an effective Hamiltonian for a quantum particle with renormalized parameters $t_{\rm ren}$ and g due to the coupling to the bath. Hence, two main effects arise from the environment: the renormalization of the hopping, and the confinement at the center of the array due to a quadratic potential. The results have a strong dependence on the number of sites in the array, with qualitative differences when odd or even chains are considered.

Let us understand these results. At zero temperature, there is no phase transition when the number of sites is odd. When the number of sites is even, the results are remarkably close to those found for the SB model. This is not accidental. As shown in Fig. 4.3, due to the quadratic potential the particle is nearly almost localized at the two central sites for coupling strengths close to $\alpha = 1$. Thus, in this region of the phase diagram the system behaves as an effective two-level system, and the phase

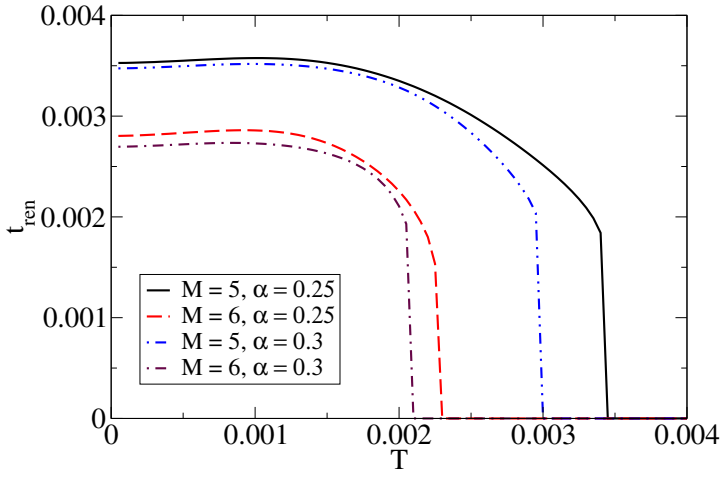

Figure 3.3: Dependence of the renormalized hopping t_{ren} on the temperature, for two representative cases of odd and even chains, $M = 5$ and $M = 6$, respectively. For $\alpha < 1$, in both cases there is a critical temperature that separates an incoherent high-temperature regime, where $t_{\mathrm{ren}} = 0$, from a coherent low-temperature one, where t_{ren} is finite. Notice that, for low temperatures, the renormalized value of the hopping grows with temperature.

transition is essentially the same found in this model. Such an argument also applies for the finite temperature case, where again we find results close to those predicted by the variational calculation in the SB model.

In the case of an odd number of sites in the chain the situation differs considerably: here, at zero temperature, the quadratic potential confines the particle around the single central site for large enough couplings, and no effective SB model physics arises. Once the particle is effectively located at the center, the renormalization of the hopping starts to reverse its tendency, as clearly shown in Fig. 4.3, increasing again for larger couplings. An explanation for this effect comes from the fact that the bath is not coupled to the central site, since here $\hat{q}|m_0\rangle = 0$. Thus the renormalization of the particle parameters can be expected to become tinier as the particle is more localized at the center. This behavior is reflected in the finite temperature phase diagram: the coherent-incoherent transition being related to the renormalization of the coupling by the bath, the critical temperature starts to increase again. For very large couplings to the environment, it can be seen that the renormalized hopping tends to its bare value.

We see, then, that the variational approach success in providing a more detailed and analytical picture of the two phases that exist in the Caldeira-Leggett model for a particle confined in a finite chain. However, as I already mentioned, regarding the actual phase transition, it does not go beyond the lowest order corrections that the Renormalization Group approach sketched above already takes into account. We know, however, that higher-order corrections can translate into a more complicated picture of the phase transition, something that already happens for the Spin-Boson model, where a Kosterlitz-Thouless phase transition is derived only when these corrections are regarded. Since, however, the RG analysis turns out to be extremely tedious for our more complicated model, in

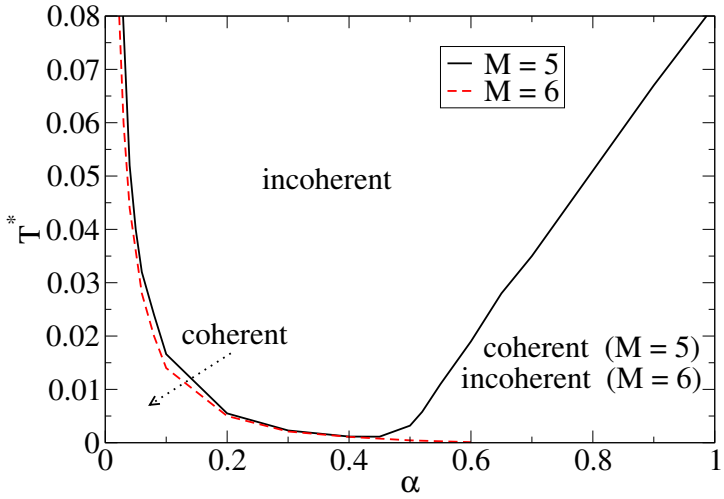

Figure 3.4: Finite temperature phase diagram of the model. The behavior is different for odd and even chains. In both cases there are two phases, one where $t_{\rm ren} = 0$ (incoherent) and other where $t_{\rm ren}$ is finite (coherent). For small coupling α to the bath, the behavior of the critical temperature is independent of the chain being odd or even. For large couplings the behavior is dramatically different, and the coherent phase only prevails for $\alpha > 1$ for chains with an odd number of sites.

the following I will resort to the Numerical Renormalization Group, that includes all the relevant corrections at the price of resigning to get numerical, and not analytical, results.

3.4 Numerical Renormalization Group approach

In this section I will use the Numerical Renormalization Group technique to obtain a more complete description of the zero-temperature phase diagram of the quantum particle in a finite chain, in the presence of an environment. We will see that the corrections not included in the approaches analyzed so far give rise to new interesting features regarding the quantum phase transition and the different phases of the model. I will start describing how to generalize the bosonic NRG explained in the last chapter to the more complicated Caldeira-Leggett Hamiltonian.

NRG for the Caldeira-Leggett model

I will follow the same lines sketched for the Spin-Boson solution, giving a more detailed account when the subtleties of the Caldeira-Leggett model play a major role. A first important point to mention is that, in the case of the CL model, the use of the *Star-NRG* version of the algorithm is almost mandatory, due to the presence of the counter-term when systems with more than two sites are addressed. Previous works on the generalization to M-levels of the bosonic NRG were not interested in translation invariant models, and hence this issue was not present [152]. The problem with the *chain-NRG*, is that it encompasses all the impurity degrees-of-freedom at the first iteration of the algorithm. The counter-term, however, is globally a large quantity, so it can give rise to important

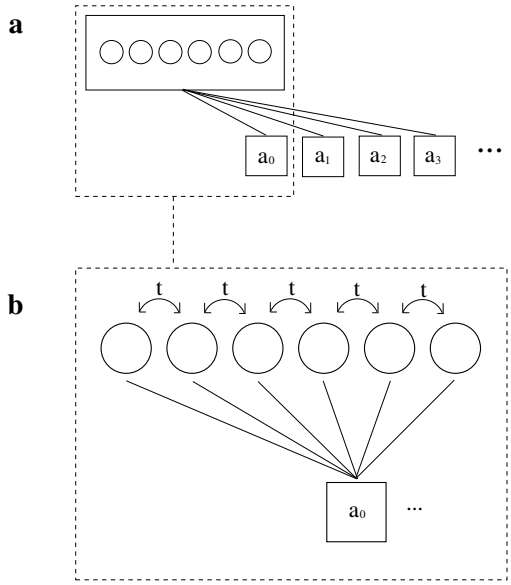

Figure 3.5: Sketch of the star-NRG Hamiltonian used throughout the calculations. a) Every bosonic site a_n couples to the particle. In every iteration a new site is added and the resulting Hamiltonian is diagonalized, giving the energy spectrum. b) The particle Hamiltonian, coupled to the first bosonic site. Notice that the structure of the couplings is the same for the rest of bosons.

numerical deviations if it is not introduced step by step, something that is only possible within the Star-NRG approach.

The first steps are essentially those discussed for the SB model. A continuous version of the Hamiltonian is introduced, from which a logarithmic discretization of the bath spectral function can be attained. The resulting discrete Hamiltonian resembles the starting one, but with couplings and energies decaying as a power law with the site label. Since the particular details were already discussed in Ch. 2, I will skip the discussion here. After carrying out this transformations, the resulting Hamiltonian reads:

$$\mathcal{H} = -t\sum_{m=1}^{M}\left(c_m^\dagger c_{m+1} + H.c\right) + \sum_{n=0}^{\infty}\xi_n a_n^\dagger a_n + \frac{q}{\sqrt{\pi}}\sum_{n=0}^{\infty}\gamma_n(a_n + a_n^\dagger) + \frac{q^2}{\pi}\sum_{n=0}^{\infty}\frac{\gamma_n^2}{\chi_n} \tag{3.43}$$

where the couplings have the same expression than those from the Spin-Boson model:

$$\xi_n = \gamma_n^{-2}\int_{\lambda^{-(n+1)}}^{\lambda^{-n}} dx J(x)x = \frac{2}{3}\left(\frac{1-\lambda^{-3}}{1-\lambda^{-2}}\right)\lambda^{-n} \tag{3.44}$$

$$\gamma_n^2 = \int_{\lambda^{-(n+1)}}^{\lambda^{-n}} dx J(x) = \pi\alpha(1-\lambda^{-2})\lambda^{-2n} \tag{3.45}$$

The structure of this Hamiltonian can be graphically depicted, as shown in Fig. 3.5. Thanks to the structure that couplings and energies have, it can be used to set an iterative algorithm, the NRG, where lower energy scales are resolved as new sites of the chain are included. The Hamiltonian for

the first N bosonic sites is:

$$\mathcal{H}_N = \lambda^N \left[-t \sum_{m=1}^{M} \left(c_m^\dagger c_{m+1} + H.c \right) + \sum_{n=0}^{N} \xi_n a_n^\dagger a_n + \frac{q}{\pi} \sum_{n=0}^{N} \gamma_n (a_n + a_n^\dagger) + \frac{q^2}{\pi} \sum_{n=0}^{N} \frac{\gamma_n^2}{\xi_n} \right] \tag{3.46}$$

which in the limit $N \to \infty$ is equal to $\mathcal{H}$:

$$\mathcal{H} = \lim_{N \to \infty} \lambda^{-N} \mathcal{H}_N \tag{3.47}$$

From this family of Hamiltonians we derive the recurrence relation:

$$\mathcal{H}_{N+1} = \lambda \mathcal{H}_N + \lambda^{N+1} \left[\xi_{N+1} a_{N+1}^\dagger a_{N+1} + \frac{q}{\sqrt{\pi}} \gamma_{N+1} (a_{N+1} + a_{N+1}^\dagger) + \frac{q^2}{\pi} \frac{\gamma_{N+1}^2}{\xi_{N+1}} \right] \tag{3.48}$$

Remember that the factor λ in the definition of $\mathcal{H}_N$ is included for the ease of comparing the lowest energy levels that the NRG produce as an output at every iteration, which is useful to identify the different fixed points. The last equation is essentially the NRG transformation. We see how, by using the Star-NRG approach, the counter-term is included iteratively, preventing the numerical distortions that may arise in the calculations by including it as a whole. As a quick reminder, the idea behind the method is to iteratively solve these Hamiltonians, and use the solution of, say, $\mathcal{H}_N$, as an input to work out $\mathcal{H}_{N+1}$. In order to keep a reasonable number of states in the calculations, only a certain number of eigenstates, those with lowest eigenenergies, are kept at every iteration, discarding the rest. According to the RG philosophy, once this Hamiltonian $\mathcal{H}_N$ is diagonalized, this is equivalent to integrate out high-energy degrees-of-freedom and study effective low-energy Hamiltonians, where the effect of the eliminated states is already encoded. The solutions of a certain $\mathcal{H}_N$ are expected to describe physics at the scale $T_N \propto \lambda^{-N}$.

Besides the problem of the counter-term, there is another important issue concerning the application of the NRG to the Caldeira-Leggett model. It has to do with the necessity of including within the procedure the only symmetry of the model, parity. Were this ignored, important features of the phase transition might be lost, since numerical errors tend to artificially break this symmetry when it is not conveniently handled. In order to shield the parity symmetry, the Hamiltonian must be projected into a basis with a well-defined parity number, i.e., a basis of states that are common eigenvectors of both the Hamiltonian and the parity operator. Since this quantum number must be conserved all along the flow of the NRG, a general procedure must be sketched for every iteration. In this regard, it is necessary to distinguish between the first iteration, where the impurity degrees-of-freedom are explicitly included, and the rest of iterations.

A basis that has parity as a good quantum number was already introduced when discussing the symmetries of the model in Section 3.2. This is useful for the first iteration of the NRG, since the tight-binding Hamiltonian for the confined particle must be handled. Following the results of the aforementioned Section, the Hamiltonian $\mathcal{H}_0$ can be written as:

$$\mathcal{H}_0 = \mathcal{H}_+ + \mathcal{H}_- + \xi_0 a_0^\dagger a_0 + \gamma_0 \frac{q}{\sqrt{\pi}} (a_0^\dagger + a_0) + \frac{q^2}{\pi} \frac{\gamma_0^2}{\xi_0} \tag{3.49}$$

Written this way, both bosonic and impurity operators are eigenvectors of the parity operator. Notice, however, that the quantum number to be preserved is the total parity, P. For a state of the form

$|m,p;n_b;P\rangle = |m,p\rangle \otimes |n_b\rangle_0$, where the first sector corresponds to the particle, and the second to the number states of the bosonic site at $N=0$, the total parity is equal to $P = p(-1)^{n_b}$. The matrix elements of this Hamiltonian, projected on the proposed basis, read then:

$$\begin{aligned}
\langle m',p';n_b';P'|\mathcal{H}_+|m,p;n_b;P\rangle &= \delta_{p,p'}\delta_{p,+}t(\delta_{m,m'+1}+\delta_{m,m'-1})\delta_{n_b,n_b'}\\
\langle m',p';n_b';P'|\mathcal{H}_-|m,p;n_b;P\rangle &= \delta_{p,p'}\delta_{p,-}t(\delta_{m,m'+1}+\delta_{m,m'-1})\delta_{n_b,n_b'}\\
\langle m',p';n_b';P'|\xi_0 a_0^\dagger a_0|m,p;n_b;P\rangle &= \delta_{m,m'}\delta_{n_b,n_b'}\delta_{p,p'}\xi_0 n_b\\
\langle m',p';n_b';P'|\gamma_0\frac{q}{\sqrt{\pi}}(a_0^\dagger+a_0)|m,p;n_b;P\rangle &=\\
\delta_{m,m'}\delta_{p,1-p'}\frac{\gamma_0}{\sqrt{\pi}}(m-m_0)\left(\sqrt{n_b+1}\delta_{n_b',n_b+1}+\sqrt{n_b}\delta_{n_b',n_b-1}\right)&\\
\langle m',p';n_b';P'|\frac{q^2}{\pi}\frac{\gamma_0^2}{\xi_0}|m,p;n_b;P>=\delta_{m,m'}\delta_{p,p'}\delta_{n_b,n_b'}\frac{1}{\pi}\frac{\gamma_0^2}{\xi_0}(m-m_0)^2 &
\end{aligned} \tag{3.50}$$

As a whole, we see that $\langle P'|\mathcal{H}_0|P\rangle \propto \delta_{P',P}$, so the matrices split into two different sectors with good total parity P.

Let us now address the case of a general $\mathcal{H}_{N+1}$. The input are the eigenstates and eigenenergies of $\mathcal{H}_N$, which we suppose to have a good parity p, $|r,p\rangle_N$. The label r classifies these states, that add to N_s of them that are kept after discarding those with the highest eigenenergies. A new bosonic site is then added to this Hamiltonian, in the way shown in Eq. (3.48). Since number states already have a well-defined parity, the states in which we project the new Hamiltonian are of the form:

$$|r,p;n_b;P\rangle_{N+1} = |r,p\rangle_N \otimes |n_b\rangle_{N+1} \tag{3.51}$$

with, again, $P = p(-1)^{n_b}$. The matrix elements read:

$$\begin{aligned}
{}_{N+1}\langle r',p';n_b';P'|\mathcal{H}_N|r,p;n_b,P\rangle_{N+1} &= \delta_{n_b,n_b'}\delta r,r'\delta p,p'E_N(r,p)\\
{}_{N+1}\langle r',p';n_b';P'|\xi_{N+1}a_{N+1}^\dagger a_{N+1}|r,p;n_b,P\rangle_{N+1} &= \delta_{n_b,n_b'}\delta r,r'\delta p,p'n_b\xi_{N+1}\\
{}_{N+1}\langle r',p';n_b';P'|\frac{q}{\sqrt{\pi}}\gamma_{N+1}\left(a_{N+1}+a_{N+1}^\dagger\right)|r,p;n_b,P\rangle_{N+1} &=\\
\delta_{p,1-p'}\frac{\gamma_{N+1}}{\sqrt{\pi}}\langle r',p'|q|r,p\rangle\left(\sqrt{m+1}\delta_{m+1,m'}+\sqrt{m}\delta m-1,m'\right)&\\
{}_{N+1}\langle r',p';n_b';P'|\frac{q^2}{\pi}\frac{\gamma_{N+1}^2}{\xi_{N+1}}|r,p;n_b,P\rangle_{N+1} = \delta_{n_b,n_b'}\delta p,p'\frac{1}{\pi}\frac{\gamma_{N+1}^2}{\xi_{N+1}}\langle r',p'|q^2|r,p\rangle &
\end{aligned} \tag{3.52}$$

where, again, $\langle P'|\mathcal{H}_{N+1}|P\rangle \propto \delta_{P',P}$.

An important observation concerning this global conservation of the parity symmetry, is that the matrices to diagonalize split now into two different sectors, corresponding to the two different values of P, that are decoupled from each other. Hence, at the same price that it helps to preserve parity symmetry, it reduces in a factor of two the size of the matrices to diagonalize, improving the computational efficiency of the algorithm.

As happened with the Spin-Boson model, a second truncation is required in order to keep the calculation computationally manageable. In principle, every bosonic site admits an infinite number of states, but in practice this number must be limited to a certain N_b. Hence, the size of the matrices to diagonalize will be $N_s N_b/2$, the factor of two corresponding to the block separation achieved by

exploiting the parity symmetry. When the number of bosons per site is limited, the issue of which basis is optimal in order to diagonalize the Hamiltonian arises. The discussion is similar to that for the SB model. As pointed out by Bulla *et al* [118], results can be optimized by using a displaced-oscillator basis, specially for large values of the coupling to the bath and non-Ohmic environments. However, for the range of parameters studied in this chapter, it is yet possible to obtain convergent results by increasing the number N_b of bosons per site when the coupling gets larger. In general, the following observations hold:

- The larger is α, the larger must be N_s and N_b to obtain convergent results.
- The same applies for M.
- However, convergence does not depend on the choice of t.

In this thesis I will study chains from $M = 2$ to $M = 6$, $t \sim 0.01$ and α as large as 2. For this set of parameters, it suffices to take $N_s = 120$ and $N_b = 50$ when needed, since sometimes it suffices to use smaller sizes. The discretization used will be always $\lambda = 2$, as we seek to explore mostly qualitative features of the phase diagram, and the corrections by approaching the continuous limit $\lambda \to 1$ do not provide extra relevant information in this regard.

Numerical results

The output of the NRG procedure are the flows of the lowest lying energy states as the cutoff is reduced iteratively. At some point the flows are expected to converge to stable (low-energy) fixed points. Then, the effective Hamiltonian can be reconstructed analyzing the evolution of those flows, as well as the evolution of other observables of the system. Here I will use the evolution of the averaged position of the particle, $\langle q \rangle_N$, and its mean square deviation $\langle q^2 \rangle_N$, evaluated in the ground state. Those flows are enough to characterize the different phases of the system.

As mentioned, due to computational limitations we have to concentrate in the study of chains with a small number of sites, ranging between 2 and 6. For two sites the NRG reproduces the phase diagram of the dissipative two-level system. For larger chains and small dissipation, the results are in qualitative agreement with the variational solution, predicting a delocalized phase with renormalized hopping and a renormalized potential which tends to localized the particle at the center as the coupling strength is enlarged. As far as the phase transition is concerned, the case of $M = 3, 4$ does not deviate too much from the dissipative two level system. In both cases there is a phase transition in which $t_{ren} = 0$, but for $M = 3$ the parity symmetry is not broken, because the particle is localized at the center. For $M = 4$ the phase transition is that of the dissipative two-level system, the edge sites being decoupled in energy from the central ones. Notice that this is all in contrast with the variational solution, where a transition to an M degenerate state is predicted.

More interesting are the cases $M = 5, 6$. Here a new behavior is observed, which should be representative of the one expected for larger chains. The energy flows for small and large dissipation are shown in Fig. 3.6 and Fig. 3.7. Again, weak dissipation induces some localization of the particle density at the center of the array, as can be seen in the inset of the figures, where $\langle q^2 \rangle_N$ is computed.

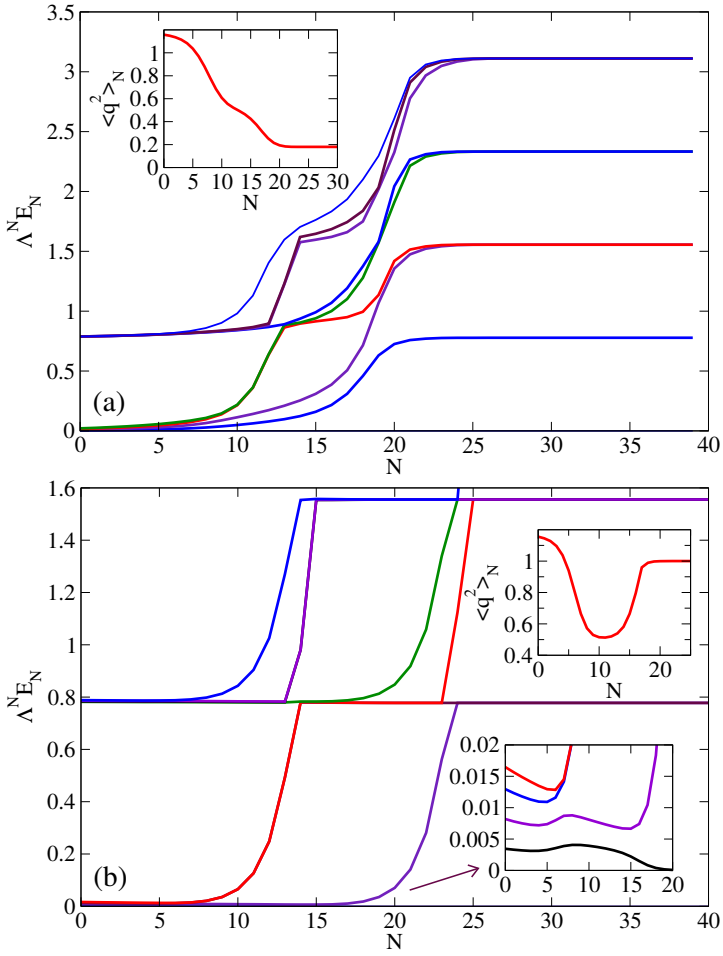

Figure 3.6: Representative flows of the NRG transformations carried out in this section, for $M = 5$ sites. The horizontal axis is the iteration number, and the graphs are scaled energy levels. a) Flow towards a non-degenerate ground state ($\alpha = 0.8$, $t = 0.01$). The inset shows the flow of the mean square position of the particle, which becomes localized around the center. b) Flow towards a degenerate ground state ($\alpha = 1.2$, $t = 0.01$). The lower inset gives details of the way in which the lowest energy levels flow to the fixed point. The top inset shows the localization of the particle beyond the center, as indicated by its mean square position.

This is a similar behavior that the one found in the variational approach, though both approaches only agree qualitatively. This is shown in Fig. 3.8, where the mean square position of the particle is calculated in both approximations for a chain of 5 sites [3].

The differences between the localized phase predicted by the variational calculation and the NRG are even sharper for these longer chains. Above a critical strength coupling α_c of order one, a doubly degenerate state is found, for odd and even number of sites, in which the parity symmetry is broken. For $M = 5$ the particle localizes next to the center, while for $M = 6$ it does initially at the central

[3] A similar plot can be obtained for 6 sites, the main difference being that the mean square position tends to a finite value for $\alpha \to 1$, having two states in the center instead of one

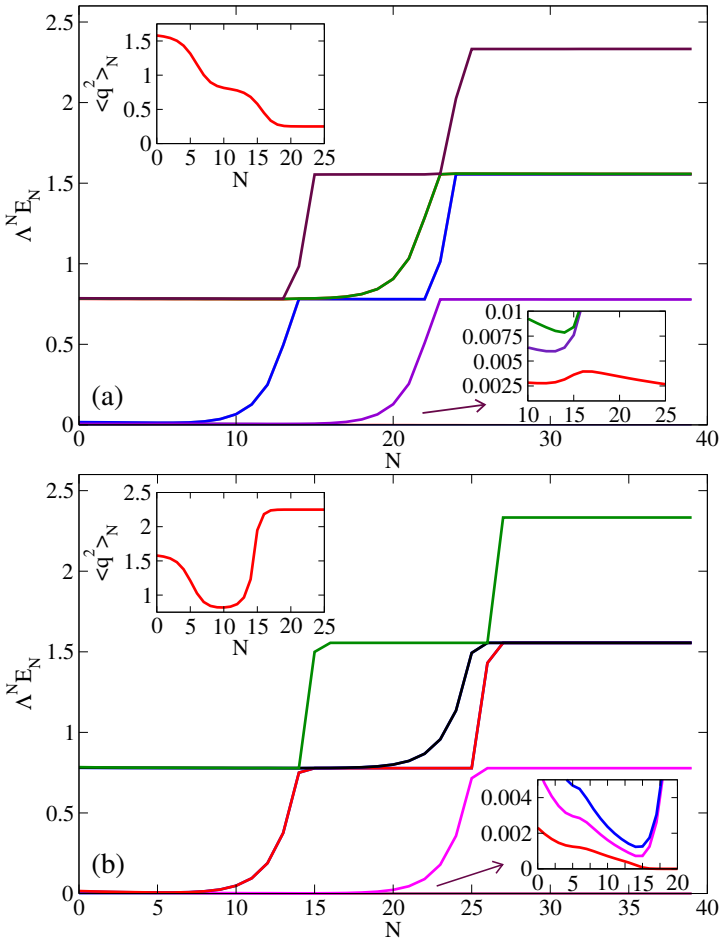

Figure 3.7: Flows of the NRG for $M = 6$ sites. a) Flows in the first region of the localized phase ($\alpha = 1.2$, $t = 0.01$), where the particle is confined at the central sites. b) Flow in the second region of the localized phase ($\alpha = 1.4$, $t = 0.01$). Here the particle is confined at the next to the center sites, suggesting the formation of a double well effective potential in the array. In both cases the lower insets show in detail the flow of the lowest energy levels, while the higher insets contain the flow of the mean square position of the particle.

sites, and for larger dissipation at the next to the center ones. This result follows from analyzing the degeneracy of the ground state, extracted from the energy flows, as well as the evolution of the mean square position operator. The converged values of the latter can be used to make an ansatz of the sort of ground state density matrix to which the flow converges.

In Table 3.1, the zoo of stable fixed points of the model is shown, for chains of $M = 5, 6$ sites. In the case of $M = 6$ there is an extra fixed point in the localized regime, corresponding to a situation in which the particle finds more favorably to become localized in the sites next to the edges than the ones next to the central sites. This second transition also occurs for a critical value of the coupling strength, but there is neither a symmetry breaking nor a change in the degeneracy of the ground state. Thus, the information provided by NRG is not enough to fully characterize the nature of this phase transition. This is, unfortunately, not the only limitation of the numerical method. It also does not al-

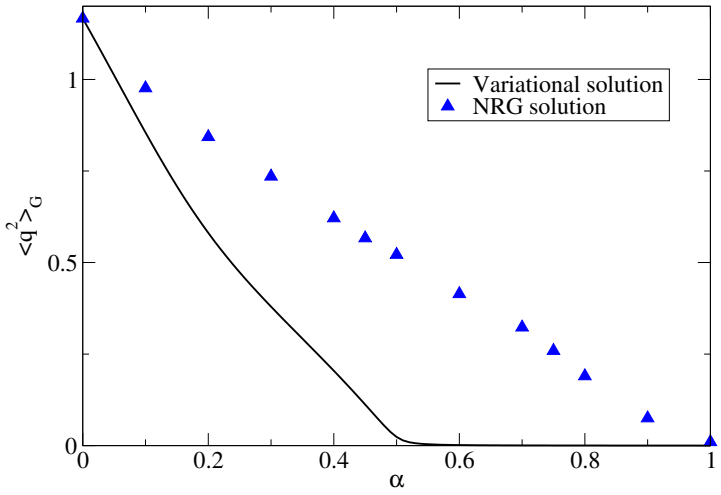

Figure 3.8: Mean square position of the particle as a function of the coupling strength in the delocalized phase of the model, for $M = 5$, as predicted by the variational calculation and the NRG.

Type	M	GS_{deg}	$\langle q^2 \rangle_{NRG}$	$\hat{\rho}$
Deloc.	5	1	$\langle q^2 \rangle_{NRG}$	$\hat{\rho} = \lvert t_{ren}, \alpha \rangle \langle t_{ren}, \alpha \rvert$
Loc.	5	2	1	$\hat{\rho} = \frac{1}{2}(\lvert 2 \rangle \langle 2 \rvert + \lvert 4 \rangle \langle 4 \rvert)$
Deloc.	6	1	$\langle q^2 \rangle_{NRG}$	$\hat{\rho} = \lvert t_{ren}, \alpha \rangle \langle t_{ren}, \alpha \rvert$
Loc. I	6	2	0.25	$\hat{\rho} = \frac{1}{2}(\lvert 3 \rangle \langle 3 \rvert + \lvert 4 \rangle \langle 4 \rvert)$
Loc. II	6	2	2.25	$\hat{\rho} = \frac{1}{2}(\lvert 2 \rangle \langle 2 \rvert + \lvert 5 \rangle \langle 5 \rvert)$

Table 3.1: Stable fixed points of the NRG for chains of $M = 5, 6$ sites. The fixed points are characterized by the ground state degeneracy, GS_{deg} and the position mean square value, $\langle q^2 \rangle_{NRG}$, whose values can be obtained with the NRG. In the localized phase there is a single value for every α, while in the delocalized one the values depends on the coupling strength, as shown in Fig. 3.8 for a chain of 5 sites. Those values are used to propose an ansatz for the ground state density matrix, $\hat{\rho}$, which fits it correctly. The states $|i\rangle$ represent a particle sitting at site i. $|t_{ren}, \alpha\rangle$ is the ground state of a free tight-binding chain with hopping t_{ren} and a parabolic potential, dependent on the strength coupling α.

low us to study large values of the dissipation, $\alpha \gg 1$, since the calculations get very computationally demanding. Hence, the question of whether other phase transitions can be ruled out for high values of α remains open.

From the energy flows some extra information can be extracted. In the delocalized phase, a single energy scale seems to be playing a part in the evolution from high-energy to low-energy behavior. In fact, the flow in this phase is similar to that found in the dissipative two-level system, and in the same way we can define a crossover scale $T^* \propto \Lambda^{-N^*}$ from the iteration N^* at which the flow changes from its initial behavior to the low-energy regime. As shown in Fig. 3.9, T^* tends to zero exponentially as the coupling strength approaches the critical value, $\log T^* \propto 1/(\alpha_c - \alpha)$. Hence, the results suggest that the transition is continuous, being consistent with the existence of a Kosterlitz-Thouless transition

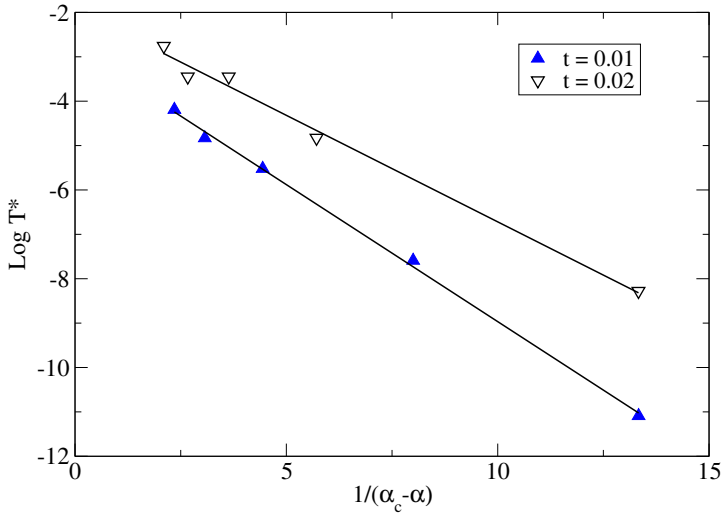

Figure 3.9: Plot of the dependence of the crossover scale T^* on the distance to the critical coupling strength. Here $T^* \propto \Lambda^{-N^*}$, with N^* chosen as the iteration for which the first excited level verifies $\Lambda^{N^*} E_{N^*,1} = 0.03$. The figure shows the results for two different hopping parameters. In both cases there is a good agreement with an exponential decay of T^* as a function of the distance from the critical coupling, $\log T^* \propto 1/(\alpha_c - \alpha)$

[153].

The flows in the localized phase show a different behavior. Here, two different energy scales appear in the course of the flow, revealing an unstable fixed point in an intermediate regime. These scales are defined now from the iterations N_1^* and N_2^* at which the energy levels decouple from the low energy sector, giving rise to two crossover temperatures $T_i \propto \Lambda^{-N_i^*}$, $i = 1, 2$. From the flow of the mean square position it can be deduced that the upper energy scale marks the decoupling of the sites located at the edges, as the values of this operator are well fitted to the expected ones in free tight-binding chains with finite hoppings but sites in the edges suppressed (effectively reducing the chain to one with two less sites). In this way, the intermediate fixed point would correspond to an effective cluster of three sites in the $M = 5$ case, and four sites in the $M = 6$ one, with a renormalized hopping parameter t_{ren}. The lower energy scale corresponds to the onset of the phase transition, for here the parity symmetry is broken and only two sites remain in the low-energy regime.

Discussion of the phase diagram

From the numerical results, a phase diagram of the model can be constructed, as shown in Fig. 3.10. Summarizing, there is a phase transition between a delocalized regime to a localized one. In the delocalized phase the effect of the bath is that of reducing the effective hopping and of generating a renormalized potential which makes the density of the particle higher close to the center. In the localized phase the parity symmetry is broken and in both cases, odd and even, the particle localizes in one of two degenerate sites. This phase transition is continuous, and the numerical results are consistent with a transition of KT type, like in similar dissipative systems.

In the variational calculation, we saw that a parabolic effective potential emerges from the coupling

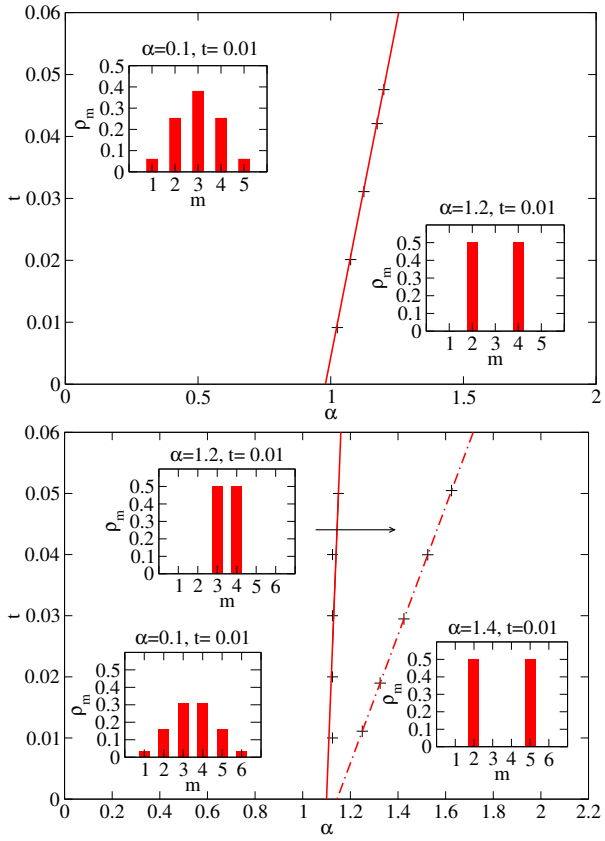

Figure 3.10: Phase diagram of the model for $M = 5$ (top) and $M = 6$ (bottom) sites, deduced from the NRG flow. The continuous lines are linear fittings to the numerical data. The insets show representative density distributions of the particle in each phase.

to the bath, being responsible of some localization of the particle at the center. However, the NRG results suggest the existence of a more complicated renormalized potential which would explain both the almost complete localization of the particle as $\alpha \to 1$ from below, and the inhomogeneous degenerate ground state in the localized phase. A simple guess which works well qualitatively is an effective potential in the form $V_m = (g_0/2)(m - m_0)^2 + (g_1/4!)(m - m_0)^4$. If $g_0 \propto (\alpha_c - \alpha)$, this ansatz has a minimum at $m = m_0$ in the delocalized phase, and at $m = m_0 \pm \sqrt{\frac{-6g_0}{g_1}}$ in the localized one, explaining not only the doubly degenerate state, but also that in the case $M = 6$ there is a second transition to a phase in which the particle localizes in the next to the center sites.

In the region of the phase diagram which we have analyzed ($\alpha < 2$), we have not found any further crossover to a region where the particle is confined at the edges. This could be explained by the role played by the intermediate unstable fixed point in the localized phase. By studying the case of three and four sites, the only way to get a phase transition in which the particle localizes at the edges is by starting with slightly lower site energies here as compared to the center. Hence, this suggest that the decoupling of the edges would be necessary to produce such a renormalization of the on-site energies, favoring the phase transition to a more stable regime.

From these results we can try to get a picture of the expected results for longer chains, that should

be closer to the expected for a confined particle in a box. Remember that the continuous model of the lattice spatial discretization is approached for $M \to \infty$ and $a \to 0$, being a the lattice spacing. As the RG results are independent of the number of sites, the phase diagram should also show a transition to a localized phase for a critical value α_c around the unity. Close to this phase transition, the renormalized potential gets quartic corrections and the particle becomes localized in the resulting double-well profile. Since the minimum of this effective potential depends on the dissipation strength, there should be several crossovers to regions in which the particle is localized at points increasingly farther from the center. However, the particle would be never localized at the edges, as their decoupling seems to be crucial to the realization of this inhomogeneous transition. Thus, in the localized phase, two or more energy scales should be playing a role, depending on the number of energy levels that are decoupled from the low-energy sector until the stable fixed point is reached. Finally, for the the continuous model, which corresponds to the case of an infinite number of sites in the array, there should be only a single phase transition, at α_c around the unity, to a phase where the particle is localized in a double well potential profile whose minimum depends on the coupling strength.

3.5 Conclusions

In this chapter I have addressed the problem of a particle confined to a finite chain, coupled to a Caldeira-Leggett bath. Essentially, three approaches have been used to study its phase diagram: Renormalization Group, variational ansatz, and Numerical Renormalization Group. Undoubtedly, the latter gives the most detailed picture of the localization quantum phase transition present in the model, as in principle, it includes all the corrections to the effective Hamiltonian in the low-energy regime. The price, of course, is the lack of analytical results like those provided by the first two approaches.

Besides the existence of a quantum phase transition (that is also reflected, as shown by the variational approach, in the finite temperature phase-diagram), the most relevant results found in this chapter are the confinement at the center in the delocalized-phase, and the complicated localization pattern found in the various localized-phases. The intuitive picture in terms of a mean-field Landau phase transition for the potential induced by the environment seems to qualitatively agree with the results. An interesting extension of this work, then, would be to find a generalization of the variational ansatz that includes higher corrections to the confining potential, hence describing the results for the localized-phase found in the NRG. Likely, this could explain the quantitative discrepancies found in the mean square position, in the delocalized phase, predicted by both approaches.

The results were all obtained for a finite chain. This, on the one hand, can be seen as a discretization of the continuous model of a dissipative particle in a box. This problem has been of academical interest since the eighties, and a satisfactory solution has not been so far obtained in the literature. The study of the discretized model, despite of not solving the complete problem, should provide us with insights about the physics expected in the limit of the continuum. Moreover, on the other hand, the study of particles living in finite chains can also be of interest to describe real systems, like arrays of quantum dots, ultracold gases in optical lattices, or atom chips. The single-particle results obtained

in this chapter should pave the way for a many-body analysis of the same problem, since these experiments usually deal with several atoms or electrons. This would require the use of a many-body generalization of the Caldeira-Leggett model, as the one proposed in [154].

4 Sudden interaction quench in the sine-Gordon model

Getting older is no problem. You just have to live long enough.
Groucho Marx

Summary

In this chapter I will describe my research concerning the out-of-equilibrium dynamics of isolated many-body quantum systems. In the first section, I will introduce the general debate about thermalization in Quantum Mechanics, as a way to put in context the particular problem to which this chapter is devoted. The second section introduces the sine-Gordon model, explains its phase diagram and the connection to experiments with ultracold gases. In addition, its solution by using the flow-equations formalism is exposed, setting the notation and the main tools I will employ henceforth. The third section is the most important one, since time-evolution of bosonic creation and anhinilation operators is worked out, by using the flow-equations based *forward-backward* scheme. These results are employed, then, in the fourth section, to study the real-time dynamics of the sine-Gordon model after a sudden interaction quench, in the weak-coupling regime. After the conclusions, several appendixes contain some of the most technical details of the calculations. The work described in this chapter is contained in [155], and was done in collaboration with S. Kehrein.

4.1 Introduction: Non-equilibrium dynamics of isolated many-body quantum systems

In the last chapter I studied how an environment influences the quantum properties of a particle living in a finite chain. There, I discussed how actually environments are the rule and not the exception in real systems. Of course, the study of isolated quantum systems is of the biggest priority not only for academical purposes, but because in many experimental situations the influence of the environment is mostly negligible, or simply because it represents the necessary building block to, later, understand the real system. Take, for instance, a metal, where the electron gas should be a genuinely quantum system even at room temperature. Many of its properties can be already understood by just using the model of an isolated quantum system of electrons, specially those regarding equilibrium situations. However, when dynamical responses are regarded, usually the behavior is strongly influenced by the environment, in this case the presence of impurity scatterers in the solid.

The latter does not entail that the dynamics of purely isolated quantum systems is not observable. It is, in the end, a matter of time-scales. The effects of an environment over a quantum system usually become unravelled after a certain time, before which the system is essentially uncoupled from it. This is well-known in the field of Quantum Computation. Here, the behavior of isolated qubits is the one of interest, and operations must be performed before the environment acquires importance. What happens in the long run, hence, has been traditionally a purely academical problem, since experimentally could not be addressed. This applies particularly to interacting many-body systems, where interactions play a major role in the evolution of a system initially out-of-equilibrium. In this regard, the main question to shed light on is about the nature of the long-time limit of the system. In other words, does an interacting many-body quantum system out-of-equilibrium thermalize in the long run, as happens usually with their classical counterparts?

This question, which can be seen to be quite subtle, has remained unanswered since the advent of Quantum Mechanics. After all, it was an academical problem that involved the most complicated aspects of quantum theory: interactions and dynamics. However, as I mentioned in the introduction to this thesis, the situation has changed since experiments with ultracold gases are available. The extremely high degree of isolation of these systems is allowing us to access the long-time regime of many-body quantum systems out-of-equilibrium. Not to mention the variety of models that can be engineered by using optical lattices. Old questions reunite the new ones in a field that is increasingly gaining importance.

The thermalization debate

Does an interacting many-body quantum system thermalize? Strictly not. Let us consider a generic non-integrable model [1]. Thermalization occurs when a system reaches an equilibrium state described by one of the ensemble predicted by Quantum Statistical Mechanics. These statistical ensembles are said to be ergodic, since they are derived under the assumption that the system can visit every possible accessible state in a certain (long enough) time-scale [2]. The probability of visiting a certain state depends on the particular ensemble. For the microcanonical one, only states with a fixed total energy are allowed, and all of them are equally probable. If a system thermalizes, its properties only depend on certain macroscopic quantities like temperature and chemical potential, having lost the memory of how equilibrium was reached and the initial condition in which the system was initialized. In Classical Mechanics, it is known that a thermal state is reached wherever a system exhibits chaotic behavior.

Now, in Quantum Statistical Mechanics, thermal ensembles are described by particular choices of density operators ρ, that contain the information about the probability of being in a certain state, in a statistical sense. This must not be confused with the probability of having a non-zero projection on

[1] For integrable models, see the next section

[2] The ergodic theorem states that ensemble averages are equivalent to time averages in the long run:

$$\frac{1}{\Sigma(E)} \int d\vec{X}^N f(\vec{X}) \delta(\mathcal{H}(\vec{X}) - E) = \lim_{T\to\infty} \int_{t_0}^{t_0+T} f(\vec{X}(t)) dt \tag{4.1}$$

where $f(\vec{X})$ is a function that depends on the degrees-of-freedom of the system, $\vec{X}$, and $\Sigma(E) = \int d\vec{X}^N \delta(\mathcal{H}(\vec{X}) - E)$.

this state, when the system is prepared in a quantum superposition. The difference lies in the fact that, in the second case, there exist a phase coherence between the states included in the superposition, in the sense that they have a fixed relative phase, and hence interference phenomena between them can be observed. In terms of the density operator, this is characterized by the trace of the squared operator. A *pure state*, one that is purely in a quantum superposition, fulfills $\mathrm{Tr}\rho^2 = 1$, while for a *mixed state*, that also contains statistical superpositions, $\mathrm{Tr}\rho^2 < 1$. However, as it was indicated in last chapter, unitary time-evolution of the density operator conserves the trace:

$$\frac{d}{dt}\mathrm{Tr}\rho^2(t) = 0 \tag{4.2}$$

Therefore, if the system is initialized in a pure state, then by means of intrinsic time-evolution cannot reach a thermal state. It does not thermalize. This is no longer the case when is coupled to an environment, indeed.

Notice that there is a second drawback concerning quantum systems: due to level quantization, a recurrent quantum dynamics is expected, hence not giving rise to any thermalization in the long-time regime. This is cured in the thermodynamic limit, where level spacing tends to zero and the effects of level quantization disappear. In real systems, this translates in time-scales much larger than the ones expected for any thermalization phenomena to be observed.

Despite of these issues, there is still an important debate about to what extent the long-time regime of one of these quantum systems can be described by a thermal ensemble, i.e., if the output of actual observables accessible in the experiment can be predicted within the Quantum Statistical Mechanics framework. Different authors have provided us with numerical evidences that in a variety of models this is the case, and a variety of hypothesis to explain this apparent contradiction have been proposed. In [156, 157], the authors considered the Bose-Hubbard Hamiltonian, a non-integrable model that has been extensively studied since its experimental realization by using optical lattices, as mentioned in the introduction. The Hamiltonian reads:

$$\mathcal{H}_{BH} = -J\sum_{\langle i,j\rangle} b_i^\dagger b_j + \frac{U}{2}\sum_{i=1}^{N} n_i(n_i-1) - \sum_{n=1}^{N}\mu_i n_i \tag{4.3}$$

where i labels the different N sites of a $d-$dimensional lattice. By initializing the system in an out-of-equilibrium initial state, they observed thermalization at the level of the observables computed. Their explanation can be coined as the *local relaxation conjecture*: local observables might be well-described by thermal ensembles due to the influence of the rest of the system, that would act as an effective environment for a small subpart of it. In order to check the hypothesis, they defined a local density operator:

$$\rho_i(N,t) = \mathrm{Tr}_{j\neq i}\left[|\psi(N,t)\rangle\langle\psi(N,t)|\right] \tag{4.4}$$

In the large N regime, they showed that for every $\epsilon > 0$ there is a certain time t far beyond the following holds:

$$||\rho_i(N,t) - \rho_G|| < \epsilon \tag{4.5}$$

where ρ_G is the expected statistical ensemble, the one that maximizes the local entropy. Hence, wherever this conjecture holds, the system would give the impression of being locally relaxated, although

the information from the initial state is still encoded in the long-time regime. Somehow, as happens with the quantum-to-classical transition, the answer comprises the way small parts of a global closed quantum-system seem to be perceived by the rest.

A different approach is that of [158]. In this work, the author states that in a majority of cases, when realistic experimental conditions are taken into account, after a certain time the difference between expectation values of an observable $\mathcal{O}$, calculated by unitary evolution, $\mathrm{Tr}\rho(t)\mathcal{O}$, or by an statistical ensemble, $\mathrm{Tr}\rho_{eq}\mathcal{O}$ would lie below the experimental resolution.

There is yet a third explanation that is strikingly different from the two discussed so far. It is also older, as it was proposed independently by Deutsch [159] and Srednicki [160] in the nineties. It is known as *Eigenstate Thermalization Hypothesis* (ETH). Essentially, it claims that individual energy eigenstates of a quantum system have already thermal properties, in the sense that:

$$\langle\alpha|\mathcal{O}|\alpha\rangle = \langle\mathcal{O}\rangle_{T_\alpha} \tag{4.6}$$

where the effective temperature of the ensemble is derived from the condition $U(T_\alpha) = E_\alpha$, being $U(T) = T^2 d\log Z/dT$ the internal energy of the system (Z is the partition function) and E_α the eigenenergy of the eigenstate $|\alpha\rangle$. The evolution of a general observable for a pure quantum state $|\psi\rangle$ can be expressed in terms of energy eigenstates:

$$\mathcal{O}(t) = \langle\psi(t)|\mathcal{O}|\psi(t)\rangle = \sum_{\alpha,\beta} c_\alpha^* c_\beta e^{i(E_\alpha - E_\beta)t/\hbar}\langle\alpha|\mathcal{O}|\beta\rangle \tag{4.7}$$

Let us suppose that the dynamical evolution leads to decoherence, in the sense that the non-diagonal matrix elements $\alpha \neq \beta$ decay in the course of the time-evolution. The long-time expectation value will be given by the so-called diagonal ensemble, reading:

$$\rho_D = \sum_\alpha |c_\alpha|^2 |\alpha\rangle\langle\alpha| \tag{4.8}$$

Under some general conditions,and in the thermodynamic limit, it can be seen that this ensemble is very peaked at a certain energy E_α, hence reproducing approximately equation (4.6). Somehow, the interpretation is that every quantum eigenstate contains a thermal ensemble, and it is the initial coherence which hides it. Under this hypothesis, decoherence and thermalization would be holding hands.

The ETH has been tested in different works. In [161], Montecarlo calculations were performed for a non-integrable system of hard-core bosons, showing that the ETH works reasonably well, meaning that a microcanonical ensemble yields quite accurate results for the long-time dynamics. The generality of such results, however, has been questioned recently when studying the Bose-Hubbard model [162].

Thermalization in integrable systems

So far, the discussion was centered in non-integrable systems. Integrable systems are somehow more subtle, as in principle the large number of constants of motion should prevent the system to reach equilibrium in the long-time regime. This is apparently the case in the experiment performed by

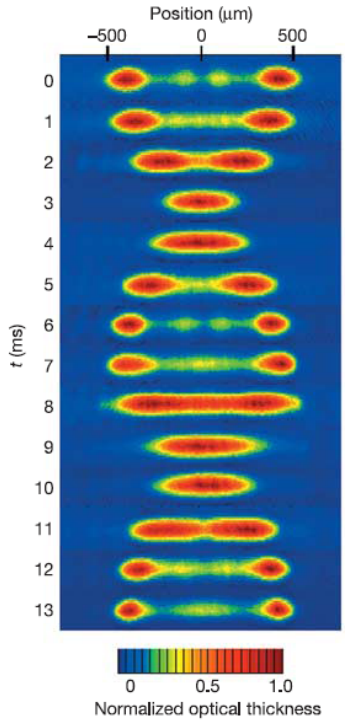

Figure 4.1: Oscillations of a one-dimensional Bose gas with repulsive interactions, in the first cycle after being released from a non-equilibrium configuration. The picture shows optical absorption from the sample. Taken from [56]

Kinoshita et al [56]. Here, a one-dimensional system of bosons was studied in the laboratory, by using very diluted ultracold gases of ^{87}Rb trapped in optical lattices with tuned repulsive interactions. In such a system, one-dimensional bosons behave roughly like fermions as they cannot *pass* through each other, though they still can be in the same state. Notice that, as explained in the introductory chapter, the actual experiment consists on a set of one-dimensional *tubes* with negligible couplings between them. The experimental observations, then, rely on averages over the different tubes.

A non-equilibrium initial state is created by applying external pulses that deplete the one-dimensional atoms in two packages with momentum peaked around $\pm 2\hbar k$, being k the wave-vector of the 1D lattice. Such a configuration reminds to a *Newton's cradle*, since both packages have opposite momenta in the initial state, from which an oscillating behavior is observed (see Fig. (4.1)) where apparently dissipation and thermalization is not observed, despite the existence of collisions between particles. The oscillations remain up to the long-time scales accessible in the experiments. Moreover, the observed momentum distribution is not matched by a thermal ensemble. Hence, although there are interactions between atoms, they do not produce momentum redistribution and do not lead to any relaxation.

The explanation of this absence of thermalization is based on the integrability of the 1D Bose-gas with point-like interactions. The large number of constants of motion of the system render collisions ineffective as a dynamical way of redistribute momentum, and the system remains oscillating because

there is not a way to dissipate the energy given by the initial pulses.

It might be thought that the experiment just described settles the question about thermalization in integrable systems. However, a recently published work served to spread the thermalization debate to these systems. In [163], the authors proposed a *generalized Gibbs ensemble* that would take into account the large set of constants of motion that integrable systems have. The underlying idea is that integrable systems may also exhibit thermalization, but relaxation does not occur in the ordinary thermal ensembles. The derivation of this generalized Gibbs ensemble is rather simple, and is based in Jaynes's approach to Statistical Mechanics [164]: ensembles are deduced by maximizing the entropy $S = k_B \mathrm{Tr}[\rho \log(1/\rho)]$ subject to the constraints imposed by the constants of motion. Let us suppose that I_m is a complete of these integrals of motion. Then, the density operator that fulfills these requisites reads:

$$\rho = \frac{1}{Z} \exp\left[-\sum_m \lambda_m I_m\right] \tag{4.9}$$

where $Z = \mathrm{Tr} \exp\left[-\sum_m \lambda_m I_m\right]$ is the partition function and λ_m the Lagrange multipliers determined by the initial conditions via the following equation:

$$\mathrm{Tr}\left[I_m \rho\right] = \langle I_m \rangle (t = 0) \tag{4.10}$$

In order to check the feasibility of the proposed generalized ensemble, the authors studied numerically the dynamics of a 1D system of Hard-Core bosons in a lattice, finding a good agreement between predictions by this ensemble and numerical results. They argued that in principle, this could also be the case in the experiment of Kinoshita et al, though they did not provide us with a rigorous analysis.

The publication of this work attracted a considerable attention, and was followed by a variety of studies concerning the long-time regime of integrable quantum many-body models initially out-of-equilibrium. For instance, one-dimensional models like the Luttinger model [165], the sine-Gordon model [166], and the Falikov-Kimball model [167]. Or exact solutions to BCS models [168, 169]. Thanks to some of these works, a better understanding of the validity of generalized Gibbs ensembles has been gained, mostly concerning the choice of the integrals of motion. On the one hand, by simply restraining us to the set of constants of motion $\{I_m\}$, correlations between them can be lost in the effective description:

$$\langle I_m I_{m'} \rangle = \mathrm{Tr}(\rho I_m I_{m'}) = \mathrm{Tr}(\rho I_m)\mathrm{Tr}(\rho I_{m'}) = \langle I_m \rangle \langle I_{m'} \rangle \tag{4.11}$$

A possible solution is to enlarge the original set with those integrals of motion that are correlated, like $I_m I_{m'}$ in the previous equation. On the other hand, it happens that for Bethe-Ansatz integrable systems, close expressions for the integrals of motion (in terms, for instance, of creation and destruction operators) are not in general possible. As pointed out in [170], a solution to this issue that works reasonably well is to use instead the set $\mathcal{H}, \mathcal{H}^2, \mathcal{H}^3, ..., \mathcal{H}^n$, with n being the number of integrals of motion.

Sudden-quenches of interactions as a tool to study non-equilibrium dynamics

In order to study non-equilibrium dynamics, sudden-quenches of interactions turn out to be a very convenient way of initializing the system in an out-of-equilibrium configuration. It is mostly conve-

nient from a theoretical point of view, as the initial state ($t = 0$) is an eigenstate of the non-interacting problem $\mathcal{H}_0$, say $|\Psi_{0n}\rangle$, hence simplifying the calculations. The general Hamiltonian to study reads then:

$$\mathcal{H} = \mathcal{H}_0 + \theta(t)\mathcal{H}_I \tag{4.12}$$

where $\theta(t)$ is a Heaviside function and $\mathcal{H}_I$ the interacting part of the Hamiltonian. Let us suppose that we start from the ground state of the non-interacting system. The time-evolution of the state is given by:

$$|\Psi(t)\rangle = e^{-i\mathcal{H}t}|\Psi_0\rangle = \sum_\alpha e^{-i\epsilon_\alpha t}\langle\Psi_\alpha|\Psi_0\rangle|\Psi_\alpha\rangle \tag{4.13}$$

where I have used the closure relation for the eigenstates of the *total* Hamiltonian $\mathcal{H}$, that reads $\mathcal{I} = \sum_\alpha |\Psi_\alpha\rangle\langle\Psi_\alpha|$. Notice that this decomposition in principle includes contributions from all the energy scales of the problem, something that enlarges the difficulties of non-equilibrium problems. Techniques based on effective Hamiltonians, as the ones discussed in the introduction to this part of the thesis, are therefore non-applicable, at least out of the box. In the last years, however, an important effort has been devoted to generalize these techniques to study non-equilibrium problems, and important advances have been achieved. For instance, the *Forward-Backward scheme* [171], based on the Flow-equations method, that I will use throughout this chapter and will be introduced in due course.

The evolution of observables can be decomposed in a similar way:

$$\langle\mathcal{O}(t)\rangle = \langle\Psi(t)|\mathcal{O}|\Psi(t)\rangle = \sum_{\alpha,\beta} e^{-i(\epsilon_\alpha-\epsilon_\beta)t}\langle\Psi_\beta|\Psi_0\rangle\langle\Psi_0|\Psi_\alpha\rangle\langle\Psi_\alpha|\mathcal{O}|\Psi_\beta\rangle \tag{4.14}$$

The matrix elements $\langle\Psi_\alpha|\Psi_0\rangle$ are called *quench* matrix elements, and are typically difficult to compute, as happens with the ones involving observables. This actual holds even when the exact-solution of the model is known, stressing the importance of approximate schemes that simplify the calculations. Most of the articles cited in this introduction make use of sudden-quenches to set the non-equilibrium initial conditions. Among them, of special interest for the topics treated in this thesis are those studying the Luttinger liquid [165] and the sine-Gordon model [166]. In the case of the Luttinger model, calculations were done by taking advantage of the quadratic (bosonic) Hamiltonian in which the model can be mapped by using bosonization techniques. For the sine-Gordon model, special quadratic points of the phase-diagram of the model were exploited to study the dynamics. In a different direction, it is remarkable that the *Forward-Backward* scheme has been successfully applied to study a sudden interaction quench in a Fermi Liquid [172].

The main advantage of working with sudden-quenches stands out, however, when the Heisenberg picture is used to carry out the calculations. In this case, remember, the time dependence is encoded in the operators, and averages are taken with respect to the initial state. Since for a sudden-quench this is the non-interacting ground state, calculations in perturbation theory and related approaches become rather simplified:

$$\langle\Psi(t)|\mathcal{O}|\Psi(t)\rangle = \langle\Psi_0|\mathcal{O}(t)|\Psi_0\rangle \tag{4.15}$$

A last general remark on sudden-quenches. There is a result that has been discussed in [173] with some detail, and that seems to be present in a variety of models, including the sine-Gordon. This is

the fact that, in perturbation theory, the averaged long-time occupations of number states after the sudden-quench do not coincide with the ones expected in equilibrium. They are still related by a factor of two:

$$\lim_{t\to\infty}\langle \Delta N^{NEQ}(t)\rangle = 2\Delta N^{EQ} + \mathcal{O}(g^3) \tag{4.16}$$

where g is the coupling constant of the interaction term, and $\Delta N(t) \equiv \langle \Psi_0|n(t)|\Psi_0\rangle - \langle \Psi_0|n|\Psi_0\rangle$, with $n(t)$ the number operator. The particular factor of two is not expected to prevail beyond lowest order perturbation theory, where there would be extra contributions of order $\mathcal{O}(g^3)$ as pointed in the last equation. This issue will be farther discussed in the context of the sine-Gordon model.

4.2 The sine-Gordon model and its flow-equations solution

The purpose of the research described in this chapter is to apply the aforementioned extension of the flow-equations method to non-equilibrium problems, the *Forward-Backward* scheme, to study a sudden-quench of interactions in the quantum sine-Gordon model. The sine-Gordon model is an ubiquitous model widely studied in many different areas of Physics. It is a $1+1$ scalar field theory already proposed in the nineteen century in the context of classical field theory. In the original studies a lot of attention was devoted to particular solutions of the classical Lagrange's equations. They are named *solitons* after *solitary waves*, since they propagate without dissipation along very narrow channels [174].

Its quantized counterpart became very popular in the seventies, not only because of the existence of these solitons, that also arise in the quantum theory as non-perturbative excitations, but also due to the large variety of models into which can be mapped. For instance, as I will explain in more detail below, it is equivalent to a one-dimensional system of fermions with *backward scattering*, something that makes it relevant to modern experiments with ultracold atoms. Other interesting mappings relate it to the one-dimensional Hubbard model near half-filling, or the Coulomb gas problem, the latter being related to the two-dimensional classical $X-Y$ model [16]. For particular values of the couplings, the sine-Gordon model can also be mapped to the Thirring model.

One of the main features of the quantum sine-Gordon model is its integrable structure, that allows us to find an exact solution by using the Bethe Ansatz [175]. However, as it was mentioned in the last section, an exact solution does not guarantee that the calculation of observables is a simple task. In that sense, it is yet interesting to implement approximated schemes to study certain observables, both to test the reliability of the approximations and to provide us with simple tools that encode the relevant physics despite not being exact. We will see, however, that the calculations carried out in this chapter do not hold up to arbitrary long-time scales. However, still relaxation phenomena is observed, something that may have implications on the thermalization debate in integrable systems.

Here I will concentrate on the weak-coupling regime of the model, where approximations can be done to obtain close flow-equations that can be solved. The effect of sudden-quenches in strong-coupling regions of the phase diagram has been recently studied in [166].

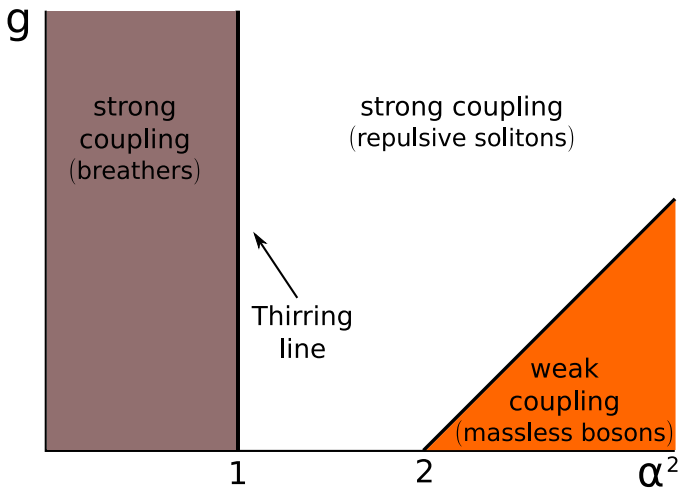

Figure 4.2: Schematic phase-diagram of the quantum Sine-Gordon model

4.2.1 The sine-Gordon model

The Hamiltonian of the sine-Gordon model is defined as follows:

$$\mathcal{H} = \int dx \left(\frac{1}{2}\Pi^2(x) + \frac{1}{2}(\frac{\partial\phi}{\partial x})^2 + \frac{g}{2\pi a^2}\cos(\beta\phi(x)) \right) \tag{4.17}$$

where $\phi(x)$ is a scalar field and $\Pi(x)$ its conjugate momentum field. In order to impose the quantum structure, they must satisfy the commutation relations:

$$[\Pi(x), \phi(y)] = -i\delta(x-y) \tag{4.18}$$

The Hamiltonian contains several parameters: g is the coupling constant, that together with the period β define the phase diagram of the model. Henceforth, we will no longer refer to this last parameter but to the related one $\alpha^2 = \beta^2/4\pi$. The rest of the parameters are used to regularize the theory: a is a lattice discretization parameter, and its inverse $1/a$ plays the role of an ultraviolet cut-off, while L is the system size, whose inverse is the infrared cutoff.

A schematic picture of the phase diagram of the quantum model is shown in Fig. 4.2. At $\alpha^2 = 1$ the exact Thirring line is found, in which the Hamiltonian can be translated to the non-interacting Thirring model, whose relevant degrees of freedom are fermions instead of bosons. Close to this line, the mapping is to the interacting Thirring model, and the weakly interacting fermions can be identified with quantized solitons of the sine-Gordon equation. The mapping between coupling constants being $\lambda/\pi = \frac{\alpha^2-1}{\alpha^2}$, the region $\alpha^2 > 1$ corresponds to repulsive quantum solitons, whereas in the region $\alpha^2 < 1$ there are attractive ones, that form bound states called breathers. The picture in terms of weakly interacting solitons is expected to hold far from the Thirring-line.

The other interesting point of the phase diagram is $\alpha^2 = 2$. Here, a Kosterlitz-Thouless continuous phase transition can be shown to occur by working out the Renormalization Group equations for the

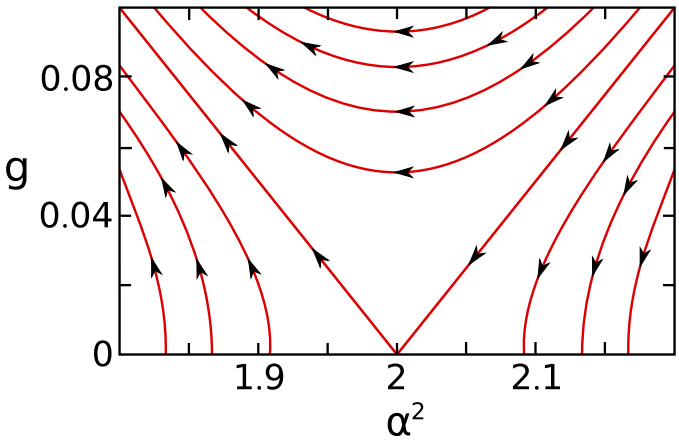

Figure 4.3: Kosterlitz-Thouless kind of flow, close to $\alpha^2 = 2$

flowing coupling constants [145]:

$$\frac{dg}{d\log\Lambda} = (\alpha^2 - 2)g \tag{4.19}$$

$$\frac{d\alpha^2}{d\log\Lambda} = \alpha^4 g^2 \tag{4.20}$$

where $\Lambda = 1/\sqrt{2\pi}a$ is the ultraviolet cut-off. A graphical solution of these equations is shown in Fig. 4.3. For $\alpha^2 < 2$, the coupling constant g flows to strong coupling, signaling the opening of a gap in the spectrum of bosons and the emergence of solitons as the good degrees of freedom of the problem. For $\alpha^2 > 2$ we have the weak-coupling regime, where the coupling constant g flows to zero, and the relevant degrees of freedom are massless bosons. In this region, an approximate solution of the equations can be obtained regarding that the flow of α^2 is almost negligible. Hence, at lowest order, we have:

$$g(\Lambda) \simeq g_0 (\frac{\Lambda}{\Lambda_0})^{\frac{2-\alpha_0^2}{2}} \tag{4.21}$$

$$\alpha^2(\Lambda) \simeq \alpha_0^2 \tag{4.22}$$

As mentioned above, in this work we will be mainly interested in the weak-coupling region of the phase diagram. It is useful then to write the Hamiltonian in terms of bosonic modes:

$$\phi(x) = -\frac{i}{\sqrt{4\pi}} \sum_{k>0} \frac{e^{-\frac{ka}{2}}}{\sqrt{k}} \left(e^{-ikx}(a_{l,k}^\dagger + a_{r,-k}) - e^{ikx}(a_{l,k} + a_{r,-k}^\dagger) \right) \tag{4.23}$$

$$\Pi(x) = \frac{1}{\sqrt{4\pi}} \sum_{k>0} e^{-\frac{ka}{2}} \sqrt{k} \left(e^{-ikx}(a_{l,k}^\dagger - a_{r,-k}) + e^{ikx}(a_{l,k} - a_{r,-k}^\dagger) \right) \tag{4.24}$$

In order to construct the Hamiltonian, we can resort to the so-called Mandelstam vertex-operators

[176]:

$$V_l(\alpha;x) \equiv : \exp(\alpha \sum_{k>0} e^{-ak/2} \frac{1}{\sqrt{k}} (e^{-ikx} a^\dagger_{l,k} - e^{ikx} a_{l,k})) :$$
$$= (\frac{L}{2\pi a})^{\alpha^2/2} \exp(\alpha \sum_{k>0} e^{-ak/2} \frac{1}{\sqrt{k}} (e^{-ikx} a^\dagger_{l,k} - e^{ikx} a_{l,k})) \quad (4.25)$$

$$V_r(\alpha;x) \equiv : \exp(\alpha \sum_{k>0} e^{-ak/2} \frac{1}{\sqrt{k}} (e^{-ikx} a_{r,-k} - e^{ikx} a^\dagger_{r,-k}))$$
$$= (\frac{L}{2\pi a})^{\alpha^2/2} \exp(\alpha \sum_{k>0} e^{-ak/2} \frac{1}{\sqrt{k}} (e^{-ikx} a_{r,-k} - e^{ikx} a^\dagger_{r,-k})) \quad (4.26)$$

where $: \mathcal{O} := \mathcal{O} - \langle 0|\mathcal{O}|0\rangle$ means normal ordering of the operator $\mathcal{O}$ with respect to the non-interacting ground state [177]. The Hamiltonian then acquires the form:

$$\mathcal{H} = \sum_{k>0} k(a^\dagger_{l,k} a_{l,k} + a^\dagger_{r,-k} a_{r,-k})$$
$$+ \frac{g}{2\pi a^2} (\frac{2\pi a}{L})^{\alpha^2} \int dx (V_l(\alpha;x) V_r(-\alpha;x) + V_r(\alpha;x) V_l(-\alpha;x)) \quad (4.27)$$

Relation to the one-dimensional Fermi gas

As I have mentioned at the beginning of this section, one of the mappings of the sine-Gordon model is to a one-dimensional system of interacting fermions with backward scattering. In fact, due to the properties of the Luttinger Liquid, the mapping can be extended to a system of one-dimensional fermions with density-density type of interactions, since the effect of the latter is essentially to renormalize the dispersion relation of the bosonic elementary excitations.

An introduction to the exotic phenomena arising from the study of one-dimensional electron systems is out of the scope of this thesis, and an excellent account is given, for instance, in [16]. The reader interested in the many realizations of one-dimensional systems that have been tested in real experiments should be referred to Chapter 1 of this thesis, where an overview of this topic was provided. Mathematically, in order to understand these systems is necessary to become familiar with the subtleties of bosonization, a technique that allows for the construction of fermionic (or bosonic) operators from bosonic (or fermionic) ones [177]. This way, a Hamiltonian in terms of fermionic degrees-of-freedom can be expressed in terms of bosonic degrees-of-freedom, or viceversa. Why is this an advantage? Well, it depends on the system. In general, as Landau showed many years ago, the elementary excitations of an interacting system of electrons are of fermionic nature –almost free fermions. This is the case, on general grounds, for systems of electrons in 2D and 3D. However, in one-dimension this is no longer the case, and the elementary excitations of a variety of fermionic models are of bosonic nature. Here is where the mapping works better. The extreme case is that of the Luttinger model, that can be exactly diagonalized by using these techniques, being the elementary excitations free bosons. In general, however, after such a mapping the Hamiltonian, written in terms of bosonic degrees-of-freedom, will still contain residual interactions. Remarkably, it happens sometimes that this transformation yields a Hamiltonian whose weak-coupling regime corresponds to the strong-coupling regime of the original model. Non-perturbative phenomena can be then explored in these situations.

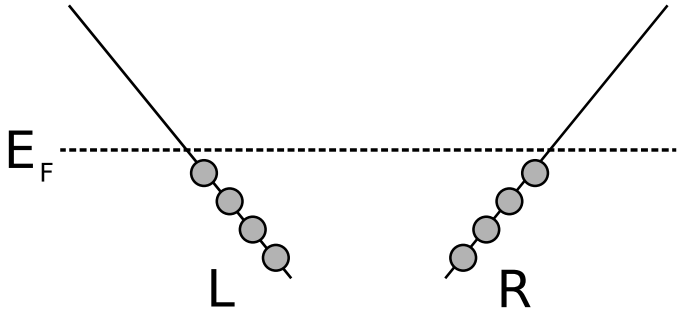

Figure 4.4: Linearization around the Fermi points of a one-dimensional system of electrons. Since there are two Fermi points, two family of low-energy fermionic excitations come along: left (L) and right (R)

This is the case of the sine-Gordon model, as already mentioned. For $\alpha^2 = 1$, it can be mapped to a model of non-interacting fermions. The connection is given by virtue of the vertex operators that appear in the interacting term, that in this limit fulfill fermionic symmetrization relationships:

$$\{V_i(1;x), V_i(-1;y)\} = L\delta(x-y) \tag{4.28}$$

$$\{V_i(1;x), V_i(1;y)\} = \{V_i(-1;x), V_i(-1;y)\} = 0 \tag{4.29}$$

where $i = l, r$, and the lattice spacing has been sent to zero, $a \to 0$.

Let us start with a model of 1D fermions with spin, linearized around the Fermi points (giving rise to left and right movers, as shown in Fig. 4.4), and with density-density interactions:

$$\mathcal{H} = \mathcal{H}_0 + \mathcal{H}_2 + \mathcal{H}_4 \tag{4.30}$$

$$\mathcal{H}_0 = \sum_{k,\sigma} v_F(k-k_F) c^\dagger_{k,R\sigma} c_{k,R\sigma} + \sum_{k,\sigma} v_F(-k-k_F) c^\dagger_{k,L\sigma} c_{k,L\sigma} \tag{4.31}$$

$$\mathcal{H}_2 = \int dx \sum_{\uparrow,\downarrow} \left[g_{2\parallel} \rho_{R,\sigma}(x)\rho_{L,\sigma}(x) + g_{2\perp} \rho_{R,\sigma}(x)\rho_{L,-\sigma}(x) \right] \tag{4.32}$$

$$\mathcal{H}_4 = \int dx \sum_{r=R,L} \sum_{\sigma=\uparrow,\downarrow} \left[\frac{g_{4\parallel}}{\rho}_{r,\sigma}(x)\rho_{r\sigma}(x) + \frac{g_{4\perp}}{2} \rho_{r,\sigma}(x)\rho_{r,-\sigma}(x) \right] \tag{4.33}$$

here, density operators have been introduced, $\rho_{r,\sigma} = \psi^\dagger_{r,\sigma}(x)\psi_{r,\sigma}(x)$, being:

$$\psi_{r,\sigma}(x) = \frac{1}{\sqrt{L}} \sum_k e^{ikx} c_{k,r,\sigma} \tag{4.34}$$

a fermionic field operator.The notation follows the standard in the classification of electron-electron interactions, the so-called *g-ology*. Once bosonization is used, this Hamiltonian is translated into a simplest one, in which spin (σ) and charge (ρ) degrees-of-freedom become decoupled:

$$\mathcal{H} = \mathcal{H}_\rho + \mathcal{H}_\sigma \tag{4.35}$$

where both Hamiltonians have a similar form:

$$\mathcal{H}_\nu = \frac{v_\nu}{2} \int dx \left(\Pi^2_\nu(x) + \left(\frac{\partial \phi_\nu(x)}{\partial x} \right)^2 \right) \tag{4.36}$$

In this Hamiltonian, $\nu = \rho, \sigma$, and the renormalized Fermi velocity v_ν is related to the original coupling constants in a specific way that is not relevant for our discussion [16]. Besides, we have introduced bosonic operators related to the fermionic ones by the bosonization identities [177]. There two important messages to gain from this analysis. On the one hand, we have obtained a quadratic Hamiltonian in terms of bosonic modes in whose parameters is contained the information about the original fermionic Hamiltonian. On the other hand, charge and spin excitations become decoupled in this description.

Now let us analyze the effect of introducing a *backward scattering* type of interaction:

$$\mathcal{H}_1 = \int dx \sum_\sigma \left(g_{1\parallel} \psi^\dagger_{L,\sigma} \psi^\dagger_{R,\sigma} \psi_{L,\sigma} \psi_{R,\sigma} + g_{1\perp} \psi^\dagger_{L,\sigma} \psi^\dagger_{R,-\sigma} \psi_{L,-\sigma} \psi_{R,\sigma} \right) \tag{4.37}$$

Once written in terms of bosonic operators, the *parallel* part can be absorbed into the free-Hamiltonian from the Luttinger model. The *orthogonal* one, however, gives a different term, that only contributes to the spin-sector:

$$\mathcal{H}_{1\perp} = \int dx \frac{g_{1\perp}}{2\pi a^2} \cos(\sqrt{8\pi K_\sigma} \phi_\sigma(x)) \tag{4.38}$$

where a is the lattice distance cutoff, already introduced in this section, and K_σ is a coefficient that comes from a rescaling of the bosonic fields in the Luttinger Hamiltonian, once bosonization is performed, in order to give it the form of a free-bosonic Hamiltonian. Again, it is related to the coupling constants of the problem in a specific way that is not relevant to this discussion. Remarkably, we see how the sine-Gordon model naturally arises from the spin sector of a one-dimensional system of interacting fermions. This provides us with a connection between the studies done in this chapter and possible experimental realizations with ultracold fermionic gases, hence the importance of this result.

4.2.2 Flow equations solution

The sine-Gordon Hamiltonian can be studied by using the flow-equations approach, as shown in Ref [178]. A short introduction to this technique was given in Ch. 2. As a quick reminder, the central idea of the method relies on finding a transformation that increasingly diagonalizes the Hamiltonian, by subsequently removing those matrix-elements that involve the largest energy differences in the non-interacting Hamiltonian. Such a transformation is generated by a certain operator that in principle must be determined for every particular problem, though some general recipes are available that may be useful to construct the transformation in many cases. The complexity of the transformed Hamiltonian usually requires to resort to some truncation scheme, and/or use perturbation theory in one of the parameters. Otherwise, it might be difficult to get close equations that can be worked out.

The first step is, thus, to find a suitable generator of the transformation. This task was performed by Kehrein in [178], though henceforth I will follow the notation used in the book of the same author [110]. It turns out more convenient to switch to a Fourier-transformed representation, where the

vertex-operators read:

$$V_l(-\alpha;k) \equiv \frac{1}{2\pi}\int dx e^{-ikx} V_l(-\alpha;x)$$
$$V_l(\alpha;k) \equiv V_l^\dagger(-\alpha;k) = \frac{1}{2\pi}\int dx e^{ikx} V_l(\alpha;x) \tag{4.39}$$
$$V_r(-\alpha;k) \equiv \frac{1}{2\pi}\int dx e^{-ikx} V_r(-\alpha;x)$$
$$V_r(\alpha;k) \equiv V_r^\dagger(-\alpha;k) = \frac{1}{2\pi}\int dx e^{ikx} V_r(\alpha;x) \tag{4.40}$$

Some relevant properties of these operators are summarized in the Appendix for this chapter. In this representation, the generator of the unitary transformation consists of two parts:

$$\eta(B) = \eta^{(1)}(B) + \eta^{(2)}(B)$$
$$\eta^{(1)}(B) = 8\pi^2 \sum_p p u(p;B)\,(V_l(\alpha;p)V_r(-\alpha;p) - h.c.) \tag{4.41}$$
$$\eta^{(2)}(B) = -\psi(B)\sum_{k>0}(a_{l,k}^\dagger a_{r,-k}^\dagger - a_{r,-k}a_{l,k}) \tag{4.42}$$

where:

$$u(p;B) = \frac{g(B)}{(2\pi a)^2}\left(\frac{2\pi a}{L}\right)^{\alpha^2} e^{-4p^2 B} \tag{4.43}$$
$$\psi(B) = -\frac{32}{a^2}\left(\frac{32B}{a^2}\right)^{1-\alpha^2(B)} g^2(B)\frac{\alpha^2(B)}{4\Gamma(\alpha^2(B)-1)} \tag{4.44}$$

The actual expressions for the parameters are obtained by solving the flow equations. By carrying out the flow to infinity, an effective diagonal Hamiltonian is generated:

$$\mathcal{H}(B=\infty) = \mathcal{H}_0 + \mathcal{H}_{diag}(B=\infty) \tag{4.45}$$
$$\mathcal{H}_0 = \sum_{k>0} k(a_{l,k}^\dagger a_{l,k} + a_{r,-k}^\dagger a_{r,-k}) \tag{4.46}$$
$$\mathcal{H}_{diag}(B=\infty) = \sum_{k>0}\omega_k(B=\infty)(P_l(\alpha_k;-k)P_l^\dagger(\alpha_k;-k)$$
$$+P_l^\dagger(\alpha_k;k)P_l(\alpha_k;k) + P_r^\dagger(\alpha_k;-k)P_r(\alpha_k;-k) + P_r(\alpha_k;k)P_r^\dagger(\alpha_k;k)) \tag{4.47}$$

Here, $\omega_k(B=\infty)$ gives the dispersion relation of the solitonic excitations, defined by conveniently normalized Fourier transformed vertex operators:

$$P_j(\alpha;k) \equiv \left[\frac{2\pi}{L}\Gamma(\alpha^2)\left(\frac{L|k|}{2\pi}\right)^{1-\alpha^2}\right]^{1/2} V_j(-\alpha;k) \tag{4.48}$$
$$P_j^\dagger(\alpha;k) \equiv \left[\frac{2\pi}{L}\Gamma(\alpha^2)\left(\frac{L|k|}{2\pi}\right)^{1-\alpha^2}\right]^{1/2} V_j(\alpha;k) \tag{4.49}$$

Notice that α_k is a scale generated during the flow. Finally, the flow of the Hamiltonian translates into flow equations for the coupling constants, given by:

$$\frac{d\alpha^2}{dl} = \frac{\alpha^4(g^2+\mathcal{O}(g^3))}{4\pi\Gamma(\alpha^2-1)} \tag{4.50}$$
$$\frac{dg}{dl} = (\alpha^2-2)g + \mathcal{O}(g^2) \tag{4.51}$$

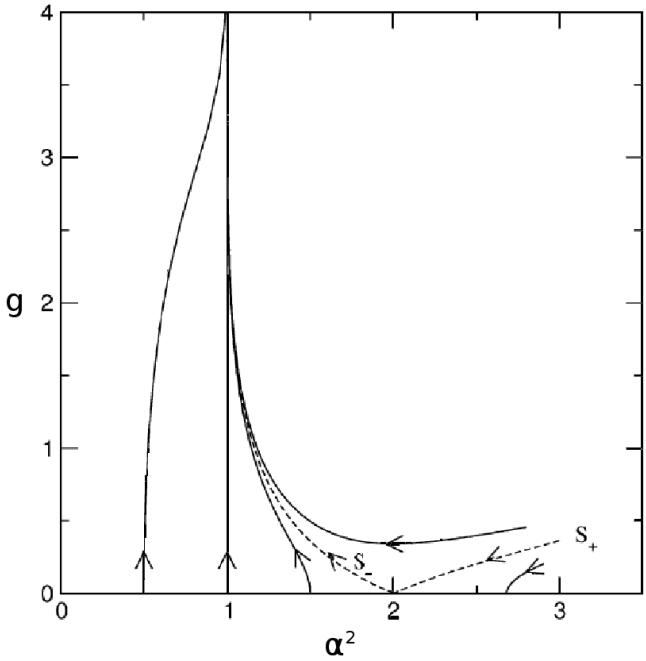

Figure 4.5: Flow of the parameters that define the sine-Gordon Hamiltonian, as given by the flow-equations solution. Notice that this approach succeeds to describe both the Kosterlitz-Thouless transition and the Thirring line.

being $l \equiv -\frac{1}{2}\log(32B/a^2)$. This solution attains to describe the different regions of the quantum sine-Gordon phase diagram: from the weak-coupling regime close to the Kosterlitz-Thouless transition, where excitations are massless bosons, to the Thirring line at $\alpha^2 = 1$, with massive solitonic excitations. A sketch of the trajectories given by these equations is shown in Fig. 4.75. The key for the success of the flow-equations approach in this case resides in the parameter that is used to control the terms generated during the flow. As discussed in the original work [178], by inspecting the terms truncated, the expansion parameter is identified to be:

$$\epsilon(B) = g^2(B)\alpha^2(B)(\alpha^2(B) - 1) \tag{4.52}$$

which remains small close to $\alpha^2 \to 1$, capturing the non-trivial behavior present in this region.

4.3 The method: *Forward-Backward transformation*

The flow-equations approach to the quantum sine-Gordon model can be used to study real time dynamics after a sudden-quench of interactions. The general idea, proposed in [171], consists of three steps. First, the flow of the observables to be studied is carried out by using the same unitary

transformation than the one used for diagonalizing the Hamiltonian:

$$\frac{d\mathcal{O}(B)}{dB} = [\eta(B), \mathcal{O}(B)] \tag{4.53}$$

This is the so-called *forward transformation* of the observable, and in most cases does not imply its diagonalization. Moreover, as it happens also with exact solutions, the structure of the operators at $B = \infty$ can be quite complicated, and approximations must be sorted-out to get close equations.

The advantage of working in this basis comes from the actual time evolution, that is trivial since the Hamiltonian $\mathcal{H}(B = \infty)$, by definition of the transformation, is diagonal. Hence, time evolution translates into phase factors once the observable is written in terms of the operators that make this Hamiltonian diagonal. As a result, $\mathcal{O}(B = \infty, t)$ is obtained.

The final step is the *backward transformation*, where the flow of the transformed and time-evolved operator to the original basis must be carried out backwards. The result, $\mathcal{O}(t)$, is the solution to the Heisenberg equations of motion. Again, this transformation can be difficult to implement, an some approximations might be in turn necessary.

The whole transformation constitutes the flow-equation's *forward-backward* scheme. As I mentioned, it has been already applied to study the real-time dynamics of a Fermi Liquid after a sudden-quench of interactions [172, 173], and also the real time-dynamics after a sudden-quench in the Ferromagnetic Kondo Model [179] . One of the main advantages of this approach is that overcomes the infamous problem of secular terms within perturbation theory: in time-dependent perturbative expansions, unbounded terms can be present in the evolution of observables, making the solution reliable only for time scales shorter than $[\textit{coupling constant}]^{-1}$. In this sense, the forward-backward scheme can be seen as the quantum version of unitary perturbation theory in classical mechanics.

In this thesis I will study the time evolution of the bosonic number operator after a sudden-quench, which will serve to later study the evolution of the bosonic occupations. Being a weak coupling problem, this observable results quite insightful in order to understand the evolution of the system from a non-equilibrium situation. In order to carry out this study, hence, we need to implement the *forward-backward* scheme on the creation/anhinilation operators.

4.3.1 Forward transformation

The *forward* transformation requires the solution of the flow equations:

$$\frac{da_{i,k}(B)}{dB} = [\eta(B), a_{i,k}(B)] \tag{4.54}$$

where $i = l, r$ corresponds to left and right movers. In order to get close equations we make an ansatz for these operators:

$$\begin{aligned} a_{l,k}(\infty) = h^{(l)}_{l,k}(B)a_{l,k} + h^{(l)}_{r,k}(B)a^\dagger_{r,-k} \\ +4\pi^2 \sum_p \Omega^{(l)}_k(p;B)\left(V_l(\alpha, p-k)V_r(-\alpha;p) - V_r(\alpha;-p)V_l(-\alpha;k-p)\right) \end{aligned} \tag{4.55}$$

and likewise for the right movers. The ansatz is parametrized by various functions that must be calculated by working out the commutators in equation (4.54). It is convenient, however, to decompose

the transformation in two stages, given by $\eta^{(1)}(B)$ and $\eta^{(2)}(B)$. The lowest order contribution from the first part of the generator yields the following flow equation:

$$\frac{d\Omega_k^{(l)}(p;B)}{dB} = \frac{2\alpha}{\sqrt{k}}\left(h_{l,k}^{(l)}(B) + h_{r,k}^{(l)}(B)\right) pu(p;B) \tag{4.56}$$

Now, let me focus on the weak-coupling regime. Since the coupling constant $g(B)$ flows to zero, we can use it as a perturbative parameter in the flow equations. It can be shown that in order to preserve the bosonic commutation relations during the flow,

$$[a_{i,k}(B), a_{j,k'}^{\dagger}(B)] = \delta_{i,j}\delta_{k,k'}\frac{L}{2\pi} \tag{4.57}$$

it is consistent to assume an expansion of the form: $h_{l,k}^{(l)}(B) = 1 + \mathcal{O}(g^2)$ and $h_{r,k}^{(l)} = 0 + \mathcal{O}(g^2)$. The details that support this assumption are discussed in the appendixes.

In the weak coupling regime, the flow of the coupling constants can be approximated by equations (4.21) and (4.22), simplifying the integration of the differential equation. The result of carrying out the whole flow is:

$$\Omega_k^{(l)}(p;\infty) = p^{\alpha^2-3}\frac{F_\alpha}{\sqrt{k}}\Gamma(2-\frac{\alpha^2}{2},(2pa)^2) \tag{4.58}$$

where $F_\alpha = \frac{\alpha}{2\pi^2}\frac{g_0}{(2a)^{4-\alpha^2}}(\frac{2\pi a}{L})^{\alpha^2}$, and the result is valid for $\alpha^2 < 4$, which is the region we are mainly interested in. Notice that the initial condition has been set to $\Omega_k^{(l)}(p;B_0) = 0$.

Now let us discuss the effect of the second part of the generator, $\eta^{(2)}(B)$, on the flow equations. Due to the structure of the generator, a different approach to that used for $\eta^{(1)}(B)$ is possible. The complete infinitesimal transformation can be rewritten as:

$$\begin{aligned} a_{l,k}(B+dB) &\simeq a_{l,k}(B) + [\eta(B), a_{l,k}(B)]dB \\ &= e^{\eta^{(2)}}\left(a_{l,k}(B) + [\eta^{(1)}(B), a_{l,k}(B)]dB\right)e^{-\eta^{(2)}} \end{aligned} \tag{4.59}$$

The term in brackets corresponds to the transformation already worked-out. The advantage of this expression arises from the fact that we already know the effect of the exponentiated $\eta^{(2)}(B)$ on the bosonic and vertex operators:

$$e^{\eta^{(2)}(B)}a_{l,k}e^{-\eta^{(2)}(B)} = a_{l,k}\cosh(\psi(B)) + a_{r,-k}^{\dagger}\sinh(\psi(B)) \tag{4.60}$$

$$e^{\eta^{(2)}(B)}a_{r,-k}^{\dagger}e^{-\eta^{(2)}(B)} = a_{r,-k}^{\dagger}\cosh(\psi(B)) + a_{l,k}\sinh(\psi(B)) \tag{4.61}$$

$$e^{\eta^{(2)}(B)}V_l(\alpha;p)e^{-\eta^{(2)}(B)} \simeq V_l(\alpha(1+\psi(B);p) \tag{4.62}$$

$$e^{\eta^{(2)}(B)}V_r(-\alpha;p)e^{-\eta^{(2)}(B)} \simeq V_r(-\alpha(1+\psi(B);p) \tag{4.63}$$

Hence, the effect on the ansatz of the second part of the transformation is:

$$\begin{aligned} e^{\eta^{(2)}(B)} a_{l,k}(B) e^{-\eta^{(2)}(B)} = \\ \left(h_{l,k}^{(l)}(B)\cosh(\psi(B)) + h_{r,k}^{l}(B)\sinh(\psi(B))\right) a_{l,k} \\ + \left(h_{l,k}^{(l)}(B)\sinh(\psi(B)) + h_{r,k}^{(l)}(B)\cosh(\psi(B))\right) a_{r,-k}^{\dagger} \\ +4\pi^2 \sum_p \Omega_k^{(l)}(p;B)\left(\frac{2\pi s\sqrt{B}}{L}\right)^{2\psi(B)\alpha^2} \\ \times \left(V_l(\alpha\,(1+\psi(B))\,;p-k)V_r(-\alpha(1+\psi(B));p)\right. \\ \left. - V_r(\alpha\,(1+\psi(B))\,;-p)V_l(-\alpha(1+\psi(B));k-p)\right) \end{aligned} \tag{4.64}$$

Now, carrying out the whole transformation in second order of the coupling constant yields:

$$\begin{aligned} a_{l,k}(\infty) \simeq \left(1 - g_0^2 \sum_p z_p^{(l)}\right) a_{l,k} + \left(g_0^2 \sum_p z_p^{(l)} + \psi(\infty)\right) a_{r,-k}^{\dagger} \\ +4\pi^2 \sum_p \Omega_k^{(l)}(p;\infty)\left(V_l(\alpha;p-k)V_r(-\alpha;p) - V_r(\alpha;-p)V_l(-\alpha;k-p)\right) \end{aligned} \tag{4.65}$$

where we have used a decomposition derived in Appendix B, $h_{l,k}^{(l)}(\infty) \simeq 1 - h_{r,k}^{(l)}(\infty) \simeq 1 - g_0^2 \sum_p z_p^{(l)}$. We will later see that in the present order of the calculation the contribution coming from the second part of the transformation can be neglected since $\psi(\infty) \propto g_0^2$. This is consistent with our assumption that we neglect the flow of $\alpha^2(B)$ in the weak-coupling regime: neglecting the flow of $\alpha^2(B)$ in fact just corresponds to neglecting the generator part $\eta^{(2)}$.

4.3.2 Time evolution in the diagonal basis

The second step in the *forward-backward* scheme is the time evolution of the observable in the (approximately) diagonal basis. Here, however, an extra approximation is required in order to solve the time evolution problem: in the diagonal Hamiltonian (4.45) only the bosonic kinetic term $\mathcal{H}_0$ is taken into account. We will later see that this approximation implies a maximum time scale up to which our calculation can be trusted. The time evolution dictated by $\mathcal{H}_0$ is very simple, thanks to the simple transformation of the vertex operators:

$$e^{i\mathcal{H}_0 t} V_l(-\alpha,p) e^{-i\mathcal{H}_0 t} = e^{-ipt} V_l(-\alpha,p) \tag{4.66}$$

$$e^{i\mathcal{H}_0 t} V_r(-\alpha,p) e^{-i\mathcal{H}_0 t} = e^{ipt} V_r(-\alpha,p) \tag{4.67}$$

Therefore the time evolved anhinilation operator in the diagonal basis reads:

$$\begin{aligned} a_{l,k}(\infty,t) = \left(1 - g_0^2 \sum_p z_p^{(l)}\right) e^{-ikt} a_{l,k} + \left(g_0^2 \sum_p z_p^{(l)} + \psi(\infty)\right) e^{ikt} a_{r,-k}^{\dagger} \\ +4\pi^2 e^{-ikt} \sum_p \Omega_k^{(l)}(p;\infty) e^{2ipt}\left(V_l(\alpha,p-k)V_r(-\alpha;p)\right. \\ \left. - V_r(\alpha;-p)V_l(-\alpha;k-p)\right) \end{aligned} \tag{4.68}$$

4.3.3 Backward transformation

The final step of the scheme requires to undo the flow-equation transformation for the time-evolved operator (4.68). This is straightforward due to the perturbative nature of this transformation. Let us write a general ansatz for the operator:

$$\begin{aligned} a_{l,k}(B,t) = h^{(l)}_{l,k}(t;B)e^{-ikt}a_{l,k} + h^{(l)}_{r,k}(t;B)e^{ikt}a^\dagger_{r,-k} \\ +4\pi^2 e^{-ikt}\sum_p \Omega^{(l)}_k(p,t;B)e^{2ipt}\left(V_l(\alpha;p-k)V_r(-\alpha;p)\right. \\ \left. -V_r(\alpha;-p)V_l(-\alpha;k-p)\right) \end{aligned} \tag{4.69}$$

with initial conditions $h^{(l)}_{l,k}(t;\infty) = 1 - g_0^2\sum_p z^{(l)}_p$, $h^{(l)}_{r,k}(t;\infty) = g_0^2\sum_p z^{(l)}_p$, and $\Omega^{(l)}_k(p,t;\infty) = \Omega^{(l)}_k(p;\infty)$. The flow equations resemble those for the forward transformation. I will be solely interested in the flow equation for the function $\Omega^{(l)}_k(p,t;B)$, since the contributions from the other functions in the ansatz follow directly via the bosonic commutation relation. The former reads:

$$\frac{d\Omega^{(l)}_k(p,t;B)}{dB} = \frac{2\alpha}{\sqrt{k}}pu(p;B)e^{-2ipt} \tag{4.70}$$

whose solution is:

$$\Omega^{(l)}_k(p;t;0) = \Omega^{(l)}_k(p;\infty)(1-e^{-2ipt}) \tag{4.71}$$

By also applying the second part of the generator, and keeping only the second order contributions, the final time-evolved operator reads:

$$\begin{aligned} a_{l,k}(t) = \left(1 - g_0^2\sum_p(1-e^{2ipt})z^{(l)}_p\right)e^{-ikt}a_{l,k} \\ + \left(g_0^2\sum_p(1-e^{2ipt})z^{(l)}_p + \psi(\infty)\right)e^{ikt}a^\dagger_{r,-k} \\ +4\pi^2 e^{-ikt}\sum_p \Omega^{(l)}_k(p;\infty)(e^{2ipt}-1)\left(V_l(\alpha,p-k)V_r(-\alpha;p)\right. \\ \left. - V_r(\alpha;-p)V_l(-\alpha;k-p)\right) \end{aligned} \tag{4.72}$$

This is the main technical result of this chapter of the thesis, which can be used as a building block to study the time evolution of all other observables.

4.3.4 Check of the formalism: ground state energy and perturbation theory

The reliability of the calculations performed so far, which are supported by several approximations, can be checked by calculating the ground state energy of the equilibrium model. The result, then, can be compared to the prediction given by ordinary second-order perturbation theory. In general, at this order it suffices to calculate the ground state kinetic energy, since it is easy to show that is related to the total energy as $E^{(2)}_{K,0} = -E^{(2)}_0$.

Our goal is therefore to calculate:

$$E_{K,0} = \langle\bar{0}|\mathcal{H}_K|\bar{0}\rangle = \sum_k k\left(\langle\bar{0}|n_{l,k}|\bar{0}\rangle + \langle\bar{0}|n_{r,k}|\bar{0}\rangle\right) \tag{4.73}$$

where $|\bar{0}\rangle$ is the ground state of the *interacting* model.

Within the flow equation formalism this is most conveniently evaluated in the diagonal basis with the forward transformed operators:

$$E_{K,0}^{feq} = \sum_k k \left(\langle 0|a_{l,k}^\dagger(\infty)a_{l,k}(\infty)|0\rangle + \langle 0|a_{r,k}^\dagger a_{r,k}|0\rangle \right) \tag{4.74}$$

where we have used that $\langle \bar{0}|n_{i,k}|\bar{0}\rangle = \langle 0(\infty)|n_{i,k}(\infty)|0(\infty)\rangle$. Here $|0\rangle$ is the bosonic vacuum since this is trivially the ground state in the diagonal basis. If this calculation is carried out by using the full-expression derived within FE formalism, the result does not coincide with that from perturbation theory. This is understandable, since the FE calculation includes the flow of the coupling constant $g(B)$. In order to compare with perturbation theory, this effect must be removed, setting $g(B) = g_0$. Hence, at leading order in $a \to 0$, the calculation yields:

$$E_{K,0}^{feq} = \frac{g_0^2}{a}\frac{L}{2\pi a}\frac{\Gamma(2\alpha^2-2)}{\Gamma^2(\alpha^2)} \tag{4.75}$$

The same result can be obtained now by working out the kinetic energy in second order perturbation theory:

$$E_{K,0}^{(2)} = \int_0^\infty d\lambda \sum_{n\neq 0} |\langle n|\mathcal{H}_I|0\rangle|^2 e^{-\lambda\sum_k k(n_{l,k}+n_{r,k})} \tag{4.76}$$

where $|n\rangle \equiv |n_{l,k_1}, n_{l,k_2}, ..., n_{r,k_1}, n_{r,k_2}, ..\rangle$. By using the matrix elements of vertex operators given in Appendix A, we arrive at the following expression:

$$E_{K,0}^{(2)} = 2L\frac{g_0^2}{(2\pi a^2)^2}\left(\frac{2\pi a}{L}\right)^{2\alpha^2}\int dx \int_0^\infty d\lambda e^{2\alpha^2\sum_k \frac{1}{k}\cos(kx)e^{-\lambda k}} \tag{4.77}$$

After working out the integrals, it can be shown the flow-equations result (4.75) is reproduced.

4.4 Real-time dynamics after a sudden-quench of interactions

Once the dynamics of the bosonic operators has been derived, we can investigate the real-time evolution of the bosonic occupations after a sudden-quench of interactions. General statements about sudden-quenches were discussed in the introduction to this chapter. The Hamiltonian to investigate is that given in (4.12). As mentioned there, in the Heisenberg picture the time evolution is translated to the operators. Since the system is prepared in the non-interacting ground state $|0\rangle$ (bosonic vacuum) of $\mathcal{H}_0$ for $t < 0$, the time-dependent occupation number for left movers is simply:

$$\langle n_{l,k}\rangle(t) = \langle 0(t)|n_{l,k}|0(t)\rangle = \langle 0|a_{l,k}^\dagger(t)a_{l,k}(t)|0\rangle \tag{4.78}$$

where we insert the time-evolved operators (4.72). It is this conceptual simplicity which makes sudden interaction quenches very appealing to study non-equilibrium problems. As mentioned, a similar expression for right-movers can be easily derived, therefore I will restrict the discussion to left-movers only.

An expression for (4.78) can be worked out readily from the results obtained within the *forward-backward* scheme:

$$\langle n_{l,k}(t)\rangle = \frac{\alpha^2 g_0^2}{k}\frac{L}{2\pi a}\frac{4^{\alpha^2-2}}{(\Gamma(\alpha^2))^2} I(ka, \frac{t}{a}) \tag{4.79}$$

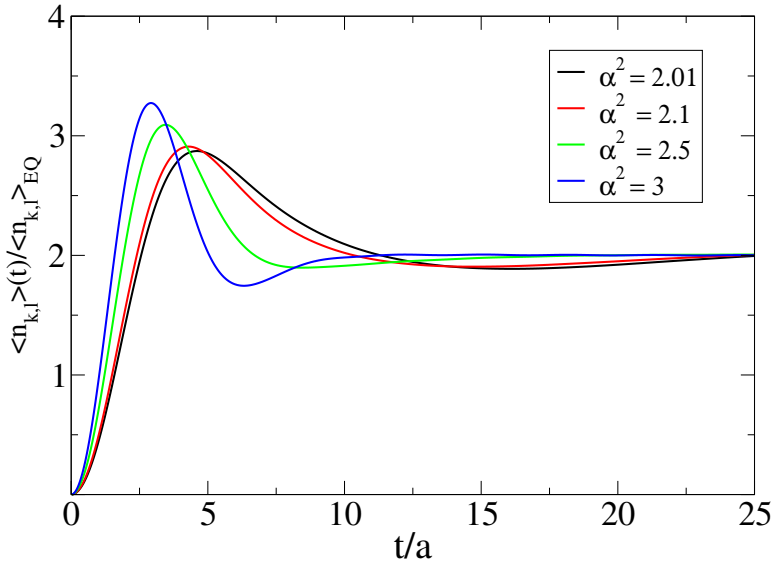

Figure 4.6: Real-time dynamics of the normalized occupations, for different values of α^2. All the plots correspond to $ka = 0.1$. After a few oscillations, the occupations converge to twice their equilibrium values.

where this integral reads:

$$I(ka, \frac{t}{a}) = \int_{ka}^{\infty} dx \sin^2(x\frac{t}{a})(\Gamma(2-\frac{\alpha^2}{2}, 4x^2))^2 x^{3\alpha^2-7}(ka-x)^{\alpha^2-1}e^{-x}$$

In order to get this result, we have made use of the properties of vertex operators summarized in Appendix A, as well as the expression for $\Omega_k^{(l)}(p;\infty)$ given in (4.58). However, it is more convenient to express this result in terms of the equilibrium bosonic occupation numbers. Fortunately, these follows directly from the flow equation calculation:

$$\begin{aligned}\langle n_{l,k}\rangle_{EQ} = \langle\bar{0}|n_{l,k}|\bar{0}\rangle &\simeq \langle 0|a_{l,k}^{\dagger}(\infty)a_{l,k}^{\dagger}(\infty)|0\rangle \\ &= \frac{\alpha^2 g_0^2}{k}\frac{L}{2\pi a}\frac{4^{\alpha^2-2}}{(\Gamma(\alpha^2))^2}I_{EQ}(ka)\end{aligned} \tag{4.80}$$

where:

$$I_{EQ}(ka) = \frac{1}{4}\int_{ka}^{\infty} dx(\Gamma(2-\frac{\alpha^2}{2}, 4x^2))^2 x^{3\alpha^2-7}(ka-x)^{\alpha^2-1}e^{-x} \tag{4.81}$$

and $|\bar{0}\rangle$ denotes, again, the interacting ground state. Finally, we arrive at the following compact expression for the ratio of non-equilibrium to equilibrium occupation numbers:

$$\frac{\langle n_{l,k}(t)\rangle}{\langle n_{l,k}\rangle_{EQ}} = \frac{I(ka, \frac{t}{a})}{I_{EQ}(ka)} \tag{4.82}$$

The integrals in this expression must be computed numerically. Plots of these ratios are shown in Fig. 4.6, for different values of α^2, and in Fig. 4.7, for fixed α^2 and different ka. After the quench, the occupations show damped oscillations in a scale of a few units of time, measured in terms of the lattice cutoff a. They are somehow equivalent to those observed in a classical underdamped harmonic oscillator, with the critical damping being approached as $ka \to 0$.

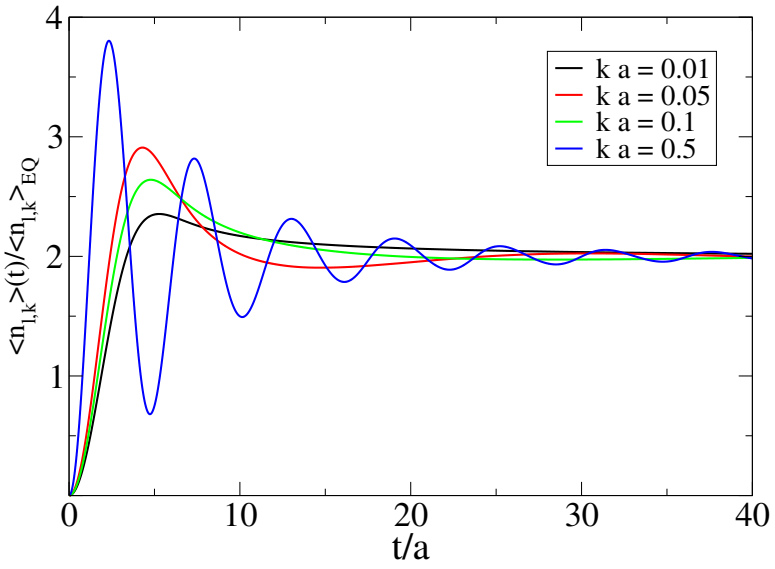

Figure 4.7: Real-time dynamics of the normalized occupations, for different values of ka. All the plots correspond to $\alpha^2 = 2.1$.

The asymptotic value of the mode occupation universally converges to twice its equilibrium value:

$$\langle n_{l,k}(t \to \infty) \rangle = \left(2 + O(g_0^2)\right) \langle n_{l,k} \rangle_{EQ} \tag{4.83}$$

This can be understood easily by noticing that $I_{EQ}(ka)$ and $I(ka, t/a)$ only differ by replacing a factor $1/4$ by $\sin^2(xt/a)$ in the integrand. Clearly the limit $\langle n_{l,k}(t \to \infty) \rangle$ just amounts for taking the time average over $\sin^2(xt/a)$ in the integrand, which gives $1/2$ and therefore $I(ka, t/a \to \infty) = 2\, I_{EQ}(ka)$. Notice that (4.83) implies a non-thermal mode distribution function for the asymptotic state of this closed quantum system: the equilibrium system with nonzero temperature cannot reproduce this expression.

This factor 2 is *universal* for weak interaction quenches and has been previously found for the momentum distribution function in the non-equilibrium Hubbard model [172, 173] and for the magnetization of the non-equilibrium ferromagnetic Kondo model [179, 180]. A general analysis seem to suggest that it occurs for quenches in quantum systems where i) second order perturbation theory is valid (at least up to a certain time scale) and ii) for observables like the mode occupation number operator which commute with $\mathcal{H}_0$. For a proof and more details on the conditions I suggest the readers to check Ref. [173].

The results found in this section might serve to provide a better understanding of non-equilibrium quantum many-body systems in general. Therefore, it is important to critically re-examine the approximations done so far in the calculations. Due to the weak-coupling behavior of the running coupling constant, the second order calculation presented here becomes more and more reliable in the infrared limit. Therefore higher order corrections to the universal factor 2 will vanish in the low-energy limit. However, an additional approximation was done when neglecting the time evolution generated by

$\mathcal{H}_{diag}(\infty)$. This means that the result (4.83) can only be trusted up to the time scale:

$$\tau_k \propto \omega_k^{-1}(B=\infty) \propto g_0^{-2}\, k^{3-2\alpha^2} \tag{4.84}$$

Whether this central result

$$\langle n_{i,k}(t\to\infty)\rangle = 2\langle n_{i,k}\rangle_{EQ} \tag{4.85}$$

really holds beyond the time scale τ_k or only in a time window $a \ll t \ll \tau_k$ cannot be answered based on this calculation.

4.5 Conclusions

In this chapter I have addressed the dynamics of the sine-Gordon model after a sudden interaction quench in the weak-coupling regime. It shows an interesting behavior that is remarkably different from that found when the only the forward scattering is switched. Quenching the forward scattering does not induce any dynamics for the bosonic occupation numbers, which are in fact constants of motion in this case [165]. When the backscattering term in the weak-coupling regime is included, the excitation energy of the quench is converted into bosonic mode occupations that oscillate on a time scale set by the ultraviolet cutoff and eventually reach twice their equilibrium values (4.83), a universal result that can be expected on general grounds in perturbative calculations. However, the calculation carried out here cannot be trusted up to arbitrary time scales, and hence if this result holds at any time cannot be answered within our formalism.

Nevertheless, it should be enough to state that the interaction quench in the weak-coupling phase of the sine-Gordon model occupies an interesting place between the ferromagnetic Kondo model, where the factor 2 is in fact asymptotically exact [179, 180], and the non-equilibrium Hubbard model in $d \geq 2$ dimensions, where the factor 2 describes the prethermalization regime [172, 173] before the system eventually thermalizes. The integrability of the sine-Gordon model might induce us to reckon that the non-equilibrium distribution function (4.85) remains stable for all times and does not approach a thermal limit form. However, the conserved quantities in the sine-Gordon model do not impose any obvious constraints on the dynamics of the momentum distribution function, unlike in the case of quenching the forward scattering [165]. As was discussed in the context of the thermalization debate, the integral structure of a model is still compatible with relaxation phenomena at the level of observables.

Further studies of this question would be very worthwhile, either numerical or based on an exact solution. Being the sine-Gordon model on the borderline between thermalization and non-thermalization seen through the eyes of the mode distribution function, it is therefore similar to the role played by the celebrated Fermi-Pasta-Ulam problem for classical many-body systems [181, 182]. A better understanding of the weak-coupling quench in the quantum sine-Gordon model could be an important step in elucidating the fundamental question of thermalization in the quantum world.

APPENDIX A: Properties of vertex operators

I will summarize here some important properties of vertex operators:

$$V_l(\alpha;-k)|0\rangle = V_l(-\alpha;k)|0\rangle = V_r(\alpha;k)|0\rangle = V_r(-\alpha;-k)|0\rangle = 0, \forall k>0 \tag{4.86}$$

$$\begin{aligned}\langle 0|V_l(-\alpha;k)V_l(\alpha;k')|0\rangle &= \langle 0|V_r(\alpha;k)V_r(-\alpha;k')|0\rangle \\ &= \delta_{k,k'}\Theta(k)\left(\frac{L}{2\pi}\right)^{\alpha^2+1}\frac{|k|^{\alpha^2-1}}{\Gamma(\alpha^2)} \qquad (4.87)\\ \langle 0|V_l(\alpha;k)V_l(-\alpha;k')|0\rangle &= \langle 0|V_r(-\alpha;k)V_r(\alpha;k')|0\rangle \\ &= \delta_{k,k'}\Theta(-k)\left(\frac{L}{2\pi}\right)^{\alpha^2+1}\frac{|k|^{\alpha^2-1}}{\Gamma(\alpha^2)} \qquad (4.88)\\ \langle 0|V_l(\alpha;k)V_l(\alpha;k')|0\rangle &= \langle 0|V_r(\alpha;k)V_r(\alpha;k')|0\rangle = 0 \qquad (4.89)\end{aligned}$$

Operator Product Expansion of left-handed vertex operators:

$$\begin{aligned}*V_l(-\alpha;k)V_l(\alpha;k')* &= \frac{\alpha}{\Gamma(\alpha^2-1)}\left(\frac{L}{2\pi}\right)^{\alpha^2} \\ &\times\Big(\sqrt{k'-k}|k|^{\alpha^2-2}\theta(k)\theta(k'-k)a^\dagger_{l,k'-k} \\ &+\sqrt{k-k'}|k'|^{\alpha^2-2}\theta(k')\theta(k-k')a_{l,k-k'}+...\Big) \qquad (4.90)\\ *V_l(\alpha;k)V_l(-\alpha;k')* &= -*V_l(-\alpha;-k)V_l(\alpha;-k')* \qquad (4.91)\end{aligned}$$

Matrix elements of vertex operators between number states:

$$\langle n|V_l(\alpha;x)|0\rangle = \Pi_{k>0}\left(\frac{\alpha}{\sqrt{k}}\sqrt{\frac{2\pi}{L}}\right)^{n_{l,k}}\frac{e^{-ikn_{l,k}x}}{\sqrt{n_{l,k}!}} \tag{4.92}$$

$$\langle n|V_r(\alpha;x)|0\rangle = \Pi_{k>0}\left(\frac{\alpha}{\sqrt{k}}\sqrt{\frac{2\pi}{L}}\right)^{n_{r,k}}\frac{e^{ikn_{r,k}x}}{\sqrt{n_{r,k}!}} \tag{4.93}$$

APPENDIX B: Flow equation for $h^{(l)}_{l,k}(B)$

The flow equations for the parameter $h^{(l)}_{l,k}(B)$ can be obtained from the commutator of the generator with the second part of the ansatz. Only the terms linear in $a_{l,k}$ are kept, and they come from the operator product expansion of two vertex operators:

$$\begin{aligned}&-4(2\pi)^4\sum_{p,p'}pu(p;B)\Omega^{(l)}_k(p';B) \\ &\times\big(*V_l(\alpha;p)V_l(-\alpha;k-p')*\langle 0|V_r(-\alpha;p)V_r(\alpha;-p')|0\rangle \\ &+*V_l(-\alpha;p)V_l(\alpha;p'-k)*\langle 0|V_r(\alpha;-p')V_r(-\alpha;p)|0\rangle\big) \qquad (4.94)\end{aligned}$$

Now, by using the expressions given in Appendix A, we get the flow equation:

$$\frac{dh_{l,k}^{(l)}(B)}{dB} = -\alpha\sqrt{k}\frac{4(2\pi)^4}{\Gamma(\alpha^2)\Gamma(\alpha^2-1)}\left(\frac{L}{2\pi}\right)^{2\alpha^2} \times \left(\sum_{p>0} u(p;B)\Omega_k^{(l)}(p;B)p^{2\alpha^2-2} + \sum_{p>k} u(p;B)\Omega_k^{(l)}(p;B)p^{\alpha^2}|p-k|^{\alpha^2-2}\right) \tag{4.95}$$

which is of second order in the coupling constant g_0. The integration of this equation turns out to be easy by using the flow equation (4.56) for the parameter $\Omega_{k,l}^{(l)}(B)$. At lowest order in the coupling constant the solution reads:

$$h_{l,k}^{(l)}(B) = 1 - \frac{(2\pi)^4 k}{\Gamma(\alpha^2)\Gamma(\alpha^2-1)}\left(\frac{L}{2\pi}\right)^{2\alpha^2} \times \left(\sum_{p>0} (\Omega_k^{(l)})^2(p;B)p^{2\alpha^2-2} + \sum_{p>k} (\Omega_k^{(l)})^2(p;B)p^{\alpha^2}(p-k)^{\alpha^2-2}\right) \tag{4.96}$$

Defining $\Omega_k^{(l)}(p;\infty) \equiv \Omega^{(l)}(p;\infty)/\sqrt{k}$, and at lowest order in $ka \ll 1$, we get:

$$h_{l,k}^{(l)}(B) = 1 - \frac{2(2\pi)^4}{\Gamma(\alpha^2)\Gamma(\alpha^2-1)}\left(\frac{L}{2\pi}\right)^{2\alpha^2}\sum_{p>0}\Omega^2(p;B)p^{2\alpha^2-2} \tag{4.97}$$

Notice that a similar derivation can be done for the right-handed flow operator, yielding $h_{r,k}^{(l)}(B) \simeq 1 - h_{l,k}^{(l)}$.

APPENDIX C: Sum-rule

The canonical commutation relations must be fulfilled during the entire flow:

$$[a_{l,k}(B), a_{l,k'}^\dagger(B)] = \frac{L}{2\pi}\delta_{k,k'} \tag{4.98}$$

From this requirement we can derive a consistency condition for the flowing operator. Evaluating this condition in the ground state:

$$\delta_{k,k'} = h_{l,k}^2\delta_{k,k'} - h_{r,k}^2\delta_{k,k'} + \frac{(2\pi)^4}{\Gamma(\alpha^2)^2}\left(\frac{L}{2\pi}\right)^{2\alpha^2} \times \left(\sum_{p>0}\Omega_k^2(p;B)p^{\alpha^2}(p+k)^{\alpha^2-1} - \sum_{p>k}\Omega_k^2(p;B)p^{\alpha^2}(p-k)^{\alpha^2-1}\right) \tag{4.99}$$

Using some straightforward algebra one can verify that this is indeed fulfilled for the flow equations derived in this chapter of the thesis.

Part II

Interactions in graphene monolayers

5 Introduction: Coulomb interactions in graphene monolayers

It's not who I am underneath but what I do that defines me
Bruce Wayne/Batman

5.1 Introduction: The Fermi Liquid

In the introductory chapter, the basic electronic properties of graphene were explained on the basis of a low-energy model of massless Dirac fermions without intrinsic interactions. This description suffices to describe most of the experiments, and only extra ingredients like disorder, particular geometries of graphene samples or external fields are required to provide a good explanation. Electron-electron interactions, remarkably, do not seem to play an important part in the phenomenology of graphene samples. The purpose of this chapter is to analyze in detail to what extent is this fact remarkable. After all, modern electron liquid theory also relies on the formation of barely interacting quasiparticles, thus explaining many of the properties of the system in terms of a free-electron picture with renormalized parameters. But electrons interacting in undoped graphene samples cannot be trivially mapped to the usual electron theory, since there is not a Fermi surface, but a Dirac point, and screening of interactions close to this point is considerably suppressed. In order to understand the role of electron-electron interactions in graphene layers, a good starting point is precisely the modern theory of the electron liquid. Once analyzed, we will be in a better position to understand the peculiarities (or not) of graphene electrons. Being graphene a two-dimensional system, I will only discuss the theory of two-dimensional electron liquids, which is essentially the same as its three-dimensional counterpart.

The basis of the electron liquid theory was established by the famous physicist L. D. Landau, whose purpose was to explain the properties of ^3He, a system composed of fermionic isotopes of Helium in interaction [183]. The range of applicability of his ideas turned out to cover a much broader range though, in principle almost every interacting system of fermions at low temperatures and with dimensionality $d \geq 2$, i.e., the so-called Fermi liquids [184]. And where this Landau's Fermi liquid paradigm does not apply, most of the deviations can be understood in terms of its instabilities. This is because Fermi liquids represent an universality class for interacting systems of fermions. In terms of a Renormalization Group picture, it happens that a large class of Hamiltonians flow in the low-energy regime to the same fixed point, which is the one that Fermi liquid theory describes.

The central point of Landau's theory are systems with a well-defined Fermi surface in the non-interacting regime. Based on his deep intuition, Landau was able to give general arguments about the

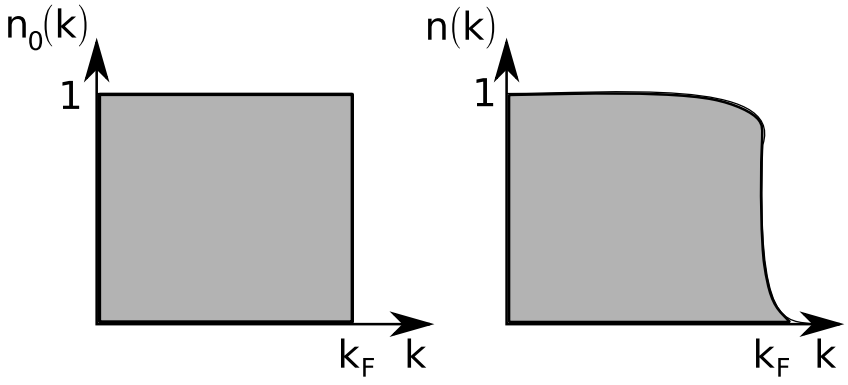

Figure 5.1: Momentum distribution showing the occupation of k states before (left) and after (right) an adiabatic switch on of the interactions, at $T = 0$.

way interactions affect the low-energy excitations around this Fermi surface, at least when interactions are adiabatically switched on. According to Landau, this interacting system or Fermi liquid would have a correspondence in quantum numbers with the free Fermi gas, at least close enough to the Fermi surface, that would remain stable. This would imply that the low-energy excitations of this system are weakly interacting fermionic *quasiparticles*, with spin $1/2$ and momentum k in a one-to-one correspondence with the non-interacting electrons. Still, residual interactions between quasiparticles are of a major importance, being crucial in order to explain many thermodynamic properties of the system, as well as its response to external probes. From the point of view of free-electron states, the interactions have a clear signature in the momentum distribution, since they produce a broadening of the sharp step at the Fermi surface (Fig. 5.1). This signals the formation of quasiparticles in the system, that will have a finite life-time since they are no longer good eigenstates of the Hamiltonian. Moreover, although the quasiparticles have the same quantum numbers as the original free electrons, their mass is renormalized due to the interactions.

Landau's theory of the Fermi Liquid was later microscopically founded by using techniques imported from Quantum Field Theory: the Green's function formalism [185, 10] and the Renormalization Group [186, 113]. In terms of Green's functions, the effect of interactions can be studied by analyzing the analytic form of certain correlation functions, like the single particle retarded propagator, whose general form is:

$$G^R_\sigma(\mathbf{k},\omega) = \frac{1}{\omega - [\epsilon_\mathbf{k} + \Re\Sigma^R_\sigma(\mathbf{k},\omega)] - i\Im\Sigma^R_\sigma(\mathbf{k},\omega)} \tag{5.1}$$

where the function $\Sigma^R_\sigma(\mathbf{k},\omega)$ is the self-energy function, and $\epsilon_\mathbf{k} = k^2/2m - \mu$ are the free-electron energies. For the non-interacting system, the self-energy vanishes, yielding a simple function with a pole at the free-particle energies. The microscopic derivation of the Fermi Liquid theory relies on calculating the self-energy from a Hamiltonian of electrons interacting via the Coulomb potential. From this, an expansion of this quantity near the Fermi surface can be carried out, yielding the

following expression:

$$G^R_\sigma(\mathbf{k},\omega) \simeq \frac{1}{\omega - \omega\partial_\omega \Re\Sigma^R_\sigma(\tilde{k}_F,0) - (\mathbf{k}-\tilde{\mathbf{k}}_F)\partial_{\mathbf{k}}\left(\epsilon_{\mathbf{k}} + \Re\Sigma^R_\sigma(\tilde{k}_F,0)\right) - i\Im\Sigma^R_\sigma(\tilde{k}_F,0)} \equiv \frac{Z}{\omega - \tilde{\epsilon}_{\mathbf{k}} + \frac{i}{2\tau_{\mathbf{k}}}} \tag{5.2}$$

where we have introduced the Fermi momentum for the interacting system from $\epsilon_{\tilde{k}_F} + \Re\Sigma(\tilde{\mathbf{k}}_F,0) = 0$, and defined the new parameters:

$$Z^{-1} = 1 - \frac{\partial}{\partial\omega}\Re\Sigma^R_\sigma(\tilde{\mathbf{k}}_F,0) \tag{5.3}$$

$$\tilde{\epsilon}_{\mathbf{k}} = (\mathbf{k}-\tilde{\mathbf{k}}_F)Z\frac{\partial}{\partial\mathbf{k}}\left(\epsilon_{\mathbf{k}} + \Re\Sigma^R_\sigma(\mathbf{k},0)\right)\Big|_{k=k_F} \tag{5.4}$$

$$\tau^{-1}_{\mathbf{k}} = -2Z\Im\Sigma^R_\sigma(\mathbf{k},\omega) \tag{5.5}$$

An inspection of this expression shows that it corresponds to what is expected for free fermionic excitations with renormalized energies $\tilde{\epsilon}_{\mathbf{k}}$, a finite life-time $\tau_{\mathbf{k}}$ and the so-called *renormalization constant* Z, which is nothing but the residue of G at the pole of the function. The latter measures the weight of the *quasiparticle* defined from the pole of the interacting propagator, which is an indication of how important these excitations are compared to other complicated many-body ones. Notice that for strictly free electrons, $Z = 1$, meaning that they account for all the excitations present in the system. For a Fermi liquid, by definition, the quasiparticles carry an important part of the spectral weight, since they are the most important excitations of the interacting system, and usually Z ranges between 0.7 and 1. When this does not happen, it might signal the breakdown of the picture in terms of Landau's quasiparticles, meaning that it is likely that the effects of interactions translate into a different behavior.

Let me now provide some details of the picture just sketched, and analyze the way it manifests itself through certain (in principle) measurable observables. The starting point is the Hamiltonian for the interacting electron gas:

$$\mathcal{H} = \sum_{\mathbf{k},\sigma}\epsilon_{\mathbf{k}}c^\dagger_{\mathbf{k}\sigma}c_{\mathbf{k}\sigma} + \frac{1}{2}\sum_{\mathbf{q}}v(\mathbf{q})n(\mathbf{q})n(-\mathbf{q}) \tag{5.6}$$

where $v(\mathbf{q}) = 2\pi e^2/q$ is the Coulomb potential in two-dimensions[1], and $n(\mathbf{q}) = \sum_{\mathbf{k},\sigma}c^\dagger_{\mathbf{k}+\mathbf{q}\sigma}c_{\mathbf{k}\sigma}$ the Fourier transformed local density operator. The self-energy can then be calculated by using perturbation theory, usually with the assistance of Feynman diagrams. In order to do the calculations, it is important to keep in mind that the global system is neutral, something that can be incorporated into the model by postulating the existence of a positive homogeneous charge background. Such a perturbative expansion in terms of diagrams is shown in Fig. 5.2.

If the calculations are done naively, it can be seen that perturbation theory breaks down due to the presence of logarithmic divergences in the diagrams. This is similar to what happened with the short-range potential discussed in Chapter 2, signaling the emergence of non-trivial phenomena in the low-energy sector of the theory. In the aforementioned chapter, we learnt from RG arguments

[1] In cgs units, where $4\pi\epsilon_0$ is equal to one

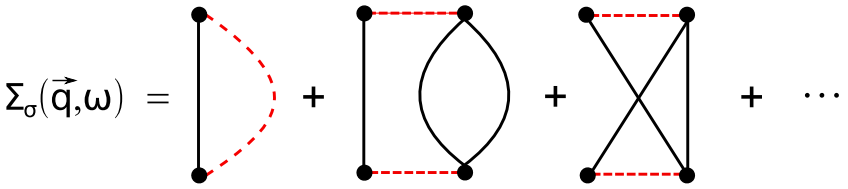

Figure 5.2: Lowest order diagrams contributing to the self-energy for the electron liquid, calculated in perturbation theory.

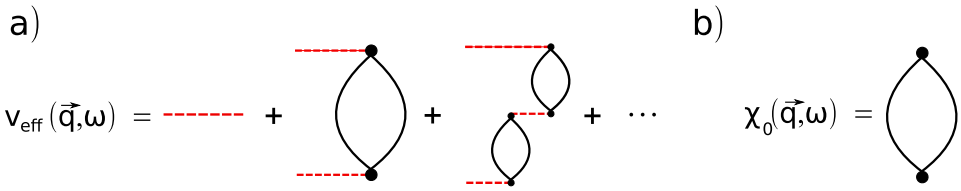

Figure 5.3: a) Diagrammatic calculation of the RPA effective interaction. b) The polarization bubble, $\chi_0(\mathbf{q},\omega)$.

that this can be traced back to the lack of characteristic scales in the theory, and requires a caraful treatment of the effect that high-energy excitations have on the low-energy spectrum. From the RG point of view, this means that the coupling constant depends on the energy scale, and therefore the bare coupling constant should not be employed to weight the interactions among excitations for arbitrary energy scales. This RG analysis yields, in fact, that the effective coupling constant flows to zero in the low-energy regime [186, 113], as happened with the repulsive impurity potential studied in Chapter 2.

The RG picture can be understood in terms of the microscopic foundations of the Fermi Liquid theory. After all, the system is still composed of strongly interacting electrons, although its phenomenology can be explained in terms of compound excitations, quasiparticles, that interact weakly . The central concept in this regard is screening. The idea is that the interaction between a couple of electrons in the system is affected by the media, i.e., by the rest of electrons, that respond in a way that attenuates the overall interaction. As we learnt from the Spin-Boson model in Chapter 2, high-energy excitations of the electron gas can be thought as rapidly accommodating to the interactions, giving rise to effective dressed electrons made of the bare electron plus a cloud of excitations. These are the quasiparticles.

These general arguments can be supported in a more technical way. This is done by resorting to something similar to the scaling perturbation theory discussed in Chapter 2. By making a resummation of a set of diagrams, commonly referred to as the *Random Phase Approximation* (RPA), an effective interaction can be defined, with respect to which perturbative calculations can be carried out without stumbling into divergences. The resummation that gives this effective interaction is shown in Fig. 5.3, whose analytic expression reads:

$$v_{eff}(\mathbf{q},\omega) = \frac{v(\mathbf{q})}{1 - v(\mathbf{q})\chi_0(\mathbf{q},\omega)} \tag{5.7}$$

where $\chi_0(\mathbf{q},\omega)$ is called the polarization bubble, since it is related to the response to the system to an external potential. Its diagrammatic expression has also been depicted in Fig. 5.3.

This result is pivotal in modern electron theory, and it is worth to analyze it in more detail. It can already be understood in terms of classical linear response theory. If the (interacting and neutral) system is subject to an external potential $\phi_{ext}(\mathbf{q},\omega)$, it will response by creating an induced charge $\rho_{ind}(\mathbf{q},\omega) \equiv \chi(\mathbf{q},\omega)\phi_{ext}(\mathbf{q},\omega)$. Now, due to the non-negligible response of the system, the total potential felt by the sample will be a combination of the external one plus the one created by the induced charge. The final response of the system then reads:

$$\phi_{tot}(\mathbf{q},\omega) = \phi_{ext}(\mathbf{q},\omega) + v(\mathbf{q})\chi(\mathbf{q},\omega)\phi_{tot}(\mathbf{q},\omega) \tag{5.8}$$

which is a self-consistent equation whose solution is actually quite simple:

$$\phi_{tot}(\mathbf{q},\omega) = \frac{\phi_{ext}(\mathbf{q},\omega)}{1 - v(\mathbf{q})\chi(\mathbf{q},\omega)} \equiv \frac{\phi_{ext}(\mathbf{q},\omega)}{\epsilon(\mathbf{q},\omega)} \tag{5.9}$$

Here, we have introduced the *dielectric* function, $\epsilon(\mathbf{q},\omega) \equiv 1 - v(\mathbf{q})\chi(\mathbf{q},\omega)$, that encodes the way the system screens the external potential. Notice that this expression matches that from the RPA approximation. Indeed, the RPA resummation gives already the effective interaction that is expected to arise from a polarizable electron gas, in which bare interactions are screened, and weakly coupled quasiparticles account for the real response of the system. This RPA potential can be seen as the interaction between quasiparticles, and it is no longer strong and long-ranged, as can be seen straightforwardly by calculating its static limit [10]:

$$v_{eff}(\mathbf{q},0) = \frac{2\pi e^2}{q + \kappa_{TF}} \tag{5.10}$$

where κ_{TF} is the Thomas-Fermi wave-vector in two-dimensions. Its inverse is related to the screening-length, which is the effective range of the (now short-range) potential. If now the calculations are done with respect to this interaction, an expression for the electron Green's functions as the one given in Eq. (5.2) is derived, completing the task of providing us with a microscopic picture of Landau's theory of the Fermi Liquid.

The RPA resummation together with second order perturbation theory suffices to describe the physics of the electron liquid in the high-density regime. For the low-density regime, other corrections must be included. Notice that in this task, it is always possible to organize perturbation theory in terms of the effective interaction given by RPA, which is nothing but a resummation of a certain set of diagrams. The actual approximations come later, when the calculations are kept at some order of the (reorganized) perturbative expansion.

But the RPA approximation still has further implications. It predicts the existence of another coherent excitation in the electron liquid, besides Landau quasiparticles: the plasmon, a collective excitation of the whole electron gas. Plasmons are known already in a classical context as self-sustained oscillations of the electron gas. Analytically, this can be seen by rewriting equation (5.9) as $\phi_{ext}(\mathbf{q},\omega) = \epsilon(\mathbf{q},\omega)\phi_{tot}(\mathbf{q},\omega)$. If there are non-trivial solutions for the condition $\epsilon(\mathbf{q},\omega) = 0$, then the system can sustain oscillations without an external probe. These solutions define a dispersion relation $\omega(\mathbf{q})$ given by those points where they can exist, meaning that $\epsilon(\mathbf{q},\omega(\mathbf{q})) = 0$.

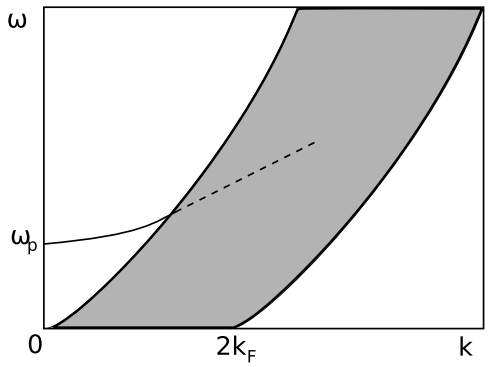

Figure 5.4: Sketch of $\Im\chi_0(\mathbf{k},\omega)$ for the electron gas, in the plane $\omega - k$. The grey area stands for the electron-hole excitations (so-called the electron-hole continuum), while the branch $\omega(\mathbf{k})$ starting at ω_p, the plasma frequency, represents the plasmon collective excitation.

The global picture comprised in the RPA theory can be summarized as follows. The electron liquid turns out to have well-defined quasiparticle excitations of fermionic nature, in which a quasiparticle is excited from the Fermi sea, creating at the same time a quasihole. Therefore, they will henceforth be called *particle-hole* excitations. At the same time, there is a collective excitation of bosonic nature: the plasmon. The geography of the excitations contained in the low-energy spectrum of the problem can be analyzed through the interacting susceptibility $\chi(\mathbf{q},\omega)$. Its imaginary part can be shown to be related to the sources of dissipation of the system, i.e., the way the system can absorb energy from an external probe. A plot of the non-zero values of this function is shown in Fig. 5.4, where both types of excitations leave their imprint naturally. The plasmon is well-defined wherever there are no electron-hole excitations. Otherwise, it has a finite life-time, since it can decay into these excitations (dashed line in the figure).

In short, the Fermi Liquid theory provides us with an explanation of why interactions in many Fermi systems are somehow less important than expected *a priori*. Of course, by adding different ingredients, like phonons or a lattice discretization, the situation can change, leading to a breakdown of the Fermi Liquid picture. Phonons, for instance, can lead to the phenomenon of superconductivity, where Cooper pairs are formed due to the attractive interaction between electrons that the mediation of phonons may induce [187]. In the presence of short-range screened interactions an insulating phase transition might also occur if the system lives in a lattice, becoming a so-called Mott insulator. Such an effect has been widely explored in the context of the Hubbard model [188]. Moreover, Landau's picture is expected to break down in the low-density regime, where the ground state would be that of periodically arranged electrons forming a Wigner crystal [10].

Now we are in a better position to understand the issue of interactions in graphene monolayers. In the following, I will try to sketch the state of the art of the field, emphasizing the case of undoped graphene samples, where the subtleties coming from the Dirac point are amplified. This will not preclude an analysis of the experimentally relevant case of doped samples, where a Fermi surface does exist and therefore most of what we have analyzed so far is expected to hold.

5.2 Undoped graphene

As it was explained in Chapter 1, a graphene sample is undoped when the Fermi level located at the Dirac point, therefore leaving the upper cone empty and the lower one full of electrons, the latter constituting the Dirac sea. This particular level of doping is extremely peculiar, since only here the density of states strictly vanishes, rendering the system quite ineffective to screen interactions. It is a matter of lack of excitations. In ordinary Fermi liquids, there are many degenerated low-energy excitations around the Fermi surface. But in graphene there is a single point, only a few excitations are available to respond to interactions or external probes, and therefore it might happen that the Coulomb potential remains essentially unaltered. If this were the case, in fact any perturbative treatment of interactions would be futile, and the nature of elementary excitations around the Dirac point, or even the stability of this point itself, could be strikingly affected, drawing the system to a very different regime to that of the non-interacting system.

The answer to the issues just risen essentially belongs to the theoretical realm. This is due to the difficulties to reach the Dirac point in real experiments, since it seems that in every experiment performed so far there is always a certain degree of doping[2], usually having an uncertainty on the electron or hole densities that ranges around $n \sim 10^{11} - 10^{12} cm^{-2}$. One of the main sources of uncertainty would be the formation of charge instabilities or puddles in real samples [104]. As mentioned in Chapter 1, theoretical calculations suggest that they might originate from the presence of charge impurities in the environment [105]. The question, of course, is to what extent the low-energy regime of graphene samples, whose excitations typically have long wavelengths by definition, becomes influenced by these puddles of finite size. In other words, we expect that below a certain energy scale, graphene excitations no longer feel the effects of these inhomogeneities, though it could happen that current experiments cannot resolve such small scales.

There are, yet, other reasons to explain the absence of a pure Dirac point behavior besides the level of doping. It could also happen that interactions become screened by the response of some agents present within the environment in which real graphene samples live, in the form of phonons from the substrate, charge impurities, or even water molecules. We will have the opportunity to address this issue in more detail in next chapter, since it is one of the topics covered in this thesis.

Once briefly explained the situation from an experimental point of view, let me move again to theoretical issues. The Hamiltonian for this *Dirac liquid* consists of the free Dirac Hamiltonian plus the Coulomb interaction. If we restrain ourselves to a single valley and neglect the spin degree-of-freedom [3], the Hamiltonian reads:

$$\mathcal{H} = v_F \sum_{\mathbf{k}} \begin{pmatrix} a_{\mathbf{k}}^\dagger & b_{\mathbf{k}}^\dagger \end{pmatrix} \begin{pmatrix} 0 & k_x + ik_y \\ k_x - ik_y & 0 \end{pmatrix} \begin{pmatrix} a_{\mathbf{k}} \\ b_{\mathbf{k}} \end{pmatrix} + \frac{1}{2} \sum_{\mathbf{q}} v(\mathbf{q}) n(\mathbf{q}) n(-\mathbf{q}) \tag{5.11}$$

The first term corresponda to free Dirac fermions, and was analyzed with some detail in Chapter 1. The interaction term, in this basis, has the same form as the one in the conventional electron liquid.

[2] Moreover, the actual level of doping must be estimated from related measurements, hence increasing the uncertainty on this quantity.

[3] At low-energies, interactions do not mix electrons from different valleys, and in the absence of an external magnetic field, the spin degree-of-freedom translates simply into an extra degeneracy.

What differs is the actual expression for the density operators, reading $n(\mathbf{q}) = \sum_{\mathbf{k}} \left(a^{\dagger}_{\mathbf{k}+\mathbf{q}} a_{\mathbf{k}} + b^{\dagger}_{\mathbf{k}+\mathbf{q}} b_{\mathbf{k}} \right)$. The Coulomb potential in two-dimensions is given by $v(\mathbf{q}) = \frac{2\pi e^2}{\kappa q}$, with κ being the dielectric constant of the environment. A dimensionless coupling constant can be introduced by rescaling the whole equation by $\hbar v_F$ (notice that in general, $\hbar = 1$). This defines the following dimensionless *fine structure constant*, in analogy to Quantum Electrodynamics:

$$g \equiv \frac{e^2}{\kappa \hbar v_F} \tag{5.12}$$

If graphene samples live in vacuum, $\kappa = 1$, and $g \simeq 2.16$.

The Hamiltonian just introduced is valid up to a certain ultraviolet cutoff Λ_E, that defines the region where the low-energy description of graphene in terms of Dirac fermions holds.

Weak-coupling analysis

An early analysis of this interaction in the weak coupling regime was already carried out in the nineties [189, 190]. By means of a Renormalization Group analysis of the Hamiltonian, the flow of the dimensionless coupling constant g was derived, yielding:

$$\frac{dg}{d\log\Lambda} = -\frac{g^2}{4} \tag{5.13}$$

This flow equation entails clearly the existence of an infrared fixed point at $g = 0$, which can be proved to be stable. Notice that this result is somehow peculiar, since an analysis of the independent flows corresponding to the electron charge and the Fermi velocity v_F reveals that the latter is the one that rules the flowing, since the electron charge remains unaltered. High-energy degrees-of-freedom tend to renormalize the Fermi velocity to larger values, whose value is in principle unbounded down to low energy scales. Of course, physically this quantity cannot surpass the velocity of light, something that can be rigorously derived by introducing explicitly the photon in the model [189]. In principle, however, this is not expected to be necessary, since the size of the sample should provide us with an infrared cutoff for the flows before this point is remotely reached.

The dispersion relation of the quasiparticles near this fixed point acquires a logarithmic correction due to the residual interactions:

$$\epsilon(p) \sim p + \frac{g}{4} p \log \frac{\Lambda}{p} \tag{5.14}$$

a result that can be found by computing the Hartree correction to the self-energy in graphene. This correction is similar to that predicted in the context of carbon nanotubes [192], where a natural cutoff is given by the radius of the cylinder. Remarkably, this has been measured experimentally [191], as shown in Fig. 5.5.

The RG study shows that the Coulomb interaction is marginally irrelevant, hence flowing to zero in the low-energy regime. The result applies for weak couplings of the model, being still compatible with a different strong-coupling behavior, as I will discuss later. Besides, in order to go into more depth in the comparison with the Fermi liquid, the lifetime of the effective quasiparticles in graphene can be studied, finding a different dependence on the energy [193]. In Fermi liquids it goes like

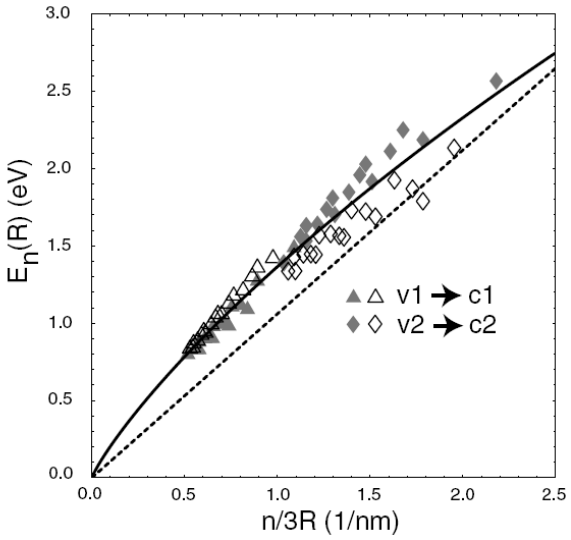

Figure 5.5: Electronic dispersion relation for semiconducting carbon nanotubes, obtained by studying optical transitions in their first subbands E_n, where n is the subband index, as a function of the rescaled radius $n/3R$. The experimental data corresponds to [191]. The dashed line is the theoretical prediction from the non-interacting theory. The continuous one incorporates the logarithmic corrections resulting from Coulomb interactions. Figure taken from [192].

$\tau(E) \propto (E - E_F)^{-2}$, but in graphene it reads $\tau(E) \propto E^{-1}$. In the literature, this has been related to the so-called marginal Fermi Liquid, where a similar dependence of the lifetime on energy does occur. However, the analogy is not complete, and low-energy graphene electrons can be considered as a particular class of interacting electrons, termed in some references as *Dirac liquid*.

Notice that I have introduced the term *graphene quasiparticle*, in analogy with Fermi Liquids. There is not, however, a satisfactory mapping between both systems, since Landau's theory does not hold for undoped graphene. First, because as mentioned there is not a Fermi surface to perform a low-energy expansion. Nevertheless, RG predicts a low-energy spectrum resembling that of electron-hole excitations. Being these strongly interacting through Coulomb, only by invoking a concept similar to that of quasiparticles we are in condition to explain such a result. In the last section, we saw that quasiparticles can be understood from a microscopic picture in which the electron gas screens the interactions. In graphene, however, such a picture has not been sufficiently established so far, mainly due to the failure of the main approximation supporting the Fermi Liquid analysis, i.e., the RPA approximation. However, we already count with interesting suggestions in the literature.

A microscopic analysis might shed some light on this issue. The spectrum of excitations of a weakly coupled theory can be analyzed, as we learnt from the last section, by analyzing the electronic susceptibility, related straightforwardly to the bubble polarization diagram. For non-interacting Dirac electrons, the latter reads [189, 193]:

$$\chi_0(\mathbf{q}, \omega) = -\frac{g_s g_v}{16} \frac{q^2}{\sqrt{v_F^2 q^2 - \omega^2}} \tag{5.15}$$

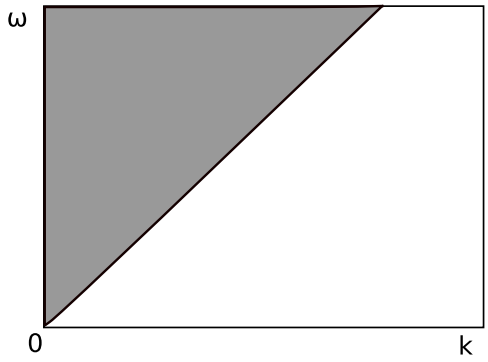

Figure 5.6: Sketch of $\Im\chi_0(\mathbf{k},\omega)$ for undoped graphene, in the plane $\omega - k$. The grey area represents the interband electron-hole excitations.

where g_s and g_v are the spin and valley degeneration, respectively. Actually, in order to study excitations, the relevant quantity is its imaginary part, because it contains information about the sources of dissipation in the system, which are in turn the excitations that couple to any external probe. Strictly speaking, the imaginary part of the electronic susceptibility describes excitations that couple to external charge fluctuations through density-density interactions. Other excitations could be left out of this description, but for our purposes this is sufficient. The imaginary part of Eq. (5.15) follows trivially:

$$\Im\chi_0(\mathbf{q},\omega) = -\frac{g_s g_v}{16}\frac{q^2}{\sqrt{\omega^2 - v_F^2 q^2}}\Theta(\omega - v_F q) \tag{5.16}$$

Non-zero solutions of this function are plotted in Fig. 5.6. Notice the important differences with respect to the ordinary system of electrons, plotted in the last section: in the infrared limit, $\omega \to 0$, the particle-hole excitations, which always involve promoting an electron from one band to the other (*interband transitions*), have very little phase space available. Let us now include the interactions by using the RPA approximation [193]. Again by analyzing the imaginary part of the susceptibility, information can be gained about excitations described within this approach[4]:

$$\Im\chi_{RPA}(\mathbf{q},\omega) = -\frac{g_s g_v}{16}\frac{q^2\sqrt{\omega^2 - v_F^2 q^2}}{\omega^2 - (v_F q)^2 + (\frac{\pi g}{2})^2 (v_F q)^2} \tag{5.18}$$

Remarkably, the RPA resummation does not change the free-electron picture. This can be rooted to the poor capabilities of undoped graphene electrons to screen interactions, at least within this approximation. The resulting screened potential given by RPA preserves the long-range tail typical of Coulomb,

[4]This form of the polarization is only valid for energies much smaller than the high energy cutoff of the theory, Λ_E. In the whole regime the real part is known to be nonzero, by virtue of the Kramers - Krönig relation [194]:

$$\Re\chi_0(\mathbf{q},\omega) = \frac{2}{\pi}\text{P.P}\int_0^{\Lambda}\frac{d\omega'\omega'}{\omega'^2 - \omega^2}\Im\chi_0(\mathbf{q},\omega') =$$
$$= \frac{g_s g_v}{\pi 16}\frac{q^2}{\sqrt{\omega^2 - (v_F q)^2}}\log\left[\frac{\sqrt{\Lambda_E^2 - (v_F q)^2} + \sqrt{\omega^2 - (v_F q)^2}}{\sqrt{\Lambda_E^2 - (v_F q)^2} - \sqrt{\omega^2 - (v_F q)^2}}\right] \tag{5.17}$$

However, this difference only turns out to be relevant for energies close to the cutoff.

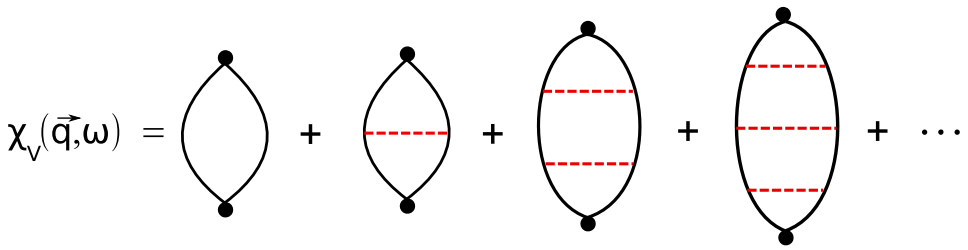

Figure 5.7: Sketch of the ladder resummation for the calculation of the polarizability in undoped graphene.

and only accounts for a reduction of the effective dielectric constant of the media, something that immediately follows from analyzing the static screening or Thomas-Fermi limit:

$$v_{eff}(\mathbf{q}) = \frac{2\pi e^2}{\epsilon(1+\frac{\pi g}{2})q} \tag{5.19}$$

As it was discussed in the last section, the RPA resummation can be seen both as an (exact) way to reorganize the perturbative expansion, or additionally as an approximation on its own, where only a subset of diagrams (the bubble resummation) is retained in the calculations. In the case of Fermi liquids, the RPA approximation suffices to describe the high-density regime of the model. However, in undoped graphene this seems no longer to be the case, something that has led to some controversy in the literature [195, 196].

The idea is that in undoped graphene, some non-RPA diagrams are of the same order of magnitude as the RPA ones, and therefore the RPA approximation becomes eventually uncontrollable when higher order corrections in g are included in the calculation. Strictly speaking, RPA only would suffice in the limit of a large number of fermion species, N_f (in graphene, there are four, two for the spin and two for the valley, therefore technically RPA does not hold[5]). Close to the threshold $\omega \simeq v_F q$, a more rigorous analysis yields that another subclass of diagrams is crucial, the so-called ladder diagrams, which can be also resummated to give an interaction corrected bubble polarization, as shown in Fig. 5.7:

$$\chi_V(q,\omega) = -\frac{q}{v_F g}\frac{1+\frac{2}{\pi}\arcsin(x)-(1+\frac{2}{\pi}x)\sqrt{(1-x^2)}}{\log(\frac{v_F q}{|v_F q-\omega|})x\sqrt{(1-x^2)}} \tag{5.20}$$

Here, we have defined $x = \frac{g}{2\sqrt{2}}\sqrt{\frac{v_F q}{v_F q-\omega}}\ln(\frac{v_F q}{|v_F q-\omega|})$. This new bubble polarization can be used to replace the non-interacting one on the RPA resummation, yielding a new susceptibility [196]:

$$\chi(q,\omega) = \frac{\chi_V(q,\omega)}{1-v_q\chi_V(q,\omega)} \tag{5.21}$$

The imaginary part of this function is shown in Fig. 5.8, together with the other susceptibilities analyzed so far for undoped graphene. The most striking feature of this susceptibility is the new threshold of excitations that appears under $\omega = v_F q$. Due to the Coulomb interaction, electron-hole pairs reduce their energy, giving rise to excitons. The new lower threshold for excitations is hence no

[5]However, this is also controversial, and the actual number of species from which RPA is acceptable still represents an issue.

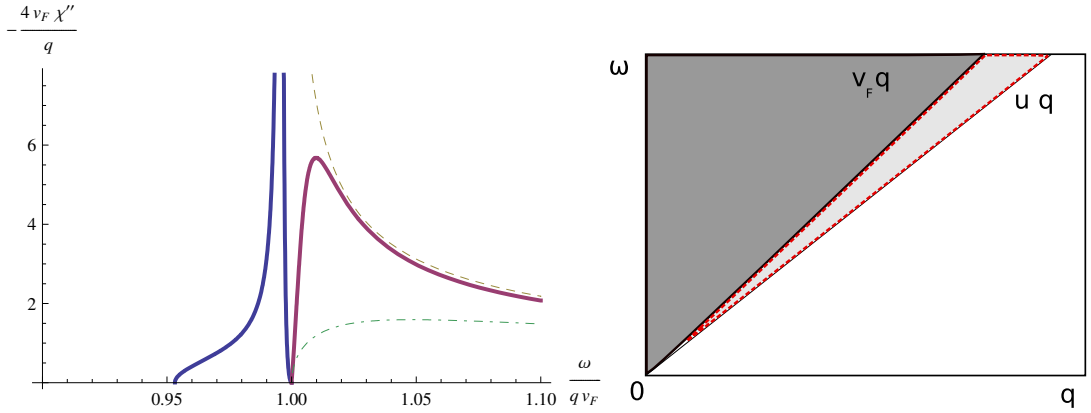

Figure 5.8: Imaginary part of the susceptibility function for undoped graphene close to the resonance. Left: plot of the different approximations, for $g = 0.2$. The thick solid line shows the total susceptibility, with both bubble and ladder resummations. The dashed-dotted line is the RPA approximation. The dashed line corresponds to the non interacting susceptibility. Right: sketch of this function, in the $\omega - q$ plane, for the RPA case and the ladder resummation, whose most prominent feature is to lower the threshold for excitations to uq

longer $\omega = v_F q$, but a new one determined through the condition $x = 1$, that can be shown to be linear, with a *renormalized* Fermi velocity that we will call u. This is quite remarkable. In the weak-coupling regime, we might state that due to the existence of Coulomb interactions electron and holes can bind together, becoming the lowest energy excitations available in the system. However, this does not open up a gap in the spectrum of excitations, being therefore compatible with the RG fixed point of free-electrons. Residual interactions would give rise to particular excitations, different from those of the Fermi Liquid, since they are not necessarily short ranged. In my opinion, however, this picture still demands further research to clarify many of its peculiar aspects.

There are more interesting features coming from this new susceptibility, mostly when the new region of excitations is analyzed. There, a prominent peak is observed, where the real part of the susceptibility becomes positive, being related to a damped collective mode. As the interaction strength is increased, the threshold is pulled downwards, at the same time that the collective mode becomes less damped. In the limit $g \gg 1$ the latter gets stable, and its dispersion relation can be derived analytically: $\omega_q = v_F q(1 - e^{-N_f})$. Notice that, for those strong interactions, the contribution from excitons is negligible. Unfortunately, as happens in many situations, for intermediate couplings, precisely those where real graphene samples are expected to lie, the threshold goes beyond the region of applicability of this susceptibility, which is only valid close to the resonance $\omega = v_F q$. For those values of the parameters a more detailed study should be performed. Being non-perturbative, however, it will require the use of different approaches, as I will discuss in Section 5.4.

Of course, there is the question of to what extent do we expect that these excitations leave some imprint in the experiments. This will be discussed below. However, let me anticipate that so far this is not the case, and there are several reasons, some of them pointed out in the following chapters, to reckon that they will be difficult to isolate in an experimental context.

Conductivity and interactions

In real experiments, the observable that is most often proved is the conductivity, so it is natural to inquire which are the corrections that interactions induce on it. There is actually a simple relation between the susceptibility and the conductivity, namely:

$$\sigma(\mathbf{q},\omega) = ie^2\frac{\omega}{q^2}\chi(\mathbf{q},\omega) \tag{5.22}$$

Normally, experiments measure the so-called optical conductivity, which is the limit $q \to 0$ of the general expression:

$$\sigma(\omega) = \lim_{q\to 0} ie^2\frac{\omega}{q^2}\chi(\mathbf{q},\omega) \tag{5.23}$$

For instance, by plugging into this expression the non-interacting susceptibility, Eq. (5.15), we find:

$$\sigma_0(\omega) = \frac{e^2}{4} \tag{5.24}$$

The RPA approximation does not change this result, something that can be technically rooted to the fact that the optical conductivity only includes non-reducible diagrams. Therefore, in order to find corrections coming from the interactions, it is necessary to go further into the perturbative expansion. First order perturbation theory calculations have logarithmic dependencies that make diverge the result, requiring some scaling approach to conveniently reorganize the perturbative series. As we have seen, Renormalization Group approach predicts that the effective coupling constant depends on energy, and it tends to zero in the low-energy regime. This means that any interaction in the weak-coupling regime is essentially residual. Hence, it should be possible to do perturbation theory in the renormalized coupling constant, yielding the following correction to the conductivity [197]:

$$\sigma(\omega) = \sigma_0\left(1 + \frac{Cg}{1+\frac{g}{4}\log\Lambda_E/\omega}\right) \tag{5.25}$$

where Λ_E is the ultraviolet energy cutoff. The constant C depends on the actual calculation, the diagrams included and the cutoff procedure, and its value is still controversial [197–199]. Theoretical predictions render values around $C \sim 0.01$ [197] and $C \sim 0.5$ [198].

Experimental evidences

As it has already been pointed out, experimental evidences align always in the direction of assigning a minor role to electron-electron interactions in graphene physics. However, it is fair to say that experiments might not be reaching the Dirac point, as I discussed before, not to mention that the environment could be producing some external screening of the interactions. The question, however, is from which level of doping one expects to find a physical behavior related to the Dirac point. This question has not been answered theoretically so far.

The experimental observations are in agreement with the theoretical predictions as long as graphene samples are in the weak-coupling regime, in a RG sense[6]. As we have seen, in this regime interactions are marginally irrelevant and therefore they are not expected to account for a large effect on

[6]Which is compatible with real graphene samples with non-perturbative couplings. Actually, results using DFT techniques [200] seem to explain the experimental results in [104] by using intermediate values of the coupling, i.e., $g \sim 0.5 - 2$.

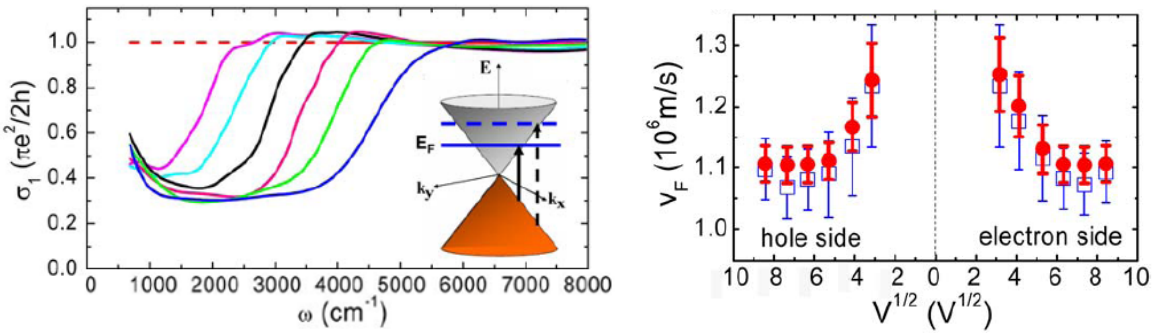

Figure 5.9: Left: optical conductivity measured by infrared spectrography, in doped samples. Despite the doping, the technique succeeds to prove the infrared spectrum, finding a residual background. Right: Fermi velocity renormalization extracted from the optical conductivity measurements. Both images correspond to the experiment in [203].

the low-energy physics. In the last section, however, we learnt that the underlying microscopic mechanism supporting this picture requires a more detailed analysis, since the picture in terms of barely interacting quasiparticles is not completely satisfactory, and other excitations like excitons could be playing a role. It is important to notice at this point that, as we will see later, this does not necessarily apply for the strong-coupling regime of the model, where interactions could even change the nature of the ground state of the system. Were this the case, then the reason why experiments show a weak-coupling behavior should be clarified. Two explanations can in principle be suggested. As mentioned, it could simply happen that so far, the environment is strongly screening interactions, drawing the effective coupling constant to a value below which the critical coupling marks the onset of a new phase. If this is the case, improving the isolation of experiments should finally lead to the observation of a prominent role of interactions in the system. However, it might also be that this critical coupling, if it exists, is above the coupling constant predicted for graphene electrons in vacuum. In this case, still theoretical calculations should shed light on the validity of the weak-coupling regime for already strong couplings like those of graphene in vacuum, but a new phase would no longer be expected.

Nevertheless, even in the weak-coupling scenario, interactions are supposed to give measurable (though not certainly leading) corrections to the observables proved in the experiments. Summarizing, we expect a renormalization of the Fermi velocity changing the slope of the Dirac point [189], an anomalous behavior of the quasiparticles life-time [190], a correction to the conductivity [197, 201], and excitonic/plasmonic excitations under the threshold $\omega = v_F q$ [196]. There is also a proposal to explain the behavior of the optical conductivity for doped graphene in terms of an ansatz inspired by marginal Fermi liquid behavior [202].

Corrections to the Fermi velocity have been reported in some experiments. In [92], graphene over SiC was studied by ARPES techniques, showing a band renormalization that was associated with interactions (though most of the effect seems to be explained by interactions with phonons).

In [203], graphene on top of SiO_2 was proved by using infrared spectrography, obtaining the optical conductivity for doped samples. Interestingly, by using this technique, excitations in the infrared

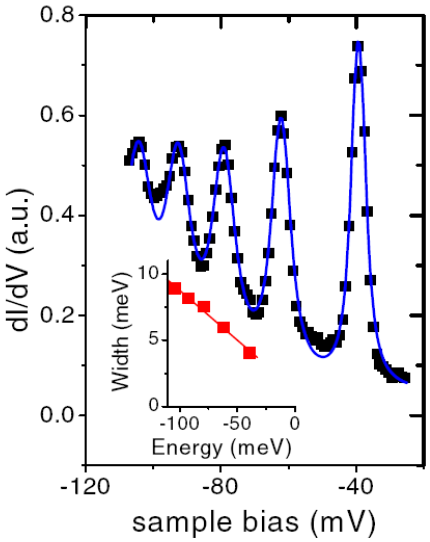

Figure 5.10: Inverse quasiparticle lifetime measured from Landau levels broadening in graphene, in the presence of a magnetic field. The results are well fitted by a linear law, in agreement with a marginal Fermi liquid behavior.

$\omega \to 0$ region of the spectrum can be proved, so the results could be affected by the physics at the Dirac point. Particularly, as shown in Fig. 5.9, in the interval $0 < \omega < 2E_F$, a residual conductivity was measured. Various explanations have been proposed that could partly justify this result: clearly, the effect of charged impurities [204] produces a similar background, though there is room enough for other explanations, like those invoking unitary scatterers (edge effects, cracks,...). In [202], the background was roughly fitted by using a phenomenological model of Dirac quasiparticles whose inverse lifetime is linear in the energy, as expected near the Dirac point according to RG calculations. Of course, why such an ansatz apparently work requires further research, since a linear dependence on energy of the lifetime is only expected to work in the low-energy regime close to the Dirac point, and there are other external mechanism that also render this behavior. Infrared spectrography also serves to analyze the corrections to the Fermi velocity (Fig. 5.9, right), that apparently shows a dependence on the energy scale.

A call for awareness must be done here. Corrections to the Fermi velocity are not directly measurable from the experiments, and its actual magnitude depends somehow on the way it is extrapolated from real data. However, all the approaches in which corrections have been reported agree at least on finding an enhancement of this quantity in the experiment, with respect to the theoretical value predicted for non-interacting Dirac electrons.

Another result ascribed to electron interactions was obtained in [205], for graphene samples weakly coupled to bulk graphite, where single graphene physics is also expected to be dominant. The measurements were done by using Scanning Tunneling Spectroscopy, a technique that allows to obtain the local density of states of the sample. In the presence of a magnetic field, Landau Levels are formed, with a characteristic broadening that can be associated to the finite life-time of quasiparticles. The

results are well fitted to a law $1/\tau_n = a|E_n| + b$, where n is the Landau Level index. Despite of this result also being expected from electron-phonon interactions, it still survives below the typical scales associated to phonon excitations. Therefore it could be a signature of electron-electron interactions in graphene.

Finally, in [206], the optical conductivity of suspended graphene samples was measured, finding an almost perfect agreement with the expected result for non-interacting Dirac fermions, i.e., $\sigma(\omega) = \sigma_0 = e^2/4$. The actual experimental value is $\sigma/\sigma_0 = 1.01 \pm 0.04$, which is even smaller than the minimum value theoretically predicted.

5.3 Doped graphene

When the graphene sample is doped, say, by filling the upper band with electrons (alternatively, holes can be created in the lower band), the behavior of the system changes abruptly: now it has a Fermi surface, and a new kind of excitations arises, the *intraband* electron-hole excitations, that dominate the spectrum at low energies. The *interband* excitations are suppressed, for now the energy threshold to excite them is $2E_F$ in the limit $q \to 0$ (see Fig. 5.11). As usually, the geography of the excitations can be inspected through the study of the electronic susceptibility. In Fig. 5.11 (left), a plot of the imaginary part of this function is given for a non-interacting doped graphene, where interband and intraband excitations are clearly demarcated. The analytical expression of this function was obtained independently in [207–209]. In the long wave-length limit, it has the following form:

$$\Im\chi_0^{doped}(\mathbf{q},\omega) = \begin{cases} -\frac{g_s g_v}{16}\frac{q^2}{\omega}, & \omega > 2E_F \\ 0, & v_F q < \omega < 2E_F \\ -\frac{g_S g_v k_F}{2\pi v_F}\frac{\omega}{\sqrt{v_F^2 q^2 - \omega^2}}, & \omega < v_F q \end{cases} \tag{5.26}$$

where $E_F = v_F k_F$, and $k_F = (4\pi n/g_s g_v)^{1/2}$, being n the electronic density in the upper cone.

Since the low-energy behavior of doped graphene samples is dominated by the intraband excitations, that have a well-defined Fermi surface, Landau's picture of barely interacting quasiparticles and screened interactions is expected to hold. In fact, from a microscopic point of view, the RPA approximation becomes again a good description of the underlying physics. Intraband excitations do have good screening properties, and the Coulomb interaction becomes effectively weak and short-ranged. In the case of doped graphene, the RPA approximation is expected to be exact in the limit $g \ll 1$, and whenever $v_F q$, $\omega \ll E_F$, i.e., in the long wavelength regime. An analysis of the electron self-energy yields a stable expansion around the Fermi surface, with quasiparticles stable at this point and with a finite lifetime nearby, that goes as $\tau(E) \propto (E - E_F)^{-2}$, like in a Fermi liquid. Yet, there is an issue concerning the crossover between doped and undoped, or those observables that have contributions from excitations with energies that do not lie in the aforementioned range of $\omega \ll E_F$. RPA is not supposed to hold in this range, since also contributions from the lower cone start to imbricate the behavior of the system. Theoretically, this region has not been addressed satisfactorily, something quite notorious regarding that it is the one experimentally more relevant.

The technicalities of the RPA approximation can also be analyzed in terms of the susceptibility,

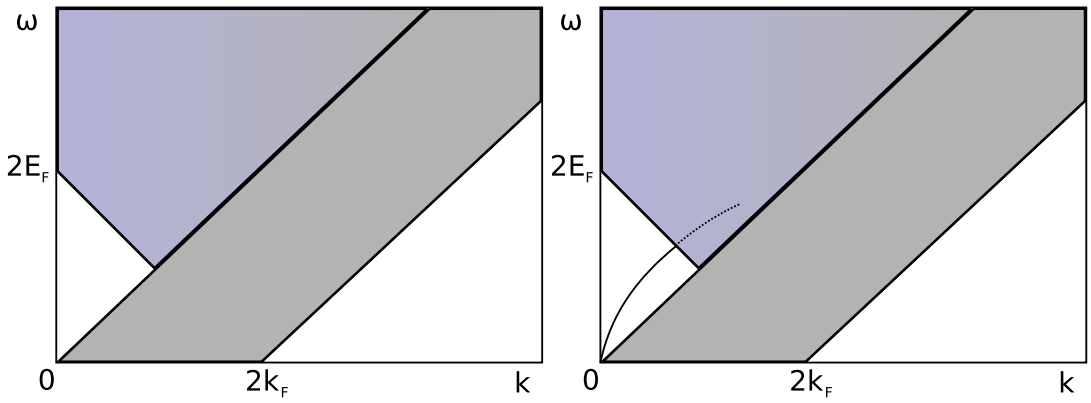

Figure 5.11: Imaginary part of the susceptibility function for doped graphene. Left: non-interacting case, where the effect of doping translates into new *intraband* excitations, and the suppression of the *interband* excitations. Right: RPA susceptibility, predicting the existence of a plasmon (collective) mode, apart from the particle-hole background.

whose expression is given by [208, 209]:

$$\Im\chi^{doped}_{RPA}(\mathbf{q},\omega) = \begin{cases} -\frac{g_S g_v}{16}\frac{q^2}{\omega}, & \omega > 2E_F \\ -\frac{\omega_0^3}{4e^2}\frac{q^{5/2}}{\omega^2}[1-\frac{\omega^2}{4E_F^2}]\delta(\omega-\omega_0 q^{1/2}), & v_F q < \omega < 2E_F \\ -\frac{2\omega}{\pi g_s g_v e^4 E_F}\sqrt{v_F^2 q^2-\omega^2}, & \omega < v_F q \end{cases} \tag{5.27}$$

in the limit $v_F q \ll gE_F$. Here, $\omega_0 = (g_s g_v e^2 E_F/2)^{1/2}$ is the plasma frequency for graphene. Its most prominent novel feature is a well-defined (undamped) plasmon mode in the region of prohibited interband excitations. The dispersion relation of this plasmon is given by $\omega = \omega_0 q^{1/2}$, which has the same q-dependence as the 2D electron gas[7]. Besides, the intraband and interband particle-hole excitations remain in the dissipative spectra.

Regarding screening, the static regime of the RPA approximation is enough to provide us with an analytic expression for the screened interaction, that is similar to the one found in the Fermi liquid, but with a Thomas-Fermi screening length given by [81]:

$$\lambda_{TF} \simeq \frac{1}{4g}\frac{1}{\sqrt{\pi n}} \tag{5.28}$$

which clearly shows that the description breaks down in the limit of zero density in the upper cone, $n \to 0$, since the screening length diverges, and the Coulomb potential preserves its long range tail.

The experimental consequences of interactions in doped graphene have been addressed by many authors. All the experiments mentioned in the previous section have in fact been performed in doped graphene samples, although I tended to emphasize the information that might have implications for undoped samples. The fact that doped graphene behaves like a Fermi liquid can be considered well established experimentally. The research in that direction concerns mostly the detection of signatures

[7] As opposed to the density dependence of the plasma frequency: in graphene, it goes like $\omega_0 \propto n^{1/4}$, while in the conventional 2DEG is $\omega_0 \propto n^{1/2}$.

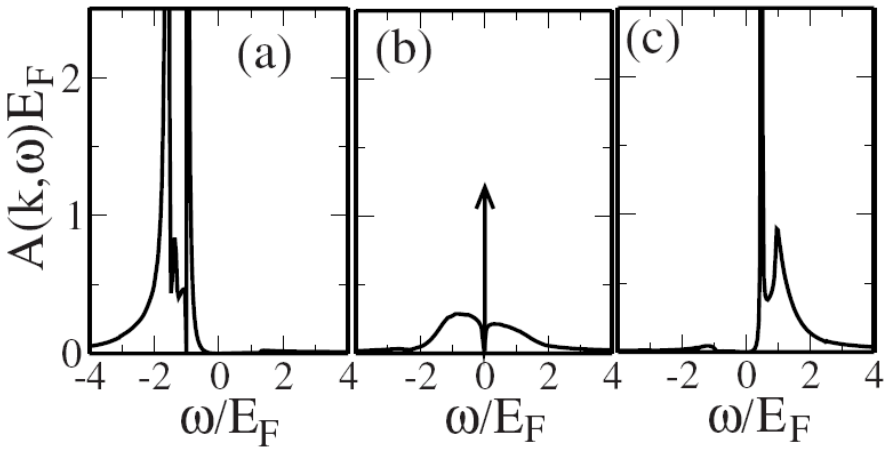

Figure 5.12: Plot of the spectral function for doped graphene, when interactions are included within the RPA approximation. The plots show the dependence with respect to the frequency in units of the Fermi energy. Three values of k are chosen: a) $k = 0$, b) $k = k_F$ and c) $k = 1.5k_F$. For $k \neq k_F$, a two-peak structure reflects the existence of the quasiparticle and the plasmon. The figure belongs to [211].

of the collective modes (plasmons), that could be detected in ARPES experiments [92]. By using this approach, the so called spectral function can be calculated [210, 211], namely:

$$A(\mathbf{q},\omega) \equiv \frac{2\Im\Sigma(\mathbf{q},\omega)}{[\omega - \epsilon_{\mathbf{q}} - \Re\Sigma(\mathbf{q},\omega)]^2 + [\Im\Sigma(\mathbf{q},\omega)]^2} \tag{5.29}$$

which is interesting in order to resolve the different excitations, as it fulfills a sum-rule:

$$\int (d\omega/2\pi) A(\mathbf{q},\omega) = 1 \tag{5.30}$$

Particularly, a signature of the Fermi liquid is the presence of a peak in this function corresponding to the quasiparticles, which has the form $A \sim 2\pi Z\delta(\omega - \tilde{\epsilon}_{\mathbf{q}}) + A_{in}(\omega)$, where Z is the renormalization constant introduced in the first section, and A_{in} is an incoherent background that contains the rest of the excitations. The integrated spectral weight of the delta function gives a contribution of Z for the quasiparticle, so the incoherent part contributes in $1 - Z$ to the sum-rule. As mentioned, in Fermi liquids typical values of Z range between 0.7 and 0.8.

The theoretical calculations of $A(\mathbf{k},\omega)$ including electron-electron interactions in RPA show, for $k \neq k_F$, a two-peak structure that reflects the existence of quasiparticle and plasmon excitations (Fig. 5.12). The quasiparticle peak is broadened, something that can be related to the finite quasiparticle lifetime. For $k = k_F$ there is only one well defined sharp quasiparticle peak, since at the Fermi surface quasiparticles are stable ($\tau \to \infty$). Besides these features, the figure clearly shows the existence of an incoherent background.

When addressing the experimental data [92], a theoretical fitting turns out to be complicated, since the spectral function gets contributions from other interactions, like disorder or electron-phonon interactions. Actually, one of its most pronounced features is the presence of a kink at $200meV$ below

the Fermi level, related to the coupling to graphene phonons [212]. Once this feature is subtracted, the agreement between theory and experiment is reasonable, supporting the validity of the RPA description in doped graphene, as well as the plasmon excitation it predicts.

The study of electron-electron interactions can be extended to the case of non-zero magnetic fields, where collective excitations have been predicted theoretically, the so-called magnetoplasmons [213].

5.4 Strong coupling phases in undoped graphene

So far, I have limited the discussion to the weak-coupling regime of graphene, i.e., strictly to the region $g \ll 1$. However, by using RG arguments, the results can be expected to be valid for a wider range of couplings, as far as the low-energy weak-coupling fixed point still dominates the flow. Of course, RG calculations are also perturbative in g, and nothing assures us that this is necessary true for the whole range of g. Therefore the results explained so far are fully compatible with the existence of another fixed-point in the strong-coupling regime. This is particularly relevant regarding that the theoretical coupling constant predicted for a perfect graphene in vacuum is $g \simeq 2.16$, a value that clearly falls into the strong-coupling regime. Is the weak-coupling fixed-point the one that dominates the low-energy physics when we start from this non-perturbative coupling? Or is there a different phase, probably insulating, in which low-energy electrons arrange? These are questions that are drawing a considerable attention in the present days.

Strong coupling problems, however, are of great difficulty, as most of the techniques that we know rely on some expansion in a perturbative parameter[8]. This is, as I mentioned, what happens with RG calculations, whose main assistance is usually providing us with a different perturbative parameter (the renormalized coupling, in those cases in which the flow leads to a perturbative regime). When the RG flow increases the coupling constant with which we are doing perturbation theory, it must be considered as a signature of the existence of another fixed point. RG calculations are in this case blind when trying to determine the location of this fixed point, and usually the most we can obtain is the scale from which the calculation becomes non-perturbative.

As far as I understand the field, in this case there are various possible ways to explore the non-perturbative regime:

- Resort to numerical techniques, that in general do not require of a perturbative parameter. For instance, the NRG that I described in the last part of this section, that however only applies for quantum impurity problems, or Monte Carlo calculations, performed in a discretized (*lattice*) version of the Hamiltonian.

- Try to find a mapping of the Hamiltonian to another one where perturbative calculations become possible. Usually this mapping requires finding new degrees-of-freedom, that are not necessarily the ones in which the original theory is expressed. We have seen several examples along this thesis, like for instance the Luttinger liquid, or the sine-Gordon model for $\alpha^2 \simeq 1$, that can be written in terms of the Thirring model. In the first example, a Hamiltonian for fermions

[8] During my career, I remember to have been repeatedly told that in order to do modern Physics there was only one indispensable requirement: mastering Taylor expansions.

with some interactions is fully diagonalized in terms of bosons, not demanding any further approximation. In the second example, the sine-Gordon model at $\alpha^2 = 1$, the same applies but in the reversed direction: a complicated bosonic Hamiltonian becomes diagonalized when translated to the language of fermions. Around this point, residual interactions come along, for which a perturbative treatment is possible. Of course, whenever a model has an exact solution, and this is known, then *a priori* there is no need of doing perturbative calculations (though, as I mentioned before, it can happen that calculations of certain observables turn out to be very difficult when using the exact solution).

- Calculate higher orders in perturbation theory of the RG flow equations. If it happens that a second fixed point arises for a certain (non-perturbative) g^*, it can be a signature of the existence of a different strong coupling regime. Obviously, since calculations are still based on perturbation theory, such a result cannot be completely trusted until it gets complemented by other approaches.

- Find a consistent mean field that reduces the problem to a single-body one. Mean field approximations are a good starting point to study a many-body problem, though they usually must be refined in turn if quantum correlations are important, since they are generally missed. The usual approach is to carry out the solution of the single-particle mean-field Hamiltonian, and use the solution to obtain an expression of some observable that characterizes the mean field. Self-consistent equations are then obtained, that determine the final values of the observables defining the mean field.

- Propose a variational ansatz for, say, the wave-function, that captures the relevant physics in the strong-coupling regime. It is interesting that this ansatz covers the weak-coupling regime in some limit of the variational parameters. This way the weak-coupling ground state can be ruled out whenever there are other solutions with lower energies. Variational calculations can somehow be seen as a sophisticated mean field.

- Find another perturbative parameter, different from the coupling constant. An example of this was analyzed when addressing the sine-Gordon model with the Flow Equations technique, that allow us to identify a different perturbative parameter in which strong-coupling regime was included. Another typical example is the number of species of particles in the system. Its inverse, $1/N_f$, has been extensively used in a variety of situations to carry out perturbative calculations.

Many of these approaches have been found useful to study the strong coupling regime of graphene monolayers. A final picture of the phase diagram is still under debate, though most of the results seem to coincide in the existence of a phase transition above a certain critical coupling, in which graphene becomes insulating by opening up a gap in its excitation spectrum. It is interesting to point out that this was in fact the expected behavior for graphene according to early studies of the honeycomb lattice [88]. If this phase transition is determined to exist, still the nature of the actual ground state in graphene samples requires a more extensive analysis. After all, Coulomb interactions

could make the system unstable, but the final picture might be strongly influenced by the presence of other interactions (short range, disorder,...).

The Renormalization Group picture

As I mentioned above, Renormalization Group calculations in the weak coupling phase explain the minor role that electron-electron interactions play in the low-energy regime of the model, being a marginally irrelevant interaction. Several attempts of extending these results can be found in the literature [214, 198, 215].

One of the most suggesting approaches is that of doing calculations for a large number N_f of fermion species in graphene. In this case, expansions do not rely anymore on the dimensionless coupling constant g, but on the inverse of the number of species, $1/N_f$. In [214], such a study was performed, finding in the asymptotic limit $1/N_f \to 0$ that there are two RG fixed points, an infrared stable one at $g = 0$ and an ultraviolet unstable one, at $g = \infty$. Exactly at the strong-coupling fixed point, the RG equation for the velocity reads:

$$\frac{dv(\Lambda)}{d\log\Lambda} = -\frac{4}{\pi^2 N_f} v(\Lambda) \tag{5.31}$$

which has immediate consequences on the expected dispersion relation of quasiparticles, since it acquires the form of a scaling law, namely:

$$\omega \propto p^{1-4/(\pi^2 N_f)+\mathcal{O}(N_f^{-2})} \tag{5.32}$$

For a finite coupling constant g, however, the system is driven towards the infrared fixed point, where the dispersion relation has a logarithmic correction, as it was shown in the previous sections. However, still a crossover behavior should be expected from the RG flow, with the high-energy regime being dominated by the strong-coupling fixed point, where observables would show scaling relations of the form given in Eq. (5.32).

In the case of real graphene samples, $N_f = 4$, and this RG analysis does not strictly apply. Therefore, conjectures must be formulated to sketch a global picture. In [214], the author suggests two scenarios that have been depicted in Fig. 5.13. In the first one, the results would hold for any arbitrary number of fermionic species, N_f, and hence there would be no strong-coupling stable fixed point in graphene. Nevertheless, as mentioned, some signatures of strong coupling behavior could be found in the high-energy regime of certain observables. In the second scenario,a strong-coupling stable fixed point would exist below a critical number of fermionic species, N_c, and above a critical coupling g_c, as shown in the figure. The nature of this phase cannot be inferred from the $1/N_f$ analysis, but any strong-coupling consistent theory should predict a critical number of fermionic species above which this phase does no longer exist.

On general grounds, a second possibility to study the strong-coupling behavior from the RG point of view is to compute higher orders of the weak-coupling expansion, with the hope of finding signatures of a different fixed-point. This task has been performed in [201], following the well-known analysis given in [95], since in this work also the effect of disorder was addressed, as I will briefly

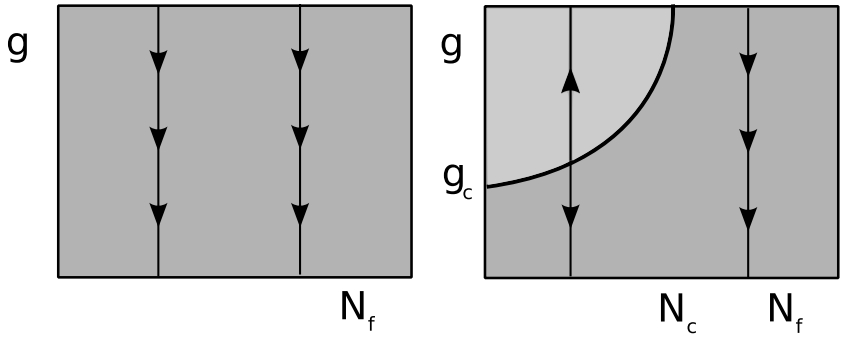

Figure 5.13: Conjectured phase diagram for a system of N_f species of Dirac fermions interacting through the Coulomb potential, whose strength is g. Left: Suggested scenario in which no strong-coupling phase exists, and the RG flow always leads to the $g = 0$ fixed point. Right: Another possible situation is that in which there is a strong coupling phase below a critical number of species N_c, and above a critical coupling g_c. Both phase diagrams are compatible with the results found in the weak-coupling RG analysis and the large N_f one.

comment later. For the moment I will describe solely the effect of Coulomb interactions. At second order in the perturbative expansion, the flow equation for the dimensionless coupling reads:

$$\frac{dg(\Lambda)}{d\log\Lambda} = -\frac{g^2}{4} + \mathcal{C}g^3 \tag{5.33}$$

where the actual value of $\mathcal{C}$ depends on the number of fermionic species:

$$\mathcal{C} = \frac{N_f}{12} - \frac{103}{96} + \frac{3}{2}\log 2 \tag{5.34}$$

If this coefficient is positive, something that happens for any nonzero integer N_f, then there is a second fixed point. For graphene, where $N_f = 4$, the predicted critical coupling is $g_c = 1/4\mathcal{C} \simeq 0.833$, which already falls into the strong coupling regime of the model. Therefore, as mentioned, the confidence on this result relies on further calculations. However, the message to gain from this calculation is that $N_f = 4$ would be already below the critical number of species (and also, of course, that there is a stable strong-coupling phase). The fixed point at g_c is unstable, since for $g < g_c$ the coupling flows to weak-coupling ($g = 0$), while for $g > g_c$ it flows to strong-coupling ($g = \infty$). The nature of the strong-coupling phase is again not determined within the RG calculation, and as mentioned in [201], it might depend on the nature of the lattice (the honeycomb lattice) and the presence of other interactions (short-range, disorder).

The latter has been addressed in different works, where the flow of the Coulomb interaction is studied in the presence of other interactions. For instance, quartic short-range couplings in the Hamiltonian are irrelevant for $N_f = 4$ in the RG sense, at least near the weak-coupling fixed point. But its role could be different close to the strong-coupling fixed point, something that would influence the nature of the strong-coupling phase. For the $1/N_f$ expansion, this scenario has been studied in [216], where it was found for the strong-coupling case, $g = \infty$, that there is a critical N_f below which these quartic interactions become relevant. Such a picture has been confirmed in the context of the weak-

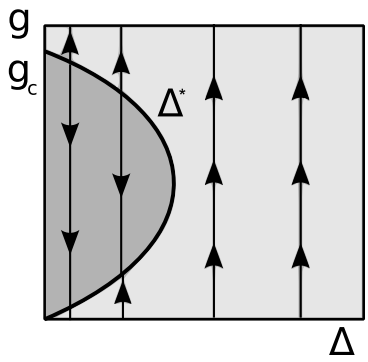

Figure 5.14: Phase diagram for interacting graphene electrons in the presence of disorder. For weak strength of interaction g and disorder Δ, there is a line of stable infrared fixed-points. For large enough disorder, the line becomes unstable, and separates the weak-coupling phase from the strong-coupling one.

coupling analysis, when quartic interactions are considered[9], finding that for finite g and large N_f, the Coulomb interaction is still marginally irrelevant, but there is a critical point (the Gross - Neveu one) that demarcates a region in which short-range interactions become relevant.

The effect of disorder in the Coulomb interacting Dirac system was already addressed in a different physical context in [95]. Its actual effect in graphene has been the subject of several works lately [217, 218, 201, 215]. For small disorder and interaction coupling, there is a general agreement on the existence of a line of stable infrared fixed points $\Delta^*(g)$, where Δ parametrizes the disorder. However, in [201] was shown that this picture changes when second order corrections to the RG expansion are computed. The new contributions not only alter the physics of the clean system, as was explained above, but also the disordered one, giving rise to a line of unstable fixed points that separate the strong-coupling from the weak-coupling behavior. According to this work, for strong enough Coulomb interactions, disorder will lower the critical coupling g_c, enhancing the phase transition.

An excitonic condensate

Now let me move to the question of the nature of this speculated strong-coupling phase. This information cannot directly be inferred from RG calculations alone. The main candidate is undoubtedly the excitonic condensate, in which electrons and holes would become bounded through the (now attractive) Coulomb interaction, giving rise to composed particles called excitons. Such a condensation has been studied extensively in the context of semiconductors [219]. In undoped graphene, the formation of excitons would occur close to the Dirac point, presumably opening a gap in the electronic density of states and rendering the system insulating at low energies. Since strong electron-electron interactions are the ones responsible for the suppression of current flow through the system, sometimes this phase is referred to in the literature as a Mott-insulator.

The nature of the phase transition has been discussed in several works, but remains an open debate up to today. Recent numerical calculations, where the continuous model of graphene was studied by

[9] Dirac fermions with short-range quartic interactions are described by a Gross-Neveu-like Hamiltonian

using Monte Carlo methods in the lattice [220–222], point out to a second order phase transition with a *chiral* symmetry breaking. Let me emphasize, in this regard, that strictly speaking, in 2D the use of the term *chirality* is incorrect, since the real symmetry is discrete, and therefore related to the *helicity* of graphene bispinors. Such a symmetry, in the discrete model, arises from the equivalence between the two sublattices in which the honeycomb lattice can be decomposed. Therefore we see how the nature of the phase transition could be influenced by details of the problem that are irrelevant in an RG sense in the low-energy regime. As pointed out in [201], this does not only happen for the underlying lattice structure, but also could apply for short-range interactions and disorder.

Let me be slightly more specific in this argumentation. If only spinless fermions with Coulomb interactions are regarded, it is expected to find a charge density wave (CDW), that unbalances the charge population between both sublattices. But adding the spin degree-of-freedom, the ground state would likely show antiferromagnetic ordering, i.e., it would be a spin density wave (SDW), with unequal spin population in the two sublattices. Moreover, disorder and short-range interactions could also change this picture, and the final ground state requires a more extensive analysis.

In the Monte Carlo calculations mentioned above, other useful information about the phase transition was reported. Studies on different models agree in the existence of a phase transition in the strong coupling regime, though they differ in the actual critical couplings. In [220, 221], the authors studied a lattice gauge theory of 2+1 fermions interacting through three-dimensional potentials. On the one hand, within this model they find a critical coupling $g_c^{MC} = 1.11 \pm 0.06$[10]. On the other hand, a study in terms of the number of fermion species was consistent with the RG results for large N_f, since they found that the phase transition disappears up to a critical value ranging between $8 < N_c < 12$[11]. In [223] Monte Carlo calculations were performed on a fully two-dimensional model, similar to the Thirring, in which the long-range tail of the Coulomb interaction is supposed not to be well described, although according to the authors this fact should not change radically the global picture. For $N_f = 4$, they found a critical value of $g_C^{Th} = 1.66$. Hence, according to both numerical calculations, real graphene samples in vacuum should be insulating. That this has not been observed, as mentioned several times, could be a consequence either of the presence of a polarizable environment, or because there are extra ingredients that current theoretical calculations are missing. Of course, it also might happen that the actual gap is too small to be resolved with current experimental techniques.

The excitonic condensate has been explored in more detail in [224, 225], by studying the gap equation for excitonic formation within the Dyson-Schwinger formalism. The non-zero solutions of this gap equation determine the existence of an stable excitonic phase. The general form, at zero temperature, for the self-consistent gap equation reads:

$$\Delta_p = \int \frac{d^2\mathbf{k}}{8\pi^2} \frac{1}{\sqrt{v_f^2 p^2 + \Delta_p^2}} \frac{\Delta_k}{|\mathbf{k} - \vec{p}|/(g v_f) + N_f \chi(0, \mathbf{k} - \vec{p})} \tag{5.35}$$

where Δ_p is the momentum dependent gap (do not confuse it with the disorder parameter that was introduced in other context), and $\chi(0, \mathbf{k} - \vec{p})$ is the interacting polarization. Notice that this gap

[10] Remember that, for graphene in vacuum, we have $g \simeq 2.16$, while on top of SiO_2, $g \simeq 0.79$

[11] Beware that in the literature, sometimes Hamiltonians are written for quadri-spinors, but they can also be found for bi-spinors. Hence, the critical number of fermionic species is, in the latter, twice the number given in the former.

equation holds for an arbitrary number of fermionic species N_f, that together with the dimensionless coupling g (and the ultraviolet cutoff Λ, that will be kept fixed), set the parameters that determine the phase-diagram.

In [225], the so-called *bifurcation approximation* was employed to solve the gap equation. In this approximation, the term Δ_p^2 in the squared root of the denominator is neglected, and its effect is reduced to provide an infrared cutoff, given by Δ_0/v_f. By combining this approximation with a large N_f expansion, the integral equation can be seen to be equivalent to a differential equation:

$$p^2\frac{d^2\Delta_p}{dp^2}+2p\frac{d\Delta_p}{dp}+\frac{4}{\pi N_f}\Delta_p=0 \tag{5.36}$$

supplemented with the boundary conditions $p^2 d\Delta/dp|_{p=\Delta_0/v_F}=0$ and $\Delta_p+pd\Delta_p/dp|_{p=\Lambda}=0$. This equation has non-trivial solutions only below the critical line:

$$g_c=\frac{8}{16-\pi N_f} \tag{5.37}$$

For graphene, $N_f=4$, $g_c\sim 2.32$. Moreover, it gives a maximum number of fermionic species for which there is an excitonic condensate, $N_c\sim 5$. Plugging this number into the coupling expression yields $g_c=\infty$, and any number above it leads to $g_c<0$, an no phase transition is predicted.

This is in contrast with the analysis done in [224], that was recently refined in [226]. In the latter, a remarkable critical value of $g_c=1.13$ was found for $N_f=4$, as well as a critical number of fermionic species of $N_c\simeq 7.18$. This result is supported by a numerical solution of the gap equation presented in [227], giving $N_c\sim 7$ for the critical number of fermionic species. In this work, it was also pointed out that disorder and finite temperatures may strongly suppress the phase transition, while the presence of quartic short-range interactions would act in the other direction, helping to preserve it. Finally, a recent analysis of the gap equation reported in [228] yields the value $g_c=0.92$ for $N_f=4$. The presence of such a variety of results should convince the reader of the difficulties encoded in the technicalities of the problem.

Regarding the nature of the phase transition, the analysis of the gap equation seems to suggest that it is a transition of infinite order, i.e., of Kosterlitz-Thouless kind. This fact is based on the behavior of the zero momentum gap, $\Delta_0\propto exp(-2\pi/\sqrt{N_c/N_f-1})$, as a function of the number of fermionic species [224].

Finally, let me mention that the formation of excitons can also be addressed without treating the whole many-body problem. In the study of the Coulomb impurity problem in graphene [229–231], a remarkable instability of the wave-function occurs above a critical coupling $g_c=0.5$. The single-body problem becomes ill-defined above this coupling, and many-body effects arising from the *Dirac sea breakdown* are expected to play a role. In these works, and other recently posted [232, 233], such an instability has been related to the possible formation of excitons, though the microscopic picture behind this statement still demands a more rigorous analysis. In this thesis I will show that this feature is still present in the two-body electronic problem in graphene, that cannot exactly be mapped to the Coulomb impurity problem. An analysis of the instabilities for the case of a pair of Coulomb interacting Dirac electrons with zero center-of-mass momentum yields a critical coupling of $g_c=1$, that is remarkably close to the many-body predictions.

Other strong-coupling phases

As we have seen, the firmest candidate for the strong-coupling behavior of graphene is the excitonic condensate. This happens somehow because the other sensible scenarios have already been ruled out theoretically, since it was found that graphene does not fulfill the necessary requirements for its existence. This is the case, for instance, of the Wigner crystal. In absence of an external magnetic field, in [234] was shown that a state in which electrons localize in a lattice is not possible even when Coulomb interactions are strong, because the kinetic energy is always comparable to the potential energy, destabilizing the crystal.

Another tested scenario is that of a ferromagnetic instability in clean graphene samples [235]. Such a phase would arise due to exchange interactions between Coulomb interacting Dirac fermions. For undoped graphene, the balance between kinetic energy and exchange energy can be worked out analytically, giving a condition for the ferromagnetic phase to exist, in terms of the strength of the Coulomb interaction, that reads: $g > g_c \simeq 5.3$. As for graphene in vacuum $g \simeq 2.16$, such a strongly correlated phase is not expected to be found in real experiments.

6 Interactions between graphene layers and their environment

Be careful the environment you choose for it will shape you;
be careful the friends you choose for you will become like them.
W. Clement Stone

Summary

In this chapter I will describe my research concerning the interactions between graphene layers and the different agents present in the environment of real experiments. The interactions studied are of electrostatic nature, most of them falling into the category of van der Waals forces. In this regard, I must emphasize that interactions involving chemical bounds will not be discussed. First section gives an overview of the current knowledge about the composition and main features of the elements present in SiO_2 substrates, the ones analyzed throughout this chapter. Second section addresses the issue of screening of electron-electron interactions by these elements, something that should complement some of the discussions from the last chapter. In the third section I will derive analytic expressions for the electrostatic interactions, which are the main results of this chapter. Four section analyzes the results, discussing some relevant consequences for graphene experiments. Finally, the last section contains the main conclusions of the chapter. The work described here is published in Ref. [236], and was done in collaboration with A. H. Castro Neto, S. Fratini and C. Seoanez.

6.1 Introduction: Graphene and the environment

I have devoted part of the general introduction, and an entire extra chapter, to depict the amazing electronic and structural properties of graphene. Particularly, from the point of view of interactions, we have learnt that undoped graphene is likely to show a rich phase diagram, with a quantum phase transition from conducting to insulating behavior. However, most of the interesting phenomena underlying graphene physics has remained so far experimentally unaccessible, and although the intrinsic behavior of this material must be yet clarified (in order to know what to expect), there is general consensus about the necessity of reducing the influence of the experimental environment in order to get a better understanding of its novel features.

Graphene is a genuinely two-dimensional material, something that translates into a complete exposition to the elements present in the surroundings. This is in contrast to three-dimensional materials,

in which there exist a bulk essentially uncoupled from surface phenomena, and hence from most of the interactions with the environment. Nevertheless, it is interesting to remark that such an exposure of graphene also involve some advantages, since it allows us to use the huge variety of surface physics techniques (STM, AFM,...) that are known to be useless to explore bulk three-dimensional materials.

As I mentioned in the introduction, the environment in which graphene is embedded depends mostly on the way this material is produced. For mechanically exfoliated graphene, it is deposited on top of a substrate of SiO_2, that later can be partially removed to held the graphene suspended. For epitaxially grown graphene, the substrate is made of SiC, though there are a few layers of carbon in between. Graphene can also be studied from bulk graphite, if the outer layers are sufficiently decoupled as to get a genuinely two-dimensional behavior. Every environment shows its own peculiarities, that must be understood in order to improve the degree of isolation of the experimental samples, by removing the most disrupting elements. Moreover, whenever this task can not be accomplished, knowledge of the actual effect of the environment in the measurements is still useful in order to isolate intrinsic graphene effects directly from the data, as it is usually done in experimental techniques like STM and ARPES.

In this chapter I will concentrate on SiO_2 substrates, where a majority of graphene experiments have been carried out. Some of the results can be easily exported to other substrates, though some others are very particular to this environment. The reason for which SiO_2 has become so popular can be rooted to the large degrees of isolation of graphene samples that provides us with, having the present record on the number of intrinsic phenomena reported. However, the fact that it is deposited and not grown implies that some chemically active agents present in the environment could be trapped at the interface between graphene and substrate. For instance, the presence of trapped ions and water molecules is something generally accepted, and those can interact directly with graphene, sometimes even chemically saturating its p_z orbitals. But once again, wisely you can make enemies become friends, and the exposition of graphene to chemicals is opening a new field of research that brings the promise of extra degrees of tuning the properties of this material, like opening a gap in its electronic spectrum. An example of this is the recently synthesized *graphane* [237], where the electronic p_z orbitals are saturated with hydrogen atoms.

Let me analyze a typical experiment composed of a mechanically exfoliated graphene deposited on top of a SiO_2 substrate. Figure 6.1 shows a sketch of the different polarizable elements present in the environment. These are:

- **Ambient species like** H_2O**,** N**,** O**, and** Ar. When the experiments are not performed in ultrahigh vacuum conditions, the presence of ambient species is something well known among the community of Surface Science scientists. Graphene is not an exception. There are already experimental evidences pointing out the existence of these chemical species, that would become trapped at the interface between graphene and the substrate in the process of deposition. In [101], the atomic structure of graphene on SiO_2 was analyzed by using STM and AFM techniques, in both ambient and ultrahigh vacuum conditions. Remarkably, it was found that AFM measurements of the distance between graphene and the substrate varies from 0.9 nm in air and 0.4 in vacuum, suggesting a significant presence of ambient species at the interface. In [238] the

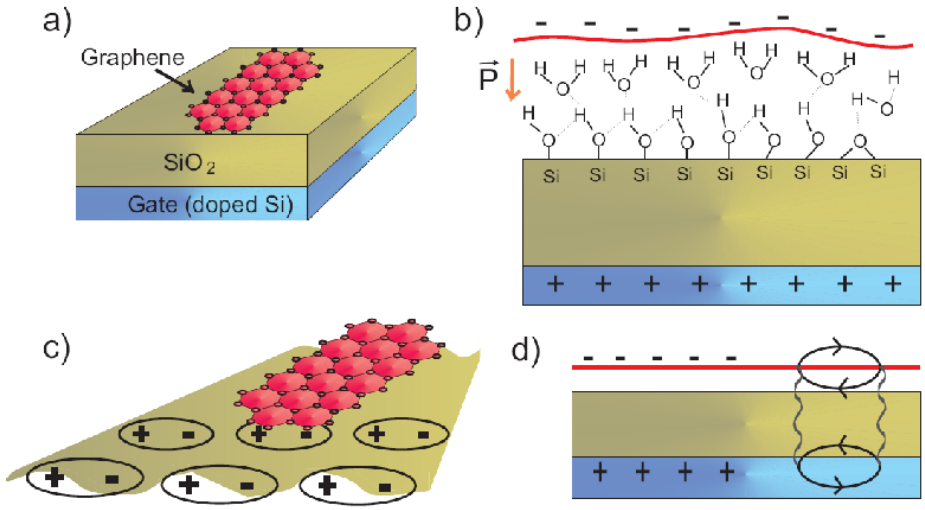

Figure 6.1: Sketch of a typical experimental setup regarding graphene over SiO_2. a) The substrate is composed of 300 nm layer of SiO_2, insulating, grown from a metallic gate made of heavily doped Si. The distance between graphene and SiO_2 is around 1 nm. b) Being graphene deposited, water molecules can get trapped at the interface with the SiO_2. c) The insulating SiO_2 has still a non-negligible polarizability, whose main contribution comes from the excitation of surface polar modes. d) Some charges can also get trapped within the SiO_2 layer. e) The metallic gate is another polarizable element, in this case due to the excitation of electron-hole pairs, that couple to graphene. Figure taken from [236].

adsorbation of gaseous chemicals by graphene was studied in a controlled way, showing that in fact graphene is so sensitive to its presence that it could serve as a single molecule chemical detector. Recently, it has been pointed out that molecules of air trapped between graphene and SiO_2 are an important source of backscattering for graphene electrons, and could explain the origin of electron-hole puddles [239].

Specially important should be the presence of water molecules. Water interacts with the SiO_2 surface, and it is known to form a layer of silanol groups ($SiOH$) [240], with a typical density of about $5 \times 10^{14} cm^{-2}$, unless extra steps like thermal annealing in ultrahigh vacuum are taken during the fabrication process [241]. Silanol sites are active centers for water absorption, so SiO_2 surface becomes usually hydrated under normal conditions, and several layers of water molecules could be formed between the SiO_2 surface and graphene after its deposition. An analogous situation has been shown to happen in experiments with carbon nanotubes deposited on SiO_2 [242]. For graphene experiments, this scenario is sketched in Fig. 6.1, b).

- **Charged impurities trapped within the SiO_2 layer**. This is likely the most discussed issue concerning the influence of SiO_2 on the properties of graphene. As I mentioned in the introduction, they have been invoked to explain many experimental observations, like the density dependence of the conductivity and the formation of electron-hole puddles. The presence of these charges belongs to the common wisdom in the field of Semiconductor Physics. In ref.

[243], several mechanisms are invoked for the existence of trapped impurities: (i) accumulated charges at the interface between SiO_2 and Si, with an origin mostly due to the interruption of the periodic lattice structure, (ii) mobile ionic charges, related to trace contamination by alkali metal ions, with effective densities around $10^{10} cm^{-2}$, (iii) oxide traps associated with defects in SiO_2, usually neutral, but that can become charged by introducing electron and holes into the oxide, (iv) dopant impurities (B, P, As or Sb) left withing the oxide layer during the process of oxygen diffusion when the SiO_2 is grown.

Unfortunately, it is not easy to find reliable quantitative estimations for the density of these charges in typical graphene experiments. By fitting the experimental data on graphene samples by using models of trapped impurity charges, the typical densities that are extracted range around $10^{10} - 10^{12} cm^{-2}$ [244, 245]. These numbers are of the order of magnitude of the ones employed in semiconductor physics. The net effect of these charges is an inhomogeneous and fluctuating electric field near the surface of SiO_2 [246].

- **Dielectric response of** SiO_2. A charge near the surface of SiO_2 generates a response from this dielectric due to its non-negligible polarizability. The latter have two components, an electric one and another associated with the displacement of the ions. Once again, this has been known for years in the field of Semiconductor Physics, where these issues are of major importance when studying Si MOSFETS. The overall response seems to be dominated by collective modes of the ions at the surface, i.e., surface phonons [247], and particularly its optical branch, that has been invoked to explain the behavior of the mobility in graphene samples at room temperature [248]. The surface polar modes of SiO_2 are already well characterized in the laboratory, something that supposes a real advantage to get reliable tests on the influence of these modes in graphene physics. This is in contrast, as I mentioned, to the effects of other active elements present in the environment (water, charged impurities...), that in general lack of independent studies for their characterization. This situation, however, is changing nowadays [246, 239].

- **Charge fluctuations in the** Si **gate**. To produce the field effect in graphene, a potential is applied between the metallic Si gate below the layer of SiO_2 and the graphene sample. Its net effect is a reorganization of the charge between both systems, changing the level of doping and generating a constant electric field, as happens in capacitors. Si is an insulator, and in order to render it metallic it must be heavily doped. In commercial samples, this is something standard, with well controlled doping densities. In the case of a p-doped gate, a typical impurity concentration is of the order of $10^{15} cm^{-3}$. Once the potential difference is established, it is a good approximation to consider that the charge is concentrated at the Si/SiO_2 interface, due to the capacitor effect.

  The interaction with graphene samples is a consequence of the charge density fluctuations around the equilibrium configuration. These can have either a thermal or a quantum origin, being persistent at $T = 0$. Charge fluctuations are likely to occur in both graphene bands and metallic Si, generating dipole-dipole interactions. The effect of charge fluctuations from the gate in mesoscopic systems is not a fully developed field yet, though studies in connection with quantum dots [142, 249] and quantum wires [250, 251] have been performed. Gates could

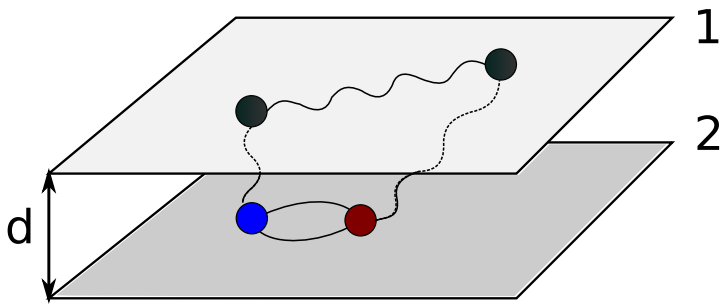

Figure 6.2: Sketch of the screening of interactions in a system of a couple of two-dimensional layers, separated a distance d.

induce important changes in electronic properties, like their lifetimes, dispersion relation, and even produce dissipative quantum phase transitions.

In this chapter of the thesis I will analyze extensively some of the expected consequences that interactions with the environment may have. Of course, many experimental and theoretical studies have already addressed this issue, helping to clarify the experimental data collected so far. To give just a quick overview, graphene seems to be stuck to the substrate, since its corrugation in non-suspended samples follows the geographic profile of the SiO_2 layer underneath [101]. Electron-hole puddles were measured in graphene samples [104], and most of the explanations point out to the environment as the major cause, either due to the trapped charge impurities [105, 200] or the ambient species trapped between graphene and the substrate [239]. The role that charge impurities might play in conductivity experiments has been discussed extensively in the introduction, and I will not repeat it here. Density Functional Theory calculations seem to suggest that water does not significantly change the band structure of graphene, when adsorbated [252]. However, as I already mentioned, graphene is extremely sensitive to the presence of molecules or atoms over it [238]. Polar modes of SiO_2 might explain the room temperature behavior of the mobility [248]. The latter could also induce spin-relaxation phenomena, as pointed out in [253]. Experiments performed on graphene nano electro mechanical systems (NEMSs) indicate that the substrate induces significant stresses in a few layer graphene samples [254]. Moreover, the interaction between graphene and the substrate determines the frequency of the out of plane (flexural) vibrations, which also might influence transport measurements [255].

Of course, one of the most relevant effects of the environment concerning graphene physics is the screening of the electron-electron interactions. Being this in relation to the topics studied in this thesis, I will discuss it briefly in the next section.

6.2 Screening of electron-electron interactions by the environment

.

Let me address for a moment the general problem of two polarizable systems in interaction. In our case, one is a graphene sample, and the other an element of the environment. The response of

these systems is described by the susceptibilities χ_1 and χ_2. The standard approach is to consider an external charge placed, for instance, upon system 1 (graphene). It produces an external potential v_i^{ext}. For simplicity, I will consider two planar systems at a distance d, which are translationally invariant along the plane directions, as sketched in Fig. 6.2. The linear response of a system to an external potential is an induced charge given by $\rho_i^{ind} = \chi_i v_i^{tot}$, where $v_i^{tot} = v_i^{ext} + v_i^{ind}$ and $v_1^{ext} = v_q = 4\pi e^2/q$ and $v_2^{ext} = e^{-qd} v_q$. The electrons within each of the systems interact via Coulomb, v_q, as well. This yields the following system of equations:

$$\begin{aligned} v_1^{tot} &= v_1^{ext} + v_1^{ind} = v_1^{ext} + v_q \chi_1 v_1^{tot} + v_q e^{-qd} \chi_2 v_2^{tot} \\ v_2^{tot} &= v_2^{ext} + v_2^{ind} = v_2^{ext} + v_q \chi_2 v_2^{tot} + v_q e^{-qd} \chi_1 v_1^{tot} \end{aligned} \tag{6.1}$$

In order to get the the total potential exerted to the electrons of these systems, we need to invert the matrix:

$$\begin{pmatrix} v_1^{tot} \\ v_2^{tot} \end{pmatrix} = \frac{1}{(1 - v_q\chi_1)(1 - v_q\chi_2) - v_q^2 e^{-2qd}\chi_1\chi_2} \begin{pmatrix} 1 - v_q\chi_2 & v_q e^{-qd}\chi_2 \\ v_q e^{-qd}\chi_1 & 1 - v_q\chi_1 \end{pmatrix} \begin{pmatrix} v_1^{ext} \\ v_2^{ext} \end{pmatrix} \tag{6.2}$$

Since we are mainly interested in the screened potential within the graphene layer, and the external potential is that created by an electric charge, we have:

$$v_q^{ren} = \frac{1 - v_q\chi_E + v_q e^{-2qd}\chi_E}{(1 - v_q\chi_G)(1 - v_q\chi_E) - v_q^2 e^{-2qd}\chi_G\chi_E} v_q \tag{6.3}$$

where G stands for graphene and S for the environment. So far, I have sketched the general case for the renormalized interaction in linear response. In practice, considering graphene and its environment, the following approximations work reasonably well:

- The environment is composed of non-interacting particles, and hence the terms $v_q\chi_2$ can be neglected from Eq. (6.2).
- We work in the regime $qd \ll 1$.

In this case, we recover the typical expression:

$$v_q^{ren} = \frac{v_q}{1 - v_q(\chi_S + \chi_E)} = \frac{v_q}{\epsilon_{ave}(\vec{q}, \omega)} \tag{6.4}$$

where $\epsilon_{ave} \equiv= \frac{1}{2}(\epsilon_G + \epsilon_S)$ is the averaged dielectric constant for graphene and environment, being $\epsilon_i = 1 - v_q\chi_i$, as usual. For the dielectric elements of the environment, typically this is well approximated by a static dielectric constant, and hence the interaction keeps its Coulomb pole and its long-range tail.

6.3 Electrostatic interactions between graphene layers and its environment

There is a second important effect due to the coupling to the environment. As mentioned, some experiments indicate that graphene samples are attracted to the substrate, modifying their structural properties. This is reflected, for instance, in the correlation between substrate geography and

graphene corrugations, as shown in [101], or in a change in the frequency of vibration of flexural modes of graphene [255].

We know that once graphene is deposited on top of SiO_2, they do not get chemically bounded, enabling experimentalists to study weakly coupled system. There are, however, interactions between graphene and its environment, although they are of a different nature. As it was already well understood in the case of graphite, graphene monolayers tend to bound to other graphenes, as well as other elements of the environment, via Van der Waals forces.

6.3.1 Van der Waals forces

Van der Waals forces (VdW's) have their origin in the coupling between charge fluctuations in neutral systems. If two (or more) systems are electrically polarizable, thermal and/or quantum fluctuations of charge produce electric dipoles that can become coupled, changing the ground state energy of the system. Since the strength of the interaction change with the distance, it results in a force that can be measured and quantified [256].

The typical example is that of two neutral atoms with their respective clouds of orbital electrons. In a first approximation, the system con be modellized as two polarizable spheres. Due to quantum or thermal fluctuations, both spheres have instantaneous induced dipoles d_i, that on average compensate $\langle d_i \rangle = 0$, but whose quadratic deviation is finite, $\langle d_i^2 \rangle \neq 0$. The net force is not zero due to the correlations induced between fluctuations in both spheres: the instantaneous dipole d_1 produces an electric field at the position of the other sphere of a magnitude $-d_1 R^{-3}$ (R is the separation between both spheres), inducing a dipole fluctuation of the latter due to its polarizability α_2 that reads $d_2 \propto -\alpha_2 d_1 / R^{-3}$. In turn, the latter generates a back electric field $-d_2/R^{-3}$ that affects the first sphere. The energy of this sphere, with dipolar momentum p_1, in the presence of the field is: $E \propto -\alpha_2 d_2^2 / R^{-6}$. Averaging over time, it gives an attractive non-zero net force, proportional to $\langle d_2^2 \rangle$ and decaying as:

$$E = -\frac{C_6}{R^6} \tag{6.5}$$

where C_6 is known as the Hamaker constant. Van der Waals forces are named after Johannes Diderik van der Waals, who aimed to understand the gas-to-liquid phase transition. The term includes generically all the forces that have their origin in dipole interactions. The particular case of fluctuating dipoles is usually refer to as *dispersive forces* as well.

If the systems are sufficiently weakly coupled, a microscopic derivation of van der Waals forces coming from quantum fluctuations can be obtained working out the ground state energy of the complete system in second-order perturbation theory. To exemplify it, let me consider again the situation depicted in Fig. 6.2. Two planar systems are separated a distance d, and both of them are electronic systems coupled via the Coulomb interaction:

$$v_q(d) = \frac{2\pi e^2}{\kappa q} e^{-qd} \tag{6.6}$$

where $kappa$ is the static dielectric constant, that in vacuum reads $\kappa = 1$. The lowest order contribution to the energy in perturbation theory has the following form, in terms of the susceptibilities χ_1 and χ_2

[257]:

$$E^{(2)}_{VdW} = -\sum_q \int_0^\infty \frac{d\omega}{2\pi} v_q^2(d)\chi_1(\vec{q}, i\omega)\chi_2(\vec{q}, i\omega) \tag{6.7}$$

where Matsubara imaginary time formalism has been employed, and a discrete set of momenta has been considered. Notice that, being a second order correction in perturbation theory, it is always negative in sign, yielding an attractive force:

$$F = -\frac{dE^{(2)}_{VdW}(z)}{dz}|_{z=d} \tag{6.8}$$

In general, the particular expression for this second order correction depends on the system considered, as we will see below.

Van der Waals interactions have been extensively studied in a large variety of systems. Depending on the separation between both polarizable systems, the approximation that the interaction is instantaneous might be valid or not. For long distances (how long depends on the particular system) retardation effects could be important, and then we speak of Casimir-Polder forces [65].

6.3.2 Interactions between graphene and specific environments

In this thesis, I have calculated the different van der Waals forces between graphene layers and the elements of the environment that I described in the introduction of this chapter. The order of magnitude and the distance dependence of the interacting energies can be used to rule out the less relevant elements of the environment, providing us with a criterion to analyze some of experimental results.

As already exemplified, all these interactions have been calculated by using second order perturbation theory, assuming a perfect graphene sheet so that the momentum parallel to it is conserved. The corresponding diagrams are given in Fig. 6.3. All interactions depend, at this order, linearly on the polarizability of the graphene layer. Since RPA screening in undoped graphene only changes the dielectric constant, leading to a finite correction $\pi e^2/8\hbar v_F \sim 1$ to the dielectric constant, this approximation does not change significantly the estimates obtained by using second order perturbation theory.

For the graphene layer at half filling I will use the bare susceptibility that was already extensively discussed in the introduction to this part of the thesis:

$$\chi_G(\vec{q}, i\omega) = \frac{g_v g_s}{16\hbar} \frac{q^2}{\sqrt{v_F^2 q^2 + \omega^2}}, \tag{6.9}$$

Remember that it is valid up to a cutoff in momentum $\Lambda \sim a^{-1}$ and energy $\omega_c \sim v_F \Lambda$, where a is the lattice spacing. Beyond this scale, the susceptibility has a more complicated form, and it is influenced by the trigonal warping of the bands. Since the component of the electrostatic potential induced by a system at distance z from the graphene layer with momentum $\vec{q}$ is suppressed by a factor $e^{-|\vec{q}|z}$, the integrations over $\vec{q}$ can be restricted to the region $0 \leq q = |\vec{q}| \lesssim q_{max} \sim z^{-1}$. The combination of a term proportional to $e^{-|\vec{q}|z}$ and scale invariant quantities such as the susceptibility in Eq. (7.6) leads to interaction energies which depend as a power law on z. In general, only the leading term will be considered, neglecting higher order corrections.

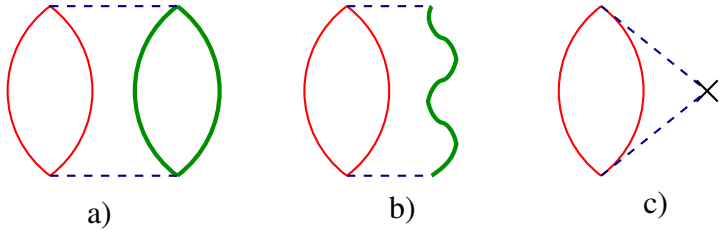

Figure 6.3: Lowest order diagrams that contribute to the interaction between: a) graphene and a metal, b) graphene and a polar dielectric, and c) graphene and a static charge distribution. The thin red bubble stands for the graphene susceptibility. The thick green bubble represents the metallic susceptibility. The wavy green line stands for the propagator of a phonon mode in the dielectric. Crosses stand for static charge distributions, and dashed lines represent the electrostatic potential. Taken from [236]

The calculation described above, which is valid for a single graphene layer at the neutrality point, can be extended to finite dopings and to systems with more than one layer. In all cases, the calculations are formally the same, and the interaction energies can be written as integrals over energies and momenta of the susceptibility of the system being considered, which replaces the susceptibility of a single layer, Eq. (7.6). The susceptibility of a doped single layer is well approximated by that of an undoped system for momenta such that $q \gtrsim k_F$ [208]. Analogously, the susceptibilities of a stack of decoupled layers of graphene and multilayered graphene become similar for $q \gtrsim t_\perp/\hbar v_F$ [258], where $t_\perp$ is the hopping in the perpendicular direction. The susceptibility of a single undoped plane of graphene is an increasing function of q, so that the integrals are dominated by the region $q \sim q_{max} \sim z^{-1}$. Hence, if $q_{max} \gg k_F$ or $q_{max} \gg t_\perp/\hbar v_F$, the interaction energies do not change appreciably from the estimates obtained for a single layer. The corrections can be obtained as an expansion in powers of either $k_F z$, or $(t_\perp z)/\hbar v_F$. The expression given by Eq. (7.6) can be considered as the lowest order expansion in these parameters. For $z \sim 1$ nm, $t_\perp \sim 0.35eV$ and carrier densities such that $n \sim 10^{10} - 10^{12}$ cm^{-2}, we have $k_F z \sim 10^{-2} - 10^{-1}$ and $t_\perp/\hbar v_F \sim 10^{-2} - 10^{-1}$. In the following, I will analyze mostly the interaction energies using the susceptibility of a single undoped layer for the graphene polarizability.

Metallic gate

The metallic gate in the experiments analyzed in this chapter is doped Si, separated from the graphene layer by a 300nm thick slab of SiO_2 dielectric. For the Si doping and voltages applied, most of the charge in the Si gate is concentrated on a layer of about 10 nm thickness [**?**], much narrower than the distance to the graphene sheet, so that the gate is effectively two dimensional. The response of such a heavily doped system can be described by the susceptibility of a dirty two dimensional electron gas:

$$\chi_{gate}(\vec{q}, i\omega) = -\frac{dn}{d\mu}\frac{Dq^2}{Dq^2 + |\omega|}, \tag{6.10}$$

where $D = v_{\mathrm{F}gate} l_{gate}$ is the diffusion coefficient of the electrons in the gate, $v_{\mathrm{F}gate}$ is the Fermi velocity, l_{gate} is the mean free path, and $dn/d\mu$ is the bare compressibility, given by the density of states at the

Fermi level (see, for instance, Ref. [142]).

The interaction between the graphene layer and the gate is given by Eq. (6.6). The lowest order contribution to the energy in perturbation theory has the form already given in Eq. (6.7):

$$E^{(2)}_{gate} = -\hbar \sum_q \int_0^\infty \frac{d\omega}{2\pi} v_q^2(z) \chi_G(\vec{q}, i\omega) \chi_{gate}(\vec{q}, i\omega)$$

For future reference, note that I am using the symbol E for energies per unit area, and $\mathcal{E}$ for total (integrated) energies. The resulting integrals can be calculated analytically in the limit $z_s \equiv D/4v_F \ll z$:

$$E^{(2)}_{gate} = -\frac{1}{12}\frac{dn}{d\mu}\frac{D}{v_F}\frac{e^4}{\kappa^2}\frac{1}{(2z)^3}\left[\log\left(\frac{z}{z_s}\right) + \frac{1}{3}\right]. \tag{6.11}$$

Notice that this dependence on $z^{-3}\log(z/z_s)$ was already obtained in [259].

Let me take, as representative parameters for the gate and the graphene layer, $D \approx 10^{-3}$ m^2/s, $v_F = 10^6$ m/s, $z = 300$ nm, $dn/d\mu \simeq g(E_F) = 0.04$ eV^{-1} Å^{-2} and $\kappa = 4$ for the SiO_2 substrate. These parameters lead to interaction energies of order $\sim 10^{-8}$ meV Å^{-2}.

Polar dielectric

We have seen that the dominant coupling to the SiO_2 is via its surface phonons. Thermal or quantum fluctuations can excite phonons, which are collective distortions of the SiO_2 surface lattice. They produce electric fields that couple to the electron-hole dipoles in graphene. The microscopic coupling has the form [143]:

$$H_I = \sum_q M_q \rho_q \left(b_q + b^\dagger_{-q}\right) \tag{6.12}$$

where ρ_q is the electron density operator and $b^\dagger_q$,b_q the creation/destruction operators for phonons. $M_q^2 = (\hbar^2 v_F^2) g e^{-2qz}/(qa)$ is the interaction matrix element, with g a dimensionless coupling constant. In SiO_2 we have two dominant phonon modes at $\hbar\Omega_1 = 59$ meV and $\hbar\Omega_2 = 155$ meV, with $g_1 = 5.4 \cdot 10^{-3}$ and $g_2 = 3.5 \cdot 10^{-2}$ respectively [248].

In perturbation theory, the lowest order contribution to the energy is given by:

$$E^{(2)}_{subs} = \sum_i \sum_{\vec{q}} \int \frac{d\omega}{2\pi} \chi_G(\vec{q}, i\omega) |M_q(z)|^2 D_i^{(0)}(\vec{q}, i\omega) \tag{6.13}$$

where I have introduced the free phonon propagators:

$$D_i^{(0)}(\vec{q}, i\omega) = -\frac{2\Omega_i}{\omega^2 + \Omega_i^2}. \tag{6.14}$$

The calculation can be again carried out analytically in the limit $z \ll l_i \equiv v_F/\Omega_i$, yielding:

$$E_{SiO_2} = -\sum_i \frac{\hbar v_F}{a}\frac{g_i}{(2z)^2}, \tag{6.15}$$

which has a z^{-2} dependence on the distance. Let me mention for completeness that in the opposite limit $z \gg l_i$, which is not the case of interest here, one obtains a $l_i z^{-3}$ dependence.

For $z \sim 1$ nm and $z \gg l_i$, this term gives interaction energies of order $E^{(2)}_{SiO_2} \sim -4 \times 10^{-1}$meV Å^{-2}.

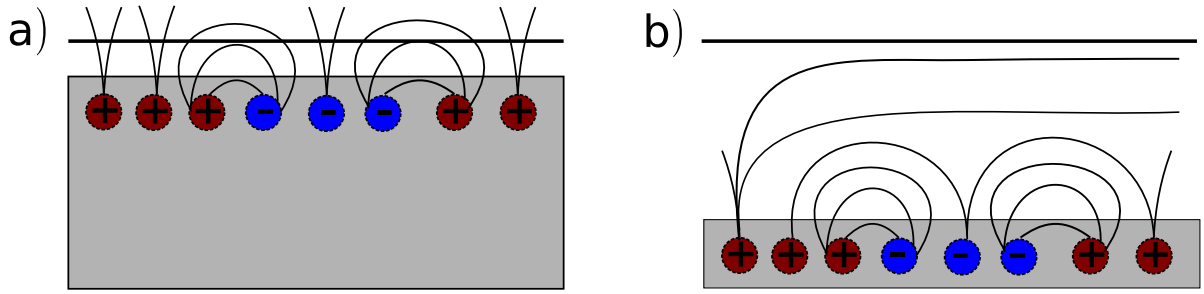

Figure 6.4: Interactions between graphene and the charges located at the SiO_2 surface. a) For non-suspended samples, the electrons feel the local field generated by the charges. b) For suspended samples, there is a compensation of the different fields, due to the neutrality of the substrate as a whole. However, fluctuations from neutrality can still give a non-zero electric field.

Charges within the substrate

In this case the calculations are done considering that effectively all the charge is concentrated close to the surface of the SiO_2 dielectric, where it is homogeneously distributed, having on average the same number of positive charges than negative charges. The interactions then depend strongly on the distance between graphene and substrate. If they are close enough (say, in samples deposited on top of SiO_2), we expect that electrons in graphene are sensitive to local electric fields created by the charges, that do not have a dipolar origin and hence are not rigorously van der Waals forces (they decays as R^{-2} instead of R^{-3}). However, for suspended samples, the electrons in graphene feel the compensated field produced by all the charges, that on average is zero. Still, one can think of the SiO_2 as a collection of macroscopic systems where on average the net charge is zero, but there are gaussian deviations around neutrality. This implies that the electric field is not completely compensated, though quite attenuated, as I will discuss later. An sketch of this situation is depicted in Fig. 6.4.

Let us consider the first case, valid for non-suspended samples. The second order correction to the energy, averaged over the charge distribution, reads:

$$E_{ch}^{(2)} = -\sum_{\vec{q}} \chi_G(\vec{q},0) v_q^2(z) n_{imp} \tag{6.16}$$

where the Coulomb interaction v_q between graphene electrons and charges is statically screened by the effective dielectric constant at the interface, $(\kappa+1)/2$. Again, this contribution can be carried out analytically:

$$E_{ch}^{(2)} = -\left(\frac{2e^2}{\kappa+1}\right)^2 \frac{\pi n_{imp}}{2\hbar v_F} \frac{1}{2z} \tag{6.17}$$

This interaction has a z^{-1} dependence, like the image potential in ordinary metals. In this case, however, such a behavior arises from the combination of a vanishing density of states and lack of screening in graphene.

Reasonable values for the impurity concentration in graphene are in the range $n_{imp} \sim 10^{10} - 10^{12}$ cm^{-2} [244, 245]. Setting $z \sim$ 1nm, typical interaction energies are of the order $E_{ch} \sim -10^{-4}$– 10^{-2}

meV Å^{-2}.

This result is not expected to hold in the case of suspended graphene. If the distance between the sample and the substrate is larger than the typical distance between charges, $d_{imp} \sim \sqrt{n_{imp}} \sim 1-10nm$, the electrons are supposed to feel the net effect of the effective charge in the substrate, which in average is zero due to the compensated number of positive and negative charges. However, as I mentioned above, if we consider a random distribution of charges, we expect gaussian fluctuations to the average, and we must perform the replacement $N_{imp} = n_{imp}l^2 \rightarrow \sqrt{n_{imp}l^2}$ in the total energy $\mathcal{E}_{ch} = E^{(2)}_{ch}l^2$, where l is the lateral sample size. The final result is that of an homogeneous sample with a reduced number of impurities contributing to the interaction, its number given by the typical deviation around the average in a gaussian distribution.

Layer of water molecules

In the introduction, many evidences were given pointing to the existence of a layer of water molecules trapped between substrate and graphene, when experiments are not performed in ultrahigh vacuum conditions. The interactions are of van der Waals type, as water molecules are neutral, but have strong electric dipoles, $p_w = 6.2 \times 10^{-30}$ C m ≈ 0.04e nm. Since typical fields applied in present experimental setups are $\mathcal{E} \sim 0.1$ V nm^{-1}, the energy of a water dipole when it is aligned with this field is 4 meV $\sim$ 50K, so that, at low temperatures, it will be oriented along the field direction, perpendicular to the substrate and the graphene layer. For this reason, in the following I will assume that the water dipoles are aligned perpendicular to the substrate and the graphene layer. This arrangement can be considered an upper bound to the interaction energy with a neutral water layer, as inhomogeneities and thermal fluctuations will induce deviations in the orientation of the dipoles, and will lower the interaction energy.

This model may not be valid for high applied electric fields, where a charging of water molecules of the order $Q_{H_2O} \sim 0.1|e|$ has been reported [242]. Such a presence of extra charges would considerably enhance the interaction between the graphene layer and the water molecules, though is not the case I will consider here (the analytical expressions, anyway, would correspond to that derived for charge impurities, but changing the corresponding density of charges).

A water molecule which is located at a distance z from the graphene layer induces an electrostatic potential:

$$\Phi(\vec{q}, z) = 2\pi p_w e^{-|\vec{q}|z} \tag{6.18}$$

This potential polarizes the graphene layer and gives rise to an interaction energy in a similar way to the static charges discussed in the preceding section. The lowest order contribution to the energy is:

$$E^{(2)}_{water} = -(ep_w)^2 \frac{\pi}{6} \frac{n_w}{\hbar v_F} \frac{1}{(2z)^3} \tag{6.19}$$

where n_w is the concentration of water molecules and the z^{-3} behavior arises from the dipolar nature of the interactions. For $z = 0.3$nm, which is the approximate thickness of a water monolayer [260, 261] the interaction energy is $E^{(2)}_{water} \sim -12n_w$ meV which, for a typical water concentration $n_w = 10^{15}$ cm^{-2}, yields $E^{(2)}_{water} \sim 1$ meV/Å^2.

The expression in Eq. (6.19) can be extended to a semi-infinite stack of water layers. For simplicity let us take a distance z between graphene and the uppermost layer of water molecules equal to the interlayer distance. In this case we obtain:

$$E^{(2)}_{water} = -(ep_w)^2 \frac{\pi}{6} \frac{n_w}{\hbar v_F} \frac{\zeta(3)}{(2z)^3} \tag{6.20}$$

where $\zeta(3) \approx 1.202$ is Riemann's zeta function. The present result indicates that the first water layer is the one that mostly contributes to the binding.

Before finishing, let me consider the case of water molecules forming an ordered array, which is also a possible scenario when modelizing the layer of water expected to be present in real experiments. If that were the case, the average in Eq. (**??**) will show peaks when the vector $\vec{q}$ coincides with a reciprocal lattice vector of the water array, $\vec{G}_i$, and it will be suppressed otherwise. Then, the dependence on distance of the interaction potential will be a sum of terms of the type $e^{-2|\vec{G}_i|z}$. The disorder in the SiO_2 substrate observed experimentally [101, 262] implies that the existence of an ordered array of water molecules is not likely.

Van der Waals interaction between graphene layers

For comparison, in this Section I will evaluate the van der Waals interaction between two graphene layers at the equilibrium distance. Using the same approximations as for the other contributions, we recover the result of [259], namely:

$$E^{(2)}_{G-G} = -\frac{\pi e^4}{16\hbar v_F} \frac{1}{(2z)^3} \tag{6.21}$$

For $z = 0.3$nm, this expression gives an interaction energy of 30 meV Å^{-2}. This estimate is similar to other experimental and theoretical values of the graphene-graphene interaction [263, 264] and is at least one order of magnitude larger than the other contributions analyzed earlier.

6.4 Analysis of the results and implications for real experiments

6.4.1 Comparison of the different interactions

Let me summarize the numerical estimates for the different interaction energies that we obtained, for reasonable values of the parameters, in the last section. These are listed in Table 6.1. The results show that the leading interactions are those between graphene and the polar modes of the SiO_2 substrate, and between graphene and a possible water layer on top of the substrate. Both effects are of similar order of magnitude regarding our approximations: remember that we have assumed that the water molecules are aligned in the direction perpendicular to the substrate, and this should provide us with only an upper bound for the energy. Although they are not explicitly shown in the table, from the interaction energies it is easy to infer the values of the Hamaker constants, C^i_H, since they are given by the coefficient in the law $E_i = C^i_H z^{-\alpha_i}$, being α_i the corresponding exponent that rules the speed of decay of the interaction with the distance z.

	Distance (nm)	Dependence on distance	Energy (meV Å^{-2})
Gate	300	$z^{-3}\log(z/z_s)$	10^{-8}
Charged impurities	1	z^{-1}	$10^{-4} - 10^{-2}$
SiO_2 substrate	1	z^{-2}	0.4
Water molecules	0.3	z^{-3}	1
Graphene	0.3	z^{-3}	30

Table 6.1: Interaction energy per unit area for the mechanisms studied in this chapter. For the numerical estimates typical concentrations of $10^{10} - 10^{12}$cm^{-2} charged impurities and 10^{15}cm^{-2} water molecules have been used.

The interactions for multi-layer graphene samples can be obtained by adding the separate contributions from each layer. The different dependences on distance imply that the relative strength of the interactions in samples with many layers can change compared to the results of Table I. For instance, the effects of the polar substrate $\propto z^{-2}$ and of charged impurities $\propto z^{-1}$, which are of longer range, sum up more effectively than the binding effect of water. Indeed, the z^{-3} decay of the graphene-water interaction suggests that only the first graphene layer is affected by the presence of water on the substrate. For the same reason, the presence of several layers of aligned water molecules should not increase the binding, since only the closest layer effectively contributes to the interaction energy. On the other hand, the binding effect of water could be enhanced if the molecules were allowed to rotate freely, therefore approaching the high polarizability of liquid water [238], or if they were partly ionized by the applied field [242], leading to additional charges similar to the Coulomb impurities present in the SiO_2 substrate.

It should be noted that I have considered only long-range electrostatic interactions, for which reliable expressions can be obtained, in terms of well understood material parameters, like the molecular polarizability, electric dipoles, or surface modes. Still, there is a significant uncertainty in some parameters, like the distance of the relevant charges to the graphene layer and the concentration of charged impurities and water molecules. The possible formation of chemical bonds between the carbon atoms and the water or silanol groups at the SiO_2 surface has not been analyzed here. Calculations based on the Local Density Functional approximation [265, 266] suggest that individual molecules can (weakly) bind to a graphene layer with energies of $10 - 50$ meV, although it is unclear how these estimates are changed when the molecules interact at the same time with the graphene layer and the substrate.

6.4.2 Corrugation of the graphene layer induced by the substrate

The attractive forces calculated in the preceding section imply that graphene is bound to the SiO_2 substrate, as observed in experiments. The previous analysis does not include the short-range repulsive forces which determine the equilibrium distance. Let us assume that the total energy near the surface is the sum of the terms analyzed above, which have a power law dependence on the distance, and a

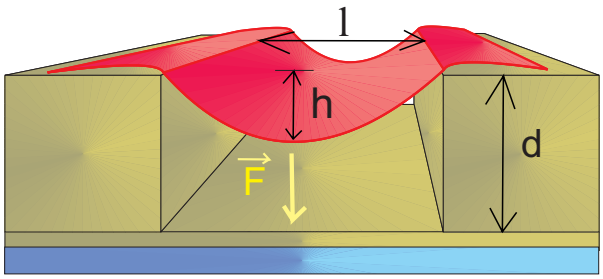

Figure 6.5: Sketch of the deformation of a NEM device studied in the text. Figure taken from [236].

repulsive term of the form $E_{rep}(z) = \epsilon_{rep}(z_0^n/z^n)$, which also decays as a power law at long distances. Here, z_0 is an undetermined length scale. For simplicity, we assume that the leading attractive term is due to the presence of a water layer, which behaves as $E_{water} = -\epsilon_w(z_0^3/z^3)$. The total energy per unit area reads then:

$$E(z) = \epsilon_{rep}\frac{z_0^n}{z^n} - \epsilon_w\frac{z_0^3}{z^3}. \tag{6.22}$$

At the equilibrium distance, z_{eq}, we have:

$$\frac{\epsilon_{rep}}{\epsilon_w} = \frac{3}{n}\left(\frac{z_{eq}}{z_0}\right)^{n-3}, \tag{6.23}$$

so that:

$$\begin{aligned} E''(z_{eq}) &= \frac{1}{z_{eq}^2}\left[n(n+1)\epsilon_{rep}\left(\frac{z_0}{z_{eq}}\right)^n - 12\epsilon_w\left(\frac{z_0}{z_{eq}}\right)^3\right] \\ &= 3(n-3)\frac{\epsilon_w}{z_{eq}^2}\left(\frac{z_0}{z_{eq}}\right)^3 = 3(n-3)\frac{E_{water}(z_{eq})}{z_{eq}^2}. \end{aligned} \tag{6.24}$$

Hence, the order of magnitude of the pinning potential induced by the environment on the out of plane modes of graphene is given by $K \propto E_{water}(z_{eq})/z_{eq}^2 \sim 10^{-2} - 10^{-1}$ meV Å^{-4}. Defining the out of plane displacement as $h(\vec{r})$, the energy stored in a corrugated graphene layer is:

$$\mathcal{E} \approx \int d^2\vec{r}\left[\kappa_b(\Delta h)^2 + Kh^2\right], \tag{6.25}$$

where $\kappa_b \approx 1$eV is the bending rigidity of graphene [77, 267]. For modulations $h(\vec{r})$ defined by a length scale l, the bending energy dominates if $l \ll l^* = (\kappa/K)^{1/4}$, while the graphene layer can be considered rigidly pinned to the substrate if $l \gg l^*$. Using the previous estimates, we find $l^* \sim 10$Å, so that the graphene layer should follow closely the corrugations of the substrate.

The pinning by the substrate implies that the dispersion of the flexural modes becomes:

$$\omega_k = \sqrt{\frac{K}{\rho} + \frac{\kappa k^4}{\rho}} \tag{6.26}$$

where ρ is the mass density of the graphene layer. At long wavelengths, $\lim_{k\to 0}\omega_k = \omega_0 \sim 10^{-4} - 10^{-3}$meV $\sim 10^{-3} - 10^{-2}$K.

The estimates obtained above also allow us to analyze the bending of graphene NEMS due to the interaction with the material below, at distance d [254, 268]. Let us assume that the lateral dimension of the graphene cantilever is l. The maximum displacement of the graphene layer from a flat position is h. A sketch of the graphene cantilever is shown in Fig. 6.5. We consider the force induced by charges in the substrate below the cantilever, as this is the contribution which decays more slowly as function of the distance between the graphene layer and the substrate (see Table 6.1). If the distance of the cantilever to the substrate is d, and supposing $d \gg h$, the gain in energy due to the deformation of the graphene layer is $\mathcal{E} \sim \epsilon_{ch} l^2 z_0 h d^{-2}$, where I have again defined z_0 and ϵ_{ch} through $E_{ch}(d) = \epsilon_{ch} z_0 / d$, having $\epsilon_{ch} \sim 0.1$ meV Å^{-2} and $z_0 \sim 1$nm from the estimates of Section 6.3. This energy should compensate the elastic energy associated to the deformation, $\mathcal{E}_{el} \sim \kappa h^2 / l^2$. Finally, the result reads:

$$h \sim \frac{\epsilon_{ch} z_0}{\kappa} \frac{l^4}{d^2} \sim 10^{-4-1} \frac{l^4}{d^2} \tag{6.27}$$

For structures such that $l \sim d$, this estimate suggests that the graphene layer will be significantly deformed if $l \gtrsim 100$ nm.

6.4.3 Interaction with a metallic tip in an STM experiment

It is known that STM tips on graphite surfaces sometimes deform the surface graphene layer [269, 270]. The understanding of these deformations can be of interest when addressing the interpretation of the different experiments performed in graphene layers. The analysis of the electrostatic interactions between a graphene layer and its environment allows us to estimate possible deformations induced by an STM tip. Let me analyze the setup sketched in the inset of Fig. 6.6. The tip has a lateral dimension l and it is located at a distance d from a graphene layer. This graphene layer interacts with an underlying substrate, and a voltage V is applied between the graphene layer and the tip. I will consider three interactions:

- An attraction between the tip and the graphene layer, which tends to deform the graphene, in the way shown in Fig. 6.6. If we assume that this energy is purely electrostatic, then a simple estimate can be obtained by describing the setup as a capacitor where the area of the plates is l^2, the distance between the plates is d, and the applied voltage is V. The interaction energy is thus of the order:

$$\mathcal{E}_{G-tip} \approx \frac{V^2 l^2}{8\pi e^2 d}, \tag{6.28}$$

  where V is given in energy units.

- The pinning of the graphene layer to the substrate. This contribution opposes the deformation of the layer. Its expression reads:

$$\mathcal{E}_{pin} \approx \epsilon_{pin} l^2, \tag{6.29}$$

  where ϵ_{pin} is the pinning energy per unit area. As typical values, we will use 1 meV/Å^2 for graphene on a water layer, and 30 meV/Å^2 for graphene interacting with another graphene layer, as in graphite.

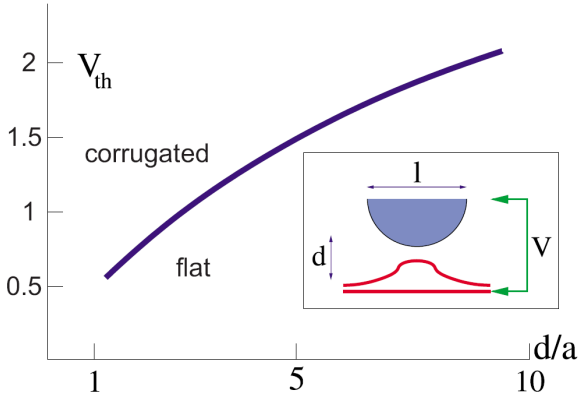

Figure 6.6: Estimate of the threshold voltage required to detach a graphene sample from the substrate, as function of the graphene-tip separation. The inset shows a sketch of the geometry considered in the text. Picture taken from [236]

- The rigidity of the layer against flexural deformations. This term tends to keep the layer flat. The deformed region is likely to be (at least) as large as the size of the STM tip. As a result, an upper bound to the energy stored in a deformation is:

$$\mathcal{E}_{el} \approx \kappa \frac{d^2}{l^2} \tag{6.30}$$

The graphene layer will be deformed when:

$$\mathcal{E}_{G-tip} \gtrsim \mathcal{E}_{pin} + \mathcal{E}_{el}. \tag{6.31}$$

Note that the approximations involved in obtaining the various terms are valid only if $d \gtrsim a$.

In the following I will consider a situation where ϵ_{pin}, κ and l are fixed. Then Eq. (6.31) entails that the layer is deformed if the voltage exceeds a threshold:

$$V \gtrsim V_{th}(d) \approx \sqrt{8\pi \left(\frac{\kappa e^2 d^3}{l^4} + \epsilon_{pin} e^2 d \right)} \tag{6.32}$$

Assuming $l \sim 10a$ and $d \sim a$, the dominant contribution comes from the pinning term, Eq. (6.29). Hence, in the physically relevant range $a \lesssim d \ll l$, we can write:

$$V_{th}(d) \approx \sqrt{8\pi \epsilon_{pin} e^2 d}, \tag{6.33}$$

A result that is independent on the tip size. The threshold values for graphene on SiO_2 are of about 0.5-2 V for $d \sim 1 - 10$Å, as schematically shown in Fig. 6.6.

6.5 Conclusions

In this chapter of the thesis I have analyzed some of the consequences that the presence of active elements in experimental environments might have on graphene layers. On the one hand, I have

briefly addressed on general grounds the influence that can be expected from these elements on the screening of electron-electron interactions. This is specially important to shed light on the different approximations made usually in the literature. However, the pivotal results of the present chapter concern the electrostatic interactions that arise between graphene and these polarizable materials that may be present in the environment. This analysis mainly applies for samples deposited on top of SiO_2 substrates, as well as suspended ones in the same experimental setup.

In order to do this study, the elements of the environment have been modelized based either on the information provided by graphene experiments or the current knowledge on the properties of SiO_2 substrates. This has allowed us to obtain analytic expressions for the interactions, that only involve a few well understood microscopic parameters that can be inferred from the experiments. Moreover, these expressions show a simple dependence on the distance between the graphene layer and the system that induces the electrostatic field. The coefficients for these dependences are the Hamaker constants for the van der Waals forces. Probably the main virtue of this analysis relies on the provision of reliable estimates of the different interactions, as well as their relative strengths. It should be emphasized again that I have not considered the possible formation of chemical bonds, which may alter the results when the distances between the carbon atoms in the graphene layer and the surrounding materials are sufficiently small.

The results show that the leading effects in samples where graphene is deposited on top of the substrate arise from the polar modes of the SiO_2 substrate, and the water which may form layers on top of it. However, for suspended graphene samples is the interaction with the charged impurities the one that rules, since it decays more slowly. These results can be obtained straightforwardly by analyzing the Table 6.1, that summarizes the main results of this chapter. The interaction energies with systems with N layers can be obtained, to a first approximation, by adding the contributions from each layer.

Finally, some results relevant to experiments with suspended graphene, graphene NEMS's and STM tips have been derived. The strength of the interactions suggests that a single graphene layer is pinned to the substrate on length scales greater than a few lattice spacings, $\sim$ 10Å. This interaction modifies the long wavelength, out of plane flexural modes, which acquire a finite frequency, $\omega_0 \sim 10^{-4} - 10^{-3}$ meV. The long range forces considered here can also induce large deformations in graphene NEMS. Regarding STM tips, an analysis of the possible deformations that they can induce on graphene layers has been provided, finding that a voltage drop of 0.5 - 2 V between the tip and the sample at distances 1 - 10 Å is sufficient to deform the samples.

7 f-Sum rule for graphene electrons

You are remembered for the rules you break.
Douglas MacArthur

Summary

This chapter continues the description of my research in the field of electron interactions in graphene monolayers. Here, an exact identity, the f-sum rule, is derived for two-dimensional Dirac electrons in the presence of non-relativistic potentials. This is in fact the relevant case for the low-energy regime of graphene. A f-sum rule for Dirac electrons in graphene is quite useful to check the validity of different approximations to the interacting problem in graphene, as to analyze the spectral weight carried by the excitations predicted within any of the aforementioned approximations. First section is an introduction to the f-sum rules, giving some generalities about spectral-weight analysis in the context of two-dimensional electron gases. This will provide us with a reference to later compare the results obtained for Dirac electrons. Second section introduces the f-sum rule for Dirac electrons, which is the main result of this chapter. The purpose of this section is to discuss some of the peculiarities of this f-sum rule, while the technicalities are left for the next section, that contains a detailed derivation of this identity. Section four is devoted to study the spectral-weight transfer between the excitations predicted within the approximations to the interacting problem that were discussed in Chapter 5. An analysis of these results is given in section five. Finally, the last section summarizes the main conclusions of this chapter. The contents of this work have been published in [194], and it was done in collaboration with A. H. Castro Neto and J. Nilsson.

7.1 Introduction: f-sum rule for the electron liquid

Dealing with interactions is not simple. Interacting problems are difficult to modelize, since sometimes it is not even clear which are the relevant degrees-of-freedom and the way they interact with each other. But once we have proposed a Hamiltonian, it is not guaranteed that useful and accurate information can be derived from it. We must resort to approximations, trying to capture limiting behaviors that may allow us to reconstruct the general picture from them. Powerful techniques have been developed for years to facilitate this work of analysis. But how reliable are their results? Of course, in many situations the answer is provided from a comparison with the experimental data that we aim to explain. However, as theorists we expect our approximations to also be consistent within the theoretical framework we are dealing with. It is here where exact identities come into play.

It happens that sometimes, although we do not count with an exact expression for an observable related to a certain Hamiltonian, we can derive general identities that this observable must necessarily fulfill in order to be consistent with the general model. These identities are usually related to symmetries and conserved quantities of the Hamiltonian, and can be used to check the goodness of certain approximations and to analyze experimental data once we believe there are some exact constraints over it.

For every theory defined by a Hamiltonian[1], its particular set of exact identities, in case they exist, must be found independently. Some of these identities, however, may hold for a large set of Hamiltonians. This is the case of the one I will analyze throughout this chapter of the thesis, the so-called f-sum rule for interacting systems of electrons.

The f-sum rule was originally derived for a three-dimensional system of Schrödinger electrons in interaction [184, 10]. Essentially, it can be seen as an statement of the conservation of particles in the system. Therefore, every interaction that preserves particle number should lead to results that fulfill the f-sum rule. This fact makes this exact identity specially attractive: it can be calculated within the non-interacting theory, but then it must hold for the complete set of Hamiltonians with interactions that conserve particle number. This includes the Coulomb interaction, the one at the heart of the Fermi liquid theory.

In the introduction to this part of the thesis, I devoted an entire section to study the microscopic foundations of Fermi liquid theory. Since the subject of this thesis are low-dimensional quantum systems, I will concentrate here on the two-dimensional electron gas, which is also the relevant case to later compare with the results for graphene. For Schrödinger electrons, the Hamiltonian of the Coulomb interacting system is given by:

$$\mathcal{H} = \sum_{\mathbf{k},\sigma} (\frac{k^2}{2m} - \mu) c^\dagger_{\mathbf{k},\sigma} c_{\mathbf{k},\sigma} + \frac{1}{2} \sum_{\mathbf{q}} v(\mathbf{q}) n(\mathbf{q}) n(-\mathbf{q}) \tag{7.1}$$

where m is the mass of the electrons, μ is the chemical potential, that sets the Fermi surface, $v(\mathbf{q}) = 2\pi e^2/(\kappa q)$ is the Coulomb interaction in two dimensions, and:

$$n(\mathbf{q}) = \sum_{\mathbf{k}} c^\dagger_{\mathbf{k}+\mathbf{q}} c_{\mathbf{k}} \tag{7.2}$$

is the Fourier transform of the local density operator. The conservation of particle-number happens when the *continuity equation* is fulfilled:

$$[n(\mathbf{q}), \mathcal{H}] = \mathbf{q} \cdot \vec{J}_{\mathbf{q}} \tag{7.3}$$

where:

$$\vec{J}_{\mathbf{q}} = \sum_{\mathbf{k}} \frac{\mathbf{k}}{m} c^\dagger_{\mathbf{k}+\mathbf{q}} c_{\mathbf{k}} \tag{7.4}$$

is the current operator.

[1] Since the Hamiltonian formalism is the one mostly used throughout this thesis, I am keeping the discussions strictly restrained to it. However, this general arguments do apply to other formalisms.

Derivation of the f-sum rule

The f-sum rule has the following form for the electron liquid [184]:

$$-\int_0^\infty \frac{d\omega}{\pi}\omega\Im\chi(\mathbf{q},\omega) = \frac{q^2 N}{2m} \tag{7.5}$$

where N is the number of particles in the system, that is related to the chemical potential. $\chi(\mathbf{q},\omega)$ is the electron susceptibility. As we learnt in Chapter 5, it determines the response of the system to external perturbations that couple to the density. The electron susceptibility is in fact a density-density correlation function, defined at zero temperature by the following exact expression:

$$\chi(\mathbf{q},\omega) = \sum_n |\langle n|n^\dagger(\mathbf{q})|0\rangle|^2 \frac{2\omega_{n0}}{(\omega+i\eta)^2-\omega_{n0}^2} \tag{7.6}$$

where n are the *exact* eigenstates of the *full* interacting Hamiltonian, and $\omega_{n0} = \epsilon_n - \epsilon_0$ their excitation energies.

The proof of the f-sum rule follows straightforward from the identity:

$$\langle 0|[[n(\mathbf{q}),\mathcal{H}]]|0\rangle = -2\int_0^\infty \frac{d\omega}{\pi}\omega\Im\chi(\mathbf{q},\omega) \tag{7.7}$$

that can itself be derived by expanding the commutators and using the closure relation for the electron gas, $\mathcal{I} = \sum_n |n\rangle\langle n|$. In the process of derivation the continuity equation must be imposed, explaining why this conservation law lies at the heart of the f-sum rule. If the calculation can be carried out exactly is by virtue of the vanishing commutator $[n(\mathbf{q}),\mathcal{H}_{int}] = 0$ for those interactions that preserve particle number, in particular the Coulomb interaction.

Consequences for the many-body problem

The f-sum rule is an exact identity that every approximation to the electron liquid Hamiltonian must fulfill. Therefore it can be used as a consistency check for these approximations. Additionally, it also turns out to be very useful to analyze the relative importance of the different excitations present in the system. For $q \to 0$, we have seen that according to the RPA approximation to the susceptibility, two kind of coherent excitations can be identified: electron-hole excitations and a collective plasmon mode. Moreover, there are incoherent excitations that excite multiple pairs in a non-coherent way. All these excitations can be analyzed in terms of the matrix elements of the density operator, $n(\mathbf{q})$, the one from which the electron susceptibility is built.

In the non-interacting system the excitations $|n\rangle$ are purely of electron-hole nature, and they satisfy:

$$\langle n|n^\dagger(\mathbf{q})|0\rangle = 1 \tag{7.8}$$

However, in the Fermi liquid there are other excitations, and this identity does not hold anymore. Excitations of quasielectrons and quasiholes give $\langle n|n^\dagger(\mathbf{q})|0\rangle < 1$ in the long wave-length limit ($q \to 0$), while the matrix elements of incoherent multiple pair excitations directly vanish like q^2 [271]. Hence, their matrix elements are negligible in the long wave-length limit.

This discussion can be translated into the f-sum rule language. The imaginary part of the electron susceptibility reads, according to Eq. (7.6):

$$\Im\chi(\mathbf{q},\omega) = -\pi\sum_n |\langle n|n^\dagger(\mathbf{q})|0\rangle|^2 \left(\delta(\omega-\omega_{n0}) - \delta(\omega+\omega_{n0})\right) \tag{7.9}$$

By integrating this, we have:

$$-\int_0^\infty \frac{d\omega}{\pi}\omega\Im\chi(\mathbf{q},\omega) = \sum_n (n^\dagger(\mathbf{q}))_{n0}|\langle n|n^\dagger(\mathbf{q})|0\rangle|^2\omega_{n0} \tag{7.10}$$

where, remember, $|n\rangle$ are the excitations of the total Hamiltonian. On the other hand, the f-sum rule constrains this sum over excitations:

$$\sum_n |\langle n|n^\dagger(\mathbf{q})|0\rangle|^2\omega_{n0} = \frac{q^2N}{2m} \tag{7.11}$$

(Quasi)electron-hole excitations and incoherent multiparticle ones have matrix elements whose squared modulus vanishes as q^2 for $q \to 0$. Since their excitation energies go, in this limit, linear in q, and the density of states is constant, it is easy to show that they give a contribution to the f-sum rule that vanishes as q^4. Moreover, the contribution of multipair incoherent excitations to the f-sum rule is also of order q^4 [271].

Then, how is the f-sum rule fulfilled in the long wave-length limit? The answer is that the collective plasmon mode absorbs all the *spectral weight*, i.e., the frequency averaged values of the imaginary part of the electron susceptibility. The total spectral weight is, after all, the quantity to be conserved by the f-sum rule. Varying different parameters (momentum of the excitation, range of energies, temperature,...) of the model, the spectral weight is redistributed among the different excitations. The implications of this statement are in turn far-reaching: take, for instance, an experiment in which the imaginary part of the susceptibility is measured[2]. By integrating the spectral weight in the accessible energy range, the relative importance of the different excitations can be inferred. Moreover, it might be employed to dilucidate the existence of relevant excitations in an energy range out of the experimental one, whose signature would be a strong suppression of the integrated spectral weight available.

Interestingly, the f-sum rule can be used as well to determine matrix elements of dominant excitations, were they unknown or if a check of the predicted ones from a different calculation is wished. Let us take, for instance, the plasmon mode in the electron liquid. By doing the approximation, for $q \to 0$, and supposing that the plasmon mode is the leading excitation in terms of spectral weight, we have the following equation:

$$\sum_n |\langle n|n^\dagger(\mathbf{q})|0\rangle|^2\omega_{n0} \simeq |(n^\dagger(\mathbf{q}))_{n0}|^2_{pl}\omega_p(q) \tag{7.12}$$

This allows us for the identification $(n^\dagger(\mathbf{q}))_{n0} \simeq \sqrt{N/(2m\omega_p(q))}q$. In the two-dimensional electron gas, the plasmon dispersion relation reads $\omega_p(q) \sim q^{1/2}$ (a remarkable difference with the three-dimensional case, where is constant in the long wave-length limit).

That the plasmon carries all the spectral weight for $q \to 0$ is in fact a consequence of the classical limit of the theory: the long wave-length plasmon is a collective mode of oscillation of the classical electron gas in a positive background [184].

[2]This can be done in principle with X-ray experiments. However, as we will see later, it turns out that the most relevant quantity to measure in experiments is the optical conductivity, that can be easily related to the electron susceptibility in a certain limit.

Consequences for experiments

In order to connect the f-sum rule with relevant experiments, it is useful to resort to a highly relevant observable, the optical conductivity [143]. The optical conductivity is a sophisticated way to name a frequency-dependent conductivity[3]. It was already introduced in this thesis when discussing experimental evidences of electron-electron interactions in graphene. There, it was pointed out that it has a straightforward relation with the electron susceptibility:

$$\sigma(\omega) = \lim_{q\to 0} ie^2 \frac{\omega}{q^2}\chi(\mathbf{q},\omega) \tag{7.13}$$

This connection allows us to write an f-sum rule for the optical conductivity:

$$\int_0^\infty d\omega \Re\sigma(\omega) = \frac{\omega_p^2}{8} \tag{7.14}$$

where $\omega_p = 4\pi N/(me^2)$ is the classical plasma frequency. All the discussion regarding excitations applies also for this case (remembering that now the limit $q \to 0$ has been taken). By means of Infrared Spectroscopy (IS) the optical conductivity can be resolved, and the integrated spectral weight must fulfill the f-sum rule. Were this not the case, it could be a signature of some anomalous behavior that requires further investigation. Spectral weight transfer analysis is of great importance in the field of strongly correlated systems [272].

Consequences for van der Waals forces

Since we have already devoted a complete thesis chapter to the study of van der Waals forces, it is interesting to point out that they are connected to the f-sum rule. The bridge between them is given by the spectral weight introduced earlier in this section. Excitations that carry more spectral weight account in many situations for the main response to external probes that couple to the density. Since in the long wave-length limit of the 2DEG we have seen that the plasmon the excitation that saturates the f-sum rule, this allows us to write the following expression for the interaction energy in second order perturbation theory [257]:

$$E_{VdW}^{(2)} = -\frac{1}{2}\sum_q v_q^2(d)\frac{|(n^\dagger(\mathbf{q})_{n0}|^2}{\omega_p(q)} \tag{7.15}$$

where I have assumed that the systems in interaction are identical. From this expression, we learn that van der Waals forces between two 2DEGs are dominated by the coupling between plasmon modes. In general, this is expected to be the case whenever an excitation saturates the f-sum rule.

7.2 The f-sum rule for graphene electrons

The analysis of the f-sum rule for the two-dimensional electron liquid should have served to persuade us of the virtues of this exact identity. Its applications range from strictly theoretical consistency checks to the understanding of relevant experimental information. Therefore, an f-sum rule for graphene electrons is expected to be a powerful tool for the theoretical analysis.

[3] The conductivity can be defined as the current-current correlation function. The connection between susceptibility and conductivity is provided, then, by the continuity equation.

The identity derived in the context of Schrödinger electrons does not hold for graphene electrons, and the derivation must be carried out from the beginning, following the steps given in [184] and sketched in the introduction. The technicalities of the derivation are the content of next section. At the moment, let me summarize the main results and point out some relevant considerations. If we restrict ourselves to the low-energy sector of the theory, i.e., to electrons ruled by the Dirac equation, the new f-sum rule reads:

$$\int_0^{\Lambda_E} d\omega\, \omega\, \Im\chi(\mathbf{q},\omega) = -\frac{g_S g_v q^2 \Lambda_E}{16} \tag{7.16}$$

where Λ_E is the energy cutoff up to which Dirac physics holds, and $g_s g_v$ the valley and spin degeneration of graphene.

A first thing to allude is that the f-sum rule has already been studied in the context of the relativistic Dirac problem in three-dimensions [273]. In this case, where there is not a natural lattice spacing, the sum rule gives an infinite contribution that is considered part of the "vacuum" energy and hence unmeasurable. In a system with a finite band-width, which is the case of graphene, such a cutoff dependent contribution represents a real response of the system (the inter-band electron-hole excitations), and is non-negligible. This issue was raised originally in Ref. [274], where a relativistic generalization of the f-sum rule is discussed as well. Notice that, as we will see below, in order to deduce a non-zero f-sum rule for Dirac electrons we must proceed carefully, since some of the typical steps to follow in the derivation do not apply out of the box due to the peculiar structure of the Dirac Hamiltonian.

The second important observation is that an f-sum rule can also be derived for the whole band of graphene, i.e., working directly with the tight-binding model of the honey-comb lattice. This task has been already performed in the $q \to 0$ limit, i.e., for the optical conductivity of graphene [275]. Although this approach may be more realistic when applied to experiments, the f-sum rule for the continuous case provides us with more insights when studying models of interacting electrons in the low-energy regime, which is my main interest in this thesis.

For completeness, I will also derive the expression of the f-sum rule for the optical conductivity in the continuous (low-energy) case, being the most relevant quantity when addressing real experiments. It can be easily derived from the f-sum rule for the electron susceptibility, yielding:

$$\int_0^{\infty} d\omega \Re\sigma(\omega) = \frac{g_s g_v \Lambda}{16} \tag{7.17}$$

The f-sum rule for Dirac electrons has many peculiarities not present in its electron liquid counterpart. The contribution from the lower filled band makes the sum rule cutoff dependent. This is easy to understand from the existence of interband particle-hole transitions for arbitrary energy if we do not cut off the spectrum. Moreover, it does not depend on the level of doping (or the chemical potential) since Eq. 7.16 is also valid for doped graphene. Even more striking, the sum rule applies in the case of massive Dirac fermions (i.e. in a gapped system) as long as the gap is much smaller than the cutoff: $m \ll \Lambda_E$. As I mentioned in Chapter 1, a way to generate a gap in real graphene samples is by using a substrate that breaks the their sublattice symmetry [93].

7.3 Detailed derivation of the f-sum rule

In this section I will derive the f-sum rule for Dirac electrons in graphene, discussing separately the cases of intrinsic (undoped) graphene, extrinsic (doped) graphene and, finally, the case of massive electrons.

7.3.1 Undoped graphene

Low-energy excitations of graphene are ruled by the Dirac equation. If we focus on a single valley and neglect the spin degree of freedom, the Hamiltonian reads:

$$H_0 = v_F \sum_{\mathbf{k}} \Psi^\dagger_{\mathbf{k}} \begin{pmatrix} 0 & k_x - ik_y \\ k_x + ik_y & 0 \end{pmatrix} \Psi_{\mathbf{k}} \tag{7.18}$$

where $\Psi^\dagger_{\mathbf{k}} = (a_{\mathbf{k}}, b_{\mathbf{k}})$ stands for two-component spinors. Remember that a and b operators refer to the two different sublattices in the unit cell of the honeycomb lattice. In the same basis, the density operator is given by:

$$n^\dagger_{\mathbf{q}} = \sum_{\mathbf{k}} \Psi^\dagger_{\mathbf{k}+\mathbf{q}} \Psi_{\mathbf{k}} = \sum_{\mathbf{k}} (a^\dagger_{\mathbf{k}+\mathbf{q}} a_{\mathbf{k}} + b^\dagger_{\mathbf{k}+\mathbf{q}} b_{\mathbf{k}}) \tag{7.19}$$

The Coulomb interaction has the usual form $H_{int} = \sum_{\mathbf{q}} v_{\mathbf{q}} n^\dagger_{\mathbf{q}} n_{\mathbf{q}}$, and therefore it is simple to show that the condition $[n_q, H_{int}] = 0$ is realized. We see clearly the advantage of the f-sum rule: it can be calculated within the non-interacting theory, at the time that it must be satisfied by the interacting one.

With these expressions, the commutators in Eq. (**??**) can be evaluated.Let me emphasize that the first commutator is nothing but the particle conservation equation written in momentum space:

$$[n_{\mathbf{q}}, H] = \mathbf{q} \cdot \vec{J}_{\mathbf{q}}, \tag{7.20}$$

where $\vec{J}_{\mathbf{q}} = v_F \sum_{\mathbf{k}} \Psi^\dagger_{\mathbf{k}} \vec{\sigma} \Psi_{\mathbf{k}+\mathbf{q}}$ is the velocity (current) operator. The double commutator then reads:

$$[[n_{\mathbf{q}}, H], n^\dagger_{\mathbf{q}}] = -v_F \sum_{\mathbf{k}} (\Psi^\dagger_{\mathbf{k}+\mathbf{q}} \mathbf{q} \cdot \vec{\sigma} \Psi_{\mathbf{k}+\mathbf{q}} - \Psi^\dagger_{\mathbf{k}} \mathbf{q} \cdot \vec{\sigma} \Psi_{\mathbf{k}}). \tag{7.21}$$

We should proceed carefully with this result. In principle, our free theory describes massless electrons with an unbounded linear dispersion relation. But when handling operators that are defined in an unbounded region, we are not allowed, for instance, to simply state that $\sum_k G(k+q) = \sum_k G(k)$. The same issue can be found in the theory of the one dimensional electron liquid when calculating the commutator $[n_q, n^\dagger_q]$, which turns out to be nonzero, giving rise to the anomalous commutator problem [10]. When we work with unbounded operators we need to refer the calculations to bounded quantities, which usually are defined with respect to the ground state value. This way, we define normal ordered operators:

$$: G(k) := G(k) - \langle 0|G(k)|0\rangle \tag{7.22}$$

that are by definition bounded, and satisfy $\sum_k : G(k+q) := \sum_k : G(k) :$. Applying this rule to our commutator, we get:

$$[[n_{\mathbf{q}}, H], n^\dagger_{\mathbf{q}}] = -v_F \sum_{\mathbf{k}} \big(\langle 0|\Psi^\dagger_{\mathbf{k}+\mathbf{q}} \mathbf{q} \cdot \vec{\sigma} \Psi_{\mathbf{k}+\mathbf{q}}|0\rangle - \langle 0|\Psi^\dagger_{\mathbf{k}} \mathbf{q} \cdot \vec{\sigma} \Psi_{\mathbf{k}}|0\rangle \big), \tag{7.23}$$

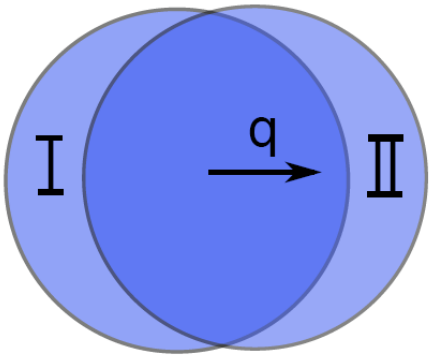

Figure 7.1: Regions subtracted in the calculation of the f-sum rule.

where the ground state for undoped graphene consists on the lower band completely filled (Dirac sea) and the upper band completely empty.

The result involves the difference between two infinite sums, something not well-defined *a priori*. In order to compute it, we need to regularize the sums, for instance, by using an ultraviolet cutoff. In addition, we need to switch to the diagonal basis. As usual, this is done with the unitary transformation that diagonalizes Hamiltonian (7.18), namely:

$$U_{\mathbf{k}} = \frac{1}{\sqrt{2}} \begin{pmatrix} e^{-i\frac{\theta_{\mathbf{k}}}{2}} & e^{-i\frac{\theta_{\mathbf{k}}}{2}} \\ e^{i\frac{\theta_{\mathbf{k}}}{2}} & -e^{i\frac{\theta_{\mathbf{k}}}{2}} \end{pmatrix}, \tag{7.24}$$

which leads to the following relation:

$$U^{\dagger}_{\mathbf{k}+\mathbf{q}'}\mathbf{q}\cdot\vec{\sigma}U_{\mathbf{k}+\mathbf{q}'} = q \begin{pmatrix} \cos(\theta_{\mathbf{q}}-\theta_{\mathbf{k}+\mathbf{q}'}) & i\sin(\theta_{\mathbf{q}}-\theta_{\mathbf{k}+\mathbf{q}'}) \\ -i\sin(\theta_{\mathbf{q}}-\theta_{\mathbf{k}+\mathbf{q}'}) & -\cos(\theta_{\mathbf{q}}-\theta_{\mathbf{k}+\mathbf{q}'}) \end{pmatrix}, \tag{7.25}$$

Once we have introduced explicitly the cutoff, we can shift the sums:

$$\langle 0|[[n_{\mathbf{q}},H],n^{\dagger}_{\mathbf{q}}]|0\rangle = -v_F\Big[\sum_{\mathbf{k}\in I}\cos(\theta_{\mathbf{k}}) - \sum_{\mathbf{k}\in II}\cos(\theta_{\mathbf{k}})\Big] \tag{7.26}$$

where only the contribution from the lower band survives, and the regions of summation are shown in Fig. 7.1. For a large momentum space cutoff $\Lambda = \Lambda_E/(2v_F)$, the calculation of this difference can be carried out easily. Both regions give the same contribution but with opposite sign due to the cosine term. By going to the continuum limit of the sum we find:

$$\langle 0|[[n_{\mathbf{q}},H],n^{\dagger}_{\mathbf{q}}]|0\rangle = \frac{q^2\Lambda_E}{8\pi} \tag{7.27}$$

Reinstating the degeneracy of spin and valley entails an extra multiplicative factor $g_v g_s = 4$. The final result for the f-sum rule is Eq. (7.16):

$$\int_0^{\Lambda_E} d\omega\omega\Im\chi(\mathbf{q},\omega) = -\frac{g_S g_v q^2\Lambda_E}{16}$$

7.3.2 Doped graphene

The effect of doping the graphene sheet translates into a nonzero chemical potential. The ground state no longer has a particle-hole symmetry. Therefore, the modifications to the f-sum rule calculation

performed in the last section are: (1) The Hamiltonian must be replaced by $H - \mu N$, with μ being the chemical potential. (2) The ground state has a contribution from electrons of the upper band, for positive chemical potential, or from holes in the lower band, for negative chemical potential.

First let me discuss (1). Since $N = n_{\vec{0}}$, this immediately leads to $[n_q, N] = 0$, thus giving no new contribution. Therefore, at the level of commutators the result is again Eq. (7.16). However, still from (2) we might expect a contribution from the electron (holes) in the ground state, above (below) the Dirac point. However, this contribution is no longer unbounded (the operators are only nonzero under (over) the Fermi momentum), and now we can shift the operators:

$$\sum_{\mathbf{k}} \cos(\theta_{\mathbf{q}} - \theta_{\mathbf{k}+\mathbf{q}}) \langle 0 | c^{\dagger}_{\mathbf{k}+\mathbf{q}} c_{\mathbf{k}+\mathbf{q}} | 0 \rangle - \sum_{\mathbf{k}} \cos(\theta_{\mathbf{q}} - \theta_{\mathbf{k}}) \langle 0 | c^{\dagger}_{\mathbf{k}} c_{\mathbf{k}} | 0 \rangle = 0 \tag{7.28}$$

This means that there is no contribution coming from the ground state evaluation of the commutators, and the result is the same than the undoped one, Eq. (7.16).

7.3.3 Massive Dirac electrons

The case of massive electrons requires more attention. The Dirac Hamiltonian is modified in the following way:

$$H_0 = \sum_{\mathbf{k}} \Psi^{\dagger}_{\mathbf{k}} \begin{pmatrix} m & v_F(k_x - ik_y) \\ v_F(k_x + ik_y) & -m \end{pmatrix} \Psi_{\mathbf{k}} \tag{7.29}$$

which is the same as Eq. (7.18) with the additional term $m \sum_k \Psi_{\mathbf{k}} \sigma_z \Psi_{\mathbf{k}}$. Again, modifications to the f-sum rule could arise either from the new term in the commutator or from the final ground state evaluation. The first contribution can be readily seen to be zero: $[n_q, H_m] = 0$, due to the cancellation of the sublattice contributions independently. The second modification is more subtle, since requires the diagonalization of the Hamiltonian in Eq. (7.29). The result gives an hyperbolic dispersion relation of the form $E_k = \sqrt{v_F^2 k^2 + m^2}$. Applying it to the commutators which give the f-sum rule (following the same lines than above) we get:

$$\langle 0 | [[n_{\mathbf{q}}, H], n^{\dagger}_{\mathbf{q}}] | 0 \rangle = -v_F \Big[\sum_{\mathbf{k} \in I} \frac{v_F k}{\sqrt{(v_F k)^2 + m^2}} \cos(\theta_{\mathbf{k}}) - \sum_{\mathbf{k} \in II} \frac{v_F k}{\sqrt{(v_F k)^2 + m^2}} \cos(\theta_{\mathbf{k}}) \Big] \tag{7.30}$$

The result involves again the subtraction of two regions, which is nonzero only for momenta close to the cutoff, as it is depicted in Fig. 7.1. If $m \ll \Lambda_E$ we can expand the prefactor to leading order in k, recovering the massless result. This is to be expected since the mass term is irrelevant in this region. The result for the massive case turns out to be the same than the massless one of Eq. (7.16), so the existence of a gap does not change the nature of the sum rule. At this point it is convenient to remark that the particular form of the f-sum rule for Dirac electrons comes mainly from the asymptotic linear spectrum and the existence of an unbounded spectrum.

7.4 Spectral weight transfer in the low-energy sector of graphene

As I mentioned in the introduction, one of the most interesting applications of the f-sum rule is to the analysis of the spectral-weight transfer between the different excitations present in graphene,

that in turn give indications of their relative response to external probes, determination of forces, etc. Particularly, in this section I will use the f-sum rule to study the different approximations for the Coulomb-interacting Dirac problem that were described in Chapter 1. To set the language, and see how the spectral weight transfer reflects in the contributions to the f-sum rule, I will firstly address the case of free electrons, in both doped and undoped graphene. Then I will turn to discuss the more controversial issue of graphene with interactions. Here, the case of intrinsic (undoped) graphene remains controversial even in the weak-coupling regime. The strong-coupling regime of graphene will be not analyzed in this chapter. From here on, let me concentrate on the particular case of $N_f = 4$ fermion species, which is the relevant case for graphene electrons.

7.4.1 Free Dirac electrons

If graphene is undoped, i.e. the Fermi level is located at the Dirac Point, the susceptibility is given by Eq. (5.15):

$$\chi_0(\mathbf{q},\omega) = -\frac{g_s g_v}{16}\frac{q^2}{\sqrt{v_F^2 q^2 - \omega^2}}$$

This susceptibility saturates the f-sum rule for Dirac electrons, as expected. This means that the contribution from interband particle-hole excitations has a q^2 dependence and that the number of these excitations is only limited by the high-energy cutoff.

When the level of doping is changed away from half filling, we have two different particle-hole excitations: intraband and interband. Since the f-sum rule does not depend on doping, the spectral weight must be distributed among those. By using Eq. (5.26), in the long-wavelength limit, we find a contribution from interband transitions that reads:

$$\frac{q^2}{4}\int_{2E_F}^{\Lambda_E} d\omega = \frac{q^2\Lambda_E}{4} - \frac{q^2 E_F}{2} \tag{7.31}$$

On the other hand, the contribution from the intraband excitations is:

$$\frac{2k_F}{v_F\pi}\int_0^{v_F q} d\omega \frac{\omega^2}{\sqrt{v_F^2 q^2 - \omega^2}} = \frac{q^2 E_F}{2}, \tag{7.32}$$

meaning that there is an exact transfer of spectral weight between the two types of excitations that is proportional to the level of doping. When the Fermi level is changed, some interband transitions are prohibited by Pauli exclusion, and they no longer saturate the f-sum rule. Both excitations have a contribution proportional to q^2. However, the contribution from intraband excitations is not cutoff dependent, but density (or doping) dependent. As I shall show when connecting the interactions, these excitations resemble those of the conventional Fermi liquid, where the contribution to the f-sum rule due to particle-hole excitations does depend on the density of electrons.

7.4.2 Interacting Dirac electrons

RPA in undoped graphene

As I have already remarked several times throughout this thesis, the Random Phase Approximation is somehow the simplest approximation we can use to study the effect of electron-electron interactions.

For an undoped sheet, by using equations (5.3) and (**??**) we find that the RPA approximation fulfills the f-sum rule. The main issue related to the RPA comes when analyzing the spectral weight. In principle, in undoped graphene at the RPA level, there are no new low-energy excitations besides the particle-hole ones. However, it can be seen that the low-energy sector loses some spectral weight. If we take an intermediate energy scale, say Λ_I, such that $v_F q \ll \Lambda_I \ll \Lambda_E$ and integrate over energy in this range, we get:

$$\int_0^{\Lambda_I} d\omega\omega\Im\chi_{RPA}(\mathbf{q},\omega) = -\frac{q^2\Lambda_I}{4} + \frac{\pi^2}{16} g v_F q^3 \tag{7.33}$$

Therefore, there is a cutoff independent loss of spectral weight in the low-energy sector. This is an unconventional result in the sense that the usual RPA approximation for Fermi liquids only rearranges the low-energy spectral weight, remaining decoupled from the high-energy sector of the theory. On the contrary, in undoped graphene it seems to be a spectral transfer to higher energy scales. In particular, the spectral weight is distributed close to the cutoff, where a new resonance is found and even a plasmon condition is fulfilled. Of course, the particular high-energy excitations that arise cannot be described within our effective theory, which only applies to the low-energy regime. The transfer is proportional to the interaction strength, g, and it depends on the momentum as q^3, instead of the typical q^2 dependence of single particle excitations, being negligible at leading order in the long-wavelength limit. As it was shown in the introduction to this chapter, subleading contributions to the sum rule were associated to incoherent multiparticle excitations. Therefore, this might be the case here.

RPA in doped graphene

In the doped case, the RPA susceptibility is given by Eq. (5.27), which predicts three relevant excitations: interband and intraband particle-hole ones, and a plasmon mode. The contribution from interband excitations is again given by Eq. (7.31), which states that these excitations have lost a contribution to the f-sum rule given by $E_F q^2/2$. As opposed to the non-interacting theory, this contribution is not transferred to the intraband particle-hole transitions, whose contribution is in this case:

$$\frac{1}{2\pi e^4 E_F}\int_0^{v_F q} d\omega\omega^2\sqrt{v_F^2 q^2 - \omega^2} = \frac{v_F^2 q^4}{32 g^2 E_F}, \tag{7.34}$$

which is proportional to q^4 and thus much smaller in the long-wavelength limit than the loss from the interband transitions. As in the case of the Fermi liquid, it is the plasmon mode the responsible for the absorption of most of the spectral weight:

$$\frac{(2e^2E_F)^{3/2}q^{5/2}}{4e^2}\int_{v_F q}^{2E_F}\frac{d\omega}{\omega}[1-\frac{\omega^2}{4E_F^2}]\delta(\omega-\omega_0 q^{1/2}) = \frac{q^2 E_F}{2} \tag{7.35}$$

In the limit $q \to 0$, the transfer to the plasmon mode totalizes the complete spectral weight.

In the interacting system the response is dominated by the plasmon, instead of the intraband particle-hole excitations. Notice, however, that graphene, due to its particular two-band structure, is different from the electron gas in the sense that the main contribution comes always from the interband transitions, which essentially saturate the f-sum rule. Despite this fact, as I will mention in next section, the existence of this collective mode may have measurable consequences.

Far above the energy scale E_F, we recover the same polarizability that for undoped graphene, as expected, since now the only relevant excitations are the intraband ones. Therefore a transfer of spectral weight to the high-energy sector is also observed. Notice that, at the same order of this transfer, q^3, further rearrangements of spectral weight occur in the low-energy sector of doped graphene, as can be shown by computing next-order corrections to expression (5.27).

Beyond RPA in undoped graphene

As mentioned in Chapter 5, in doped graphene the RPA approximation seems to work well, at least as far as we concentrate in the weak-coupling regime and the long wave-length limit. Therefore, I will limit myself from the rest of this section to discuss undoped graphene physics. As it was explained in Section 5.2, when vertex corrections are taken into account, the polarization function close to the threshold $\omega = v_F q$ is given by Eqs. (5.21) and (5.20). As this approximation does not describe the whole energy range, we cannot verify immediately the validity of the f-sum rule. However, we expect that for high energies (as compared to the scale $v_F q$) the RPA approximation is valid, so we expect a loss of spectral weight similar to the one found before. The most relevant question is how the spectral weight is distributed among the new low-energy excitations that arise.

Let me address this issue in more detail. Since the contribution that a certain excitation has to the f-sum rule is related to the role they play in the response of the system, we might expect that new excitations give deviations from the free-electron picture. However, the new modes found in Ref. [197] can only be calculated reliably close to $\omega = v_F q$, preventing the integration of the susceptibility given in Eq. (5.20) in the entire energy range. Nevertheless, we can concentrate on the transfer of spectral weight close to $\omega = v_F q$ by defining the following quantity:

$$S_p(g, C) = \frac{4}{v_F q^3} \int_0^{\Lambda_q} d\omega\, \omega\, \Im\chi(q, \omega)\,, \tag{7.36}$$

where $\Lambda_q = C v_F q$ and C is a constant that has to be chosen appropriately. If we define $s = \omega / v_F q$ we find:

$$S_p(g, C) = \int_0^C ds s(4 v_F \Im\chi(q, s)/q) \tag{7.37}$$

which is momentum independent but cutoff and interaction strength dependent. We find that the approximation of Eq. (5.20) works well for $C - 1 \sim 10^{-1}$ (in such a way that $N_f = 4 \simeq \log(v_F q/(\Lambda_q - v_F q))$) and this is the value I will use from now on. Readily, one notices that all the contributions to the f-sum rule that come from this region are of order q^3. Therefore, all the spectral rearrangement due to interactions is of subleading order.

Now I will turn to analyze the dependence on the interaction strength g of the different approximations analyzed for undoped graphene. In Fig. 7.2 a plot of their contributions to the partially integrated spectral weight, $S_p(g, 1.1)$, is given. This Figure shows a similar behavior for the electron-hole background in both RPA and non-RPA approximations: as the interaction strength is increased, the spectral weight covered in the integration becomes smaller. Notice that this should not be related only to the transfer of spectral weight to the high-energy sector (which is linear in g), but mostly to the fact that the maximum of the imaginary part of the susceptibility is shifted away from the

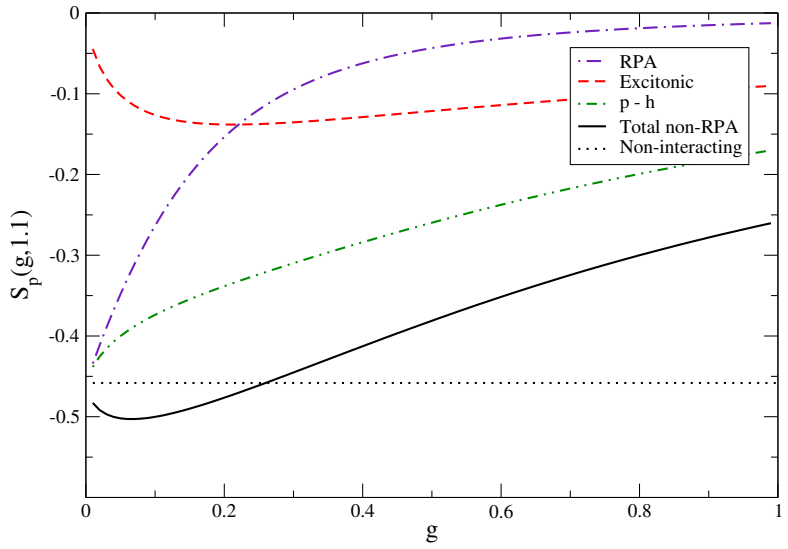

Figure 7.2: Contributions to the f-sum rule in the low-energy region of undoped graphene. The integrals are done with a high-energy cutoff such that $\omega < 1.1 v_F q$. The dotted line corresponds to the non-interacting theory. The dash-dotted line shows the RPA contribution. The solid line is the non-RPA contribution, sum of the excitonic contribution (under the threshold, $\omega < v_F q$) and the particle-hole contribution (over the threshold, $\omega > v_F q$).

threshold as the interaction grows. More interesting is the behavior of the so-called excitonic part, the one that arises under the threshold, $\omega < v_F q$: it shows a maximum for $g \simeq 0.2$, and then starts to decrease.

In order to understand this behavior, we must notice that the contribution to the f-sum rule from the plasmon can be easily worked out in the limit $g \gg 1$, where the plasmon gets well defined:

$$\int_{pl} d\omega \omega (\Im\chi)_{pl} = -\frac{v_F q^3}{4} [\frac{8e^{-N_f}}{g}(1 - e^{-N_f})], \tag{7.38}$$

Here, an analytical plasmon dispersion relation for generic number of fermion species has been used (remember that in the case of graphene we have $N_f = 4$), namely $\omega(q) = v_F q(1 - e^{-N_f})$, as well as the spectral weight of this excitation, $|(n^\dagger(\mathbf{q}))_{pl}|^2 = 2v_F q^2/(ge^{-N_f})$. We see that the plasmon contribution to the f-sum rule decreases as the interaction strength grows. On the other hand, although the excitonic domain becomes broader (and, therefore, out of the region of validity of our approximations), its contribution is also negligible for large interactions. Hence, the appearance of a maximum in the contribution to the f-sum rule under the threshold can be understood as an interplay between excitonic response and plasmon response.

In any case, these results imply that there is not an important transfer of spectral weight from the particle - hole excitations to the new modes predicted in the context of vertex corrections, since they are all of order q^3. Moreover, this approximation only rearranges spectral weight close to the threshold, and we still expect a flow of spectral weight to the high-energy sector of the theory as the interaction strength is increased, as occurred in the RPA approximation.

7.5 Analysis of the results and further implications of the f-sum rule

The different contributions to the f-sum rule have been summarized in Table 7.1. The Dirac liquid shows particular features from the point of view of spectral weight transfer and contributions to the f-sum rule. The results provide us with many insights into the role played by Coulomb interactions in graphene.

The f-sum rule is essentially saturated by the particle-hole excitations in the long wave-length limit. This is true for small doping levels compared to the cutoff, as the intraband excitations have the largest contribution. In the case of doped graphene, Coulomb interactions give rise to a collective mode which absorbs to leading order all the spectral weight of interband excitations. However, this does not remain true in the case of undoped graphene, where all the spectral (re)arrangement due to the Coulomb interaction is always at subleading order, q^3. New excitations which could be arising close to the threshold contribute much less to the f-sum rule than the particle - hole ones, even when the interaction strength is infinitely large. This effect must be understood not only because of the subleading dependence of these excitations, but because of the spectral weight transfer to the high-energy sector we have found in every approximation studied for the interacting Dirac liquid. Hence, the latter should be a remarkable feature of this system.

An apparently related behavior has been described in high-Tc literature, where spectral weight transfer between different energy scales has been reported in several works [276, 277]. In the context of strongly correlated systems, a spectral weight transfer from the high-energy sector to the low-energy one has been related to possible issues arising in the definition of the low-energy theory [278]. In this sense, studies concerning the whole graphene band-structure could help to clarify this issue [279].

When turning to graphene, the Dirac liquid is only a low-energy approximation to the electronic structure, and the f-sum rule derived here does not cover the whole band. However, according to the results derived so far, there is the possibility of a transfer of spectral weight beyond the artificial cutoff Λ_I introduced to delimitate the continuous description. In fact, some related effect has been observed in the Coulomb impurity problem in graphene [229], where a bound state appears beyond the band, i.e., in the high-energy sector.

The relative lack of importance of Coulomb effects in graphene is in agreement with the experimental observation that electronic carriers are very well described by free Dirac fermions. This is specially true for undoped graphene, but it also applies to doped graphene, where dissipative processes would be dominated by the excitation of the incoherent particle - hole background. Systematic experimental studies, however, are still expected to give a clear trace of the plasmon mode in doped graphene, which in fact seems to have been observed in ARPES experiments [92, 210, 211] and could be in principle detected in inelastic X-ray scattering experiments, where information about the imaginary part of the electron susceptibility may be in principle extracted.

Moreover, as mentioned in the introduction to this chapter, another physical quantity where this analysis might have implications is the van der Waals force between graphene and other neutral

	Free Undoped	Free Doped	RPA Undoped	RPA Doped	Beyond RPA Undoped
Inter-band	$\Lambda_E q^2$	$(\Lambda_E - 2E_F)q^2$	$\Lambda_E q^2$	$(\Lambda_E - 2E_F)q^2$	$\Lambda_E q^2$
Intra-band	-	$2E_F q^2$	-	$v_F^2 q^4/g^2 E_F$	-
Plasmon/excitons	-	-	-	$2E_F q^2$	$v_F q^3/g$
High energy sector	-	-	$g v_F q^3$	$g v_F q^3$	$g v_F q^3$

Table 7.1: Contributions to the f-sum rule from the different excitations present in different approximations to the interacting problem in graphene, both for doped and undoped samples.

systems, i.e., another graphene layer or a substrate [236]. Remember that in principle when one excitation saturates the f-sum rule at leading order, it is responsible of most of the coupling to another neutral system via van der Waals forces. Hence, according to Table 7.1, in undoped graphene is not expected that the collective excitations, if they exist, change the leading behavior of the van der Waals force, that would be dominated by the electron-hole contribution, $E^{(2)} = -V_i(\frac{z_0}{z})^3$, as was calculated in [259]. On the contrary, in doped graphene, the response of the plasmon does give a new contribution, since it is no longer of subleading order:

$$E^{(2)} = -V_i(\frac{z_0}{z})^3 - V_{pl}(\frac{z_0}{z})^{5/2} \tag{7.39}$$

For an intermediate regime of distances, the dominant interaction is the one coming from the response of particle - hole excitations, as $V_i \gg V_{pl}$. The leading contribution, however, should be the one coming from the plasmon, being the one which decays more slowly.

7.6 Conclusions

In this chapter I have derived the f-sum rule for Dirac electrons in graphene and applied it to the spectral transfer analysis of different approximations to the Coulomb interacting problem, sometimes referred to as the Dirac liquid. The f-sum rule is a powerful tool to study many-body systems, since it must be satisfied by a general class of interactions that conserve particle number, including Coulomb, but its expression can be easily derived within the the non-interacting theory. This, in turn, occurs because the f-sum rule itself is an statement of the particle number conservation. Among the applications of this exact identity, I can recount self-consistency checks of approximations for the interacting theory and analysis of spectral weight transfer between excitations. Additionally, if some excitations turn out to saturate the f-sum rule, it is expected on general grounds that they will rule the response of the system to external probes that couple to the density, as well as a dominant role in certain interactions like van der Waals forces.

In this regard, I have shown that the RPA theory for undoped and doped graphene fulfills the f-sum rule, though an analysis of the spectral weight transfer gives signatures of an unconventional behavior. Instead of showing a transfer among states around the same energy scale, it involves two different scales, one being at the order of the cutoff. When vertex corrections are included, this behavior is not

changed, being a feature of the Dirac liquid. Although the f-sum rule derived here only applies to low-energy graphene, it is expected that a similar transfer of spectral weight still occurs if the the whole band is taken into account.

Finally, I have studied the relative importance of the different excitations predicted close to the Dirac point in graphene. The f-sum rule is essentially saturated by interband particle-hole excitations, though in doped graphene the collective plasmon acquires some importance which should have measurable consequences in ARPES or X-ray inelastic scattering experiments. This is not the case in undoped graphene, where any new excitation coming from Coulomb interactions is essentially negligible compared to the electron-hole ones, as far as the spectral weight is concerned. Surprisingly, this feature remains true even for the collective mode predicted when vertex corrections are taken into account. Therefore, its possible experimental observation, as happens to other excitations different from the electron-hole ones in undoped graphene, can be technically challenging. As far as the measurements imply a certain average of the spectral weight, the analysis presented here indicates that undoped graphene will respond to experimental probes essentially as a non-interacting system.

8 The two-body problem and strong coupling phases in graphene

There was a sound like that of the gentle closing of a portal as big as the sky, the great door of heaven being closed softly. It was a grand AH-WHOOM.

Kurt Vonnegut (Cat's Cradle)

Summary

This chapter constitutes the bulk of my research done in the field of interactions in graphene monolayers. It is an attempt to shed light on the controversial problem of strong coupling phases in graphene, though it contains various other results that may have consequences in different problems. As it was remarked in Chapter 5, there is an increasing number of evidences in the recent literature pointing out the existence of an insulating phase above a certain critical coupling g_c. Low-energy electrons of undoped graphene, that for interactions weaker than this critical one preserve the electronic structure of non-interacting graphene, suddenly become aware of the impossibility of *ignoring* the existence of other electrons and find more favorable to relaxate to a new configuration in which, likely, they form composed objects (excitons) that require a finite energy to be excited. The system loses its capabilities of sustaining currents for arbitrary low energies, and becomes insulating. Such a dramatic change of the delicate balance that safeguards the order of things, this *grand AH-WHOOM* of graphene, will be the *leiv motiv* of this chapter.

From the many ways one can try to gain some understanding on this speculated phase transition in the strong coupling regime, I will approach the problem from the point of view of two-body instabilities. The reason to follow this course of action is rooted to the study of the Coulomb impurity problem in graphene. As it was explained in Chapter 5, this problem shows an anomalous behavior of the wave-function above a critical coupling that has been related to the formation of excitons. However, it is the case of two electrons the one that should be better connected to the many-body problem, mostly if, as we will learn throughout this chapter, that for Dirac electrons the two-body problem cannot be mapped to that of a single impurity.

Since somehow this tale starts from a single particle to end up dealing with many-body phenomena, it is structured from an inductive perspective: in section I, I will review the Coulomb impurity problem, emphasizing why it may contain some information about the many-body phase transition. Section II is devoted to the two-body problem in graphene, showing that it cannot be reduced to the single-particle one, and how it also contains important information about strong-coupling many-

body behavior. Nevertheless, we will learn that it represents an interesting problem itself, and most of this chapter will be devoted to the understanding of its most prominent features. In Section III we will give the first steps to the real many-body problem, studying the problem of a single exciton in graphene, i.e., modifying the results of the previous section by including the filled Dirac sea in the description. Then, in section IV, I will describe the variational solution to the many-body problem, trying to reconnect with previous approaches. Last section summarizes the main conclusions of the chapter. The contents of this chapter regarding the two-body problem are contained in [280]. The rest of is still in preparation for publication.

8.1 Introduction: the Coulomb impurity problem in graphene

Let me start with a single Dirac particle in a Coulomb potential. This problem has an analytical solution that was published in [229–231, 281]. As it has been usual so far in this thesis, I will restrict the discussion to a single valley and spin channel of the problem, since these four degrees-of-freedom remain uncoupled in the presence of a Coulomb potential. The Dirac equation reads ($\hbar = v_f = 1$):

$$\begin{bmatrix} \frac{g}{r} & -i\partial_x - \partial_y \\ -i\partial_x + \partial_y & \frac{g}{r} \end{bmatrix} \begin{bmatrix} \Psi_A(\mathbf{r}) \\ \Psi_B(\mathbf{r}) \end{bmatrix} = E \begin{bmatrix} \Psi_A(\mathbf{r}) \\ \Psi_B(\mathbf{r}) \end{bmatrix} \tag{8.1}$$

where, remember, the pseudo-spin index $i = A, B$ refers to the two inequivalent sites of the unit cell in the honeycomb lattice. In order to obtain the solution, it is convenient to switch to polar coordinates (r, ϕ), by using:

$$i\partial_x + \partial_y = e^{-i\phi}(i\partial_r + \frac{1}{r}\partial_\phi) \tag{8.2}$$

In this basis, the total angular momentum $J_z = L_z + \sigma_z/2$ (where $L_z = -i\partial_\phi$) is a conserved quantity. Therefore, an ansatz for the solution based on the eigenfunctions of this operator can be proposed:

$$\Psi_l(r, \phi) = \frac{1}{\sqrt{r}} \begin{bmatrix} e^{i(l-(1/2))\phi}\psi_l^A(r) \\ ie^{i(l+(1/2))\phi}\psi_l^B(r) \end{bmatrix} \tag{8.3}$$

where $l = \pm 1/2, \pm 3/2, ...$ Now, the equation for the radial components of the wave-function is the following:

$$\begin{bmatrix} \frac{g}{r} & \partial_r + \frac{l}{r} \\ -\partial_r + \frac{l}{r} & \frac{g}{r} \end{bmatrix} \begin{bmatrix} \psi_l^A(r) \\ \psi_l^B(r) \end{bmatrix} = E \begin{bmatrix} \psi_l^A(r) \\ \psi_l^B(r) \end{bmatrix} \tag{8.4}$$

A more convenient form of this equation can be found by analyzing its long and short distances behavior. For $r \to 0$, the wave-function behaves like $\psi(r \to 0) \sim r^\gamma$, where $\gamma \equiv \sqrt{l^2 - g^2}$ [281] and we are only considering the physically normalizable solutions. For $r \to \infty$ the solutions are plane-waves, $\psi(r \to \infty) \sim e^{\pm iEr}$. Then we make the following ansatz for the radial wave-function:

$$\psi(r) = \rho^\gamma e^{-\rho/2}\phi(r) \tag{8.5}$$

where $\rho = i2Er$ is a dimensionless distance. The new system of equations reads:

$$\begin{bmatrix} g + i\frac{\rho}{2} & \rho\partial_\rho - \frac{\rho}{2} + \gamma + l \\ -\rho\partial_\rho + \frac{\rho}{2} - \gamma + l & g + i\frac{\rho}{2} \end{bmatrix} \begin{bmatrix} \phi_l^A(\rho) \\ \phi_l^B(\rho) \end{bmatrix} = 0 \tag{8.6}$$

Finally, we can rotate the wave-functions in the way:

$$Q_1(\rho) = \phi_l^A(\rho) - i\phi_l^B(\rho)$$
$$Q_2(\rho) = \phi_l^A(\rho) + i\phi_l^B(\rho) \tag{8.7}$$

The new wave-functions satisfy the following system of equations:

$$(\rho\partial_\rho + \gamma - ig)Q_1 - lQ_2 = 0$$
$$(\rho\partial_\rho - \rho + \gamma + ig)Q_2 + lQ_1 = 0 \tag{8.8}$$

that is equivalent to second order Kummer differential equations for every independent component. Hence, the solutions are confluent hypergeometric (Kummer) functions $\mathcal{F}(a, c; z)$ [282]:

$$Q_1 = C_1\mathcal{F}(\gamma - ig, 2\gamma + 1; \rho) \tag{8.9}$$
$$Q_2 = C_2\mathcal{F}(\gamma + 1 - ig, 2\gamma + 1; \rho) \tag{8.10}$$

being the coefficients C_i dependent by imposing the overall normalization of the wave-function, namely [281]:

$$c_{12} = \frac{C_1}{C_2} = \frac{\gamma + ig}{l} \tag{8.11}$$

The final solution to the radial equation is given by:

$$\psi_l^A(r) = \rho^\gamma e^{-\rho/2}\frac{C_1}{2}\left(\mathcal{F}(\gamma - ig, 2\gamma + 1; \rho) + ic_{12}\mathcal{F}(\gamma + 1 - ig, 2\gamma + 1; \rho)\right) \tag{8.12}$$
$$\psi_l^B(r) = \rho^\gamma e^{-\rho/2}\frac{C_1}{2}\left(\mathcal{F}(\gamma - ig, 2\gamma + 1; \rho) - ic_{12}\mathcal{F}(\gamma + 1 - ig, 2\gamma + 1; \rho)\right) \tag{8.13}$$

These steps will be useful later in this chapter to obtain the analytical solution of the two-body problem in some limiting cases. However, in order to extract the most important information from the point of view of the many-body problem, we do not need to know the exact solution. It is already contained in the short-distances limit of the equations, that was shown to go like $r^{\gamma-1/2}$, where $\gamma = \sqrt{l^2 - g^2}$. When $|g| > g_c \equiv |l|$, γ is a complex number, and the short-distances wave-function becomes ill-defined, since it oscillates dramatically as $r \to 0$ is approached. Since $l = \pm 1/2, \pm 3/2, ...$, this means that higher angular-momenta have increasingly large critical couplings, the lower corresponding to $l = \pm 1/2$, $g_c = 1/2$.

The interpretation given in the literature to this phenomenon is named the *Dirac vacuum breakdown*, and it connects the ill-behavior of the wave-function to the generation of particle-hole pairs from the Dirac sea for strong enough interactions [281]. In principle, this means that the whole many-body Dirac sea should be included in the description of the problem. However, several consequences of this scenario can be yet addressed within the single-particle picture following the lines already sketched by Friedel [283]. In [229] and [230], non-linear screening effects due to the excess of charge in the impurity were reported, the screening being produced by the Dirac sea polarization. This excess of charge can be understood by generalizing the Coulomb impurity to Z positive charges, giving therefore a dimensionless coupling:

$$\beta \equiv \frac{Ze^2}{\kappa\hbar v_F} = Zg \tag{8.14}$$

Now the condition for Dirac breakdown is $\beta > \beta_c$, being the lowest critical value $\beta_c = 1/2$. The excess of charge is given, for this channel, by $\beta - 1/2 > 0$. In this scenario the impurity charge is said to be supercritical (as opposed to subcritical charges for $\beta < \beta_c$) . The polarization of the Dirac sea entails spatial oscillations of the charge density near the impurity, whose amplitude increases as the nucleus is approached. Being somewhat similar to Friedel oscillations in solids, the main difference arises from the fact that in this case the Fermi energy is zero, and the period of the oscillations depends on the only scale left in the problem, the underlying lattice cutoff Λ^{-1}. Another striking consequence of supercritical charges is the appearance of quasi-Rydberg states in the region $r < r_0 = \beta/E$ [231], being r_0 the classical turning point. They can be seen as quasibound states trapped as a consequence of the existence of a classical forbidden region. However, due to Klein tunnelling, they become hybridized with the scattering states, and its main manifestation is the appearance of resonances in the scattering processes.

From the point of view of electron interactions in graphene, it has been pointed out in the literature [232, 233] that this Dirac breakdown in the Coulomb impurity problem might have implications in the many-particle Dirac problem with Coulomb interactions. After all, $Z = 1$ in this approach is equivalent to the problem of an electron and a hole in interaction. The main difference, however, comes from the fact that here the impurity is placed at rest. For Schrödinger electrons, of course, this is sufficient to find the solution of the problem in any other reference system, since center-of-mass and relative coordinates are decoupled in the Hamiltonian. As I will show in the next section, this is not in fact the case for graphene Dirac electrons, and the general two-body problem must be addressed independently.

8.2 The two-body problem in graphene

8.2.1 General features

My aim is to address the problem of two Dirac electrons living in two-dimensions and interacting through non-relativistic central potentials, with a special emphasis in the Coulomb interaction. This makes the problem suitable to understand graphene physics, being also the source of its novelty, since the two-body problem for relativistic Dirac particles in three dimensions is already well understood.

Once again, let me concentrate on a single valley of graphene, as well as one of the spin components. As there are not external magnetic fields, and spin-orbit couplings are not considered in this description, valley and spin degrees of freedom are decoupled, and in order to analyze the spatial wave-functions it suffices to study a single channel and consider later the extra degeneracy. Notice, however, that these degrees-of-freedom can yield non-trivial consequences on the symmetry properties of the wave-function, something that I will address in a specific section.

The single-body Dirac equation has been discussed in several places along this thesis, so I will not introduce it again. Two-particle wave functions can be constructed from the tensor product of single-particle ones, $\Psi_{ij}(\mathbf{r}_1, \mathbf{r}_2) \equiv \Psi_i(\mathbf{r}_1) \otimes \Psi_j(\mathbf{r}_2)$. This allows us to write the Schrödinger equation for

the interacting problem,

$$(\mathcal{H}_1 + \mathcal{H}_2 + \mathcal{H}_{1,2})\Psi(\mathbf{r}_1, \mathbf{r}_2) = E\Psi(\mathbf{r}_1, \mathbf{r}_2) \tag{8.15}$$

in the language of four-component spinors:

$$\begin{bmatrix} v(r) & -i\partial_{x_2} - \partial_{y_2} & -i\partial_{x_1} - \partial_{y_1} & 0 \\ -i\partial_{x_2} + \partial_{y_2} & v(r) & 0 & -i\partial_{x_1} - \partial_{y_1} \\ -i\partial_{x_1} + \partial_{y_1} & 0 & v(r) & -i\partial_{x_2} - \partial_{y_2} \\ 0 & -i\partial_{x_1} + \partial_{y_1} & -i\partial_{x_2} + \partial_{y_2} & v(r) \end{bmatrix} \begin{bmatrix} \Psi_{AA}(\mathbf{r}_1, \mathbf{r}_2) \\ \Psi_{AB}(\mathbf{r}_1, \mathbf{r}_2) \\ \Psi_{BA}(\mathbf{r}_1, \mathbf{r}_2) \\ \Psi_{BB}(\mathbf{r}_1, \mathbf{r}_2) \end{bmatrix} = E \begin{bmatrix} \Psi_{AA}(\mathbf{r}_1, \mathbf{r}_2) \\ \Psi_{AB}(\mathbf{r}_1, \mathbf{r}_2) \\ \Psi_{BA}(\mathbf{r}_1, \mathbf{r}_2) \\ \Psi_{BB}(\mathbf{r}_1, \mathbf{r}_2) \end{bmatrix} \tag{8.16}$$

Since we are dealing with translationally invariant potentials, we can switch to the center-of-mass frame, defining the new coordinates $\mathbf{R} = \frac{\mathbf{r}_1 + \mathbf{r}_2}{2}$ and $\mathbf{r} = \mathbf{r}_1 - \mathbf{r}_2$. It is also convenient to apply the unitary transformation

$$\begin{aligned} \Psi_1 &= \Psi_{AA} \\ \Psi_2 &= \frac{1}{\sqrt{2}}(\Psi_{AB} + \Psi_{BA}) \\ \Psi_3 &= \frac{1}{\sqrt{2}}(\Psi_{AB} - \Psi_{BA}) \\ \Psi_4 &= \Psi_{BB} \end{aligned} \tag{8.17}$$

and use a plane wave ansatz for the center-of-mass part of the wave function, $\Psi_i(\mathbf{R}, \mathbf{r}) = e^{i\mathbf{K}\cdot\mathbf{R}}\psi_i(\mathbf{r})$. We arrive at the following eigenvalue problem:

$$\begin{bmatrix} v(r) & \frac{1}{\sqrt{2}}Ke^{-i\theta_K} & \sqrt{2}e^{-i\phi}(i\partial_r + \frac{1}{r}\partial_\phi) & 0 \\ \frac{1}{\sqrt{2}}Ke^{i\theta_K} & v(r) & 0 & \frac{1}{\sqrt{2}}Ke^{-i\theta_K} \\ \sqrt{2}e^{i\phi}(i\partial_r - \frac{1}{r}\partial_\phi) & 0 & v(r) & -\sqrt{2}e^{-i\phi}(i\partial_r + \frac{1}{r}\partial_\phi) \\ 0 & \frac{1}{\sqrt{2}}Ke^{i\theta_K} & -\sqrt{2}e^{i\phi}(i\partial_r - \frac{1}{r}\partial_\phi) & v(r) \end{bmatrix} \begin{bmatrix} \psi_1 \\ \psi_2 \\ \psi_3 \\ \psi_4 \end{bmatrix} = E \begin{bmatrix} \psi_1 \\ \psi_2 \\ \psi_3 \\ \psi_4 \end{bmatrix} \tag{8.18}$$

where $\theta_K \equiv \arctan(K_y/K_x)$ and polar coordinates are used for the relative coordinate. As a first remark on this equation, let me point out that the center-of-mass coordinate does not decouple from the relative one, even though the potential only depends on the latter. Since the free-problem has the structure of a relativistic one, it could be tempting to apply a Lorentz transformation in order to simplify its structure. However, the presence of non-covariant potentials prevents this approach to simplify the analysis, and we will not follow it.

The coupling of center-of-mass and relative coordinates can be seen in turn as a consequence of the chiral nature of the electron carriers, where pseudo-spin and momentum are coupled. This kind of coupling also prevents the Hamiltonian from commuting with the relative angular momentum, thus frustrating a possible decomposition of the problem in terms of partial waves. Moreover, it makes not possible to reduce the problem to the form studied in Section I for the Coulomb impurity problem. Therefore, from here on, we can expect new exciting phenomena arising.

8.2.2 The case $K = 0$

In order to gain insight into the many-body problem, the most interesting case is that of zero total center-of-mass momentum. Then the two particles have opposite momenta, like in the Cooper channel in metals. Any pairing effect should be particularly important in this energetically most favorable case. It is also the simplest one, because it decouples the second component $\psi_2(r)$ from the rest. In effect, the equation for this component reads

$$[v(r) - E]\psi_2(r) = 0 \tag{8.19}$$

whose solution is $\psi_2(r) = 0$ except at the particular point $v(r) = E$, if it exists. That point having measure zero, we can henceforth ignore the ψ_2 component as physically irrelevant. However, we will see later that, at the point where $v(r) = E$ is satisfied, zero-energy states are responsible for important non-analyticities in the other components.

We are thus left with an effective three-component problem. Remarkably, the $K = 0$ Hamiltonian commutes with the relative angular momentum, given by:

$$L = L_1 + L_2 = -i(x_1\partial_{y_1} - y_1\partial_{x_1})\mathcal{I}_1 + \sigma_{z1} + -i(x_2\partial_{y_2} - y_2\partial_{x_2})\mathcal{I}_2 + \sigma_{z2} \tag{8.20}$$

so we can use its eigenstates to make an ansatz for the wave-function:

$$\begin{bmatrix} \psi_1(\mathbf{r}) \\ \psi_3(\mathbf{r}) \\ \psi_4(\mathbf{r}) \end{bmatrix} \equiv \begin{bmatrix} e^{i(l-1)\phi}\phi_1(r) \\ -\frac{i}{\sqrt{2}}e^{il\phi}\phi_2(r) \\ e^{i(l+1)\phi}\phi_3(r) \end{bmatrix} \tag{8.21}$$

where the prefactors have been chosen for convenience. Here, l refers now to the eigenvalues of the operator L, and takes integer values, $l = 0, \pm 1, \pm 2, ...$ It must not be confused with the single-particle angular momentum introduced in the last section, for the Coulomb impurity problem. In addition, notice that the labeling of the components in Eq. (8.21) has been changed in order to accommodate it to the three-component case. After using this ansatz, the system of equations reads:

$$\begin{bmatrix} v(r) - E & \partial_r + \frac{l}{r} & 0 \\ -2(\partial_r - \frac{l-1}{r}) & v(r) - E & 2(\partial_r + \frac{l+1}{r}) \\ 0 & -\partial_r + \frac{l}{r} & v(r) - E \end{bmatrix} \begin{bmatrix} \phi_1(r) \\ \phi_2(r) \\ \phi_3(r) \end{bmatrix} = 0 \tag{8.22}$$

It is interesting to note that these equations, as well as those directly derived from the full Hamiltonian for $K = 0$, Eq. (8.18), can also be obtained as the continuum limit of a one-particle lattice Hamiltonian, defined in a triangular lattice with three sites in the unit cell, as initially considered by Sutherland [284]. A scheme of this lattice is shown in Fig. 8.1. It has three bands, one with a flat energy dispersion relation. For two of the bands, the single particle density of states (DOS) is linear in the energy, $N(E) \propto |E|$, like in graphene. The third band being flat, translates into a singularity in the DOS at $E = 0$. These zero-energy states will have striking consequences in the physics of the two-body problem, as we will see later.

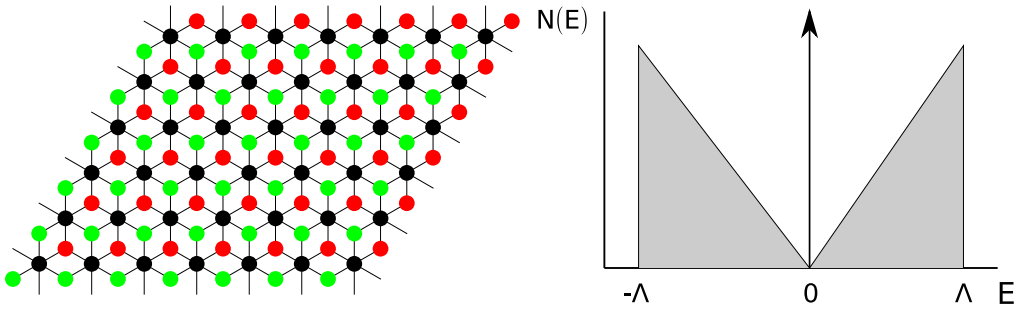

Figure 8.1: Left: Scheme of the lattice proposed by Sutherland in Ref. [284]. The two-body problem in the low-energy sector of the honeycomb lattice, for $K = 0$, is mathematically equivalent to a single-particle problem in this lattice. Right: Density of states of a free-particle in the Sutherland lattice. Zero-energy states appear due to the existence of a flat band.

Within this formulation, the case $l = 0$ is the most symmetric one:

$$\psi(r) = \begin{bmatrix} e^{-i\phi}\phi_1(r) \\ -\frac{i}{\sqrt{2}}\phi_2(r) \\ e^{i\phi}\phi_3(r) \end{bmatrix} \tag{8.23}$$

Henceforth, it will be referred to as the s-wave, and later we will learn that simple solutions can be obtained for this case taking advantage of its symmetry, that reduces the problem to an effective single-particle one.

Symmetry properties

Let me now analyze the symmetry properties of the $K = 0$ solutions. In the original basis, the two-body wave-functions read:

$$\begin{bmatrix} \Psi_{AA}(\mathbf{r}_1, \mathbf{r}_2) \\ \Psi_{AB}(\mathbf{r}_1, \mathbf{r}_2) \\ \Psi_{BA}(\mathbf{r}_1, \mathbf{r}_2) \\ \Psi_{BB}(\mathbf{r}_1, \mathbf{r}_2) \end{bmatrix}_{K=0} = \begin{bmatrix} e^{i(l-1)\phi}\phi_1(r) \\ -\frac{i}{2}e^{il\phi}\phi_2(r) \\ \frac{i}{2}e^{il\phi}\phi_2(r) \\ e^{i(l+1)\phi}\phi_3(r) \end{bmatrix} \tag{8.24}$$

where the symmetric combination has been taken $\psi_2 = 0$, as argued above. This wave function has a spinorial structure, due to the pseudo-spin of the particles, and a spatial structure coupled to the first. The symmetry properties under exchange of particles are studied by doing the transformation:

$$\begin{aligned} \mathbf{r}_1 &\rightleftharpoons \mathbf{r}_2 \\ \Psi_{AB} &\to \Psi_{BA} \end{aligned} \tag{8.25}$$

The first transformation, for $K = 0$, translates into $\phi \to \phi + \pi$. It follows immediately that wave-functions with l even are antisymmetric under particle exchange, while those with l odd are symmetric. Hence, the s-wave is, interestingly, antisymmetric. This somewhat counterintuitive result reflects the role of the sublattice pseudo-spin in the orbital wave-function.

This has consequences on the total wave-functions, once both spin and valley degrees of freedom are also considered. In this chapter I only will consider two particles that belong to the same valley. Since their total wave function must be antisymmetric, the following two families of solutions appear:

$$\begin{aligned} &\text{(i)} \quad \Psi_{K=0,l=\text{odd}}(\mathbf{r}_1,\mathbf{r}_2)\otimes\tfrac{1}{\sqrt{2}}\left(|\uparrow\downarrow\rangle-|\downarrow\uparrow\rangle\right)\\ &\text{(ii)} \quad \Psi_{K=0,l=\text{even}}(\mathbf{r}_1,\mathbf{r}_2)\otimes|\uparrow\uparrow\rangle\\ &\qquad\quad \Psi_{K=0,l=\text{even}}(\mathbf{r}_1,\mathbf{r}_2)\otimes|\downarrow\downarrow\rangle\\ &\qquad\quad \Psi_{K=0,l=\text{even}}(\mathbf{r}_1,\mathbf{r}_2)\otimes\tfrac{1}{\sqrt{2}}\left(|\uparrow\downarrow\rangle+|\downarrow\uparrow\rangle\right)\end{aligned} \tag{8.26}$$

Therefore, the lowest angular-momentum channel ($l = 0$) corresponds to a triplet spin-state, as opposed to what happens with ordinary Schrödinger electrons.

Other mathematical properties

Equation (8.22) comprises three coupled differential equations. Adding the first and the third equation we may solve for ϕ_2 in terms of ϕ_1 and ϕ_3:

$$\phi_2 = \frac{r}{2l}\varepsilon(r)(\phi_1+\phi_3) \tag{8.27}$$

where $\varepsilon(r) \equiv E - v(r)$. Subtracting the same two equations, we obtain:

$$\partial_r\phi_2 = \varepsilon(r)(\phi_3-\phi_1) \tag{8.28}$$

Deriving Eq. (8.27) and relating the result to Eq. (8.28), the result reads:

$$\partial_r[\varepsilon(\phi_1+\phi_3)] = \frac{\varepsilon}{r}\left[(2l-1)\phi_3-(2l+1)\phi_1\right] \tag{8.29}$$

On the other hand, the second equation of system (8.22) can be rewritten as:

$$\partial_r(\phi_1-\phi_3) = \left(\frac{l-1}{r}-\frac{\varepsilon^2 r}{4l}\right)\phi_1+\left(\frac{l+1}{r}-\frac{\varepsilon^2 r}{4l}\right)\phi_3 \tag{8.30}$$

Thus, system (8.22) can be solved in principle by first solving for ϕ_1 and ϕ_3 from (8.29) and (8.30) and then obtaining ϕ_2 from (8.27). The absolute values of ϕ_1 and ϕ_2 should remain bounded as long as $\varepsilon(r)$ is bounded.

Another important issue arises when $\varepsilon \to 0$, i.e., at those points where the kinetic energy vanishes, whenever $l \neq 0$. For a smooth potential, a linear approximation of $\varepsilon(r)$ around the vanishing point r_0 holds, $\varepsilon(r) = \lambda x + \mathcal{O}(x^2)$, where $x \equiv r - r_0$. The differential equations (8.29) and (8.30) can be approximated around this point, yielding:

$$\frac{d}{dx}\left[x(\phi_1+\phi_3)\right] \simeq 0 \tag{8.31}$$

$$\frac{d}{dx}(\phi_1-\phi_3) \simeq -\frac{1}{r_0}(\phi_1+\phi_3) \tag{8.32}$$

The solution for these equations reads $\phi_1+\phi_3 \simeq -2C_2/x$ and $\phi_1-\phi_3 \simeq 2C_1+(2C_2/r_0)\log(x)$. We see that, for $l > 0$, a smooth potential will show non-analyticities close to r_0 in ϕ_1 and ϕ_3, while ϕ_2

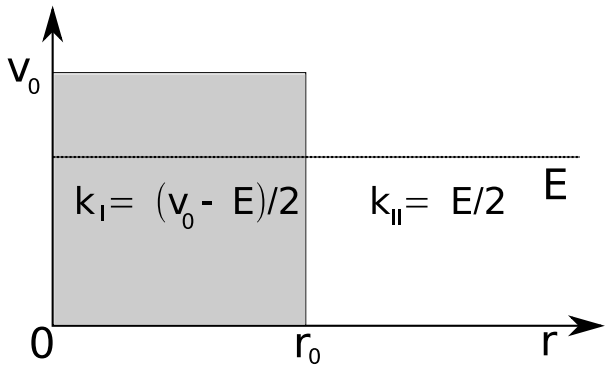

Figure 8.2: Scattering of two particles interacting through a short-range potential. The energy E is taken below the classical barrier v_0.

will remain continuous:

$$\begin{aligned} \phi_1 &\simeq C_1 + \frac{C_2}{r_0}\log(x) - \frac{C_2}{x} \\ \phi_2 &\simeq \frac{\lambda r_0}{2l} C_2 \\ \phi_3 &\simeq -C_1 - \frac{C_2}{r_0}\log(x) - \frac{C_2}{x} \end{aligned} \tag{8.33}$$

Notice, however, that these non-analyticities give a finite contribution to the probability $\int dr\, r\, |\phi|^2$. Therefore they are physical solutions of the Dirac equation.

8.2.3 Step potential

Some physical insight into the subtle properties of the interacting two-particle problem can be obtained by studying the simpler case of a step potential, which is typically considered a good effective description of the more general class of short-range potentials. Its expression is:

$$v(r) = \begin{cases} v_0 & r < r_0 \\ 0 & r > r_0 \end{cases} \tag{8.34}$$

To obtain the solutions, I will follow the typical procedure sketched in Quantum Mechanics textbooks for the Schrödinger equation, i.e., to construct the solutions for each region and eventually match them, as shown schematically in Fig. 8.2.

For arbitrary energy E, the solutions are given by Bessel functions of the form:

$$\chi_1 = \begin{bmatrix} aJ_{l-1}(kr) \\ bJ_l(kr) \\ cJ_{l+1}(kr) \end{bmatrix}, \chi_2 = \begin{bmatrix} aY_{l-1}(kr) \\ bY_l(kr) \\ cY_{l+1}(kr) \end{bmatrix} \tag{8.35}$$

where the coefficients and the eigenvalues are determined from the diagonalization of Eq. (8.22), the

result being:

$$E = v_0 + 2k, \left(\tfrac{1}{2}, \quad 1, \quad \tfrac{1}{2} \right) \tag{8.36}$$

$$E = v_0 - 2k, \left(\tfrac{1}{2}, \quad -1, \quad \tfrac{1}{2} \right) \tag{8.37}$$

$$E = v_0, \frac{1}{\sqrt{2}} \left(1, \quad 0, \quad -1 \right) \tag{8.38}$$

The first solution corresponds to two electrons located in the upper Dirac cone, while in the second solution the two electrons are in the lower cone. The third solution describes the case where one particle is in the upper cone and the other one in the lower cone. Due to the zero total center-of-mass momentum, this solution has zero total energy. Notice that, for fixed E, the relation of k with the energy depends on the solution chosen. The third one is valid for arbitrary k. Importantly, when $E = v_0$ there are other zero-energy states that are also solutions of the two-particle Dirac equation. They have the form

$$\chi_3 = \frac{r^\alpha}{[1 + (\frac{\alpha - l + 1}{\alpha + l + 1})^2]^{1/2}} \left(1, \quad 0, \quad \tfrac{\alpha - l + 1}{\alpha + l + 1} \right), \tag{8.39}$$

where α is a continuous parameter that can take any real value. These polynomial solutions are in general non-physical, since they cannot be properly normalized. However, they can be considered responsible for the non-analyticities shown to exist at those points where the kinetic energy vanishes, as it was shown before. For the step potential, which is non-analytic itself, the existence of zero-energy states induces discontinuities in the radial wave-function, thus changing the usual matching conditions. How such an anomalous behavior arises is explained in detail in Appendix A.

Notice that the traditional criterion of imposing continuity of the wave-functions does not work here due to the insufficient number of matching parameters. Let me exemplify this issue by considering the situation shown in Fig. 8.2, where $k_I = (v_0 - E)/2 > 0$ and $k_{II} = E/2 > 0$. The solution for region I only includes Bessel functions of the first kind, $J_l(k_I r)$, as those of the second kind ones are singular at the origin. Hence $\phi_i^I \sim A_1 J_{l_i}(k_I r)$. For region II both solutions must be considered, $\phi_i^{II} \sim B_1 J_{l_i}(k_I r) + B_2 Y_{l_i}(k_{II}(r)$. Due to the freedom for global normalization, only two relative values of the three constants are relevant. Thus only two parameters remain to satisfy the continuity of three equations, one for every component of the wave-function, leaving the problem overdetermined.

In Appendix A it is shown that, when zero-energy states at the matching point are taken into account, a third matching parameter arises naturally which permits a discontinuity in the radial wave-function. Namely, we obtain

$$\begin{aligned} \Delta\phi_1(r_0) \equiv \phi_1^{II}(r_0) - \phi_1^I(r_0) &= -2C \\ \Delta\phi_2(r_0) &= 0 \\ \Delta\phi_3(r_0) &= -2C\,, \end{aligned} \tag{8.40}$$

where C is the extra parameter to determine. With the new matching conditions, an exact solution of the $K = 0$ case becomes possible, as detailed in Appendix B. It is also interesting to compute the solution of the differential equations numerically, as shown in Fig. 8.3. Here, the first two components of the radial wave-function are plotted. As predicted in equation (8.40), the first component shows

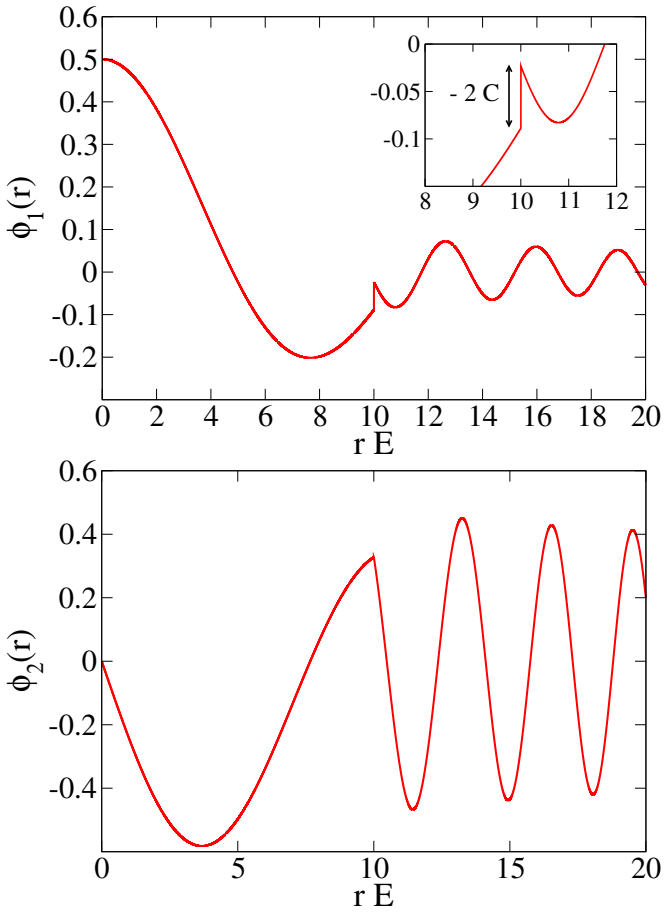

Figure 8.3: Numerical solution of the step-potential for $K = 0$ and $l = 1$ ($r_0 E = 10$, $E = v_0/2$). Top: first component of the radial wave-function. The discontinuity induced by the zero energy states arises naturally in the numerical solution. Bottom: second component of the radial wave function. As also predicted by the new matching conditions, the second component does not have a discontinuity.

a discontinuity induced by zero-energy states at the point $r = r_0$. The same consideration applies to the third component (not shown) but not for the second one.

It is also worth noting that, as expected, the s-wave shows a simpler behavior by virtue of its symmetric form. In this case, inspection of Eq. (8.22) shows $\phi_1(r) = -\phi_3(r)$ and the problem reduces to a two-component one. The matching conditions simplify then to continuity and the s-wave problem essentially behaves as that of a single particle. As a corollary, Eq. (8.40) leads to $C = 0$ in this case. Thus we may state that the $l = 0$ case has a structure similar to that of the impurity one-body problem in graphene, as it was already pointed out above.

Coulomb potential

Let me now turn to the more relevant case of a long-range Coulomb potential, $v(r) = g/r$, where $g = e^2/\epsilon\hbar v_F$ for low-energy graphene electrons. It is convenient to find a more suitable form of Eq. (8.22) in order to obtain analytical solutions when possible. This is done by the usual procedure of

analyzing the short and long distance limits, as it was done in the introduction for the Coulomb impurity problem. I will use the same notation, so be aware of the differences between both results. At short distances the wave-function components have the form $\phi_i(r \to 0) \sim r^{\gamma-1/2}$, with $\gamma^2 = \frac{1}{4}(1+4l^2-g^2)$. On the other hand, the long-distance wave-function behaves like a plane-wave of the form $\phi_i(r \to \infty) \sim e^{\pm iEr/2}$. Hence, we can make the following ansatz for the radial wave-function:

$$\phi_i(\rho) = \rho^{\gamma-1/2} e^{-\rho/2} \hat{\phi}_i(\rho) \tag{8.41}$$

where I have introduced the dimensionless radial complex coordinate $\rho = iEr$. By applying this transformation, Eq. (8.22) becomes:

$$\begin{bmatrix} i\rho+g & \rho\partial_\rho - \frac{\rho}{2} + \gamma + l - \frac{1}{2} & 0 \\ -2(\rho\partial_\rho - \frac{\rho}{2} + \gamma - l + \frac{1}{2}) & i\rho+g & 2(\rho\partial_\rho - \frac{\rho}{2} + \gamma + l + \frac{1}{2}) \\ 0 & -\rho\partial_\rho + \frac{\rho}{2} - \gamma + l + \frac{1}{2} & i\rho+g \end{bmatrix} \begin{bmatrix} \hat{\phi}_1(\rho) \\ \hat{\phi}_2(\rho) \\ \hat{\phi}_3(\rho) \end{bmatrix} = 0\,. \tag{8.42}$$

The general case is difficult to handle and only the s-wave channel admits an analytical solution, since it reduces to an effective single particle problem. Its solution can be derived following the steps given in the introduction, and is detailed in Appendix C. For general angular momentum l, Eq. (8.42) must be solved numerically, by discretizing the differential equations and setting the initial condition at $r = 0$.

Before addressing the full solution, let me point out the remarkable behavior of the wave-functions at short distances. As it happened to the Coulomb impurity, it goes like a power law $r^{\gamma-1/2}$, where now $\gamma = \frac{1}{2}\sqrt{1+4l^2-g^2}$. This sets a different critical coupling $g_c \equiv \sqrt{1+4l^2}$. For $|g| < g_c$ only positive γ is acceptable, since the other solution is not normalizable. For $|g| > g_c$ both solutions are possible, but the γ parameter becomes imaginary and the wave-function shows a pathological short-distance behavior, going like $r^{-1/2}[\cos(|\gamma|\log r) \pm i\sin(|\gamma|\log r)]$. Thus the wave-function oscillates dramatically towards the center. We saw in the Coulomb impurity problem that such a behavior has been related to an instability of the wave-function that could signal the breakdown of the Dirac vacuum. For strong enough couplings, the two-particle interaction could produce electron-hole pairs from the vacuum, and a full quantum field-theoretical treatment of the problem might be necessary. I will go into this issue in depth in Section 8.2.5. Notice that in this thesis, however, I have not studied possible single-body consequences for $g > g_c$, like the formation of quasi-bound states or oscillations in the electron density. Such a treatment has been left for future research.

The analogies with the Coulomb impurity problem can be farther stretched by doing a semiclassical analysis like that from Ref. [231]. The starting point is Eq. (8.22) for the Coulomb potential with the ansatz $\phi_i(r) = \bar{\phi}_i \frac{e^{i2p_r r}}{\sqrt{r}}$, where p_r is a slowly varying function of r. This justifies the assumption $\partial_r p_r \simeq 0$. Eq. (8.22) then reads:

$$\begin{bmatrix} \frac{g}{r} - E & i2p_r + \frac{l-1/2}{r} & 0 \\ -i4p_r + \frac{2l-1}{r} & \frac{g}{r} - E & i4p_r + \frac{2l+1}{r} \\ 0 & -i2p_r + \frac{l+1/2}{r} & \frac{g}{r} - E \end{bmatrix} \begin{bmatrix} \bar{\phi}_1 \\ \bar{\phi}_2 \\ \bar{\phi}_3 \end{bmatrix} = 0 \tag{8.43}$$

The determinant vanishes if one of the following relations is satisfied:

$$\frac{g}{r} = E\,, \tag{8.44}$$

$$p_r^2 = (\frac{g}{r} - E)^2 - \frac{1}{r^2}(4l^2+1) \tag{8.45}$$

The first equation defines a point, $r_0 \equiv g/E$, where any function p_r gives a solution thanks to the existence of zero-energy states, as discussed in the previous section for the step potential. Notice that this condition only is fulfilled for repulsive electrons with positive energy or attractive electrons with negative energy, two cases which are related through a symmetry transformation. The second equation, on the other hand, defines a non-classical region where $p_r^2 < 0$. The region is $r_1 < r < r_2$, where $r_{1,2} = \frac{g}{E} \mp \frac{1}{E}\sqrt{4l^2+1}$. Remarkably, we see that $r_1 < r_0 < r_2$, i.e. the point where zero-energy states nucleate belongs to this classically forbidden region. In the Coulomb impurity problem, the existence of a non-classical region was responsible for the appearance of quasi-bound states for $g > g_c$, and such a scenario may still hold for the two-body problem for $K = 0$, mostly when $l = 0$, where the physics is qualitatively similar. For $l \neq 0$ the existence of these states should be reconciled with the influence of zero-energy states.

So far, the two-body Coulomb problem has shown many similarities, at least qualitatively, with the Coulomb impurity problem. Let me now analyze the most striking differences, that happen when $l \neq 0$. In Fig. 8.4, a numerical estimate of the radial wave-functions is shown for $l = 1$ and two different signs of the interaction below the critical value. The main feature in this solution concerns again zero-energy states: when the condition $g/r_0 = E$ is fulfilled, zero-energy states must be taken into account and become responsible for singularities in the first and third components of the wave-function when $l \neq 0$, as shown above on general grounds. Particularly, in the Coulomb case this effect seems to yield particular consequences, such as a drastic suppression of the probability of finding the particle in $r < r_0$, and a tendency to increasingly localize the radial wave-function near $r = r_0$ when the critical point g_c is approached from below (see Fig. 8.5). We find numerically that for $g = g_c$ the relative wave-function becomes effectively localized near $r = r_0$.

These results are confirmed by studying the problem of a single particle in the Sutherland lattice [284] with a Coulomb potential. As it has been pointed out several times in this chapter, the two-body problem can be mapped into a single-body problem in this lattice. In order to do the calculations, shown in Fig. 8.6, a 30×30 lattice was employed with the structure of Ref. [284] (see Fig. 8.1) and periodic boundary conditions. The potential was set $v(r) = v_0 e^{-r/r_d}/\sqrt{r^2 + r_1^2}$, with $v_0 = t > 0, r_d = 20a$ and $r_1 = 0.5a$, where t is the hopping, and a is the distance between nearest neighbor equivalent atoms. The states considered to construct the density plots are in the range of energies $0.25t \leq E \leq 0.35t$. Since they are not eigenstates of the Hamiltonian, they are expected to contain several angular channels. However, as shown in Fig. 8.6, this energy spread is sufficient to find an enhancement of the density in the region near $E = v(r)$, which is what it was aimed to reproduce in these simulations. On the other hand, when states in the range $E < 0$ are considered, i.e., when there is not classical turning point, the density shows a delocalized distribution. In the plots, notice that there are details coming from the underlying lattice structure that are not relevant for this discussion, that is centered on the continuum limit.

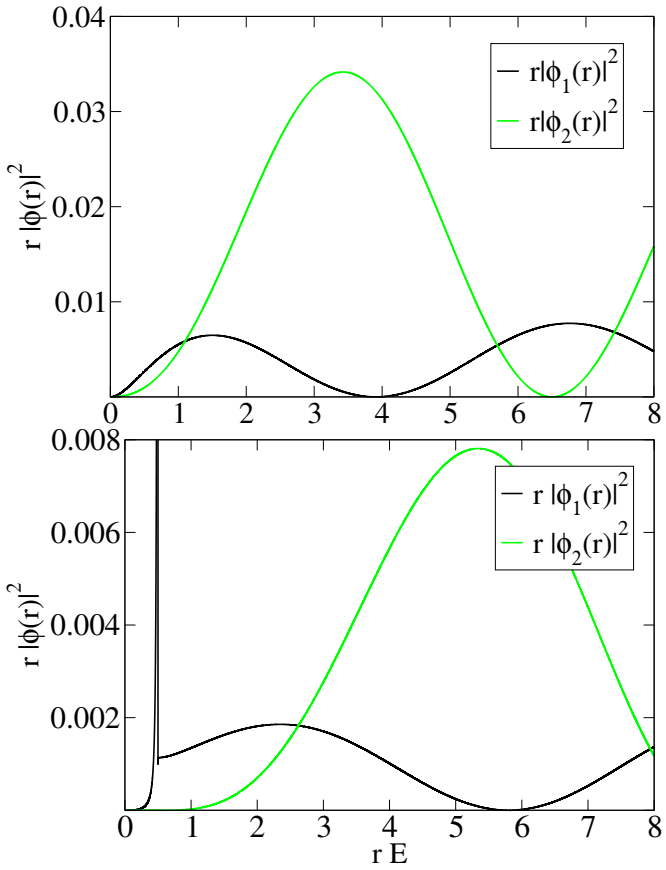

Figure 8.4: Numerical solution of the radial wave-function for the case of Coulomb interaction and zero center-of-mass momentum. The chosen angular momentum is $l = 1$. Top: wave functions for $g = -0.5$ and $E > 0$. Bottom: wave functions for $g = 0.5$ and $E > 0$. Notice that, where the condition $g/r_0 = E$ is satisfied, a singularity is induced by the localized zero-energy states.

8.2.4 Extension to finite K

Summarizing, the most salient features found so far in the problem of two interacting particles in graphene are the peculiar influence of zero-energy states and the appearance of instabilities for the Coulomb potential. A full extension of these results to a non-zero center-of-mass would require to work out the whole problem numerically, something beyond the scope of this work, where the main interest is to get insights into the many-body problem, and for this it is sufficient to consider the case $K = 0$. However, for completeness, I will discuss on general grounds to what extent the main results still apply for the general case of nonzero center-of-mass momentum.

Zero-energy states are investigated by taking $v(r) = E$ in the eigenvalue problem (8.18). Inspection of the resulting Hamiltonian reveals that it separates into two independent sectors. The Hamiltonian for the first sector reads:

$$\begin{pmatrix} \frac{1}{\sqrt{2}} K e^{i\theta_K} & \frac{1}{\sqrt{2}} K e^{-i\theta_K} \\ \sqrt{2} e^{i\phi}(i\partial_r - \frac{1}{r}\partial_\phi) & -\sqrt{2} e^{-i\phi}(i\partial_r + \frac{1}{r}\partial_\phi) \end{pmatrix} \begin{pmatrix} \psi_1(r,\phi) \\ \psi_4(r,\phi) \end{pmatrix} = 0 \tag{8.46}$$

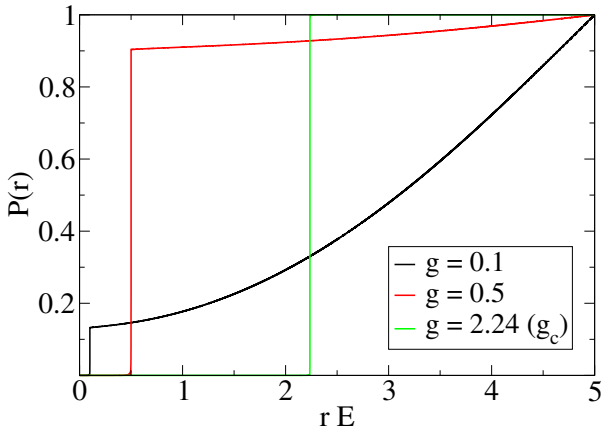

Figure 8.5: Probability of finding one electron within a distance r from the other electron, $P(r) = \sum_i \int_0^r d^2r|\phi_i(\mathbf{r})|^2$, for $K = 0$, $l = 1$, and various values of the dimensionless Coulomb coupling constant g, in the important case where a classical turning point exists ($rE = g$). Here, the influence of zero-energy states translates into (i) a suppression of the electron density for $r < r_0$, and (ii) a tendency to concentrate the probability near $r = r_0$ as the critical coupling g_c is approached. The results are normalized to their value at $rE = 5$.

As $\psi_4 = -e^{2i\theta_K}\psi_1$, the system reduces to a single differential equation:

$$(r\partial_r - \tan(\phi - \theta_K)\partial_\phi)\psi_1(r,\phi) = 0 \tag{8.47}$$

whose solution is:

$$\psi_1(r,\phi) = A_1 r^\alpha \sin^\alpha(\theta_K - \phi) \tag{8.48}$$

$$\psi_4(r,\phi) = -A_1 e^{2i\theta_K} r^\alpha \sin^\alpha(\theta_K - \phi) \tag{8.49}$$

where A_1 and α are arbitrary constants. On the other hand, the second sector has a Hamiltonian of the form:

$$\begin{pmatrix} \frac{1}{\sqrt{2}}Ke^{-i\theta_K} & \sqrt{2}e^{-i\phi}(i\partial_r + \frac{1}{r}\partial_\phi) \\ \frac{1}{\sqrt{2}}Ke^{i\theta_K} & -\sqrt{2}e^{i\phi}(i\partial_r - \frac{1}{r}\partial_\phi) \end{pmatrix} \begin{pmatrix} \psi_2(r,\phi) \\ \psi_3(r,\phi) \end{pmatrix} = 0 \tag{8.50}$$

In this case we have $\psi_2 = -\frac{2}{K}e^{-i(\phi-\theta_K)}(i\partial_r + \frac{1}{r}\partial_\phi)\psi_3$, that reduces the problem to the same differential equation given above:

$$(r\partial_r - \tan(\phi - \theta_K)\partial_\phi)\psi_1(r,\phi) = 0 \tag{8.51}$$

with solution, again:

$$\psi_2(r,\phi) = A_2\frac{K}{2} r^\beta \sin^\beta(\theta_K - \phi) \tag{8.52}$$

$$\psi_3(r,\phi) = A_2 r^{\beta-1} \sin^{\beta-1}(\theta_K - \phi) \tag{8.53}$$

Therefore the Hilbert space of solutions is two-dimensional, with the general solution for the zero-

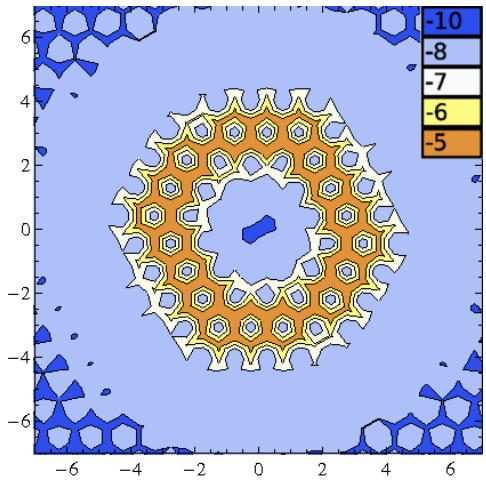

Figure 8.6: Logarithmic density distribution of the two-particle wave-function, when the interaction is Coulomb-like, for $K = 0$. One of the particles is assumed to be placed at the center of the square. The equations are discretized using the Sutherland lattice, and the energy range of the integrated states is chosen such that they cover the region where the condition $g = r_0 E$ is fulfilled. As expected, the results show a clear concentration of the density at this point r_0. The short-length features of the density plot reflect the underlying lattice structure.

energy states reading now:

$$\psi(r,\phi) = A_1 \begin{bmatrix} r^\alpha \sin^\alpha(\theta_K - \phi) \\ 0 \\ 0 \\ -r^\alpha \sin^\alpha(\theta_K - \phi) \end{bmatrix} + A_2 \begin{bmatrix} 0 \\ \frac{K}{2} r^\beta \sin^\beta(\theta_K - \phi) \\ r^{\beta-1} \sin^{\beta-1}(\theta_K - \phi) \\ 0 \end{bmatrix} \tag{8.54}$$

where A_1 and A_2, as well as α and β, can take arbitrary values. A similar analysis to that of $K = 0$ can be performed here. For the case of a step potential, they translate into a change in the matching conditions, since the introduction of two new parameters (B_1 and B_2) changes the continuity of the wave-function:

$$\begin{aligned} \Delta\psi_1(r_0,\phi) &= B_1(\phi, K, \theta_K) \\ \Delta\psi_2(r_0,\phi) &= B_2(\phi, K, \theta_K) \\ \Delta\psi_3(r_0,\phi) &= 0 \\ \Delta\psi_4(r_0,\phi) &= -e^{2i\theta_K} B_1(\phi, K, \theta_K) \end{aligned} \tag{8.55}$$

Linearization of the equations close to the point where $\varepsilon(r) = 0$ (the classical turning point) shows that, even for smooth potentials, singularities in the relative wave-functions arise. Still, they are square integrable and give a finite contribution to the probability.

As for the Coulomb instability, its existence can be probed by checking the short-distance limit of the full Hamiltonian given in (8.18), for the case $v(r) = g/r$. It is not difficult to see that the small r limit is controlled by K-independent terms. Thus, for $r \to 0$ we recover the $K = 0$ limit, where an

instability has already been identified. Hence, this instability can be expected to be a general feature of the Coulomb problem.

8.2.5 Relevance to many-body phenomena

Let me now address in more depth the connections of the results presented so far on the two-body problem with Coulomb interactions and the more complicated many-body problem in graphene. This is specially relevant when regarding the strong-coupling regime, where the exact solution of the two-body problem can give results not available from perturbative approaches. At the price, of course, of having two instead of many particles. The question is to what extent the physics of the two-body problem resembles that of the many-body problem. For Schrödinger electrons, unless the exclusion principle of the Fermi surface is taken into account, the physics of two bodies has little to say about the complicated many-body state that arises, for instance, in a superconductor. However, for Dirac electrons things seem to be different, since the two-body problem already gives a signature of the instability that might be at the heart of the many-body phase-transition.

As we already know, some authors have already suggested that the breakdown of the Dirac vacuum in the attractive Coulomb impurity problem could be related to the formation of excitons in graphene for strong enough coupling [232, 233]. This behavior is also present in the two-body problem, which should be even more relevant to the many-body physics.

In order to understand the connection, notice that in principle the problem of an interacting electron and hole can be mapped into that of two attractive electrons, with similar symmetry properties (see next section). However, as happens with the Coulomb impurity problem, a more rigorous mapping requires to consider the existence of the Dirac sea, which constraints, by Pauli's principle, the states accessible to the electron-hole pair, in analogy to the Cooper problem [187]. Such a treatment requires to work in a different basis. In next section I will describe the solution of this problem for the case of a short-range potential, showing that in fact there is a bound state above a certain critical coupling. Numerical studies of the Coulomb potential, still at a preliminary level, suggest that the same scenario applies for this interaction.

What is the connection between both phenomena? The presence of a many-body instability in the two-body problem does not necessarily imply the formation of a bound state, mostly when this instability happens for arbitrary sign of the interaction (both repulsive and attractive). In the Coulomb impurity problem, more insights into the strong-coupling wave-functions of the model were obtained, finding that the instability leads to a non-linear screening of the excess of charge. What kind of effective interaction does arise from this non-linear screening? It might happen that it renders the Coulomb interaction short-ranged but still strong enough to allow for a bound state to be formed when the whole Dirac sea is included. Of course, it could also happen that this screening only attenuates the strength of the Coulomb interaction, in which case the connection between the Dirac sea breakdown and the excitonic instability would be obscured.

In any case, the two-body problem predicts an instability above a certain critical coupling that depends on the scattering channel. For the most symmetric one, the s-wave, it is $g_c = 1$, which is larger than the smallest critical value obtained for the Coulomb impurity problem, $g_c^{\mathrm{CI}} = 0.5$. [229–

231, 281]. For higher angular-momentum channels the critical couplings increase. As an example, $g_c = 2.24$ for $l = 1$. However, at low energies those higher angular momenta are usually less important. Hence, the s-wave critical coupling should provide us with an educated guess of the corresponding value for the expected many-body instability. Remarkably, the critical values obtained so far in the theoretical literature are close to the value predicted here for the two-body problem. For the ease of comparison, let me summarize the different values predicted for the transition, that were discussed in chapter 5. Monte Carlo calculations in the lattice give a critical coupling $g_c^{\mathrm{MC}} \simeq 1.11$ [220] and $g_c^{\mathrm{Th}} \simeq 1.66$ [223]. Renormalization Group calculations yield $g_c^{\mathrm{RG}} \simeq 0.833$ [201]. Finally, a variational approach to the excitonic condensate has been recently reported to show a transition above the critical coupling $g_c^{\mathrm{var}} \simeq 1.13$ [226]. Other approximations to the self-consistent gap equation that arises in the variational context yield close values for the critical coupling (see, for instance, [232]).

Regarding the spin degree-of-freedom, as discussed above, if both electrons belong to the same valley the s-wave channel would correspond to a triplet state in the spin sector. This fact may be highly relevant for the study of the excitonic instability in the presence of an external magnetic field.

There is a second aspect of the two-body problem in graphene that could have consequences on the more complicated many-body problem: the influence of zero-energy states for $l \neq 0$ angular momentum channels. As we have seen, in those cases where the kinetic energy vanishes at some point (positive total energy and repulsive potential, or negative total energy and attractive potential), zero-energy states induce singularities in the wave-function which translate into a larger probability of finding the particle near the classical turning point r_0. Moreover, for the Coulomb potential, when the critical coupling g_c is approached, the degree of localization is increased, in a way that for $g = g_c$ the particle can be said to be essentially confined near r_0. The probability of finding the particle in any other region is not, however, a mathematical zero, so in terms of scattering states we can think that the particle spends a lot of time near r_0 as compared to other points, somehow giving rise to a quasi-bound state.

Let me address briefly possible consequences for doped graphene by discussing the role of the carrier density. We know that the latter determines the screening length, and hence imposes a first limit to the results presented here. In doped graphene, electrons at the Fermi surface have an energy $E_F = v_F k_F = v_F (4\pi n/N_s)^{1/2}$, where n is the electron density in the upper cone and $N_s = 4$ the valley and spin degeneracy. This defines a classical return distance $r_0 \equiv g/E_F \propto n^{-1/2}$ for the Fermi surface electrons at which density correlation should peak. On the other hand, the static screening of the Coulomb interaction in doped graphene is characterized by the Thomas-Fermi (TF) screening length $\lambda_{\mathrm{TF}} = g^{-2}(4\pi n N_s)^{-1/2}$ [285, 208, 209], which shows a similar density dependence, namely, $\lambda_{\mathrm{TF}} \propto n^{-1/2}$. Thus the ratio between the classical return and screening distances is independent of the density: $r_0/\lambda_{\mathrm{TF}} = N_s g^2$. For many cases we expect $r_0/\lambda_{\mathrm{TF}} > 1$, which places r_0 beyond the screening length, i.e. where the bare Coulomb interaction, for which r_0 has been calculated, does not hold. Naively this might invalidate the physics associated to zero-energy states, which is expected to occur at $r = r_0$. However, it is easy to note that the density correlation peaks have to be a robust feature of the many-body problem.

We have seen that zero-energy states intervene at the point where $v(r) = E$. It is quite reasonable to assume that, in a many-body context, that condition must be replaced by $v_{\mathrm{scr}}(r_0) = E_F$, which

defines the classical return distance r_0 for the electron gas if $v_{\rm scr}(r)$ is the screened Coulomb interaction potential. Within the TF approximation, the screened potential has the form [4, 10] $v_{\rm scr}(r_0) = (e^2/r)F(r/\lambda_{\rm TF})$, where $F(x)$ is a monotonically decreasing function satisfying $F(x) \simeq 1$ for $x \ll 1$ and $F(x) \sim x^{-2}$ for $x \gg 1$. Dimensional analysis shows that the dressed r_0 also scales like $n^{-1/2}$, which suggests that zero-energy states play a role even in the presence of screening.

8.3 The problem of a single exciton in graphene

In this section I will address the problem of a single exciton in graphene, that should provide us with a first bridge between the two-body physics studied in last section and many-body phenomena. The idea is to study the two-electron problem in the presence of the Dirac sea, which is taken into account by limiting the number of accessible states to those unoccupied at zero temperature and zero doping. However, no further interactions between the particles, apart from that of the two-body system, are included. The two-electron problem and the excitonic one can be seen to be easily mapped into each other, as we will see next.

Mapping to the two-electron problem

If two electrons repel each other, it means that an electron and a hole feel an attractive interaction, and they may form a bound state called the exciton. In second quantization, an exciton is composed of an electron-hole pair, that is generated from the Dirac sea in the way:

$$c^\dagger_{\mathbf{k},+} c_{\mathbf{k},-} |\text{Dirac}\rangle \tag{8.56}$$

where $\pm$ denote the upper and lower cone, respectively. Let me analyze the energy and momentum of this state. The free Hamiltonian being $\mathcal{H}_0 = \sum_{\mathbf{k},\sigma} \sigma k c^\dagger_{\mathbf{k},\sigma} c_{\mathbf{k},\sigma}$, applied to the electron-hole pair we have:

$$\mathcal{H}_0 \left(c^\dagger_{\mathbf{k},+} c_{\mathbf{k},-} |\text{Dirac}\rangle \right) = (E_0 + 2k) \left(c^\dagger_{\mathbf{k},+} c_{\mathbf{k},-} |\text{Dirac}\rangle \right) \tag{8.57}$$

where $E_0 \equiv -\sum_{\mathbf{k}} k$ is the energy of the Dirac sea. On the other hand, the momentum operator reads $\mathbf{K} = \sum_{\mathbf{k},\sigma} \mathbf{k} c^\dagger_{\mathbf{k},\sigma} c_{\mathbf{k},\sigma}$, and when applied to the electron-hole state:

$$\mathbf{K} \left(c^\dagger_{\mathbf{k},+} c_{\mathbf{k},-} |\text{Dirac}\rangle \right) = 0 \tag{8.58}$$

due to the fact that $\mathbf{K} \left(c_{\mathbf{k},-} |\text{Dirac}\rangle \right) = -\mathbf{k} \left(c_{\mathbf{k},-} |\text{Dirac}\rangle \right)$, i.e., holes propagate in the opposite direction that electrons.

The properties of the electron-hole pair in the presence of a repulsive interaction are then equivalent to that of two electrons in the upper cone, with opposite momenta, and attractive interaction:

$$c^\dagger_{\mathbf{k},+} c^\dagger_{-\mathbf{k},+} |\text{Dirac}\rangle \tag{8.59}$$

This has an structure similar to that of the Cooper problem in graphene. Rigorously, however, the mapping is incomplete, since the Cooper problem involves two electrons in states which are related by a time reversal transformation. This immediately implies that the Cooper pair is composed of

electrons that belong to inequivalent valleys [1]. For the excitonic problem, however, we no longer have this requirement, and it is sufficient to study the problem of two electrons in the same valley.

General formulation of the $K = 0$ problem

I will limit the discussion to the case of zero center-of-mass momentum, i.e. $K = 0$, since it is the most energetically favorable case, not carrying kinetic energy the center-of-mass. In this case, the Hamiltonian for the two-body problem is the one studied in last section. For convenience, let me express it in terms of the relative coordinate $\mathbf{r} = \mathbf{r}_1 - \mathbf{r}_2$, $r^2 = x^2 + y^2$:

$$\mathcal{H}_0 = \begin{pmatrix} v(r) & 0 & \sqrt{2}(i\partial_x + \partial_y) & 0 \\ 0 & v(r) & 0 & 0 \\ \sqrt{2}(i\partial_x - \partial_y) & 0 & v(r) & -\sqrt{2}(i\partial_x + \partial_y) \\ 0 & 0 & -\sqrt{2}(i\partial_x - \partial_y) & v(r) \end{pmatrix} \tag{8.60}$$

In order to impose the existence of the Dirac sea, we need to write this Hamiltonian in the basis that diagonalizes the free Dirac Hamiltonian. First, we make an expansion of the wave-function in plane-waves:

$$\psi(\mathbf{r}) = \sum_{\mathbf{k}} \psi(\mathbf{k}) e^{i\mathbf{k}\mathbf{r}} \tag{8.61}$$

This yields the following equation:

$$\begin{pmatrix} E & 0 & -\sqrt{2}(k_x + ik_y) & 0 \\ 0 & E & 0 & 0 \\ \sqrt{2}(k_x + ik_y) & 0 & E & \sqrt{2}(-k_x + ik_y) \\ 0 & 0 & -\sqrt{2}(k_x + ik_y) & E \end{pmatrix} \psi_{\mathbf{k}} = \frac{1}{L^2} \sum_{\mathbf{k}} v_{\mathbf{k},\mathbf{k}'} \psi_{\mathbf{k}'} \tag{8.62}$$

where:

$$v_{\mathbf{k},\mathbf{k}'} = \int d\mathbf{r} e^{i\mathbf{r}(\mathbf{k}-\mathbf{k}')} v(r) \tag{8.63}$$

is the Fourier transformed interacting potential, and L^2 the surface of the sample. Still we need a second step to impose the existence of the Dirac sea: rotating the Hamiltonian by using the transformation that diagonalizes the free case, namely:

$$U_{\mathbf{k}} = \begin{pmatrix} -\frac{1}{2}e^{-i\theta_k} & 0 & \frac{1}{\sqrt{2}}e^{-i\theta_k} & \frac{1}{2}e^{-i\theta_k} \\ 0 & 1 & 0 & 0 \\ \frac{1}{\sqrt{2}} & 0 & 0 & \frac{1}{\sqrt{2}} \\ \frac{1}{2}e^{i\theta_k} & 0 & \frac{1}{\sqrt{2}}e^{i\theta_k} & -\frac{1}{2}e^{i\theta_k} \end{pmatrix} \tag{8.64}$$

The overlapping matrix reads:

$$U_{\mathbf{k}}^{\dagger} U_{\mathbf{k}'} = \begin{pmatrix} \frac{1}{2}(1 + \cos(\theta_{k'} - \theta_k)) & 0 & \frac{1}{\sqrt{2}}\sin(\theta_{k'} - \theta_k) & \frac{1}{2}(1 - \cos(\theta_{k'} - \theta_k)) \\ 0 & 1 & 0 & 0 \\ \frac{1}{\sqrt{2}}\sin(\theta_{k'} - \theta_k) & 0 & \cos(\theta_{k'} - \theta_k) & -\frac{1}{\sqrt{2}}\sin(\theta_{k'} - \theta_k) \\ \frac{1}{2}(1 - \cos(\theta_{k'} - \theta_k)) & 0 & -\frac{1}{\sqrt{2}}\sin(\theta_{k'} - \theta_k) & -\frac{1}{2}(1 + \cos(\theta_{k'} - \theta_k)) \end{pmatrix} \tag{8.65}$$

[1] Taking the whole momentum, $\mathbf{K} + \mathbf{q}$, where $\mathbf{K}$ is the momentum of the Dirac point in a particular valley, and $\mathbf{q}$ a small deviation around this point, the other electron from the pair must have $-\mathbf{K} - \mathbf{q}$. However, a simple geometrical analysis of the Brillouin zone in graphene yields that $-\mathbf{K}$ necessarily belongs to the other inequivalent valley, $\mathbf{K}'$.

Hence:

$$\begin{pmatrix} E-2k & 0 & 0 & 0 \\ 0 & E & 0 & 0 \\ 0 & 0 & E & 0 \\ 0 & 0 & 0 & E+2k \end{pmatrix} \bar{\psi}_{\mathbf{k}} = \frac{1}{L^2} \sum_{\mathbf{k}} v_{\mathbf{k},\mathbf{k}'} U_{\mathbf{k}}^{\dagger} U_{\mathbf{k}'} \bar{\psi}_{\mathbf{k}'} \tag{8.66}$$

Now it is a simple task to impose that the electrons from the pair live only in the upper cone, by making zero all the components but the first one. The latter, after all, corresponds to two-electrons in the upper cone with zero center-of-mass momentum in the non-interacting limit. The wave-function is the solution to the following eigenvalue problem:

$$(E-2k)\psi_{\mathbf{k},1} = \frac{1}{L^2} \sum_{\mathbf{k}'} v_{\mathbf{k},\mathbf{k}'} \frac{1+\cos(\theta_{\mathbf{k}'}-\theta_{\mathbf{k}})}{2} \psi_{\mathbf{k},1} \tag{8.67}$$

Analytical solution for a contact interaction

The simplest situation is that of a short-range potential, particularly a contact interaction:

$$v_{\mathbf{k},\mathbf{k}'} = \begin{cases} -|V|L^2 & k,k' < \Lambda \\ 0 & \text{elsewhere} \end{cases} \tag{8.68}$$

In principle, it might be more relevant to consider the Coulomb potential, since this is the prevailing interaction for electrons in undoped graphene, where the screening properties are poor. However, in this case the solution must be addressed numerically, and the results are still at a preliminary level. They are, so far, compatible with the picture that arises from the analysis of the contact interaction, which has the advantage of yielding analytical expressions.

Let me thus proceed with this contact interaction. The general wave function can be expressed in terms of angular channels:

$$\psi(k,\theta) = \sum_{l} \psi_l(k) e^{il\theta} \tag{8.69}$$

that are decoupled one from each other. The simplest one is $l = 0$, that I will analyze henceforth. In this case the eigenvalue problem simplifies considerably, since the angular integrals can be carried out, yielding:

$$(E-2k)\psi_0(k) = -\frac{|V|L^2}{4\pi} \int dk' k' \psi_0(k') \tag{8.70}$$

which has a solution when the following self-consistent equation is satisfied:

$$1 = -\frac{|V|L^2}{4\pi} \int dk \frac{k}{E-2k} \tag{8.71}$$

Working out the integrals, this reads:

$$\frac{8\pi}{|V|L^2} \frac{1}{\Lambda} = 1 + \frac{E}{2\Lambda} \log\left|\frac{2\Lambda}{E} - 1\right| \tag{8.72}$$

This expression can be simplified by introducing the global density of states of low-energy graphene, $n(E) = L^2 E/(2\pi)$ (without the spin and valley degeneracy). Then $n(\Lambda)$ is the density of states at the

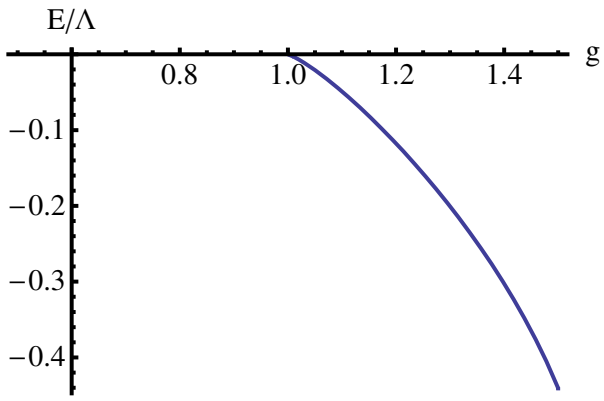

Figure 8.7: Energy of the bound state in the problem of a single exciton in graphene, normalized to the ultraviolet cutoff Λ. There is a bound state only above a certain critical coupling $g_c = 1$, where $g = n(\Lambda)|V|/4$, as defined in the text. The approximation only holds for $E \ll \Lambda$.

cutoff energy scale, and by defining, for convenience, the dimensionless coupling $g \equiv |V|n(\Lambda)/4$, the self-consistent equation is rewritten in a more compact form:

$$\frac{1}{g} = 1 + \frac{E}{2\Lambda} \log |\frac{2\Lambda}{E} - 1| \tag{8.73}$$

Since we are only interested in small energies as compared to the cutoff, $E \ll \Lambda$ holds and this equation has only negative solutions (bound states) when $g > g_c = 1$. The analytical expression for the energy of the bound state reads:

$$E = -2\Lambda \frac{g^{-1} - 1}{W_{-1}(g^{-1} - 1)} \tag{8.74}$$

where $W_{-1}(z)$ is the lower branch of the Lambert W function[2]. A plot of this energy, normalized to the cutoff Λ, is shown in Fig. 8.7. The remarkable difference between this version of the Cooper pair problem in graphene and that of conventional metals is the existence of a critical coupling below which there is not bound state. In metals, it is well-known that the presence of a Fermi surface is sufficient to stabilize a bound state for arbitrary *attractive* interactions, no matter how small they are. In graphene, this is no longer the case, and the interaction must be stronger than a critical value set by the density of states at the ultraviolet cutoff. Since in ordinary metals the coupling is defined by the DOS at the Fermi energy, we find another remarkable example where the physics of the continuous theory of graphene electrons depends on the cutoff, which plays the role of an effective bandwidth. As usual, this is due to the lack of other energy scales in the problem.

When these results are applied to the excitonic problem in graphene, the results are compatible with the sketched scenario of a phase transition above a certain critical coupling. Of course, in order to get a full connection, it would be in principle more rigorous to address of a Coulomb interaction, unless a connection between short-range interactions and physics above the Coulomb critical coupling is established, as was discussed in the context of the two-body problem. Both directions are still a subject of ongoing research.

[2]The Lambert function was defined by Euler, and it is the inverse of the equation $z = xe^x$, i.e., $x = W(z)$.

8.4 The excitonic condensate

Finally, let me address in this section the excitonic instability within the full many-body interacting theory. I will follow the usual lines to study excitonic condensation phenomena, which are based on the BCS theory of superconductivity. The idea is to make use of a variational ansatz to minimize the energy of the Hamiltonian and find a condition for the excitonic state to exist, whenever it gives a minimum of the energy. For an introduction in the context of superconductivity, I will refer the reader to the book of Schrieffer [187]. The excitonic case is explained in detail in [219].

The starting point is the Hamiltonian for Dirac electrons interacting via Coulomb potential, restricted to a single spin and valley channel for reasons already explained:

$$\mathcal{H} = \sum_{\mathbf{k}} k(c^{\dagger}_{\mathbf{k},+}c_{\mathbf{k},+} - c^{\dagger}_{\mathbf{k},-}c_{\mathbf{k},-}) + \frac{1}{2}\sum_{\mathbf{q}} v_q n_{\mathbf{q}} n_{-\mathbf{q}} \tag{8.75}$$

Here $+,-$ refer, respectively, to the upper and lower cones, and the interaction is Coulomb-like, $v_q = 2\pi g/(\kappa q)$. In order to carry out the variational calculation, it is convenient to write the interaction in the basis that diagonalizes the free Dirac Hamiltonian, yielding:

$$\mathcal{H}_I = \frac{1}{2}\sum_{\mathbf{q}} v_q \sum_{\mathbf{k},\mathbf{k}',s_1,s_2,s_3,s_4} \Gamma_{s_1,s_2}(\mathbf{k}+\mathbf{q},\mathbf{k})\Gamma_{s_3,s_4}(\mathbf{k}'-\mathbf{q},\mathbf{k}')c^{\dagger}_{\mathbf{k}+\mathbf{q},s_1}c_{\mathbf{k},s_2}c^{\dagger}_{\mathbf{k}'-\mathbf{q},s_3}c_{\mathbf{k}',s_4} \tag{8.76}$$

where I have introduced the following matrix elements:

$$\Gamma(\mathbf{k}+\mathbf{q},\mathbf{k}) = \begin{pmatrix} \cos(\frac{\theta_{\mathbf{k}+\mathbf{q}}-\theta_k}{2}) & -i\sin(\frac{\theta_{\mathbf{k}+\mathbf{q}}-\theta_k}{2}) \\ -i\sin(\frac{\theta_{\mathbf{k}+\mathbf{q}}-\theta_k}{2}) & \cos(\frac{\theta_{\mathbf{k}+\mathbf{q}}-\theta_k}{2}) \end{pmatrix} \tag{8.77}$$

They can be understood in terms of an overlapping between holes and electrons, having the following properties:

$$\Gamma_{s_1,s_2}(\mathbf{k}+\mathbf{q},\mathbf{k}) = \Gamma_{s_2,s_1}(\mathbf{k}+\mathbf{q},\mathbf{k}) \tag{8.78}$$

$$\Gamma_{s,\bar{s}}(\mathbf{k}+\mathbf{q},\mathbf{k}) = -\Gamma_{s,\bar{s}}(\mathbf{k},\mathbf{k}+\mathbf{q}) \tag{8.79}$$

In order to avoid the appearance of an (infinite) vacuum energy, we will work with the normal ordered form of this interaction:

$$:\mathcal{H}_I: = -\frac{1}{2}\sum_{\mathbf{q}} v_q \sum_{\mathbf{k},\mathbf{k}',s_1,s_2,s_3,s_4} \Gamma_{s_1,s_2}(\mathbf{k}+\mathbf{q},\mathbf{k})\Gamma_{s_3,s_4}(\mathbf{k}'-\mathbf{q},\mathbf{k}')c^{\dagger}_{\mathbf{k}+\mathbf{q},s_1}c^{\dagger}_{\mathbf{k}'-\mathbf{q},s_3}c_{\mathbf{k},s_2}c_{\mathbf{k}',s_4} \tag{8.80}$$

Variational ansatz

The variational ansatz has the standard form known in the excitonic literature, which was proposed originally by Comte and Nozières [286]. As happens with the BCS ansatz, it is a coherent superposition of vacuum and excitonic states, with the relative probabilities left as variational parameters. The generalization for graphene samples reads:

$$|\Psi\rangle = \Pi_{\mathbf{k}}(u_{\mathbf{k}} + v_{\mathbf{k}}c^{\dagger}_{\mathbf{k},+}c_{\mathbf{k},-})|\text{Dirac}\rangle \tag{8.81}$$

where the variational parameters $u_{\mathbf{k}}$ and $v_{\mathbf{k}}$ can be taken real. By imposing the normalization of this state, these parameters become constrained by the following relationship:

$$u^2_{\mathbf{k}} + v^2_{\mathbf{k}} = 1 \tag{8.82}$$

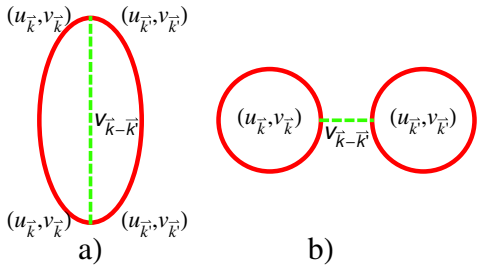

Figure 8.8: Diagrams included in the total energy of the excitonic ansatz. a) Exchange term. b) Hartree term.

The calculation follows the lines of the BCS and excitonic ones. The energy of the ansatz is evaluated by projecting the Hamiltonian into this state. The result can be seen diagrammatically as the sum of two contributions, the Hartree and the exchange one, both represented in Fig. 8.8. Notice that the Hartree contribution is zero, as there are no processes involving zero momentum transfer. The dominant contribution is the exchange one, where $\mathbf{q} = \mathbf{k}' - \mathbf{k}$. The projected Hamiltonian is the following:

$$\langle\Psi| : \mathcal{H} : |\Psi\rangle = \sum_{\mathbf{k}} k(v_{\mathbf{k}}^2 - u_{\mathbf{k}}^2) - \sum_{\mathbf{k},\mathbf{k}'} V_{|\mathbf{k}'-\mathbf{k}|} \left(2u_{\mathbf{k}}u_{\mathbf{k}'}v_{\mathbf{k}}v_{\mathbf{k}'}\right.$$
$$\left. + \cos^2(\frac{\theta_{k'}-\theta_k}{2})(u_{\mathbf{k}}^2u_{\mathbf{k}'}^2 + v_{\mathbf{k}}^2v_{\mathbf{k}'}^2) + \sin^2(\frac{\theta_{k'}-\theta_k}{2})(u_{\mathbf{k}}^2v_{\mathbf{k}'}^2 + v_{\mathbf{k}}^2u_{\mathbf{k}'}^2)\right) \tag{8.83}$$

The extreme condition can be imposed by defining $u_{\mathbf{k}} = \sin(\phi_{\mathbf{k}})$ and $v_{\mathbf{k}} = \cos(\phi_{\mathbf{k}})$, that fulfill the normalization constraint automatically, and minimize with respect to $\phi_{\mathbf{k}}$. This yields the following condition:

$$\left(k + \sum_{\mathbf{k}'} V_{|\mathbf{k}'-\mathbf{k}|}\cos(\theta_{k'}-\theta_k)(u_{\mathbf{k}'}^2 - v_{\mathbf{k}'}^2)\right) u_{\mathbf{k}}v_{\mathbf{k}} = (u_{\mathbf{k}}^2 - v_{\mathbf{k}}^2)\sum_{\mathbf{k}'} V_{|\mathbf{k}'-\mathbf{k}|}u_{\mathbf{k}'}v_{\mathbf{k}} \tag{8.84}$$

Now we set:

$$\xi_{\mathbf{k}} = k + \sum_{\mathbf{k}'} V_{|\mathbf{k}'-\mathbf{k}|}\cos(\theta_{k'}-\theta_k)(u_{\mathbf{k}'}^2 - v_{\mathbf{k}'}^2) \tag{8.85}$$

$$\Delta_{\mathbf{k}} = 2\sum_{\mathbf{k}'} V_{|\mathbf{k}'-\mathbf{k}|}u_{\mathbf{k}'}v_{\mathbf{k}'} \tag{8.86}$$

$$E_{\mathbf{k}}^2 = \xi_{\mathbf{k}}^2 + \Delta_{\mathbf{k}}^2 \tag{8.87}$$

and the solution is given by:

$$u_{\mathbf{k}}v_{\mathbf{k}} = \frac{\Delta_{\mathbf{k}}}{2E_{\mathbf{k}}} \tag{8.88}$$

$$v_{\mathbf{k}}^2 = \frac{1 - \xi_{\mathbf{k}}/E_{\mathbf{k}}}{2} \tag{8.89}$$

The variational calculation is reduced to the solution of a self-consistent gap equation:

$$\Delta_{\mathbf{k}} = \sum_{\mathbf{k}'} V_{|\mathbf{k}'-\mathbf{k}|}\frac{\Delta_{\mathbf{k}'}}{E_{\mathbf{k}'}} \tag{8.90}$$

This results is similar to the one obtained in [224] by using the Dyson-Schwinger formalism, and shown in Eq. 5.35. Notice that there are two important differences. On the one hand, in the approach described here the Coulomb interaction remains unscreened. On the second hand, the variational calculation includes the corrections to the relation dispersion that arise from the renormalization of the Fermi velocity due to the interactions, i.e., the second term of Eq. 8.85.

Discarding these differences, the resulting gap equation reproduces those already reported in the literature. Therefore, the approximations described in Chapter 5 also apply for this approach. It is expected to give a phase transition to an excitonic phase above a certain critical coupling, $g_c \sim 1$ (the particular value depending on the approximations done), a result that is remarkably close to that predicted for the two-body instability. Above the critical coupling the ground state of electrons in graphene would be an excitonic condensate. Such a phase transition implies the breaking of the sublattice symmetry of graphene, and hence it is expected that, once the honeycomb lattice is included in the description, a charge density wave is formed, whose main consequence would be a charge unbalance between both sublattices. Additionally, the quasiparticle spectrum of graphene would show a gap, whose magnitude is of major importance in order to elucidate if the phase transition will yield traces on experiments. However, once details of the lattice structure are taken into account, other short-range interactions, in principle irrelevant, might change this picture. Competition between the charge density wave and a possible spin density wave could be highly relevant in turn, and further research is needed to clarify this point.

In any case, my purpose in this section was only to provide us with a connection between the two-body physics and the many-body problem, via the excitonic ansatz where a superposition of electron - hole pairs is considered. Such an ansatz gives a gap equation that predicts an excitonic phase transition. The picture sketched here, however, must be yet complemented with more detailed studies.

8.5 Conclusions

In this chapter I have addressed the problem of strong coupling phases in graphene from the point of view of two-body instabilities. In the way, many remarkable features of the two-body problem in graphene have been found, a problem that cannot be reduced to that of a single particle, due to the coupling between center-of-mass and relative coordinates. Nevertheless, such a non trivial problem can be simplified by studying the limit of zero center-of-mass momentum, $K = 0$, which particularized to the Coulomb potential, shows an instability above a critical coupling g_c that signals an anomalous behavior of the wave-function. From similar results found in the Coulomb impurity problem in graphene, we can infer that such an instability is signaling the breakdown of the Dirac vacuum and the generation of particle-hole excitations that would screen the interaction in a nonlinear way. Moreover, it has been suggested that this behavior could be linked to the excitonic instability in the many-body context, although the rigorous connection should be yet clarified. Remarkably, the two-body problem gives a critical coupling for the instability, $g_c = 1$, that is close to the numerical and theoretical estimations obtained in the context of the excitonic condensate.

The value of the critical coupling predicted in the two-body problem corresponds to the $l = 0$ channel (s-wave) in a decomposition in terms of relative angular momenta. Higher angular momenta give larger values of the critical value, so in principle it is expected that the phase transition would be ruled by the s-wave. However, these higher angular momentum channels show non-trivial features due to the coupling of the wave-function to zero-energy states at those points where the kinetic energy vanishes. Although this can be seen to be a general feature of any central potential, for the Coulomb interaction it is reflected in a concentration of the density near this point, larger as the critical coupling is approached. Therefore, two electrons in these channels tend to form quasibound states. If this has a consequence on the many-body phenomena must be still clarified.

Two-body instabilities remain when the role of the Dirac sea is included in the two-body problem, that imposes a constraint to the available states. The solution of this problem, that resembles the Cooper problem in graphene, yields that a bound state is formed whenever a critical coupling is exceeded. Analytical calculations with a contact potential, as well as preliminary numerical calculations in the context of the Coulomb potential, agree in this point. This suggests a connection between the instabilities in the two-body problem and the formation of excitons.

Finally, I have considered a variational ansatz where the excitonic pairs are included explicitly to minimize the ground state energy, finding a gap equation that reproduces previous results in the literature, where a phase transition above a critical coupling was predicted. This calculation completes the picture of two-body instabilities and strong coupling phases in graphene, which was the main topic analyzed throughout this chapter.

APPENDIX A: Matching conditions for the two-body problem with a step-potential

As mentioned in the main text, the solutions located at the point $v(r) = E$ can induce discontinuities in the wave-function. Physically, this can be understood in terms of localized states that live in this region and which are built from the complete set of polynomial solutions given in (8.39). Let me develop this argument in detail.

For greater clarity, we may modify the step potential near the point r_0 where $v(r_0) = E$ in such a way that $v(r) = E$ [i.e. $\varepsilon(r) = 0$] in the vicinity of r_0, namely, for $r_0 - \delta < r < r_0 + \delta$, where at the end of the calculation $\delta \to 0$. From Eqs. (8.27) and (8.28) in the main text, it follows that $\partial_r \phi_2 = 0$ and, if $l \neq 0$, $\phi_2 = 0$. On the other hand, Eq. (8.30) becomes, in that small interval:

$$r\partial_r(\phi_1 - \phi_3) = (l-1)\phi_1 + (l+1)\phi_3 \tag{8.91}$$

The existence of zero-energy states [see Eq. (8.39)] allows us to introduce functions of arbitrarily high slope in the small interval of length δ. We adopt the simplest ansätze for the two components:

$$\phi_1(r) = a + b(r - r_0) \tag{8.92}$$

$$\phi_3(r) = c + d(r - r_0)\,. \tag{8.93}$$

In the slightly modified potential, both components must be continuous everywhere, so we may impose

$$\phi_1(r_0 \pm \delta) = a \pm b\delta \equiv \phi_1^{I,II}(r_0) \tag{8.94}$$

$$\phi_3(r_0 \pm \delta) = c \pm d\delta \equiv \phi_3^{I,II}(r_0)\,. \tag{8.95}$$

As a result, if $\Delta\phi_i \equiv \phi_i^{II}(r_0) - \phi_i^{I}(r_0)$,

$$b = \Delta\phi_1/2\delta, \qquad d = \Delta\phi_3/2\delta\,.$$

If we allow for nonzero discontinuities, $\Delta\phi_i \neq 0$, we conclude that, for $\delta \to 0$, both $\phi_1' = b$ and $\phi_3' = d$ tend to infinity in magnitude. Thus, Eq. (8.91) can be approximated as

$$\partial_r\phi_1(r) = \partial_r\phi_3(r)\,, \tag{8.96}$$

i.e. $b = d$ and thus

$$\Delta\phi_1 = \Delta\phi_3 \equiv -2C \tag{8.97}$$

The upshot is that, thanks to the existence of zero-energy states in the immediate vicinity of r_0, a new parameter emerges that allows for a discontinuity in the components ϕ_1 and ϕ_3. The parameter C is thus adjusted to render the matching problem well determined.

Interestingly, if one were to perform a similar analysis to the one-body problem of a step potential impurity, one would introduce a similar ansatz for the (only existing) two components of the problem. Zero-energy states could in principle also play a role in the vicinity of the point analogous to r_0. However, we find that a linear ansatz similar to that considered above would lead to a zero slope. In other words, even allowing for the existence of zero-energy states, the wave-function remains continuous at all points, including r_0. We could say that zero-energy states do not intervene because they are not necessary, and this is so because, unlike in the two-body problem, the matching problem is well defined from the start.

Once we have taken $\delta \to 0$ and accepted that the abrupt change of sign of $\varepsilon(r)$ at $r = r_0$ leads to identical discontinuities in ϕ_1 and ϕ_3 while keeping ϕ_2 continuous, we may derive, from the general relations in section 8.2.2, a few more conclusions on the behavior of the solutions around the step.

From the fact that ε and ϕ_1, ϕ_3 are bounded, it follows from Eqs. (8.27) and (8.28) that ϕ_2 and $\partial_r\phi_2$ are also bounded. If we integrate Eq. (8.29) in an infinitesimally small region around the step, we conclude:

$$\Delta(\varepsilon(\phi_1 + \phi_3)) = 0 \tag{8.98}$$

where Δ means total variation across the abrupt step. If we combine this result with Eq. (8.97), we conclude that the common discontinuity of ϕ_1 and ϕ_3 is directly determined by the step discontinuity in the potential ($\Delta\varepsilon = -v_0$). Therefore Eq. (8.98) implicitly yields the discontinuity C which is needed to allow ϕ_2 to be continuous. Specifically, we obtain:

$$C = \frac{1}{4}\left(1 - \frac{|\varepsilon^I|}{\varepsilon^{II}}\right)\left(\phi_1^I + \phi_3^I\right) \tag{8.99}$$

where $\varepsilon^I = E - v_0 < 0$ and $\varepsilon^{II} = E > 0$.

From Eq. (8.28) it follows that $\partial_r \phi_2$ experiences a discontinuity across the step which closely follows the discontinuity of $\varepsilon(r)$, given that $\phi_1 - \phi_3$ is continuous. We also note from Eq. (8.27) that, for $l \neq 0$, ϕ_2 goes quickly through zero as $\varepsilon(r)$ becomes 0 at $r = r_0$. However, it recovers quickly from that sharp dip to become globally continuous across the step, as can be inferred from (8.27) and (8.98). By contrast, when $l = 0$, ϕ_2 remains strictly continuous across the step.

APPENDIX B: Analytical solution of two-body problem with a step-potential, for $K = 0$

We start from the scattering problem sketched in Fig. 8.2. The two electron problem is written in terms of an effective single-electron radial equation in the case $K = 0$. The energy of the incident pair is $E < v_0$. For $r < r_0$, only solutions non-singular at the origin are valid, while for $r > r_0$, a general solution is a linear combination of incoming and outgoing wave functions. Hence we have, up to a normalization constant [see Eqs. (8.35)-(8.38)]:

$$\phi_l^I = \begin{bmatrix} \frac{1}{2}J_{l-1}(k_I r) \\ -J_l(k_I r) \\ \frac{1}{2}J_{l+1}(k_I r) \end{bmatrix}$$
$$\phi_l^{II} = A \begin{bmatrix} \frac{1}{2}J_{l-1}(k_{II} r) \\ J_l(k_{II} r) \\ \frac{1}{2}J_{l+1}(k_{II} r) \end{bmatrix} + B \begin{bmatrix} \frac{1}{2}Y_{l-1}(k_{II} r) \\ Y_l(k_{II} r) \\ \frac{1}{2}Y_{l+1}(k_{II} r) \end{bmatrix} \tag{8.100}$$

where the coefficients of the wave function are those of positive energy for region I and those of negative energy for region II. Moreover, in Eq. (8.100), $k_I = (v_0 - E)/2$ and $k_{II} = E/2$.

As already seen in Appendix A, both solutions must be matched at $r = r_0$ with a matching condition that includes an arbitrary coefficient, say C, to be adjusted. The system of equations reads now:

$$\begin{bmatrix} \frac{1}{2}J_{l-1}(k_{II} r_0) & \frac{1}{2}Y_{l-1}(k_{II} r_0) & 2 \\ J_l(k_{II} r_0) & Y_l(k_{II} r_0) & 0 \\ \frac{1}{2}J_{l+1}(k_{II} r_0) & \frac{1}{2}Y_{l+1}(k_{II} r_0) & 2 \end{bmatrix} \begin{bmatrix} A \\ B \\ C \end{bmatrix} = \begin{bmatrix} \frac{1}{2}J_{l-1}(k_I r_0) \\ -J_l(k_I r_0) \\ \frac{1}{2}J_{l+1}(k_I r_0) \end{bmatrix} \tag{8.101}$$

which can be solved by using Cramer's method. Invoking Bessel function properties, the coefficients are found to be

$$A = -\frac{\pi r_0}{2}\left[J_l(k_I r_0)\frac{d}{dr_0}Y_l(k_{II} r_0) + \frac{k_{II}}{k_I}Y_l(k_{II} r_0)\frac{d}{dr_0}J_l(k_I r_0)\right] \tag{8.102}$$
$$B = \frac{\pi r_0}{2}\left[J_l(k_I r_0)\frac{d}{dr_0}J_l(k_{II} r_0) + \frac{k_{II}}{k_I}J_l(k_{II} r_0)\frac{d}{dr_0}J_l(k_I r_0)\right] \tag{8.103}$$
$$C = \frac{l}{4}J_l(k_I r_0)\left(\frac{1}{k_{II} r_0} + \frac{1}{k_I r_0}\right) \tag{8.104}$$

These analytical expressions reproduce the numerical results obtained by discretizing the differential equations, including the magnitude of the jump, $-2C$, and Eq. (8.99) from Appendix A.

APPENDIX C: Analytical solution of the s-wave channel for the two-body problem with a Coulomb interaction

Let me start from the system of differential equations given in (8.42). The s-wave channel corresponds to $l = 0$. In this case, $\hat{\phi}_1 = -\hat{\phi}_3$, and the system reduces to one of only two components, with a structure resembling that of the Coulomb impurity problem. We define:

$$Q_1 = \hat{\phi}_1 - \frac{i}{2}\hat{\phi}_2 \tag{8.105}$$

$$Q_2 = \hat{\phi}_1 + \frac{i}{2}\hat{\phi}_2 \tag{8.106}$$

which fulfill the following coupled differential equations:

$$(\rho\partial_\rho + \gamma - i\frac{g}{2})Q_1 + \frac{Q_2}{2} = 0 \tag{8.107}$$

$$(\rho\partial_\rho - \rho + \gamma + i\frac{g}{2})Q_2 + \frac{Q_1}{2} = 0 \tag{8.108}$$

$$\tag{8.109}$$

The solutions are given by Kummer functions [**?**]:

$$Q_1 = C_1\mathcal{F}(\gamma - i\frac{g}{2}, 2\gamma + 1; \rho) \tag{8.110}$$

$$Q_2 = C_2\mathcal{F}(\gamma + 1 - i\frac{g}{2}, 2\gamma + 1; \rho) \tag{8.111}$$

$$\tag{8.112}$$

By using the property $\mathcal{F}(a, b; 0) = 1$ and the limit $\rho \to 0$ of the system of equations (8.109), we obtain the ratio:

$$c_{21} \equiv \frac{C_2}{C_1} = -2(\gamma - ig/2) = e^{-i\arctan\frac{g}{2\gamma}} \tag{8.113}$$

Hence the solution is:

$$\phi(r) \sim \frac{1}{2}(iEr)^{\gamma-1/2}e^{-\frac{iEr}{2}}\begin{bmatrix} \mathcal{F}(\gamma - i\frac{g}{2}, 2\gamma + 1; iEr) + c_{21}\mathcal{F}(\gamma + 1 - i\frac{g}{2}, 2\gamma + 1; iEr) \\ 2i\mathcal{F}(\gamma - i\frac{g}{2}, 2\gamma + 1; iEr) - 2ic_{21}\mathcal{F}(\gamma + 1 - i\frac{g}{2}, 2\gamma + 1; iEr) \\ -\mathcal{F}(\gamma - i\frac{g}{2}, 2\gamma + 1; iEr) - c_{21}\mathcal{F}(\gamma + 1 - i\frac{g}{2}, 2\gamma + 1; iEr) \end{bmatrix} \tag{8.114}$$

up to an overall normalization constant that can be determined by matching the solution to the $r \to \infty$ limit.

General conclusions

Concern for man and his fate must always form the chief interest of all technical endeavors.
Never forget this in the midst of your diagrams and equations.
A. Einstein

Throughout this thesis I have studied some of the consequences that interactions have on the physics of graphene monolayers and arrays of ultracold atoms, the most important realizations of low-dimensional quantum systems reported in the last years. We theorists have the possibility of changing some parameters that remain fixed in real systems, unveiling a plethora of phenomena that ranges from exotic phases to phase transitions and non-trivial dynamics. However, the study of interacting models is of great difficulty, and I had to resort to a variety of techniques to obtain those partial answers that may, in the future, help to compose the big picture of the problems that motivated the research described in this pages. A research that has been possible thanks to the support of my supervisors and of many collaborators, who sharing their interests with me, contributed to conform my own picture of what deserves to be investigated.

In this regard, since we wanted to understand how environments disrupt the properties of isolated quantum systems, we revived the well-known Caldeira-Leggett model to address the influence of the coupling to an external bath on the density profile of a single particle in a finite chain, finding that when this coupling is strong enough, coherence is destroyed and the particle becomes localized at one site of the lattice. Below this coupling, the density distribution is narrowed at the center of the chain, an effect whose origin is purely due to the finiteness of the system. The Caldeira-Leggett description of the coupling to an environment being universal, we expect these results to hold for a variety of systems, particularly atoms trapped in optical lattices.

Since we wanted to understand the thermalization problem in isolated quantum systems, we addressed the dynamics of the sine-Gordon model after a sudden quench of interactions using the flow equations formalism. This approach helped us to learn that, despite of being an integrable model, the dynamics of the bosonic occupations in the weak coupling regime is not constrained by the integrals of motion, leading to a relaxation phenomenon that is on the border line between thermalization and non-thermalization. New questions have followed the seminal ones. Is this result compatible with the standard relaxation picture sketched for integrable systems? Or maybe the latter fails, obliging us to propose new schemes to understand this issue? The answers will arrive when further research is carried out.

Since we wanted to clarify to what extent the environment of real graphene samples changes its sought-after exotic intrinsic properties, we studied the van der Waals interactions that arise from the electrostatic coupling between graphene electrons and polarizable elements of the environment. Graphene gets stuck to the substrate due to these forces, especially those arising from the surface polar modes of the SiO_2 and the thin water film that may exist between the latter and graphene. Our results should help experimentalists to understand which elements must categorically be removed, if possible, from the experimental setup. And whenever this is too difficult, at least they should provide information about the influence of these elements on graphene properties. As for example, possible changes in the out-of-plane oscillation frequencies.

And finally, since we wanted to understand the role that electron-electron interactions play in undoped graphene samples, we derived an exact identity, the f-sum rule, that must be fulfilled for any realistic approximation to the interacting theory, and which allows to classify the importance of the excitations in the weak-coupling regime in terms of its spectral weight. Experimental graphene samples are metallic, and traces of electron-electron interactions are elusive, since every real experiment seems to be well fitted by the free electron theory. But from a theoretical point of view this is still an open problem, mostly in undoped graphene samples where strong interactions could render the system insulating. In order to understand this strong coupling regime, we studied the exact solution of the two-body problem in graphene, that shows remarkable instabilities as well as other features that point to the formation of bounded electron-hole pairs, so-called excitons. From the results of this problem, we addressed the many-body theory via the problem of a single exciton constrained by the Dirac sea, to finally derive a gap equation from a variational ansatz that reproduces previous results in the literature, predicting a phase transition above a critical coupling. The different elements of this generalization from two to many particles have been analyzed in this thesis, but the way they are related to each other is still an important issue to clarify, not to mention that a more complete picture of the strong-coupling phase may require a broadening of the theoretical description sketched so far.

The questions addressed in this thesis belong to the field of interactions in low-dimensional quantum systems. Some of them just were the product of our curiosity, others arose from the current research in a trend topic with promising applications. This is, after all, the double role scientists play when doing research: a commitment to provide the basic ingredients that should lead to improve human life standards, at the same time that they enlighten our understanding of nature. A thesis is just a small grain in this enormous endeavor, a little step forward in the exciting purpose of finally grasping the big picture. I hope this one has accomplished its part in such a quest.

Resumen en castellano

Introducción

Esta tesis se enmarca en el estudio de las interacciones en nuevas realizaciones de sistemas cuánticos de baja dimensionalidad, desde un punto de vista extrictamente teórico. La Física Cuántica de sistemas de dimensionalidad reducida no es un tema nuevo, ya que podría decirse que existe desde que el propio átomo de Hidrógeno fue estudiado con el formalismo de la Mecánica Cuántica. Sin embargo, la edad de oro de este campo se vivió claramente en las décadas de los setenta y los ochenta, momento en el que se dio un espectacular avance en las técnicas experimentales para fabricar y caracterizar nanoestructuras. Hoy por hoy, sin embargo, estamos viviendo una segunda edad de oro, gracias a dos nuevos sistemas que permiten estudiar la baja dimensionalidad desde perspectivas inaccesibles hasta ahora. Hablo, por un lado, del grafeno [66, 72], un cristal genuínamente bidimensional que añade a su estructura atómica exótica unas propiedades electrónicas poco convencionales, pues a baja energía los electrones se propagan siguiendo una ecuación de Dirac para portadores sin masa [81]. Si bien había otros contextos en la Física de la Materia Condensada donde este tipo de ecuaciones emergen, es en grafeno donde esta física es más asequible. Por otro lado, en los últimos años se han perfeccionado las técnicas de enfriamiento y confinamiento de átomos neutros, lo que está permitiendo diseñar en el laboratorio sistemas de baja dimensionalidad con un altísimo grado de control sobre sus propiedades [49]. En ambos sistemas, las partículas que los componen interaccionan las unas con las otras de diferentes maneras, lo que podría dar lugar a fenómenos colectivos no observados con anterioridad.

El objetivo de esta tesis es avanzar en el conocimiento de los efectos que dichas interacciones pueden tener en ambos sistemas, grafeno y redes de átomos fríos. Las interacciones pueden ser entre partículas de dicho sistema, pero estas a su vez también pueden verse influenciadas por la presencia de agentes externos en el entorno en el que el sistema vive. De cara a estudiar la fenomenología experimental de estos sistemas, ambos tipos de interacciones son muy importantes, por lo que han sido abordadas en distintos capítulos de la tesis.

La tesis incluye tres capítulos introductorios, con los que se trata de dar una resentación autocontenida de los resultados. Uno general, en el que se pasa revista al campo de sistemas cuánticos de dimensionalidad reducida, incluyendo las nuevas realizaciones de las que trata esta tesis. Y otros dos, uno al principio de cada parte de la tesis, que incluyen resultados y técnicas relevantes para el estudio de las interacciones en los siguientes capítulos. A continuación se incluye un breve resumen de cada una de las partes que componen esta tesis.

Primera parte: Interacciones en redes de átomos fríos

La primera parte de la tesis se centra en el estudio de las interacciones en redes de átomos fríos. Este campo emergente está permitiendo simular en el laboratorio algunos modelos de sistemas en interacción que hasta ahora se consideraban de interés puramente académico. Como era de esperar, esto ha estimulado nuevos estudios teóricos con la esperanza de que con la mejora de las técnicas experimentales, todavía en fases tempranas de refinamiento, se puedan observar algunos fenómenos que hasta ahora se encontraban relegados al mundo de las ecuaciones y las simulaciones numéricas. Por lo tanto, esta parte de la tesis tiene un carácter mucho más especulativo que la siguiente, donde los experimentos ya realizados servirán de guía en muchos casos.

Esta parte de la tesis contiene dos capítulos, en los que se analizan dos problemas distintos que podrían ser realizados con redes de átomos fríos, o al menos podrían ayudar a dilucidar algunos de los aspectos básicos de experimentos ya realizados. De cara a estudiar estos modelos, juegan un papel muy importante las ideas de invariancia de escala y el Grupo de Renormalización [108]. Dichas ideas fueron desarrolladas fundamentalmente en la segunda mitad del siglo XX, y han cambiado nuestra interpretación de las teorías que describen un determinado fenómeno físico. Hoy por hoy, entendemos que todo modelo es una descripción efectiva de un fenómeno, necesariamente limitada a una cierta escala de energía (o, desde otro punto de vista, a determinado detalle microscópico). Para entender esto es útil implementar una transformación, el Grupo de Renormalización, que sirve de instrumento para analizar el efecto que tiene los grados de libertad asociados a altas energías en la física a escalas menores. La idea es generar modelos efectivos a baja energía que incluyan en forma de nuevas interacciones las contribuciones de alta energía. El Grupo de Renormalización ofrece el marco para entender si esas contribuciones son importantes, y hasta qué punto hacen que la física efectiva a baja energía sea diferente. Es, además, el marco perfecto para estudiar si el límite a baja energía (o de poco detalle microscópico) de la teoría pertenece a una determinada clase de universalidad, en el sentido de que diferentes modelos de alta energía tienen un límite común de baja energía.

Los cálculos realizados en esta parte de la tesis utilizan técnicas que han surgido a partir de las ideas del Grupo de Renormalización. En el primer capítulo se usa el Grupo de Renormalización Numérico [112, 117], una técnica muy útil de cara a estudiar problemas de impurezas cuánticas, es decir, aquellos cuyo Hamiltoniano está compuesto de un sistema cuántico relativamente simple acoplado a un entorno. Manipulando el Hamiltoniano de partida se puede implementar una transformación de Grupo de Renormalización mediante la diagonalización, numéricamente, de una secuencia de Hamiltonianos. Es decir, como contrapartida a las técnicas analíticas del Grupo de Renormalización convencional, permite estudiar propiedades generales del Hamiltoniano de baja energía, así cómo analizar la forma en que se llega a dicho límite.

En el segundo capítulo se hace uso de una técnica diferente, el método de las Ecuaciones de Flujo [123, 121, 110] . En cierta manera, se puede pensar que este método es incluso más general que el Grupo de Renormalización, dado que contiene los resultados de este en cierto límite. La idea es diagonalizar poco a poco un Hamiltoniano eliminando en cada iteración aquellos elementos de matriz que involucren mayores diferencias de energía. Como virtud, esto permite conservar todo el espacio de Hilbert del problema, algo especialmente útil de cara a estudiar problemas de dinámica.

El coste asociado es, sin embargo, una mayor dificultad técnica en la selección e implementación de la transformación que lleva a cabo dicha diagonalización iterativa. Por supuesto, en última instancia lo normal es tener que hacer los cálculos en determinados límites perturbativos. En esta tesis se emplea esta técnica para analizar un problema de evolución temporal fuera del equilibrio de un sistema cuántico de muchos cuerpos, que es una de las aplicaciones más novedosas del método de las Ecuaciones de Flujo [171].

Diagrama de fases de una partícula cuántica confinada en una cadena, en presencia de un entorno

Este primer capítulo estudia el efecto que tiene un entorno disipativo en la distribución de probabilidad de una partícula cuántica confinada en una cadena finita. El interés de este estudio es múltiple. Por un lado trata de ampliar el conocimiento actual sobre la variedad de efectos que producen los entornos en los sistemas cuánticos [41]. Pero por otro lado, podría ser de interés en experimentos de átomos fríos próximos a superficies [61], donde se dan multitud de interacciones que podrían desviar la fenomenología experimental de la esperada para un sistema aislado.

El acoplo con el entorno se describe usando el modelo de Caldeira-Leggett [135, 120], lo que da lugar al siguiente Hamiltoniano:

$$\mathcal{H} = -t \sum_{m=1}^{M} \left(c_m^\dagger c_{m+1} + c_{m+1}^\dagger c_m \right) + \sum_{k<\omega_c} k a_k^\dagger a_k + \lambda q \sum_{k<\omega_c} \sqrt{k}(a_k + a_k^\dagger) + \lambda^2 q^2 \sum_{k<\omega_c} 1 \tag{8.115}$$

El primer término describe, en segunda cuantización, un sistema de electrones independientes en una cadena finita de M sitios, siendo t la probabilidad de saltar de un sitio a otro. c_m y $c_m^\dagger$ son operadores que destruyen y crean electrones, respectivamente, en el sitio m de la cadena. En dichos operadores están incluídas *ad hoc* las condiciones de contorno. El segundo término modeliza un baño como un conjunto de osciladores armónicos independientes, en segunda cuantización, con a_k y $a_k^\dagger$ destruyendo y creando un bosón, respectivamente, en el modo k. El baño tiene un espectro de energías lineal hasta la energía de corte ω_c. El tercer término describe el acoplo entre la partícula cuántica y el baño, algo que se hace a través del operador posición $q = \sum_m^M (m - m_0) c_m^\dagger c_m$ de la partícula, siendo m_0 el centro de la cadena, y λ la fuerza del acoplo. La fuerza de los acoplos está escogida de forma que podamos reproducir el límite clásico de disipación Óhmica. Finalmente, el cuarto término se añade para asegurar que la disipación es homogénea.

Para estudiar el modelo se utilizan tres aproximaciones, el Grupo de Renormalización, el cálculo variacional y el Grupo de Renormalización Numérico. Dada la complejidad del modelo, que sólo tiene como simetría la paridad, las dos primeras técnicas mencionadas no dan un resultado completamente satisfactorio, por lo que los principales resultados son los dados por el Grupo de Renormalización Numérico, al precio de no ser analíticos sino numéricos. Mediante esta técnica es posible construir un diagrama de fases del modelo a temperatura cero y siempre y cuando el número de eslabones de la cadena no sea muy alto. Hay que tener en cuenta, además, que los resultados más interesantes se encuentran cuando se consideran cadenas de más de cuatro eslabones. En la figura 8.8 se muestra el diagrama de fases para cadenas de cinco y seis eslabones. Se puede ver que en ambos casos hay una

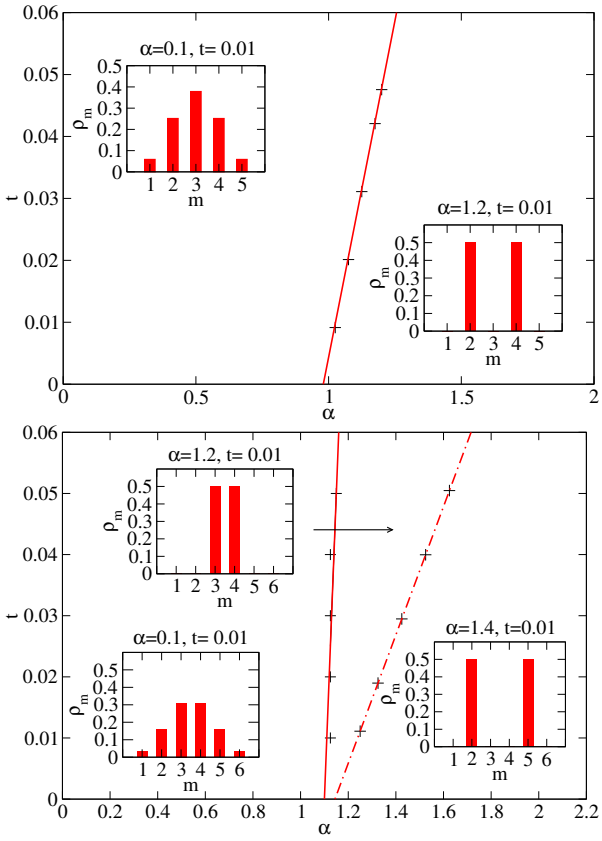

Diagrama de fases del modelo para cadenas de $M = 5$ (arriba) y $M = 6$ (abajo) eslabones, deducidos usando Grupo de Renormalización Numérico. Los gráficos insertados muestran distribuciones de probabilidad de la partícula representativas de cada fase.

transición de fase para un acoplo $\alpha_c \equiv \lambda_c^2/4\pi \sim 1 + \mathcal{O}(t/\omega_c)$. Dicha transición es de tipo Kosterlitz-Thouless, y distingue una fase deslocalizada para $\alpha < \alpha_c$ en la que la partícula puede encontrarse en todo el espacio, a una localizada para $\alpha > \alpha_c$ en la que la partícula se confina en uno de los eslabones de la cadena. La finitud de la cadena introduce inhomogeneidades en ambas fases. En la fase deslocalizada, se traduce en una creciente localización en el eslabón central para cadenas impares y en los dos centrales para cadenas pares. En la fase deslocalizada, hace que la partícula sólo puede localizarse en los sitios adyacentes al centro para cinco eslabones y en los dos centrales para la cadena de seis eslabones. En esta última, de hecho, se produce una segunda transición para acoplos mayores en la que el confinamiento se da también en los sitios adyacentes al centro. Eso sí, en ningún caso se llega a observar confinamiento en los bordes.

La idea a extraer de estos resultados es que la presencia de un baño altera dramáticamente la distribución de probabilidad de una partícula en una cadena, y que la existencia de un número finito de eslabones da lugar a inhomogeneidades en las distintas fases que aparecen por la competición entre energía cinética de la partícula y energía de interacción. De hecho, podría arguirse que el efecto del baño es suprimir dicha energía cinética a la vez que introduce un potencial efectivo que restringe el movimiento de la partícula. De esta forma, podría recuperarse una descripción de la transición al

estilo de Landau [109].

Conexión repentina de las interacciones en el modelo de sine-Gordon

En este segundo capítulo se estudia la dinámica del modelo de sine-Gordon cuando las interacciones son conectadas de forma súbita. Esto permite inducir un estado inicial muy lejano al equilibrio, haciendo que el sistema tenga una evolución temporal peculiar. Este estudio se enmarca en la cuestión general sobre si sistemas cuánticos aislados pueden alcanzar un estado final de equilibrio descrito por una distribución térmica, o si siempre es necesaria la asistencia de un entorno que introduzca disipación y decoherencia en el sistema. Es lo que se conoce en la literatura como el debate de la Termalización [159, 160, 158, 161, 156, 173]. Si bien es fácil argumentar que un sistema cuántico en un estado puro nunca puede, por sí mismo, evolucionar rigurosamente a una distribución de probabilidad térmica, la cuestión es hasta qué punto los observables calculados en el estado final de la evolución temporal pueden recuperarse aproximadamente usando dichas distribuciones. En muchos casos parece ser así, incluso cuando el sistema en cuestión es integrable, en cuyo caso haría falta trabajar con distribuciones térmicas generalizadas [163].

El modelo de sine-Gordon es, de hecho, un modelo integrable [175]. Pero analizar su evolución usando la solución exacta al modelo resulta de una complejidad técnica apreciable, por lo que resulta adecuado usar otras técnicas que permitan estudiar la dinámica en determinados regímenes. En el caso de esta tesis, se utiliza el formalismo de las Ecuaciones de Flujo para estudiar la dinámica en el régimen de acoplo débil del modelo. Para entender a qué corresponde este régimen conviene tener en mente el Hamiltoniano del modelo [16, 174]:

$$\mathcal{H} = \int dx \left(\frac{1}{2}\Pi^2(x) + \frac{1}{2}(\frac{\partial \phi}{\partial x})^2 + \frac{g}{2\pi a^2}\cos(\beta\phi(x)) \right) \tag{8.116}$$

Es el Hamiltoniano de un campo escalar $\phi(x)$ cuantizado en una dimensión espacial, siendo $\Pi(x)$ su momento conjugado. Consta de dos términos, el primero describiendo un sistema de bosones libres, y el segundo introduciendo la interacción, que es periódica en el campo escalar y viene definida por una amplitud $g/(2\pi a^2)$ y una longitud de onda $2\pi/\beta$. Definiendo $\alpha^2 \equiv \beta^2/4\pi$, el régimen de acoplo débil es aquel en el que $\alpha^2 > 2$ y $g \ll 1$, que corresponde a amplitudes y longitudes de onda suficientemente pequeñas. En este caso, el potencial se comporta como una perturbación sobre el sistema libre, y las excitaciones elementales son de carácter bosónico con interacciones débiles entre ellas.

A partir del estudio de este modelo usando el formalismo de las Ecuaciones de Flujo [178], se puede estudiar la evolución temporal de las ocupaciones de los modos bosónicos en los que puede descomponerse, típicamente, el campo escalar cuantizado:

$$\phi(x) = -\frac{i}{\sqrt{4\pi}} \sum_{k>0} \frac{e^{-\frac{ka}{2}}}{\sqrt{k}} \left(e^{-ikx}(a^\dagger_{l,k} + a_{r,-k}) - e^{ikx}(a_{l,k} + a^\dagger_{r,-k}) \right) \tag{8.117}$$

siendo $a_{i,k}$ y $a^\dagger_{i,k}$ los operadores destrucción y creación de un bosón en el modo k, e $i = L, R$ indicando dos ramas de bosones, izquierda (Left) y derecha (Right). Concretamente, el observable que se estudia es la evolución de las ocupaciones tras la conexión del término de interacción, es decir, que en la

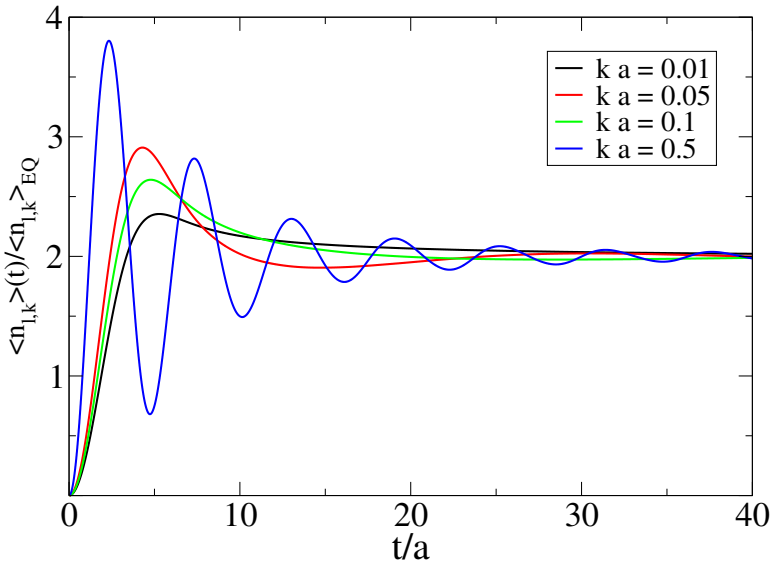

Evolución temporal de las ocupaciones de las ocupaciones de varios modos bosónicos k (a es el interespaciado de la red), normalizadas a los valores de equilibrio. El valor del acoplo es de $\alpha^2 = 2.1$.

imagen de Heisenberg está dado por $n_{i,k}(t) = \langle 0|a^\dagger_{i,k}(t)a_{i,k}(t)|0\rangle$, siendo $|0\rangle$ el estado fundamental del sistema libre.

Los resultados pueden resumirse analizando la evolución de las ocupaciones de varios modos, como se muestra en la figura 8.8, que son similares a los esperadas para osciladores armónicos clásicos en régimen de amortiguamiento débil. Para bosones con longitudes de onda más cortas, cercanas al espaciado de la red a, se tiende a un amortiguamiento crítico. Notoriamente, se alcanza un estado estable tras varias oscilaciones en el que las ocupaciones son el doble de las esperadas en equilibrio térmico. Este resultado es conocido en otros sistemas en los que las interacciones se conectan súbitamente en el régimen perturbativo [172, 173, 179, 180], si bien es esperable que tenga una expresión más complicada para acoplos más grandes. Hay que decir, sin embargo, que en el curso de los cálculos es necesario hacer algunas aproximaciones que impiden dar validez a estos resultados para tiempos arbitrariamente largos. Si existiese una evolución posterior, tendría que ser investigada con otras técnicas o con un análisis más detallado del modelo, si bien esto implicaría que el sistema alcanza una fase de equilibrio parcial en la que la distribución de probabilidad no es térmica, aunque sí en cierta manera universal. En cualquier caso, el mensaje es que pese a ser un modelo integrable, las constantes del movimiento son incapaces de restringir la evolución de observables como las ocupaciones, que muestran comportamientos de relajación a un estado de equilibrio.

Segunda parte: interacciones en monocapas de grafeno

La segunda parte de la tesis ataca el problema de las interacciones entre electrones en monocapas de grafeno, haciendo en lo posible énfasis en los resultados experimentales. Las peculiaridades estructurales y electrónicas del grafeno lo han convertido en un material intesnamente analizado en los

últimos años [81]. Desde el punto de vista electrónico, a baja energía sus excitaciones elementales son electrones sin masa descritos por una ecuación de Dirac [71]. Al tener carga, interaccionan a través del potencial de Coulomb, cuya fuerza conviene medir en términos de la energía cinética del sistema a través del acoplo adimensional $g \equiv e^2/(\kappa v_F)$, donde v_F es la velocidad de Fermi de los electrones, e la carga del electrón y κ la constante dieléctrica del medio. Si el grafeno se encuentra en el vacío, esta interacción es fuerte, haciendo del problema uno no perturbativo. Incluso en presencia de los sustratos típicos sobre los que se depositan las muestras experimentales, los valores de este acoplo lo dejan fuera del régimen perturbativo. Es esperable, por lo tanto, que las interacciones jueguen un papel importante en este sistema.

Sin embargo, la mayor parte de los experimentos pueden explicarse en términos de una imagen de electrones libres. En el caso del grafeno dopado, es decir, aquel en el que el nivel de dopaje está por encima del punto de Dirac, donde se tocan las dos bandas de este material, es posible entender esto haciendo uso de la teoría del Líquido de Fermi [184]. Esencialmente, esta dice que son los propios electrones los que apantallan las interacciones fuertes, dando lugar a cuasipartículas análogas a los electrones libres de partida. Pero en el caso de grafeno sin dopar, es decir, en el punto de Dirac, el apantallamiento de estos electrones es muy ineficaz de cara a reducir la fuerza y el alcance de la interacción de Coulomb, por lo que habría que explicar, desde un punto de vista teórico, cuál es el efecto de estas interacciones en las propiedades del sistema. Esto, incluso aunque fuese el caso de que en el caso experimental nunca se alcanzan niveles de dopaje en los que la influencia del punto de Dirac sea observable.

Surgen, por lo tanto, dos líneas de trabajo claramente delimitadas. Por un lado estudiar cómo el entorno afecta a las propiedades electrónicas del grafeno, y por otro analizar cuál es el estado fundamental del grafeno sin dopar. Ambos frentes son analizados en esta tesis, a lo largo de tres capítulos.

Interacciones electrostáticas entre capas de grafeno y su entorno

En el primer capítulo se estudian los efectos de las interacciones electrostáticas entre electrones del grafeno y aquellos elementos polarizables de uno de los entornos experimentales más frecuentes en el laboratorio, un sustrato de SiO_2 [66, 72]. Aunque en principio tanto el grafeno como el entorno son neutros, si estos elementos son polarizables pueden surgir interacciones debido al acoplo entre fluctuaciones de carga, denominadas fuerzas de van der Waals [256].

Un análisis del sustrato de SiO_2 basado tanto en los experimentos con grafeno como en otros experimentos que hacen uso del mismo [238–243, 247, 246] permite hacerse una idea de qué elementos pueden estar dando lugar a interacciones electrostáticas. Así pues, en esta tesis se consideran:

- Las fluctuaciones de carga de la puerta metálica bajo la capa de SiO_2, que es de silicio altamente dopado.
- La existencia de cargas atrapadas en la capa de SiO_2.
- Los fonones de superficie del SiO_2.

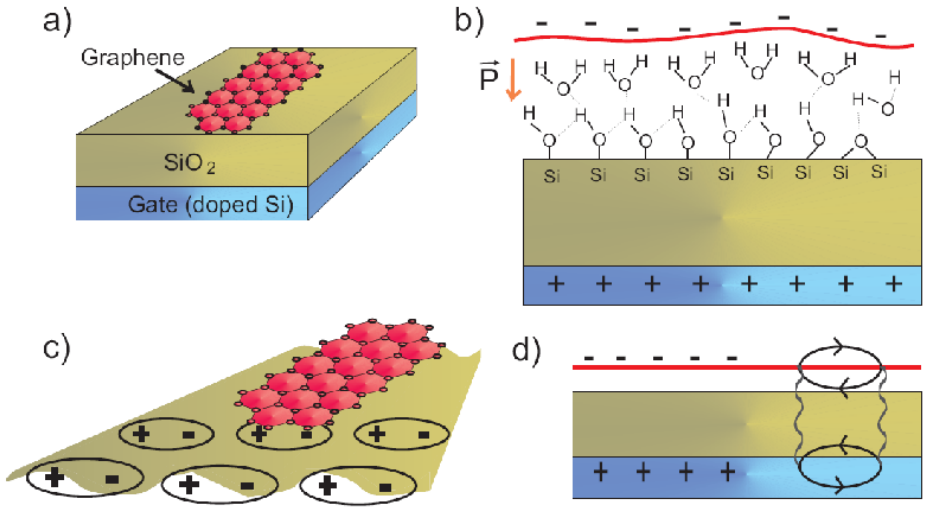

Elementos polarizables en un experimento con grafeno depositado sobre SiO_2. a) El sustrato está compuesto de una capa de 300 nm de SiO_2, aislante, sobre una puerta metálico de Si altamente dopado. b) Entre el grafeno y la superficie del sustrato puede haber moléculas de agua atrapadas. c) En la superficie del SiO_2 existen excitaciones de tipo fonónico, que también hacen las veces de pequeños dipolos de carga susceptibles de acoplarse a las fluctuaciones electrónicas. d) Algunas cargas pueden quedar atrapadas en el sustrato de SiO_2. e) La puerta metálica es otro elemento polarizable, donde las fluctuaciones de carga son de tipo electrón - hueco. Imagen tomada de [236].

- Moléculas de agua atrapadas entre el grafeno y la superficie del sustrato.

Un esquema de estos agentes y sus interacciones con las capas de grafeno se muestra en la figura 8.8. Para obtener expresiones analíticas de las correspondientes energías de interacción se utiliza teoría de perturbaciones a segundo orden en la corrección a la energía del estado fundamental de los sistemas desacoplados. Dichas expresiones dependen en general de la distancia z a la que se encuentra el agente de la capa de grafeno, en la dirección perpendicular a la misma. La tabla 8.0 recoge los principales resultados: por un lado, da las dependencias con la distancia de las distintas energías de interacción; por otro, da una estimación de las energías estimadas en experimentos típicos. Además, para ayudar a la comparación, se incluye la energía de interacción entre dos monocapas de grafeno.

Estos resultados pueden usarse para analizar diferentes situaciones experimentales. Por ejemplo, para grafenos depositados directamente sobre SiO_2, las interacciones dominantes son las que surgen del acoplo con los modos polares del SiO_2 y con las moléculas de agua. Sin embargo, en el caso de grafeno suspendido, el sustrato se encuentra mucho más distante, y la interacción más importante es aquella que surge del acoplo con impurezas cargadas, ya que es la que decae más despacio. Este análisis tiene consecuencias inmediatas en experimentos con osciladores de grafeno [254] o cuando se analiza la interacción entre una punta de un microscopio STM y el grafeno [269].

	Distancia (nm)	Dependencia en la distancia	Energía (meV Å^{-2})
Puerta	300	$z^{-3}\log(z/z_s)$	10^{-8}
Impurezas cargadas	1	z^{-1}	$10^{-4} - 10^{-2}$
Sustrato de SiO_2	1	z^{-2}	0.4
Moléculas de agua	0.3	z^{-3}	1
Grapheno	0.3	z^{-3}	30

Energías de interacción por unidad de área correspondientes a los interacciones estudiadas en la tesis. Para las estimaciones numéricas se han usado concentraciones de impurezas cargadas de $10^{10} - 10^{12}\text{cm}^{-2}$, así como 10^{15}cm^{-2} para las moléculas de agua.

Regla de suma f para electrones del grafeno

En este segundo capítulo dentro del bloque dedicado al grafeno se empieza a abordar el problema de las interacciones entre electrones del sistema. Para ello se deriva una identidad exacta, la regla de suma f, que una clase muy general de interacciones tiene que cumplir, ya que no es más que una consecuencia de la conservación del número de partículas en el sistema. Esta regla de suma se deriva para el espectro de baja energía del grafeno, es decir, para electrones de Dirac sin masa, y difiere de la correspondiente identidad para electrones de Schrödinger. La derivación, sin embargo, sigue los mismos pasos [184, 10], siendo el resultado independiente de la interacción, lo que la hace fácil de calcular. El resultado es el siguiente:

$$\int_0^{\Lambda_E} d\omega\, \omega\, \Im\chi(\mathbf{q},\omega) = -\frac{g_S g_v q^2 \Lambda_E}{16} \tag{8.118}$$

donde $\chi(\mathbf{q},\omega)$ es la susceptibilidad eléctrica del sistema de electrones en interacción, que en teoría de respuesta lineal codifica la respuesta del sistema a una sonda exterior que se acople a la carga [185]. Λ_E es una energía de corte, y $g_s g_v$ indica la degeneración de valle y espín del grafeno. La peculiaridad de esta regla de suma, y su principal diferencia con el caso de electrones de Schrödinger, radica en su dependencia con la energía de corte. Esto es debido a la existencia de un número creciente de excitaciones electrón-hueco entre las dos bandas (o conos) del espectro electrónico del grafeno a baja energía. Sin embargo, es importante notar que esta es una cantidad conservada para cualquier interacción que conserve el número de partículas, en particular la de Coulomb. Este resultado es nuevo en la literatura, donde ya se había abordado previamente el caso de la estructura de bandas completa del grafeno [275], o la regla de suma para electrones de Dirac en tres dimensiones espaciales e interacciones relativistas [273].

Una forma alternativa de esta regla de suma es la referida a la conductividad óptica [143], que es una cantidad más asequible experimentalmente que la susceptibilidad eléctrica [203]. Se deriva fácilmente del resultado anterior:

$$\int_0^{\infty} d\omega \Re\sigma(\omega) = \frac{g_s g_v \Lambda}{16} \tag{8.119}$$

donde $\sigma(\omega)$ es la conductividad óptica de los electrones, es decir, su conductividad para transferencia de momento nula.

La regla de suma f permite llevar a cabo un análisis de transferencia de peso espectral, que suele ser útil para identificar la importancia relativa de las excitaciones presentes en el sistema, e interpretar experimentos [272]. El peso espectral total es la integral dada por la regla de suma, mientras que pesos espectrales parciales corresponden a integrales parciales, ya sea porque se integra en un rango de energías finito o porque se descompone la susceptibilidad en suma de la respuesta de diferentes excitaciones. En cualquier caso, variando los parámetros del sistema (dopaje, fuerza de interacción), el peso espectral total tiene que conservarse, lo que implica que como mucho se de una transferencia de peso espectral entre excitaciones.

Si se aplica este tipo de análisis al grafeno sin dopar, se encuentra que el peso espectral está dominado por las excitaciones electrón-hueco entre bandas, dado que cualquier otra excitación predicha en la literatura [196] (plasmón amortiguado, subbanda excitónica), al menos en el régimen de acoplo débil del sistema en interacción, da contribuciones a órdenes mayores. Pese a todo, estudiando estas contribuciones se revela un comportamiento anómalo, ya que parece haber una transferencia de peso espectral entre el régimen de baja energía y el de alta energía (cerca de la energía de corte), algo peculiar dado que lo normal es que la transferencia sea entre excitaciones pertenecientes al mismo régimen de energías.

El caso de grafeno dopado resulta menos peculiar, pues tiene muchas similitudes con el de electrones de Schrödinger debido a la existencia de una superficie de Fermi. La contribución dominante sigue siendo la de la excitaciones entre bandas, pero ahora al mismo orden aparece una contribución intra banda, con un peso proporcional a la energía de Fermi E_F, y que está dominado por la presencia de un plasmón en el espectro de excitaciones [208–210].

El problema de los dos cuerpos y su relación con las fases de acoplo fuerte en grafeno

En este último capítulo se aborda el problema de las fases de acoplo fuerte en grafeno. Como ya se ha mencionado, los electrones del grafeno interaccionan a través del potencial de Coulomb, que en el caso sin dopar son incapaces de producir un apantallamiento efectivo que reduzca su alcance y lleve su intensidad a un régimen extrictamente perturbativo. Un análisis de Grupo de Renormalización de este problema [189, 193], llevado a cabo en el régimen perturbativo, muestra que la interacción de Coulomb es marginalmente irrelevante, de forma que a baja energía tiende a un punto fijo en el que de forma efectiva las interacciones no juegan ningún papel, algo que resulta compatible con los resultados experimentales. Sin embargo, las muestras reales de grafeno, incluso teniendo en cuenta el apantallamiento intrínseco y el dado por el entorno, siguen estando en un régimen de acoplo no perturbativo para las interacciones electrónicas. Si los resultados del Grupo de Renormalización son todavía válidos para estos acoplos es algo que es cuestionable, ya que podría haber otros puntos fijos que dominen el flujo del Grupo de Renormalización en acoplo fuerte. Esto ha sido muy discutido en la literatura reciente [214, 198, 215]. De hecho, algunos autores apuntan a la posibilidad de una transición de fase para acoplos fuertes en la que el sistema se haga aislante debido a la formación de

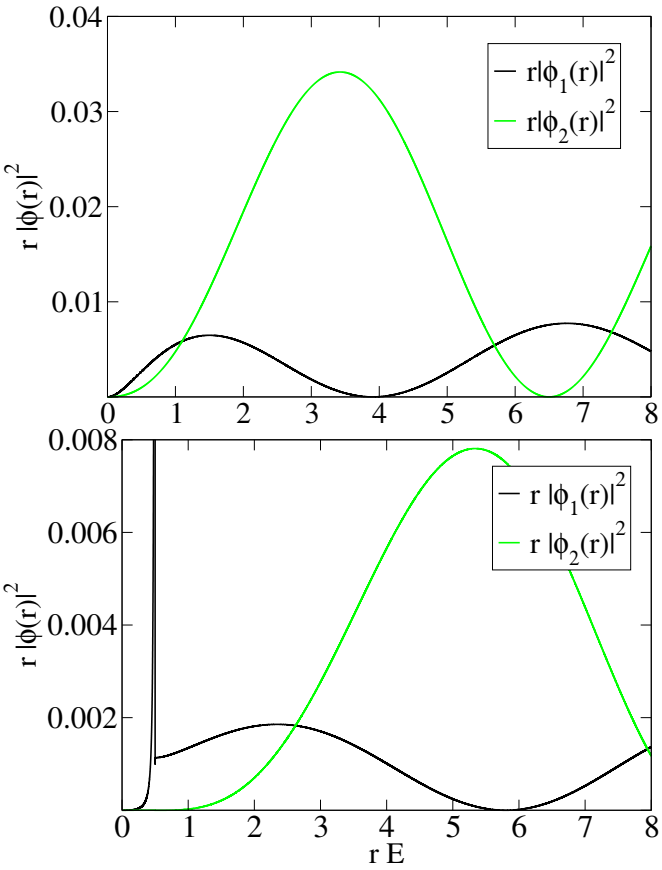

Solución numérica de la función de onda radial para el caso de un potencial de Coulomb y momento del centro de masas nulo. El momento angular es $l = 1$. Arriba: funciones de onda para $g = -0.5$ y $E > 0$. Abajo: funciones de onda para $g = 0.5$ y $E > 0$. Notar que cuando se cumple la condición de retorno clásico $g/r_0 = E$ aparece una singularidad debido a la existencia de estados de cero energía.

excitones [224, 226, 227, 232].

Como ya ocurre en el caso de la superconductividad, ocurre que en muchos problemas físicos de muchos cuerpos en interacción, la inestabilidad que conduce a una transición de fase ya está contenida en el problema de dos partículas. De hecho,incluso en el problema de una partícula de Dirac sin masa en presencia de un potencial de Coulomb externo ya aparece una inestabilidad de acoplo fuerte que podría estar relacionada con la formación de excitones [229–231]. Esto, sin ni siquiera tener en cuenta las restricciones dadas por la presencia del mar de Dirac, como ocurre en el problema de Cooper.

En este capítulo se analiza, en primer lugar, la estructura general del problema de dos partículas de Dirac sin masa, en dos dimensiones, e interaccionando a través de potenciales no relativistas. El problema general es complicado debido a que no se puede separar el centro de masas de la coordenada relativa, complicando la obtención de una solución exacta. Sin embargo, el problema en el que par tiene un momento del centro de masas nulo resulta más sencillo de analizar, a la vez que es el más relevante de cara a estudiar la formación de excitones. Al fin y al cabo, es la situación

energéticamente más favorable. La principal ventaja de este caso es que permite descomponer el problema en canales con momento angular relativo l bien definido. Un análisis detallado de este problema reducido presenta las siguientes características notables:

- Para aquellos canales con $l \neq 0$, los estados de cero energía del problema juegan un papel notable en el mismo, produciendo discontinuidades y divergencias en la función de onda en los puntos de retorno clásico, es decir, aquellos en los que la energía cinética iguala la energía potencial. Este comportamiento está reflejado en la figura 8.8 para el potencial de Coulomb.

- Para el caso de potenciales de Coulomb, el sistema se vuelve inestable a partir de un cierto acoplo crítico $g_c \equiv \sqrt{1+4l^2}$, que depende del canal de momento angular. El mínimo lo da el canal $l = 0$, para el que $g_c = 1$, que es un valor muy próximo a las estimaciones analíticas y numéricas realizadas al estudiar la transición de fase para muchos cuerpos.

- El caso $l = 0$, u onda s, presenta una simplicidad analítica considerable, lo que permite resolverlor de forma analítica siguiendo los mismos pasos que en el caso de un solo cuerpo en presencia de un potencial externo.

Extendiendo el análisis a momentos del centro de masa distintos de cero, se puede argumentar que tanto el rol peculiar de los estados de cero energía como la existencia de una inestabilidad permanecen en este caso.

El estudio de las inestabilidades del sistema de dos cuerpos se puede completar incluyendo la presencia del mar de Dirac, lo que resulta análogo al problema de Cooper para la superconductividad, pero considerando que al ser la interacción repulsiva entre electrones, la formación de pares se da entre electrones y huecos dando lugar a excitones. Para el caso de un potencial de Coulomb el problema no tiene solución analítica aparentemente, por lo que resulta más iluminador considerar el caso de un potencial de contacto. En este caso, el resultado es que se forma un estado ligado por encima de un cierto acoplo crítico. Definiendo $g \equiv |V| n(\Lambda)/4$, donde $|V|$ es la fuerza del potencial y $n(\Lambda)$ la densidad de estados en la energía de corte, la expresión analítica de la energía del excitón es:

$$E = -2\Lambda \frac{g^{-1} - 1}{W_{-1}(g^{-1} - 1)} \tag{8.120}$$

donde $W_{-1}(z)$ es la rama inferior de la función W de Lambert. Sólo para $g > 1$ dicha energía es negativa, lo que conecta en cierta manera la inestabilidad del problema de dos cuerpos sin mar de Dirac con este último.

Finalmente, el estudio de las inestabilidades de acoplo fuerte se puede finalizar analizando el problema completo de muchos cuerpos a través de un ansatz variacional que tenga en cuenta la formación de pares que tendría lugar de acuerdo a los resultados para dos cuerpos. Esto da lugar a una ecuación autoconsistente para el gap excitónico, es decir, el rango de energías en torno al punto de Dirac en el que se forman excitones, impidiendo la corriente de electrones. La expresión de esta ecuación es:

$$\Delta_{\mathbf{k}} = \sum_{\mathbf{k}'} V_{|\mathbf{k}'-\mathbf{k}|} \frac{\Delta_{\mathbf{k}'}}{E_{\mathbf{k}'}} \tag{8.121}$$

que recupera resultados ya conocidos en la literatura [224]. Para solucionar esta ecuación es necesario recurrir a aproximaciones, lo que en última instancia determina el valor del acoplo crítico en el que se daría la transición de fase. Estimaciones dadas en la literatura arrojan valores en torno a $g \sim 1$, si bien el valor concreto es todavía motivo de controversia [224, 226, 220, 227, 228]. Su cuantía resulta de la mayor relevancia, dado que si está por encima de los valores experimentales, justificaría de forma teórica que el grafeno sin dopar a baja energía se comporte como un sistema sin interacciones, a la vez que abriría la puerta a una posible observación experimental de esta transición disminuyendo el apantallamiento producido por el entorno.

Conclusiones

A lo largo de esta tesis se han estudiado algunas de las consecuencias que tienen las interacciones en la física de monocapas de grafeno y algunas realizaciones concretas de redes de átomos fríos. Ambos sistemas constituyen los dos grandes hitos de la física de baja dimensionalidad en los últimos años. Los físicos teóricos contamos con la ventaja de poder variar los parámetros de un determinado modelo a nuestro antojo, lo que nos da un acceso casi ilimitado a explorar nuevos fenómenos como transiciones de fase o la dinámica no trivial de un sistema a través de nuestras ecuaciones y simulaciones. Sin embargo, estudiar sistemas en interacción es una tarea prodigiosa, y requiere de técnicas muy sofisticadas que las más de las veces tan sólo permiten obtener respuestas parciales al problema, con la esperanza de que ayuden a entender con mayor profundidad la cuestión global que motivó la investigación.

En el caso de esta tesis, dichas cuestiones pertenecen en su totalidad al campo de la física de baja dimensionalidad. Algunas de ellas surgieron simplemente para satisfacer la curiosidad de los autores de la investigación, pero otras estuvieron motivadas por temas de actualidad que podrían clasificarse de urgentes por sus prometedoras aplicaciones. Esto viene a ejemplificar, al fin y al cabo, el doble papel social que juegan los científicos cuando hacen investigación: el compromiso de proveernos de los ingredientes básicos que conduzcan a una mejora ulterior de la calidad de vida humana, a la vez que se incrementa nuestra comprensión de cómo funciona la naturaleza. Una tesis constituye tan sólo un grano de arena dentro de esta gran empresa, un minúsculo paso adelante en la prodigiosa aventura de entender el mundo que nos rodea. Espero que esta tesis haya logrado su propósito en esta prodigiosa tarea.

List of publications

- J. Sabio, C. Seoanez, S. Fratini, F. Guinea, A.H. Castro Neto and F. Sols, *Electrostatic interactions between graphene layers and their environment*, Physical Review B **77**, 195409 (2008).
- J. Sabio, J. Nilsson and A.H. Castro Neto, *f-Sum rule and unconventional spectral-weight transfer in graphene*, Physical Review B **78**, 075410 (2008), Editor's suggestion.
- J. Sabio, L. Borda, F. Guinea and F. Sols, *Phase diagram of the dissipative quantum particle in a box*, Physical Review B **78**, 085439 (2008).
- J. Sabio, L. Borda, F. Guinea and F. Sols, *Erratum: Phase diagram of the dissipative quantum particle in a box*, Physical Review B **78**, 199902(E) (2008)
- J. Sabio and F. Sols, *Variational approach to the Caldeira-Leggett model*, Physica E, doi:10.1016/j.physe.2009.06.066 (2009)
- J. Sabio, F. Sols and F. Guinea, *The two-body problem in graphene*, arXiv:0911.0376 (2009). Accepted in PRB, Editor's suggestion.
- J. Sabio and S. Kehrein, *Sudden interaction quench in the quantum sine-Gordon model*, arXiv:0911.1302 (2009). Accepted in New Journal of Physics, special issue on Thermalization in Quantum Isolated Systems.
- J. Sabio, F. Sols and F. Guinea, *Two-body instabilities and strong-coupling phases in graphene*. In preparation.

Bibliography

[1] B. H. Bransden and C. J. Joachaim. *Quantum mechanics*. Pearson Education Ltd., Essex, 2000. (cited on pages 2, 6, and 20)

[2] A. I. Yanson, G. Rubio Bollinger, H. E. van der Brom, N. Agrait, and J. M. van Ruitenbeek. Formation and manipulation of a metallic wire of single gold atoms. *Nature*, 395:783, 1998. (cited on p. 3)

[3] Supriyo Datta. *Electronic transport in mesoscopic systems*. Cambridge University Press, Cambridge, 1995. (cited on pages 4, 7, 8, and 11)

[4] T. Ando, A. B. Fowler, and F. Stern. Electronic properties of two-dimensional systems. *Rev. Mod. Phys.*, 54:437, 1982. (cited on pages 5, 7, and 195)

[5] W.T. Sommer. Liquid helium as a barrier to electrons. *Phys. Rev. Lett.*, 12:271, 1964. (cited on p. 6)

[6] R.S. Crandall and R. Williams. Crystallization of electrons on the surface of liquid helium. *Phys. Lett.*, 7:404, 1971. (cited on p. 6)

[7] K. von Klitzing, G. Dorda, and M. Pepper. New method for high-accuracy determination of the fine-structure constant based on quantized hall resistance. *Phys. Rev. Lett.*, 45:494, 1980. (cited on p. 6)

[8] D.C. Tsui, H.L. Stormer, and A.C. Gossard. Two-dimensional magnetotransport in the extreme quantum limit. *Phys. Rev. Lett.*, 48:1559, 1982. (cited on p. 6)

[9] H.L. Stormer. Two-dimensional electron correlation in high magnetic fields. *Physica B*, 177:401, 1992. (cited on p. 6)

[10] Gabriele F. Giuliani and Giovani Vignale. *Quantum theory of the electron liquid*. Cambridge University Press, Cambridge, 2005. (cited on pages 7, 9, 10, 118, 121, 122, 162, 167, 195, and 217)

[11] R.G. Wheeler, K.G. Choi, A. Goel, R. Wisnieff, and D.E. Prober. Localization and electron-electron interaction effects in submicron-width inversion layers. *Phys. Rev. Lett.*, 49:1674, 1982. (cited on p. 8)

[12] C.W.J. Beenakker and H. van Houten. Quantum transport in semiconductor nanostructures. In H. Ehrenreich and D. Turnbull, editors, *Solid State Physics*, page 44. Academic Press, New York, 1991. (cited on p. 8)

[13] E. Y. Andrei, G. Deville, D.C. Glattli, F.I.B. Williams, E.Paris, and B. Etienne. Observation of a magnetically induced wigner solid. *Phys. Rev. Lett.*, 60:2765, 1988. (cited on p. 8)

[14] B.J. van Wees, H. van Houten, C.W.J. Beenakker, J.G. Williamson, L.P.Kouwenhoven, D. van der Marel, and C.T. Foxon. Quantized conductance of point contacts in a two-dimensional electron gas. *Phys. Rev. Lett.*, 60:848, 1988. (cited on pages 8 and 10)

[15] G. Timp, A.M. Chang, J.E. Cunningham, T.Y. Chang, P. Mankiewich, R. Behringer, and R.E. Howard. Observation of the aharonov-bohm effect for $\omega\tau > 1$. *Phys. Rev. Lett.*, 67:769, 1987. (cited on p. 8)

[16] Thierry Giamarchi. *Quantum Physics in one dimension*. Clarendon Press, Oxford, 2003. (cited on pages 9, 10, 11, 12, 96, 99, 101, and 213)

[17] J. Voit. One-dimensional fermi liquids. *Rep. Prog. Phys.*, 57:977, 1984. (cited on p. 10)

[18] R. Peierls. *Quantum theory of Solids*. Oxford University Press, Oxford, 1955. (cited on p. 10)

[19] T. Lorenz, M. Hofman, M. Grüninger, A. Freimuth, G.S. Uhrig, M. Dumm, and M. Dressel. Evidence for spin-charge separation in quasi-one-dimensional organic conductors. *Nature*, 418:614, 2002. (cited on p. 10)

[20] M. L Roukes, A. Scherer, Jr S.J. Allen, H.R. Craighead, R.M. Ruthen, E. D. Beebe, and J.P. Harbison. Quenching of the hall effect in a one-dimensional wire. *Phys. Rev. Lett.*, 59:3011, 1987. (cited on p. 10)

[21] Y. Tserkovnyak, B. Halperin, O. Auslaender, and A. Yacoby. Interference and zero-bias anomaly in tunneling between luttinger-liquid wires. *Phys. Rev. B*, 68:125312, 2003. (cited on p. 10)

[22] K.J. Thomas, J.T. Nicholls, M. Y. Simmons, M. Pepper, D.R. Mace, and D.A. Ritchie. Possible spin polarization in a one-dimensional electron gas. *Phys. Rev. Lett.*, 77:135, 1996. (cited on p. 11)

[23] M. Bockrath, D.H. Cobden, P.L. McEuen, N.G. Chopra, A. Zettl, A. Thess, and R.E.Smalley. Single-electron transport in ropes of carbon nanotubes. *Science*, 275:1922, 1997. (cited on p. 11)

[24] H. Ishii, H. Kataura, H. Shiozawa, H. Yoshioka, H. Otsubo, Y. Takayama, T. Miyahara, S. Suzuki, Y. Achiba, M. Nakatake, T. Narimura, M. Higashiguchi, K. Shimada, H. Namatame, and M. Taniguchi. Direct observation of tomonaga-luttinger-liquid state in carbon nanotubes at low temperatures. *Nature*, 426:540, 2003. (cited on p. 11)

[25] R. Egger and A.O. Gogolin. Effective low-energy theory for correlated carbon nanotubes. *Phys. Rev. Lett.*, 79:5082, 1997. (cited on p. 11)

[26] M. Kociak, A. Yu. Kasumov, S. Gueron, B. Reulet, L. Vaccarini, I.I. Khodos, B. Yu. Gorbatov, V.T. Volkiv, and H. Bouchiat. in ropes of single-walled carbon nanotubes. *Phys. Rev. Lett.*, 86:2416, 2001. (cited on p. 11)

[27] M. Henny, S. Oberholzer, C. Strunk, T. Heinzel, K. Ensslin, M. Holland, and C. Schönenberger. The fermionic hanbury brown and twiss experiment. *Science*, 284:296, 1999. (cited on p. 12)

[28] Y. Ji, Y. Chung, D. Sprinzak, M. Heiblum, D. Mahalu, and H. Shtrikman. An electronic mach-zehnder interferometer. *Nature*, 422:415, 2003. (cited on p. 12)

[29] A. M. Chang. Chiral luttinger liquids at the fractional quantum hall edge. *Rev. Mod. Phys.*, 75:1449, 2003. (cited on p. 12)

[30] P. Segovia, D. Purdie, M. Hengsberger, and Y. Baer. Observation of spin-charge separation in one-dimensional metallic chains. *Nature*, 402:504, 1999. (cited on p. 13)

[31] M. Bockrath, D.H. Cobden, J. Lu, A.G. Rinzler, R.E.Smalley, L. Balents, and P.L. McEuen. Luttinger-liquid behaviour in carbon nanotubes. *Nature*, 397:598, 1999. (cited on p. 13)

[32] D.C. Ralph, C.T. Black, and M. Tinkham. Gate-voltage studies of discrete electronic states in aluminum nanoparticles. *Phys. Rev. Lett.*, 78:4087, 1997. (cited on p. 13)

[33] Y. Alhassid. The statistical theory of quantum dots. *Rev. Mod. Phys.*, 72:895, 2000. (cited on pages 13 and 14)

[34] S. Tarucha, D.G. Austing, T. Honda, R.J. van der Hage, and L.P. Kouwenhoven. Shell filling and spin effects in a few electron quantum dot. *Phys. Rev. Lett.*, 77:3613, 1996. (cited on p. 13)

[35] J.A. Folk, S.R. Patel, S.F. Godjin, A.G. Huibers, S.M. Cronenwett, C.M.Marcus, K. Crampman, and A.C. Gossard. Statistics and parametric correlations of coulomb blockade peak fluctuations in quantum dots. *Phys. Rev. Lett.*, 76:1699, 1996. (cited on p. 14)

[36] I.L. Aleiner, P.W. Brouwer, and L.I. Glazman. Quantum effects in coulomb blockade. *Physics Reports*, 358:309, 2002. (cited on p. 13)

[37] A.C.Hewson. *The Kondo Problem to Heavy Fermions*. Cambridge University Press, Cambridge, 2003. (cited on p. 13)

[38] D. Goldhaber-Gordon, H. Shtrikman, D. Mahalu, D. Abusch-Magder, U. Meirav, and M.A. Kastner. Kondo effect in a single-electron transistor. *Nature*, 391:156, 1998. (cited on p. 14)

[39] W.H.Zurek. Decoherence, einselection, and the quantum origins of the classical. *Rev. Mod. Phys.*, 75:715, 2003. (cited on pages 14 and 62)

[40] U. Weiss. *Quantum Dissipative Systems*. World Scientific, Singapore, 1999. (cited on pages 14, 62, and 73)

[41] H.P. Breuer and F. Petruccione. *The Theory of Open Quantum Systems*. Oxford University Press, Oxford, 2002. (cited on pages 14 and 211)

[42] C. Durkan. *Current at the Nanoscale: An Introduction to Nanoelectronics*. Imperial College Press, London, 2007. (cited on p. 14)

[43] M.A. Nielsen and I. L. Chuang. *Quantum Computation and Quantum Information*. Cambridge University Press, Cambridge, 2000. (cited on p. 14)

[44] A. Pimpinelli and J. Villain. *Physics of Crystal Growth*. Cambridge University Press, Cambridge, 1998. (cited on p. 15)

[45] D.L. Huffaker, G. Park, Z. Zou, O.B. Shchekin, and D.G. Deppe. 1.3 μm room-temperature gaas-based quantum-dot laser. *Appl. Phys. Lett.*, 73:2564, 1998. (cited on p. 15)

[46] M.H. Anderson, J.R. Ensher, M.R. Matthews, C.E. Wieman, and E.A. Cornell. Observaton of bose-einstein condensation in a dilute atomic vapor. *Science*, 14:198, 1995. (cited on p. 16)

[47] K.B. Davis, M.O. Mewes, M.R. Andrews, N.J. van Druten, D.S. Durfee, D.M. Kurn, and W.Ketterle. Bose-einstein condensation in a gas of sodium atoms. *Phys. Rev. Lett.*, 75:3969, 1995. (cited on p. 16)

[48] B. DeMarco and D.S.Jin. Onset of fermi degeneracy in a trapped atomic gas. *Science*, 185:1703, 1999. (cited on p. 16)

[49] I. Bloch, J. Dalibard, and W. Zwerger. Many-body physics with ultracold gases. *Rev. Mod. Phys.*, 80:885, 2008. (cited on pages 16, 19, 20, 21, 22, and 209)

[50] M. Bartenstein, A. Altmeyer, S. Riedl, S. Jochim, C. Chin, J. Hecker Denschlag, and R. Grimm. Collective excitations of a degenerate at the bec-bcs crossover. *Phys. Rev. Lett.*, 92:203021, 2004. (cited on p. 16)

[51] M.W. Zwierlein, C.A.Stan, C.H.Schunck, S.M.F. Raupach, A.J.Kerman, and W.Ketterle. Condensation of pairs of fermionic atoms near a feshbach resonance. *Phys. Rev. Lett.*, 92:120403, 2004. (cited on p. 16)

[52] M. Greiner, O. Mandel, T. Esslinger, T. W. Hänsch, and I. Bloch. Superfluid to a mott insulator in a gas of ultracold atoms. *Nature*, 415:39, 2002. (cited on p. 16)

[53] B. Paredes, A. Widera, V. Murg, O. Mandel, S. Fölling, J.I. Cirac, G.V. Shlyapnikov, T. W. Hänsch, and I. Bloch. Tonks-giardeau gas of ultracold atoms in an optical lattice. *Nature*, 429:277, 2004. (cited on pages 17, 19, and 22)

[54] T. Kinoshita, T. Wenger, and D.S. Weiss. Observation of a one-dimensional tonks-girardeau gas. *Science*, 305:1125, 2004. (cited on pages 17 and 19)

[55] Z. Hadzibabic, P. Krüger, M. Cheneau, B. Battelier, and J. Dalibard. Berezinskii-kosterlitz-thouless crossover in a trapped atomic gas. *Nature*, 441:1118, 2006. (cited on p. 17)

[56] T. Kinoshita, T. Wenger, and D. S. Weiss. A quantum newton's cradle. *Nature*, 440:900, 2006. (cited on pages 17 and 93)

[57] C. Pethick and H. Smith. *Bose-Einstein condensation in dilute gases*. Cambridge University Press, Cambridge, 2001. (cited on p. 17)

[58] R. Grimm, M. Weidemüller, and Y.B. Ovchinnikov. Optical dipole traps for neutral atoms. *Adv. At. Mol. Opt. Phys.*, 42:95, 2000. (cited on p. 18)

[59] R.A. Duine and H.T.C. Stoof. Atom-molecule coherence in bose gases. *Phys. Rep.*, 396:115, 2004. (cited on p. 20)

[60] T. Köhler and K. Góral. Production of cold molecules via magnetically tunable feshbach resonances. *Rev. Mod. Phys.*, 78:1311, 2006. (cited on p. 20)

[61] R. Folman, P. Krüger, J. Schmiedmayer, J. Denschlag, and C. Henkel. Microscopic atom optics: from wires to an atom chip. *Adv. At. Mol. Opt. Phys.*, 48:263, 2002. (cited on pages 22 and 211)

[62] J. Fortagh and C. Zimmermann. Magnetic microtraps for ultracold atoms. *Rev. Mod. Phys.*, 79:235, 2007. (cited on p. 22)

[63] Y.J. Wang, D.Z. Anderson, V.M. Bright, E. A. Cornell, Q. Diot, T. Kishimoto, M. Prentiss, R.A. Saravanan, S.R. Segal, and W. Saijun. Atom michelson interferometer on a chip using a bose-einstein condensate. *Phys. Rev. Lett.*, 94:090405, 2005. (cited on p. 23)

[64] C. Henkel, P. Krüger, R. Folman, and J. Schmiedmayer. Fundamental limits for coherent manipulation on atom chips. *App. Phys. B*, 76:173, 2003. (cited on p. 23)

[65] P. A. Martin and P.R. Buenzli. The casimir effect. *Acta Phys. Polonica B*, 37:2503, 2006. (cited on pages 24 and 150)

[66] K.S. Novoselov, A.K. Geim, S.V. Morozov, D. Jiang, Y. Zhang, S. V. Dubonos, I.V. Grigorieva, and A. A. Firsov. Electric field effect in atomically thin carbon films. *Science*, 306:666, 2004. (cited on pages 24, 26, 27, 209, and 215)

[67] A. Barth and W. Marx. Graphene – a rising star in view of scientometrics. *arXiv:0808.3320*, 2008. (cited on p. 24)

[68] N.D. Mermin. Crystalline order in two dimensions. *Phys. Rev.*, 176:250, 1968. (cited on pages 24 and 33)

[69] D. R. Nelson, T. Piran, and S. Weinberg. *Statistical Mechanics of Membranes and Surfaces*. World Scientific, Singapore, 2004. (cited on pages 24 and 34)

[70] J.C. Meyer, A.K. Geim, M.I. Katsnelson, K.S. Novoselov, D. Obergfell, S.Roth, C. Girit, and Z. Zettl. On the roughness of single and bilayer graphene membranes. *Solid State Commun.*, 143:101, 2007. (cited on pages 24, 25, and 34)

[71] P.R. Wallace. The band theory of graphite. *Phys. Rev.*, 71:622, 1947. (cited on pages 24, 29, and 215)

[72] K.S. Novoselov, A.K. Geim, S.V. Morozov, D. Jiang, M.I. Katsnelson, I.V. Grigorieva, S.V. Dubonos, and A.A. Firsov. Two-dimensional gas of massless dirac fermions in graphene. *Nature*, 438:197, 2005. (cited on pages 25, 27, 28, 209, and 215)

[73] J.H. Chen, C. Jang, S. Adam, M. S. Fuhrer, E. D. Williams, and M. Ishigami. Charged-impurity scattering in graphene. *Nat. Phys.*, 4:377, 2008. (cited on p. 25)

[74] J. C. Meyer, A.K. Geim, M.I. Katsnelson, K.S. Novoselov, T.J. Booth, and S. Roth. The structure of suspended graphene sheets. *Nature*, 446:60, 2007. (cited on pages 25 and 28)

[75] Xu Du, I. Skachko, A. Barker, and E. Y. Andrei. Suspended graphene: a bridge to the dirac point. *Nat. Nan.*, 3:491, 2008. (cited on pages 25 and 28)

[76] K. Nakada, M. Fujita, G. Dresselhaus, and M. S. Dresselhaus. Edge state in graphene ribbons: Nanometer size effect and edge shape dependence. *Phys. Rev. B*, 54:17954, 1996. (cited on p. 25)

[77] E. Kim and A.H. Castro Neto. Graphene as an electronic membrane. *Europhys. Lett.*, 84:57007, 2008. (cited on pages 25, 34, and 157)

[78] F. Guinea, M.I. Katsnelson, and M.A.H. Vozmediano. Midgap states and charge inhomogeneities in corrugated graphene. *Phys. Rev. B*, 77:075422, 2008. (cited on pages 25 and 35)

[79] M.I. Katsnelson and K.S. Novoselov. Graphene: new bridge between condensed matter physics and quantum electrodynamics. *Solid State Commun*, 143:3, 2007. (cited on pages 25 and 33)

[80] M.A.H. Vozmediano, F. de Juan, and A. Cortijo. Gauge fields and curvature. *J. of Phys.: Conference Series*, 129:012001, 2008. (cited on p. 25)

[81] A.H. Castro Neto, F. Guinea, N.M.R. Peres, K.S. Novoselov, and A.K. Geim. The electronic properties of graphene. *Rev. Mod. Phys.*, 81:109, 2009. (cited on pages 26, 31, 32, 133, 209, and 215)

[82] A. Castro Neto, F. Guinea, and N. M. Peres. Drawing conclusions from graphene. *Phys. World*, 19:33, 2006. (cited on p. 26)

[83] A.K. Geim and K.S. Novoselov. The rise of graphene. *Nat. Mat.*, 6:183, 2007. (cited on pages 26, 28, 33, and 34)

[84] A. C. Ferrari, J.C. Meyer, V. Scardaci, C. Casiraghi, M. Lazzeri, F. Mauri, S. Piscanec, D. Jiang, K.S. Novoselov, S. Roth, and A.K. GeimNovoso. Raman spectrum of graphene and graphene layers. *Phys. Rev. Lett.*, 97:187401, 2006. (cited on p. 26)

[85] K.S. Novoselov, Z. Jiang, Y. Zhang, S.V. Morozov, H.L. Stormer, U. Zeitler, J.C. Maan, G.S. Boebinger, P. Kim, and A.K Geim. Room-temperature quantum hall effect in graphene. *Science*, 315:1379, 2007. (cited on p. 27)

[86] Y. Zhang, J.W. Tan, H.L. Stormer, and P. Kim. Experimental observation of the quantum hall effect and berry's phase in graphene. *Nature*, 438:201, 2005. (cited on p. 27)

[87] K.I. Bolotin, K.J. Sikes, Z. Jiang, M. Klima, G. Fudenberg, J. Hone, P. Kim, and H.L. Stormer. Ultrahigh electron mobility in suspended graphene. *Solid State Commun.*, 146:351, 2008. (cited on p. 28)

[88] A. H. Castro Neto. Pauling's dreams for graphene. *Physics*, 2:30, 2009. (cited on pages 28 and 136)

[89] A.L. Vazquez de Parga, F. Calleja, B. Borca, M.C.G. Passeggi Jr., J.J. Hinarejos, F. Guinea, and R. Miranda. Periodically rippled graphene: Growth and spatially resolved electronic structure. *Phys. Rev. Lett.*, 100:056807, 2008. (cited on p. 28)

[90] I. Forbeaux, J.M. Themlin, and J. M. Debever. Heteroepitaxial graphite on $6h - sic(0001)$: Interface formation trough conduction-band electronic structure. *Phys. Rev. B*, 58:16396, 1998. (cited on p. 28)

[91] W. A. de Heer, C. Berger, X. Wu, P.N. First, E. H. Conrad, X. Li, T. Li, M. Sprinkle, J. Hass, M.L. Sadowski, M. Potemski, and G. Martinez. Epitaxial graphene. *Solid State Commun.*, 143:92, 2007. (cited on p. 29)

[92] A. Bostwick, T. Ohta, T. Seyller, K. Horn, and E. Rotenberg. Quasiparticle dynamics in graphene. *Nat. Phys.*, 3:36, 2007. (cited on pages 29, 130, 134, and 174)

[93] S. Y. Zhou, G. H. Gweon, A. V. Fedorov, P. N. First, W. A. de Heer, D.H. Lee, F. Guinea, A. H. Castro Neto, and A. Lanzara. Substrate-induced bandgap opening in epitaxial graphene. *Nat. Mat.*, 6:770, 2007. (cited on pages 29 and 166)

[94] M.I. Katsnelson, K. S. Novoselov, and A. K. Geim. Chiral tunnelling and the klein paradox in graphene. *Nat. Phys.*, 2:620, 2006. (cited on p. 33)

[95] A.W.W. Ludwig, M.P.A. Fisher, R. Shankar, and G. Grinstein. Integer quantum hall transition: An alternative approach and exact results. *Phys. Rev. B*, 50:7526, 1994. (cited on pages 33, 137, and 139)

[96] J. Tworzydlo, B. Trauzettel, M. Titov, A. Rycerz, and C.W.J. Beenakker. Quantum-limited shot noise in graphene. *Phys. Rev. Lett.*, 96:246802, 2006. (cited on p. 33)

[97] V.P. Gusynin and S.G. Sharapov. Magnetic oscillations in planar systems with the dirac-like spectrum of quasiparticle excitations.ii. transport properties. *Phys. Rev. B*, 71:125124, 2005. (cited on p. 33)

[98] N.D. Mermin and H. Wagner. Absence of ferromagnetism or antiferromagnetism in one- or two-dimensional isotropic heisenberg models. *Phys. Rev. Lett.*, 17:1133, 1966. (cited on p. 33)

[99] P.C. Hohenberg. Existence of long-range order in one and two dimensions. *Phys. Rev.*, 158:383, 1967. (cited on p. 33)

[100] A. Fasolino, J.H. Los, and M.I. Katsnelson. Intrinsic ripples in graphene. *Nat. Mat.*, 6:858, 2007. (cited on p. 34)

[101] M. Ishigami, J.H. Chen, W.G. Cullen, M.S. Fuhrer, and E.D. Williams. Atomic structure of graphene on sio_2. *Nano Letters*, 7:1643, 2007. (cited on pages 34, 144, 147, 149, and 155)

[102] W. Bao, F. Miao, Z. Chen, H. Zhang, W. Jang, C. Dames, and C. Lau. Controlled ripple texturing of suspended graphene and ultrathin graphite membranes. *Nat. Nan.*, 4:562, 2009. (cited on p. 34)

[103] F. de Juan, A. Cortijo, and M.A.H. Vozmediano. Charge inhomogeneities due to smooth ripples in graphene sheets. *Phys. Rev. B*, 76:165409, 2007. (cited on p. 34)

[104] J. Martin, N. Akerman, G. Ulbricht, T. Lohmann, J.H. Smet, K. von Klitzing, and A. Yacoby. Observation of electron-hole puddles in graphene using a scanning single-electron transistor. *Nat. Phys.*, 4:144, 2008. (cited on pages 35, 123, 129, and 147)

[105] E. Rossi, S. Adam, and S. Das Sarma. Effective medium theory for disordered two-dimensional graphene. *Phys. Rev. B*, 79:245423, 2009. (cited on pages 35, 123, and 147)

[106] F. Guinea, M.I. Katsnelson, and A.K. Geim. Energy gaps and a zero-field quantum hall effect in graphene by strain engineering. *Nat. Phys.*, page doi:10.138/nphys781, 2009. (cited on p. 35)

[107] K.G. Wilson and J. Kogut. The renormalization group and the ϵ expansion. *Phys. Rep.*, 12C:75, 1974. (cited on p. 39)

[108] D.J. Amit and V. Martin-Mayor. *Field Theory, the Renormalization Group and Critical Phenomena*. World Scientific, Singapore, 2005. (cited on pages 39 and 210)

[109] J. Cardy. *Scaling and Renormalization in Statistical Physics*. Cambridge University Press, Cambridge, 1996. (cited on pages 39 and 213)

[110] S. Kehrein. *The Flow Equation Approach to Many-Body Problems*. Springer-Verlag, Heidelberg, 2006. (cited on pages 40, 42, 55, 57, 101, and 210)

[111] P. Ball. *Critical mass: how one thing leads to another*. William Heinemann, Great Britain, 2004. (cited on p. 41)

[112] K.G. Wilson. The renormalization group: Critical phenomena and the kondo problem. *Rev. Mod. Phys.*, 47:773, 1975. (cited on pages 44, 47, and 210)

[113] R. Shankar. Renormalization group approach to interacting fermions. *Rev. Mod. Phys.*, 66:129, 1994. (cited on pages 46, 118, and 120)

[114] A.C. Hewson. *The Kondo Problem to Heavy Fermions*. Cambridge University Press, Cambridge, 1993. (cited on p. 47)

[115] H. R. Krishna-murthy, J.W. Wilkins, and K.G. Wilson. Renormalization-group approach to the anderson model of dilute magnetic alloys. i. static properties for the symmetric case. *Phys. Rev. B*, 21:1003, 1980. (cited on p. 47)

[116] H. R. Krishna-murthy, J.W. Wilkins, and K.G. Wilson. Renormalization-group approach to the anderson model of dilute magnetic alloys. ii. static properties for the asymmetric case. *Phys. Rev. B*, 21:1044, 1980. (cited on p. 47)

[117] R. Bulla, T. A. Costi, and T. Pruschke. Numerical renormalization group method for quantum impurity systems. *Rev. Mod. Phys.*, 80:395, 2008. (cited on pages 47, 52, and 210)

[118] R. Bulla, H. Lee, N. Tong, and M. Vojta. Numerical renormalization group for quantum impurities in a bosonic bath. *Phys. Rev. B*, 71:045122, 2005. (cited on pages 47, 49, 54, and 80)

[119] A. J. Leggett, S. Chakravarty, A.T. Dorsey, M. P. A. Fisher, A. Garg, and W. Zwerger. Dynamics of the dissipative two-state system. *Rev. Mod. Phys.*, 59:1, 1987. (cited on pages 47, 48, and 72)

[120] A. O. Caldeira and A.J. Leggett. Quantum tunnelling in a dissipative system. *Ann. Phys. (N.Y.)*, 149:374, 1983. (cited on pages 48, 63, 65, and 211)

[121] S.D. Glazek and K.G. Wilson. Renormalization of hamiltonians. *Phys. Rev. D*, 48:5863, 1993. (cited on pages 55 and 210)

[122] S.D. Glazek and K.G. Wilson. Perturbative renormalization group for hamiltonians. *Phys. Rev. D*, 49:4214, 1994. (cited on p. 55)

[123] F. Wegner. Flow-equations for hamiltonians. *Ann. Phys. (Leipzig)*, 3:77, 1994. (cited on pages 55 and 210)

[124] W. Hofstetter. Generalized numerical renormalization group for dynamical quantities. *Phys. Rev. Lett.*, 85:1508, 2000. (cited on p. 55)

[125] A. B. Frithjof and A. Schiller. Real-time dynamics in quantum-impurity systems: A time-dependent numerical renormalization-group approach. *Phys. Rev. Lett.*, 95:196801, 2005. (cited on p. 55)

[126] S. Kehrein, A. Mielke, and P. Neu. Flow equations for the spin-boson problem. *Z. Phys. B*, 99:269, 1996. (cited on p. 57)

[127] S. Kehrein and A. Mielke. Low temperature equilibrium correlation functions in dissipative quantum systems. *Ann. Physik (Leipzig)*, 6:90, 1997. (cited on pages 57 and 58)

[128] J. Sabio, L. Borda, F. Guinea, and F. Sols. Phase diagram of the dissipative quantum particle in a box. *Phys. Rev. B*, 78:085439, 2008. (cited on p. 61)

[129] J. Sabio, L. Borda, F. Guinea, and F. Sols. Erratum: Phase diagram of the dissipative quantum particle in a box. *Phys. Rev. B*, 78:199902(E), 2008. (cited on pages)

[130] J. Sabio and F. Sols. Variational approach to the caldeira-leggett model. *Physica E*, pages doi:10–1016/j.physe.2009.06.066, 2009. (cited on p. 61)

[131] W. H. Zurek. Decoherence and the transition from quantum to classical. *Phys. Today*, 44:36, 1991. (cited on p. 62)

[132] M. Schlosshauer. Decoherence, the measurement problem, and interpretations of quantum mechanics. *Rev. Mod. Phys.*, 76:1267, 2004. (cited on p. 62)

[133] E. Joos, H.D. Zeh, C. Kiefer, D. Giulini, J. Kupsch, and I.O. Stamatescu. *Decoherence and the Appearance of a Classical World in Quantum Theory*. Springer, Heidelberg, 1996. (cited on p. 63)

[134] R.P. Feynman and F.L. Vernon. The theory of a general quantum system interacting with a linear dissipative system. *Ann. Phys. (N.Y.)*, 24:118, 1963. (cited on p. 63)

[135] A. O. Caldeira and A.J. Leggett. Influence of dissipation on quantum tunneling in macroscopic systems. *Phys. Rev. Lett.*, 46:211, 1981. (cited on pages 63, 66, and 211)

[136] J. Sánchez-Ca nizares and F. Sols. Translational symmetry and microscopic preparation in oscillator models of quantum dissipation. *Phys. A*, 212:181, 1994. (cited on p. 64)

[137] P. Schramm H. Grabert and G. Ingold. Quantum brownian motion: the functional integral approach. *Phys. Rep.*, 168:115, 1988. (cited on p. 65)

[138] V. Hakim and V. Ambegaokar. Quantum theory of a free particle interacting with a linearly dissipative environment. *Phys. Rev. A*, 32:423, 1985. (cited on pages 65 and 66)

[139] A. Schmid. Diffusion and localization in a dissipative quantum system. *Phys. Rev. Lett.*, 51:1506, 1983. (cited on pages 65 and 66)

[140] F. Guinea, V. Hakim, and A. Muramatsu. Diffusion and localization of a particle in a periodic potential coupled to a dissipative environment. *Phys. Rev. Lett.*, 54:263, 1985. (cited on pages 65, 66, and 69)

[141] F. Guinea. Friction and particle-hole pairs. *Phys. Rev. Lett.*, 53:1268, 1984. (cited on p. 65)

[142] F. Guinea, R.A. Jalabert, and F. Sols. Electronic lifetimes in ballistic quantum dots electrostatically coupled to metallic environments. *Phys. Rev. B*, 70:085310, 2004. (cited on pages 65, 146, and 152)

[143] G. D. Mahan. *Many-Particle Physics (third edition)*. Kluwer Academic/ Plenum Publishers, New York, 2000. (cited on pages 69, 152, 165, and 217)

[144] D.J. Amit, Y.Y. Goldschmidt, and S. Grinstein. Renormalisation group analysis of the phase transition in the 2d coulomb gas, sine-gordon theory and xy-model. *J. Phys. A: Math. Gen.*, 13:585, 1980. (cited on p. 69)

[145] J. M. Kosterlitz and D. J. Thouless. Long range order and metastability in two dimensional solids and superfluids. *J. Phys. C: Solid State Phys.*, 5:L124, 1972. (cited on pages 69 and 98)

[146] S. Chakravarty. Quantum fluctuations in the tunneling between superconductors. *Phys. Rev. Lett.*, 49:681, 1982. (cited on p. 69)

[147] A.J. Bray and M. A. Moore. Influence of dissipation on quantum coherence. *Phys. Rev. Lett.*, 49:1545, 1982. (cited on p. 69)

[148] R. Silbey and R.A. Harris. Variational calculation of the dynamics of a two level system interacting with a bath. *J. Chem. Phys.*, 80:2615, 1984. (cited on p. 70)

[149] R.P. Feynman. *Statistical Mechanics, 2nd ed*. Perseus Books Group, Reading, MA, 1976. (cited on p. 71)

[150] A. Chin and M. Turlakov. Coherent-incoherent transition in the sub-ohmic spin-boson model. *Phys. Rev. B*, 73:075311, 2006. (cited on p. 73)

[151] S. K. Kehrein and A. Mielke. On the spin-boson model with a sub-ohmic bath. *Phys. Lett. A*, 219:313, 1996. (cited on p. 73)

[152] S. Tornow, N. Tong, and R. Bulla. Dissipative transfer in donor-bridge-acceptor systems: numerical renormalization group calculation of equilibrium properties. *J. Phys.: Condens. Matter*, 18:5985, 2006. (cited on p. 76)

[153] R. Bulla, N. Tong, and M. Vojta. Numerical renormalization group for bosonic systems and application to the sub-ohmic spin-boson model. *Phys. Rev. Lett.*, 91:170601, 2003. (cited on p. 84)

[154] F. Marquadt and D.S. Golubev. Many-fermion generalization of the caldeira-leggett model. *Phys. Rev. A*, 72:022113, 2003. (cited on p. 87)

[155] J.Sabio and S. Kehrein. Sudden interaction quench in the quantum sine-gordon model. *arXiv:0911.1302*, 2009. (cited on p. 89)

[156] M. Cramer, C.M. Dawson, J. Eisert, and T.J. Osborne. Exact relaxation in a class of nonequilibrium quantum lattice systems. *Phys. Rev. Lett.*, 100:030602, 2008. (cited on pages 91 and 213)

[157] M. Cramer, A. Flesch, I.P. McCulloch, U. Schollwöck, and J. Eisert. Exploring local quantum many-body relaxation by atoms in optical superlattices. *Phys. Rev. Lett.*, 101:063001, 2008. (cited on p. 91)

[158] P. Reimann. Foundations of statistical mechanics under experimentally realistic conditions. *Phys. Rev. Lett.*, 101:190403, 2008. (cited on pages 92 and 213)

[159] J. M. Deutsch. Quantum statistical mechanics in a closed system. *Phys. Rev. A*, 43:2046, 1991. (cited on pages 92 and 213)

[160] M. Srednicki. Chaos and quantum thermalization. *Phys. Rev. E*, 50:888, 1994. (cited on pages 92 and 213)

[161] M. Rigol, V. Dunjko, and M. Olshanii. Thermalization and its mechanism for generic isolated quantum systems. *Nature*, 452:854, 2008. (cited on pages 92 and 213)

[162] G. Biroli, C. Kollath, and M. Läuchli. Does thermalization occur in an isolated system after a global quantum quench? *arXiv:0907.3731*, 2009. (cited on p. 92)

[163] M. Rigol, V. Dunjko, V. Yurovsky, and M. Olshanii. Relaxation in a completely integrable many-body quantum system: An *ab initio* study of the dynamics of the highly excited states of 1d lattice hard-core bosons. *Phys. Rev. Lett.*, 98:050405, 2007. (cited on pages 94 and 213)

[164] E.T. Jaynes. Information theory and statistical mechanics. *Phys. Rev.*, 106:620, 1957. (cited on p. 94)

[165] M. A. Cazalilla. Effect of suddenly turning on interactions in the luttinger model. *Phys. Rev. Lett.*, 97:156403, 2006. (cited on pages 94, 95, and 111)

[166] A. Iucci and M.A. Cazalilla. Quantum quench dynamics of some exactly solvable models in one dimension. *arXiv:0907.1205*, 2009. (cited on pages 94, 95, and 96)

[167] M. Eckstein and M. Kollar. Nonthermal steady states after an interaction quench in the falikov-kimball model. *Phys. Rev. Lett.*, 100:120404, 2008. (cited on p. 94)

[168] A. Faribault, P. Calabrese, and J. Caux. Quantum quenches from integrability: the fermionic pairing model. *J. Stat. Mech.*, page P03018, 2008. (cited on p. 94)

[169] A. Faribault, P. Calabrese, and J. Caux. Bethe ansatz approach to quench dynamics in the richardson model. *J. Math. Phys.*, 50:095212, 2008. (cited on p. 94)

[170] S. R. Manmana, S. Wessel, R. M. Noack, and A. Muramatsu. Strongly correlated fermions after a quantum quench. *Phys. Rev. Lett.*, 98:210405, 2007. (cited on p. 94)

[171] A. Hackl and S. Kehrein. Real time evolution in quantum many-body systems with unitary perturbation theory. *Phys. Rev. B*, 78:092303, 2008. (cited on pages 95, 103, and 211)

[172] M. Moeckel and S. Kehrein. Interaction quench in the hubbard model. *Phys. Rev. Lett.*, 100:175702, 2008. (cited on pages 95, 104, 110, 111, and 214)

[173] M. Moeckel and S. Kehrein. Real-time evolution for weak interaction quenches in quantum systems. *Ann. Phys.*, 324:2146, 2009. (cited on pages 95, 104, 110, 111, 213, and 214)

[174] A. O. Gogolin, A. M. Tsvelik, and A.A. Nersesyan. *Bosonization and Strongly Correlated Systems*. Cambridge University Press, Cambridge, 2004. (cited on pages 96 and 213)

[175] A. B. Zamolodchikov, 1977. (cited on pages 96 and 213)

[176] S. Mandelstam. Soliton operators for the quantized sine-gordon equation. *Phys. Rev. D*, 11:3026, 1975. (cited on p. 99)

[177] J. von Delft and H. Schoeller. Bosonization for beginners – refermionization for experts, 2004. (cited on pages 99 and 101)

[178] S. Kehrein. Flow equation approach to the sine-gordon model. *Nucl. Phys. B*, 592:512, 2001. (cited on pages 101, 103, and 213)

[179] A. Hackl, D. Roosen, S. Kehrein, and W. Hofstetter. Nonequilibrium spin dynamics in the ferromagnetic kondo model. *Phys. Rev. Lett.*, 102:196601, 2009. (cited on pages 104, 110, 111, and 214)

[180] A. Hackl, M. Vojta, and S. Kehrein. Non-equilibrium magnetization dynamics of ferromagnetically coupled kondo spins, 2009. (cited on pages 110, 111, and 214)

[181] E. Fermi, J. Pasta, and S. Ulam. *Collected Papers of Enrico Fermi: 266. Studiees of Non Linear Problems, Document LA-1940 (May 1955)*. The University of Chicago Press, 1965. (cited on p. 111)

[182] G. Gallavotti (Editor). *The Fermi-Pasta-Ulam Problem – A Status Report*. Springer, 2007. (cited on p. 111)

[183] L. Landau. The theory of a fermi liquid. *Sov. Phys. JETP*, 3:920, 1957. (cited on p. 117)

[184] D. Pines and P. Nozieres. *The Theory of Quantum Liquids*. W. A. Benjamin Inc, New York, 1966. (cited on pages 117, 162, 163, 164, 166, 215, and 217)

[185] H. Bruus and K. Flensberg. *Many-Body Quantum Theory in Condensed Matter Physics*. Oxford University Press, Oxford, 2004. (cited on pages 118 and 217)

[186] J. Polchinski. Effective field theory and the fermi surface. *Lectures presented at TASI 1992, arXiv:hep-th/9210046*, 1992. (cited on pages 118 and 120)

[187] J.R. Schrieffer. *Theory of Superconductivity –Revised printing*. Westview Press, USA, 1999 (Reprinted). (cited on pages 122, 193, and 199)

[188] J. Hubbard. Electron correlations in narrow energy bands. *Proc. Roy. Soc. A*, 276:238, 1963. (cited on p. 122)

[189] J. Gonzalez, F. Guinea, and M.A.H. Vozmediano. Non-fermi liquid behavior of electrons in the half-filled honeycomb lattice (a renormalization group approach). *Nucl. Phys. B*, 424:595, 1994. (cited on pages 124, 125, 130, and 218)

[190] J. Gonzalez, F. Guinea, and M.A.H. Vozmediano. Unconventional quasiparticle lifetime in graphite. *Phys. Rev. Lett.*, 77:3589, 1996. (cited on pages 124 and 130)

[191] S.M. Bachilo, M. S. Strano, C. Kittrell, R. H. Hauge, R. E. Smalley, and R. B. Weisman. Structure-assigned optical spectra of single-walled carbon nanotubes. *Science*, 298:2361, 2002. (cited on pages 124 and 125)

[192] C.L. Kane and E.J. Mele. Electron interactions and scaling relations for optical excitations in carbon nanotubes. *Phys. Rev. Lett.*, 93:197402, 2004. (cited on pages 124 and 125)

[193] J. Gonzalez, F. Guinea, and M.A.H. Vozmediano. Marginal-fermi-liquid behavior from two-dimensional coulomb interaction. *Phys. Rev. B*, 59:R2474, 1999. (cited on pages 124, 125, 126, and 218)

[194] J. Sabio, J. Nilsson, and A.H. Castro Neto. f-sum rule and unconventional spectral weight transfer in graphene. *Phys. Rev. B*, 78:075410, 2008. (cited on pages 126 and 161)

[195] E.G. Mishchenko. Effect of electron-electron interactions on the conductivity of clean graphene. *Phys. Rev. Lett.*, 98:216801, 2007. (cited on p. 127)

[196] S. Gangadharaiah, A.M. Farid, and E. G. Mishchenko. Charge response function and a novel plasmon mode in graphene. *Phys. Rev. Lett.*, 100:166802, 2008. (cited on pages 127, 130, and 218)

[197] E. G. Mishchenko. Minimal conductivity in graphene: interaction corrections and ultraviolet anomaly. *Europhys. Lett.*, 83:17005, 2008. (cited on pages 129, 130, and 172)

[198] I.F. Herbut, V. Juricic, and O. Coulomb interaction, ripples, and the minimal conductivity of graphene. *Phys. Rev. Lett.*, 100:046403, 2008. (cited on pages 129, 137, and 218)

[199] D. E. Sheehy and J. Schmalian. Why is the optical transparency of graphene determined by the fine structure constant? *arXiv:0906.5164*, 2009. (cited on p. 129)

[200] M. Polini, A. Tomadin, R. Asgari, and A.H. MacDonald. Density functional theory of graphene sheets. *Phys. Rev. B*, 78:115426, 2008. (cited on pages 129 and 147)

[201] O. Vafek and M.J. Case. Renormalization group approach to two-dimensional coulomb interacting dirac fermions with random gauge potential. *Phys. Rev. B*, 77:033410, 2008. (cited on pages 130, 137, 138, 139, 140, and 194)

[202] A. G. Grushin, B. Valenzuela, and M.A.H. Vozmediano. Effect of coulomb interactions on the optical properties of doped graphene. *arXiv:0907.0118*, 2009. (cited on pages 130 and 131)

[203] Z.Q. Li, E.A. Henriksen, Z. Jiang, Z. Hao, M.C. Martin, P. Kim, H.L. Stormer, and D.N. Basov. Dirac charge dynamics in graphene by infrared spectroscopy. *Nat. Phys.*, 4:532, 2008. (cited on pages 130 and 217)

[204] N.M.R. Peres, T. Stauber, and A. H. Castro Neto. The infrared conductivity of graphene. *Europhys. Lett.*, 84:38002, 2008. (cited on p. 131)

[205] G. Li, A. Luican, and E. Y. Andrei. Scanning tunneling spectroscopy of graphene on graphite. *Phys. Rev. Lett.*, 102:176804, 2009. (cited on p. 131)

[206] R.R. Nair, P. Blake, A.N. Grigorenko, K.S. Novoselov, T.J. Booth, T. Stauber, N.M.R. Peres, and A.K. Geim. Universal dynamic conductivity and quantized visible opacity of suspended graphene. *Science*, 320:1308, 2008. (cited on p. 132)

[207] K.W.K. Shung. Dielectric function and plasmon structure of stage-1 intercalated graphite. *Phys. Rev. B*, 34:979, 1986. (cited on p. 132)

[208] B. Wunsch, T. Stauber, F. Sols, and F. Guinea. Dynamical polarization of graphene at finite doping. *New. J. Phys.*, 8:318, 2006. (cited on pages 133, 151, 194, and 218)

[209] E.H. Hwang and S. Das Sarma. Dielectric function, screening, and plasmons in two-dimensional graphene. *Phys. Rev. B*, 75:205418, 2007. (cited on pages 132, 133, and 194)

[210] M. Polini, R. Asgari, G. Borghi, Y. Barlas, T. Pereg-Barnea, and A.H. MacDonald. Plasmons and the spectral function of graphene. *Phys. Rev. B*, 77:081411(R), 2008. (cited on pages 134, 174, and 218)

[211] E.H. Hwang and S. Das Sarma. Quasiparticle spectral function in doped graphene: Electron-electron interaction effects in arpes. *Phys. Rev. B*, 77:081412(R), 2008. (cited on pages 134 and 174)

[212] W. Tse and S. Das Sarma. Phonon-induced many-body renormalization of the electronic properties of graphene. *Phys. Rev. Lett.*, 99:236802, 2007. (cited on p. 135)

[213] R. Roldan, J.N. Fuchs, and M.O. Goerbig. Collective modes of doped graphene and a standard two-dimensional electron gas in a strong magnetic field: Linear magnetoplasmons versus magnetoexcitons. *Phys. Rev. B*, 80:085, 2007. (cited on p. 135)

[214] D.T. Son. Quantum critical point in graphene approached in the limit of infinitely strong coulomb interaction. *Phys. Rev. B*, 75:235423, 2009. (cited on pages 137 and 218)

[215] I. F. Herbut, V. Juricic, and O. Vafek. Coulomb interaction, ripples, and the minimal conductivity of graphene. *Phys. Rev. Lett.*, 100:046403, 2008. (cited on pages 137, 139, and 218)

[216] J. E. Drut and D.T. Son. Renormalization group flow of quartic perturbations in graphene: Strong coupling and large-n limits. *Phys. Rev. B*, 77:075115, 2008. (cited on p. 138)

[217] T. Stauber, F. Guinea, and M.A.H. Vozmediano. Disorder and interaction effects in two-dimensional graphene sheets. *Phys. Rev. B*, 71:041406, 2005. (cited on p. 139)

[218] M.S. Foster and I. L. Aleiner. Graphene via large n: A renormalization group study. *Phys. Rev. B*, 77:195413, 2008. (cited on p. 139)

[219] S.A. Moskalendo and D.W. Snoke. *Bose-Einstein Condensation of Excitons and Biexcitons*. Cambridge University Press, Cambridge, 2000. (cited on pages 139 and 199)

[220] J.E. Drut and T. A. Lähde. Is graphene in vacuum an insulator. *Phys. Rev. Lett.*, 102:026802, 2009. (cited on pages 140, 194, and 221)

[221] J.E. Drut and T. A. Lähde. Lattice field theory simulations of graphene. *Phys. Rev. B*, 79:165425, 2009. (cited on p. 140)

[222] S. Hands and C. Strouthos. Quantum critical behavior in a graphenelike model. *Phys. Rev. B*, 78:165423, 2008. (cited on p. 140)

[223] W. Armour, S. Hands, and C. Strouthos. Monte carlo simulation of the semimetal-insulator phase transition in monolayer graphene. *arXiv:0910.5646*, 2009. (cited on pages 140 and 194)

[224] D. V. Khveshchenko. Ghost excitonic insultator transition in layered graphite. *Phys. Rev. Lett.*, 87:246802, 2001. (cited on pages 140, 141, 201, 219, and 221)

[225] E.V. Gorbar, V.P. Gusynin, V.A. Miransky, and I.A. Shovkovy. Magnetic field driven metal-insulator phase transition in planar systems. *Phys. Rev. B*, 66:045108, 2002. (cited on pages 140 and 141)

[226] D.V. Khveshchenko. Massive dirac fermions in single-layer graphene. *J. Phys.:Condens. Matter*, 21:075303, 2009. (cited on pages 141, 194, 219, and 221)

[227] G. Liu and G. Cheng. Interaction and excitonic insulating transition in graphene. *Phys. Rev. B*, 79:205429, 2009. (cited on pages 141, 219, and 221)

[228] O.V. Gamayun, E.V. Gorbar, and V.P. Gusynin. Gap generation and semimetal-insulator phase transition in graphene. *arXiv: 0911.4878*, 2009. (cited on pages 141 and 221)

[229] V. M. Pereira, J. Nilsson, and A. H. Castro Neto. Coulomb impurity problem in graphene. *Phys. Rev. Lett.*, 99:166802, 2007. (cited on pages 141, 174, 178, 179, 193, and 219)

[230] A. V. Shytov, M. I. Katsnelson, and L. S. Levitov. Vacuum polarization and screening of supercritical impurities in graphene. *Phys. Rev. Lett.*, 99:236801, 2007. (cited on p. 179)

[231] A. V. Shytov, M. I. Katsnelson, and L. S. Levitov. Atomic collapse and quasi-rydberg states in graphene. *Phys. Rev. Lett.*, 99:226802, 2007. (cited on pages 141, 178, 180, 188, 194, and 219)

[232] O.V. Gamayun, E.V. Gorbar, and V.P. Gusyinin. *arXiv:0907.5409*, 2009. (cited on pages 141, 180, 193, 194, and 219)

[233] J. Wang, H.A. Fertig, and G. Murthy. *arXiv:0909.4076*, 2009. (cited on pages 141, 180, and 193)

[234] H.P. Dahal, Y. N. Joglekar, K. S. Bedell, and A. V. Balatsky. Absence of wigner crystallization in graphene. *Phys. Rev. B*, 74:233405, 2006. (cited on p. 142)

[235] N.M.R. Peres, F. Guinea, and A.H. Castro Neto. Coulomb interactions and ferromagnetism in pure and doped graphene. *Phys. Rev. B*, 72:174406, 2005. (cited on p. 142)

[236] J. Sabio, C. Seoanez, S. Fratini, F. Guinea, A.H. Castro Neto, and F. Sols. Electrostatic interactions between graphene layers and their environment. *Phys. Rev. B*, 77:195409, 2008. (cited on pages 143, 145, 151, 157, 159, 175, and 216)

[237] D.C. Elias, R.R. Nair, T.M.G. Mohiuddin, S. V. Morozov, P. Blake, M.P. Halsall, A.C. Ferrari, D. W. Boukhvalov, M.I. Katsnelson, A.K. Geim, and K. S. Novoselov. Control of graphene's properties by reversible hydrogenation: Evidence for graphane. *Science*, 323:610, 2009. (cited on p. 144)

[238] F. Schedin, A.K. Geim, S. V. Morozov, E. W. Hill, P. Blake, M.I. Katsnelson, and K.S. Novoselov. Detection of individual gas molecules adsorbed on graphene. *Nat. Mat.*, 6:652, 2007. (cited on pages 144, 147, 156, and 215)

[239] Y. Zhang, V.W. Brar, C. Girit, A. Zettl, and M. F. Crommie. Origin of spatial charge inhomogeneity in graphene. *Nat. Phys,*, 5:722, 2009. (cited on pages 145, 146, and 147)

[240] B.A. Morrow and A.J. McFarlan. Chemical reactions at silica surfaces. *J. Non-Crys. Sol.*, 120:61, 1990. (cited on p. 145)

[241] O. Sneh and S. M. George. Thermal stability of hydroxil groups on a well-defined silica surface. *J. Phys. Chem.*, 99:4639, 1995. (cited on p. 145)

[242] W. Kim, A. Javey, O. Vermesh, Q. Wang, Y. Li, and H. Dai. Hysteris caused by water molecules in carbon nanotube field-effect transistors. *Nano. Lett.*, 3:193, 2003. (cited on pages 145, 154, and 156)

[243] S. Sze. *Physics of semiconductor devices*. Wiley-Interscience, New York, 1981. (cited on pages 146 and 215)

[244] K. Nomura and A.H. MacDonald. Quantum transport of massless dirac fermions. *Phys. Rev. Lett.*, 98:076602, 2007. (cited on pages 146 and 153)

[245] S. Adam, E.H. Hwang, V. M. Galitski, and S. Das Sarma. A self-consistent theory for graphene transport. *Procl. Natl. Acad. Sci. U.S.A.*, 104:18392, 2007. (cited on pages 146 and 153)

[246] N. Garcia, Z. Yan, A. Ballestar, J. Barzola-Quiquia, F. Bern, and P. Esquinazi. Disordered electrical potential observed on the surface of sio_2 by electric field microscopy. *arXiv:0905.2941*, 2009. (cited on pages 146 and 215)

[247] S.Q. Wang and G. D. Mahan. Electron scattering from surface excitations. *Phys. Rev. B*, 6:4517, 1972. (cited on pages 146 and 215)

[248] S. Fratini and F. Guinea. Substrate-limited electron dynamics in graphene. *Phys. Rev. B*, 77:195415, 2008. (cited on pages 146, 147, and 152)

[249] L. Borda, G. Zarand, and P. Simon. Dissipation-induced quantum phase transition in a quantum box. *Phys. Rev. B*, 72:155311, 2005. (cited on p. 146)

[250] F. Guinea. Electronic dephasing in wires due to metallic gates. *Phys. Rev. B*, 71:045424, 2005. (cited on p. 146)

[251] M.A. Cazalilla, F. Sols, and F. Guinea. Dissipation-driven quantum phase transitions in a tomonaga-luttinger liquid electrostatically coupled to a metallic gate. *Phys. Rev. Lett.*, 97:076401, 2006. (cited on p. 146)

[252] O. Leenaerts, B. Partoens, and F.M. Peeters. Water on graphene: Hydrophobicity and dipole moment using density functional theory. *Phys. Rev. B*, 79:235440, 2009. (cited on p. 147)

[253] C. Ertler, S. Konschuh, M. Gmitra, and J. Fabian. Electron spin relaxation in graphene: The role of the substrate. *Phys. Rev. B*, 80:041405(R), 2009. (cited on p. 147)

[254] J. S. Bunch, A. M. van der Zande, S. S. Verbridge, I. W. Frank, D. M. Tanenbaum, J. M. Parpia, H. G. Craighead, and P. L. McEuen. Electromechanical resonators from graphene sheets. *Science*, 315:490, 2007. (cited on pages 147, 158, and 216)

[255] S.V. Morozov, K. S. Novoselov, M. I. Katsnelson, F. Schedin, D. C. Elias, J. A. Jaszczak, and A.K. Geim. Giant intrinsic carrier mobilities in graphene and its bilayer. *Phys. Rev. Lett.*, 100:016602, 2008. (cited on pages 147 and 149)

[256] J. F. Dobson, J. Wang, B.P. Dinte, K. McLennan, and H.M. Le. Soft cohesive forces. *Int. Journal of Quantum Chemistry*, 101:579, 2005. (cited on pages 149 and 215)

[257] S. L. Tan and P.W. Anderson. Long-range van der waals forces between restricted-dimensional metals. *Chem. Phys. Lett.*, 97:23, 1983. (cited on pages 150 and 165)

[258] F. Guinea. Charge distribution and screening in layered graphene systems. *Phys. Rev. B*, 75:235433, 2007. (cited on p. 151)

[259] F.J. Dobson, A. White, and A. Rubio. Asymptotics of the dispersion interaction: Analytic benchmarks vor van der waals energy functionals. *Phys. Rev. Lett.*, 96:073201, 2006. (cited on pages 152, 155, and 175)

[260] M. Antognozzi, A. Humphris, and M. Miles. Observation of molecular layering in a confined water film and study of the layers viscoelastic properties. *Appl. Phys. Lett.*, 78:300, 2001. (cited on p. 154)

[261] A. Opitz, M. Scherge, S. U. Ahmed, and J. Schaefer. A comparative investigation of thickness measurements of ultra-thin water films by scanning probe techniques. *J. Appl. Phys.*, 101:064310, 2007. (cited on p. 154)

[262] E. Stolyarova, K. T. Rim, S. Ryu, J. Maultzsch, P. Kim, L. E. Brus, T. F. Heinz, M. S. Hybertsen, and G. W. Flynn. High-resolution scanning tunneling microscopy imaging of mesoscopic graphene sheets of an insulating surface. *Proc. Natl. Acad. Sci. U.S.A.*, 104:9209, 2007. (cited on p. 155)

[263] L. X. Benedict, N. G. Chopra, M. L. Cohen, A. Zettl, S. G. Louie, and V. H. Crespi. Microscopic determination of the interlayer binding energy in graphite. *Chem. Phys. Lett.*, 286:490, 1998. (cited on p. 155)

[264] M. Hasegawa, K. Nishidate, and H. Lyetomi. Energetics of interlayer binding in graphite: The semiempirical approach revisited. *Phys. Rev. B*, 76:115424, 2007. (cited on p. 155)

[265] T.O. Wehling, K. S. Novoselov, S. V. Morozov, E. E. Vdovin, M. I. Katsnelson, A. K. Geim, and A. I. Lichtenstein. Molecular doping of graphene. *Nano. Lett.*, 8:173, 2008. (cited on p. 156)

[266] O. Leenaerts, B. Partoens, and F.M. Peeters. Adsorption of h_2o, nh_3, co, no_2 and no on graphene: A first-principles study. *Phys. Rev. B*, 77:125416, 2009. (cited on p. 156)

[267] E. Mariani and F. von Oppen. Flexural phonons in free-standing graphene. *Phys. Rev. Lett.*, 100:076801, 2008. (cited on p. 157)

[268] C. Seoanez, F. Guinea, and A.H. Castro Neto. Dissipation in graphene and nanotube resonators. *Phys. Rev. B*, 76:125427, 2007. (cited on p. 158)

[269] J.P. Batra, N. Garcia, H. Rohner, H. Salemink, E. Stoll, and S. Ciraci. A study of graphite surface with stm and electronic structure calculations. *Surf. Sci.*, 181:126, 1987. (cited on pages 158 and 216)

[270] M. Salmeron, D. F. Ogletree, C. Ocal, H.C. Wang, G. Neubauer, W. Kolbe, and G. Meyers. Tip-surface forces during imaging by scanning tunneling microscopy. *J. Vac. Sci. Technol. B*, 9:1347, 1991. (cited on p. 158)

[271] N. Iwamoto. Sum rules and static local-field corrections of electron liquids in two and three dimensions. *Phys. Rev. A*, 30:3289, 1984. (cited on pages 163 and 164)

[272] A. J. Millis. Optical spectral weight and the physics of correlated electron systems: General results and application to cmr manganites. *J. Elec. Spec. Rel. Phen.*, 114:669, 2001. (cited on pages 165 and 218)

[273] S.P. Goldman and G. W. F. Drake. Relativistic sum rules and integral properties of the dirac equation. *Phys. Rev. A*, 25:2877, 1982. (cited on pages 166 and 217)

[274] R. Cenni. On the f sum rule an its extensions. *Nucl. Phys. A*, 696:605, 2001. (cited on p. 166)

[275] V.P. Gusyinin, S. G. Sharapov, and J. P. Carbotte. Sum rules for the optical and hall conductivity in graphene. *Phys. Rev. B*, 75:165407, 2007. (cited on pages 166 and 217)

[276] J. E. Hirsch. Apparent violation of the conductivity sum rule in certain superconductors. *Physica C*, 199:305, 1992. (cited on p. 174)

[277] A. J. Millis. *Strong Interactions in Low Dimensions*. Kluwer, Berlin, 2003. (cited on p. 174)

[278] M.B.J. Meinders, H. Eskers, and G. A. Sawatzky. Spectral-weight transfer: Breakdown of low-energy-scale sum rules in correlated systems. *Phys. Rev. B*, 48:3916, 1993. (cited on p. 174)

[279] X. Yan and C.S. Ting. Interacting electrons in graphene studied under the renormalized ring diagram approximation. *Phys. Rev. B*, 76:155401, 2007. (cited on p. 174)

[280] J.Sabio, F. Sols, and F. Guinea. The two-body problem in graphene. *arXiv:0911.0376*, 2009. (cited on p. 178)

[281] D. S. Novikov. Elastic scattering theory and transport in graphene. *Phys. Rev. B*, 76:245435, 2007. (cited on pages 178, 179, and 194)

[282] M. Abramowitz and I. A. Stegun. *Handbook of Mathematical Functions*. Dover, 1965. (cited on p. 179)

[283] J. Friedel. The distribution of electrons round impurities in monovalent metals. *Phil. Mag.*, 43:337, 1952. (cited on p. 179)

[284] Bill Sutherland. Localization of electronic wavefunctions due to local topology. *Phys. Rev. B*, 34:5208, 1986. (cited on pages 182, 183, and 189)

[285] T. Ando. Screening effect and impurity scattering in monolayer graphene. *J. Phys. Soc. Jpn.*, 75:074716, 2006. (cited on p. 194)

[286] C. Comte and P. Nozieres. Exciton bose condensation: the ground state of an electron-hole gas i. mean field description of a simplified model. *J. Physique*, 43:1069, 1982. (cited on p. 199)